THE MATHEMATICAL MODELLING OF HEAT TRANSFER AND FLUID FLOW IN CELLULAR METALLIC FOAMS

by

Johan G. Fourie

Dissertation presented for the degree of Doctor of Philosophy
at the University of Stellenbosch

Promoter: Professor J. P. du Plessis

October 2000

Declaration

I, the undersigned, hereby declare that the work contained in this dissertation is my own original work and that I have not previously in its entirety or in part submitted it at any university for a degree.

ABSTRACT

A mathematical model is presented which conceptualises fluid flow and heat transfer in cellular metallic foams completely saturated with a fluid in motion. The model consists of a set of elliptic partial differential governing equations describing, firstly, a momentum balance in the fluid by the spatial distribution of its locally mean velocity, and secondly, an energy balance in the fluid and in the solid matrix of the metallic foam, by the spatial and temporal distribution of their locally mean temperatures. The separate energy balance descriptions for the fluid and the solid matrix extend the application of the model to conditions of thermal equilibrium and thermal non-equilibrium between the fluid and the solid matrix. A computational solution algorithm is presented which allows the universal application of the model to porous domains of arbitrary shape, with spatially and temporally variable heat loads in a variety of forms.

OPSOMMING

'n Wiskundige model word voorgestel wat vloei en warmteoordrag voorspel in sellulêre metaalsponse wat in geheel gevul is deur 'n bewegende vloeier. Die vloeier kan in gas- of vloeistoffase verkeer. Die model bestaan uit 'n stel elliptiese parsiële differensiaalvergelykings wat in die eerste plek 'n momentum-ewewig in die vloeier beskryf in terme van 'n ruimtelike, lokaal-gemiddelde snelheidsveld, en wat tweedens 'n energie-ewewig in die vloeier en in die soliede matriks van die metaalspons beskryf in terme van ruimtelike en tydelike lokaal-gemiddelde temperatuur verspreidings. Die aparte energie-ewewig beskrywings vir die vloeier en vir die soliede matriks van die metaalspons brei die aanwending van die model uit na gevalle waar die vloeier en die soliede matriks in termiese ewewig of in termiese onewewig verkeer. 'n Numeriese oplossingsalgoritme word ook voorgestel vir die universele toepassing van die model op ruimtelik-arbitrêre metaalspons geometrië wat onderwerp word aan 'n aantal verskillende ruimtelik- en tydveranderlike termiese laste.

ACKNOWLEDGEMENTS

I would like to express my sincere gratitude to Professor Prieur du Plessis, my supervisor, for his friendship, judgement, enthusiastic support and generous guidance during the course of this research programme.

To my wife and best friend Soni, for her love and unconditional support through many years. Without the pleasant and warm home environment she has always created, this would have been so much harder.

This thesis is dedicated to my parents, without whom none of this would have been possible. I wish to express my sincere gratitude for an upbringing that forms the basis of all my inspiration.

Financial support was provided by the Harry Crossley Foundation. The University of Stellenbosch also assisted by funding an international conference visit. I would like to thank both these institutions for their support.

And finally, to my son Michael.

CONTENTS

NOMENCLATURE

a	characteristic cell size, coefficient
A	area
A_{sf}, $A_{\alpha\beta}$	interface area
b	coefficient
$\boldsymbol{B}$	body force vector
B	body force component
Bi	Biot modulus
c	cells, mass fraction, wall momentum transfer coefficient
c_p	adiabatic specific heat capacity
C_E	inertial coefficient
$C_{D,v}$	friction coefficient
$C_{D,f}$	drag coefficient
d	differential operator
d	characteristic dimension
d_m	diffusive mass transfer coefficient
$\overline{d}$	mean linear distance
D	substantial differential operator
D	dispersivity
$\boldsymbol{D}$	dispersivity tensor
D_{ft}	thermal diffusivity
D_{fv}	viscous diffusivity
D_M	mass dispersion coefficient
$\boldsymbol{D}_M$	mass dispersion tensor
D_P	momentum dispersion coefficient
$\boldsymbol{D}_P$	momentum dispersion tensor
D_T	thermal dispersion coefficient
$\boldsymbol{D}_T$	thermal dispersion tensor
e	2.7183
e	edges

E	stored energy, relaxation coefficient
Eu	Euler number
f	weighing factor, face
$\boldsymbol{f}$	viscous shear factor (tensor)
f_t	turbulence enhancement factor
$\boldsymbol{F}$	force vector
F_v	friction force
F_f	drag force
G	Gibbs function
h	enthalpy, convection coefficient
h_{sf}, $h_{\alpha\beta}$	interphasial heat transfer coefficient
h_{ss}, h_{ff}	system boundary heat transfer coefficient
H	height
$\boldsymbol{i}$	principle direction unit vector
I	internal heat source, light intensity
$\boldsymbol{j}$	mass transfer vector, principle direction unit vector
J	mass exchange
k	thermal conductivity
$\boldsymbol{k}$	principle direction unit vector
k_{total}	total heat transfer coefficient
k_{ss}, k_{ff}, $k_{\alpha\alpha}$, $k_{\beta\beta}$	effective thermal conductivity component
$\boldsymbol{k}_{ss}$, $\boldsymbol{k}_{ff}$, $\boldsymbol{k}_{\alpha\alpha}$, $\boldsymbol{k}_{\beta\beta}$	effective thermal conductivity tensor
k_{sf}, k_{fs}, $k_{\alpha\beta}$, $k_{\beta\alpha}$	coupled thermal conductivity component
$\boldsymbol{k}_{sf}$, $\boldsymbol{k}_{fs}$, $\boldsymbol{k}_{\alpha\beta}$, $\boldsymbol{k}_{\beta\alpha}$	coupled thermal conductivity tensor
K	permeability
K_0, K_1	modified Bessel function operator
l	overall REV dimension
m	generic principle direction designation, side-length
$\boldsymbol{m}$	generic unit vector in the m-direction
$\dot{m}$	mass flow rate
M	total mass
n	number
$\boldsymbol{n}$	normal surface unit vector

n_g	row correction factor
$\boldsymbol{n}_{sf}, \boldsymbol{n}_{fs}, \boldsymbol{n}_{\alpha\beta}, \boldsymbol{n}_{\beta\alpha}$	normal surface unit vector at the interface between phases
$\boldsymbol{n}_{ss}, \boldsymbol{n}_{\alpha\alpha}, \boldsymbol{n}_{ff}, \boldsymbol{n}_{\beta\beta}$	normal surface unit vector at an REV boundary or system boundary
$\overline{n}$	average number of edges per face
Nu	Nusselt number
p	pressure
$\overset{\circ}{p}$	pressure deviation
$\overline{p}$	mean pressure
P	power, momentum
$\boldsymbol{P}$	momentum vector
P_t	momentum transfer
$\boldsymbol{P}_t$	momentum transfer vector
Pe	Peclét number
Pr	Prandtl number
q	conduction
$\boldsymbol{q}$	conduction vector
Q	heat exchange
Re	Reynolds number
R_{sf}	thermal contact resistance between the solid and the fluid phases
R_{ss}	thermal contact resistance between at a system boundary
s	entropy
S_c	source term coefficient
t	time, edge length
T	temperature
$\overset{\circ}{T}$	temperature deviation
$\overline{T}$	mean temperature
Tu	turbulence
u	internal energy per unit mass
$\boldsymbol{u}$	unit diagonal tensor
$\boldsymbol{v}$	velocity vector
v	specific volume, velocity, vertices

v_x, v_y, v_z	velocity components in the principle directions
$\overset{\circ}{\boldsymbol{v}}$	velocity deviation vector
V	volume
w	channel width
x	principle direction
y	principle direction
z	principle direction, connectivity
Z	connectivity

Greek letters

α	generic phase designation, relation factor
β	generic phase designation
χ	tortuosity
δ	dimension
δ	Kronecker delta
ε	volume fraction
Δ	finite dimension, finite duration
γ	generic phase designation
η	area size parameter
φ	generic phase designation
λ	wavelength
μ	viscosity
μ_{total}	total viscous transfer coefficient
ξ	power index
π	3.1416
π, $\pi 1$, $\pi 2$, $\pi 3$	generic finite volume boundary
$\Pi 1$, $\Pi 2$, $\Pi 3$	generic grid point
ρ	density
σ	absorption coefficient
τ	viscous shear stress

$\boldsymbol{\tau}$	viscous shear stress vector or tensor
ϕ	intensive quantity
$\overset{\circ}{\phi}$	intensive quantity deviation
Φ	extensive quantity

Symbols

∂	partial differential operator
∇	del operator
$\langle\ \rangle$	volume-averaged intensive quantity
$\langle\ \rangle_\gamma$	phasial volume-averaged intensive quantity
$\langle\ \rangle_\gamma^\gamma$	intrinsic volume-averaged intensive quantity

Subscripts

A	generic specie
b	bottom finite volume
B	bottom grid point
d	directional
e	equilibrium, eastern boundary, path length, edge
eff	effective
E	eastern grid point
f	fluid, face
ff	fluid-fluid interface
fr	frontal
FT	fixed temperature
i	internal, inner boundary
ind	independent
I	inner grid point

h	hydraulic
l	left hand side, longitudinal
m	generic principle direction
M	methylene blue
n	non-equilibrium, northern boundary
nd	directional non-equilibrium
nn	non-directional non-equilibrium
N	northern grid point
o	overall, at reference conditions, outer boundary
O	outer grid point
p	isobaric, pore
pr	projected
P	central grid point
r	right hand side, resistance, radial, relative
R	reversible
s	southern boundary, solid, strand
ss	solid-solid interface
S	southern grid point
t	top finite volume boundary, transverse
T	top grid point
w	western boundary
W	western grid point
α	generic phase designation
β	generic phase designation
ϕ	cylindrical
ϕm	minimum cylindrical
γ	generic phase designation
φ	generic phase designation
θ	tangential
$\|\|$	parallel
$\perp$	perpendicular
I, *II*, *III*, *IV*	interface designations

Superscripts

0	at time t
1	at time $t+\Delta t$
′	correction
*	incorrect parameter

Abbreviations and acronyms

FT	fixed temperature
LHS	left hand side
max	maximum
ppi	pores per inch
RDP	reduced dispersivity parameter
REV	representative elementary volume
RHD	representative hydraulic diameter
RHS	right hand side
RUC	representative unit cell
SSE	sum of squares error
STP	standard temperature and pressure
UC	unit cell
VT	variable temperature

CHAPTER 1

INTRODUCTION

1.1 Convective heat transfer between a solid wall and an adjacent fluid

The fundamentals of engineering thermodynamics conceptually represent convective heat transfer between a solid wall and an adjacent fluid in motion as being in direct proportion to the surface area between the solid and the fluid, and the differential temperature of the solid wall and some average reference temperature in the fluid. A proportionality coefficient, often referred to as the *convection coefficient* (Holman, 1976, p.12), is defined as the ratio of heat transfer to the product of the surface area and differential temperature. This ratio depends on fluid properties and flow parameters.

For a particular fluid flowing at a fixed flow rate over a solid wall of thermal conductivity higher than that of the fluid, three techniques are generally applied to enhance heat transfer between the solid and the fluid. Primarily, the surface area at the interface may be enlarged by extending sections of the solid into the fluid. An enhancement of heat transfer will generally occur providing the extension is not in thermal equilibrium with the fluid. Secondly, the effective differential temperature between the solid and the fluid is increased by proper mixing in the fluid phase. And finally, the heat transfer coefficient may be increased by disrupting established thermal boundary layers, thereby exploiting the enhanced heat transfer processes associated with the initial development of thermal boundary layers.

1.2 Convective heat transfer in porous media

When a porous medium with a thermal conductivity comparable to that of the solid wall is brought into thermal contact with the solid wall and saturated with the fluid in motion, all three heat transfer enhancement techniques are applied. A region develops near the solid wall in which the solid of the porous medium and the fluid (referred to as the *solid phase* and the *fluid phase* respectively) are not in thermal equilibrium. In this region, which is referred to as the *thermal non-equilibrium region*, locally mean temperatures of the two phases differ and there is a net exchange of heat from the higher temperature phase to the lower temperature phase. In a complex porous structure, the difference in locally mean temperatures is often increased by the mixing of fluid in this region with that outside the region, as a result of interaction between the fluid and the porous structure. This interaction also enhances heat exchange from the higher temperature phase to the lower temperature phase by disrupting established thermal boundary layers in the fluid. In the far field, away from the solid wall, the locally mean temperatures of the two phases approach each other asymptotically to a condition of thermal equilibrium.

The enhancement of heat transfer between a solid wall and an adjacent fluid in motion, by the introduction of a porous medium into the flow domain, has been demonstrated over the last few decades by the use of metallic packed beds in compact heat exchangers. More recently, advances in the manufacture of metallic porous materials have initiated several experimental investigations into the thermal properties of those materials. Wire mesh and spiral brush tube inserts (Megerlin *et al.*, 1974; Kuzay *et al.*, 1991), flat-plate rectangular microchannels (Peng *et al.*, 1995), and sintered heat sinks (Lindemuth *et al.*, 1994) have all shown phenomenal increases in the level of heat transfer. However, these investigations all support exceptional thermal performance expectations from cellular metallic foam configurations.

1.3 Characteristics of cellular metallic foams

Cellular metallic foams, as shown in Figure 1.1, have a reticulated structure of open, duodecahedronal-shaped cells with 12 to 14 pentagonal or hexagonal faces. The edges of the cells are formed by individual strands. Metallic foams are manufactured by the directional solidification of metal from a super-heated liquidus state in an environment of overpressure and high vacuum. Surface tension during solidification of the superheated metal causes both material clustering at strand vertices and each individual strand to have a triangular cross-sectional shape as shown in Figure 1.2. The three-dimensional continuous structure, with its strands of triangular cross-sectional shape, has a high surface area per unit volume ratio. This promotes eddies which in turn promote complete mixing of the fluid phase (Karniadakis *et al.*, 1988) as well as efficient scrubbing of heat exchange surfaces by the fluid phase. Furthermore, advanced aluminium braising techniques yield bonds of excellent mechanical strength and good thermal contact between aluminium foams and solid aluminium substrates.

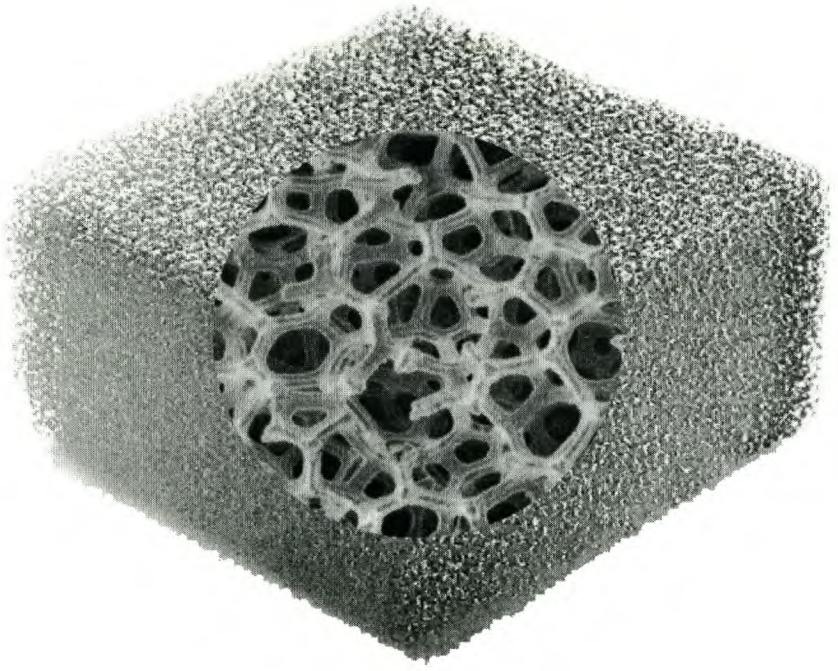

Figure 1.1 Cellular metallic foam.

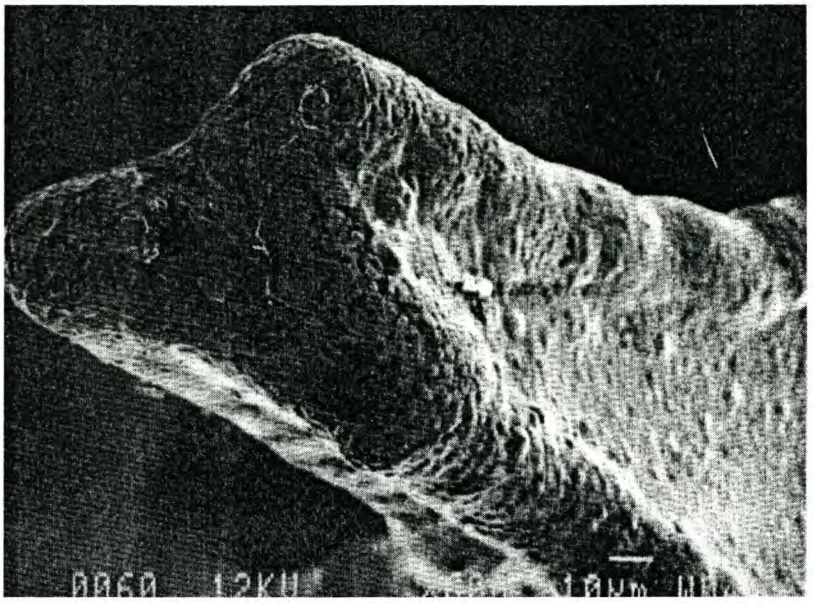

Figure 1.2 Microscopic image of the cross-section of a single strand (Du Plessis *et al.*, 1994).

Beyond the thermal attributes of metallic fibrous materials in general, metallic foams also exhibit beneficial structural characteristics, such as a relatively high strength and stiffness at low weight (Gibson and Ashby, 1988). Compared to wire mesh inserts, spiral brush inserts, microchannels and microsintered materials, metallic foams have a much broader physical characterisation (*e.g.* porosity range and cell size range), which allows precise specification with good repeatability. The manufacturing process of metallic foams has advanced to the production of metallic foams with regular cell morphologies and a variable porosity in one dimension. Moreover, there is no practical upper limitation on the ratio of the strand diameter to the dimensions of the porous system.

1.4 Thermal performance of metallic foams and their application as a heat transfer enhancement medium

Independent experimental measurements have shown that with complete thermal contact to a solid wall, the application of aluminium foam removes an order of magnitude more heat when compared to an open channel (Bastawros *et al.*, 1998). Even in the absence of thermal contact between the porous medium and the solid wall (*i.e.* considering only the contribution of dispersion in the fluid phase and the disruption of established thermal boundary layers on the solid wall), investigators have found a substantial improvement in heat transfer by the introduction of a metallic foam (Hunt and Tien, 1988; Guilleminot and Gurgel, 1990). Guilleminot *et al.* (1993) concluded that using a metallic foam as a solid adsorber can reduce the size of general industrial adsorption thermal devices by a factor of five to ten.

A recent study by NASA (1998) has demonstrated the feasibility of using metallic foam to enhance heat transfer in an annular region surrounding a liquid propellant combustion chamber. The investigation found greater heat transfer effectiveness than existing methods, which makes it possible to design smaller and lighter heat exchangers. The study also found that, in comparison with machined-channel and brazed-tube heat exchangers, metallic foam heat exchangers could be fabricated more easily and at lower cost. The study further concluded that a properly designed metallic foam heat exchanger exhibits less back pressure than a machined-channel or brazed-tube heat exchanger of equal heat transfer capacity.

One application of significant potential is in heat sinks for high power electronic devices (Lu *et al.*, 1998a), which demand power densities above 10^7 W/m^2. Moreover, in advanced high-frequency microwave systems, the signal phase characteristics of microwave modules are also sensitive to their semiconductor junction temperatures. Precise control of the signal phase from each microwave module is critical to the overall system performance of these systems. This could be achieved if the operating temperatures of identical modules were the same and, to provide reliable operation, if these temperatures were as low as possible. Inserting a metallic foam layer inside a parallel flow cold plate aperture achieves the flow and temperature uniformity required

for similar operating temperatures of identical modules mounted to the cold plate aperture (Antohe *et al.*, 1996). If the operating temperatures of identical modules differ, precise control can only be achieved by using sophisticated, computerised calibration techniques to compensate for the differences in electrical characteristics.

Other thermal applications of metallic foams include adsorption heat pumps (Guilleminot and Gurgel, 1990), heat exchangers for airborne equipment, coal combustors (Tien and Vafai, 1990), cryogenic heat exchangers as shown in Figure 1.3, regenerators for thermal engines, ablative sealing for compressor and turbine blades, air-cooled condenser cooling towers, liquid heat exchangers (Kaviany, 1985; Antohe *et al.*, 1996) as shown in Figure 1.4 and heat pumps as shown in Figure 1.5. Increased and more widely varied utilisation of this relatively new material is expected in future.

Another advantage of metallic foam heat exchangers is that all flow paths through the foam are interconnected, so that if a flow becomes obstructed by debris lodged in one place in a channel, the flow can continue elsewhere in the channel; in other words, complete blockage of a channel is unlikely. This is in contrast to the situation in a heat exchanger containing narrow tubes or narrow, precisely machined channels, which can become blocked more readily.

1.5 Previous approaches towards heat transfer modelling in cellular metallic foams

The significant interest in metallic foams has encouraged the development of mathematical models to predict their pressure drop and thermal behaviour. Both the optimal design of metallic foam heat exchangers and investigations into the effects of changing flow and morphological parameters on the overall performance of these heat exchangers, benefit from these models.

The first mathematical models dedicated to predict the thermal performance of metallic foams were mostly empirical in nature (Hunt and Tien, 1988). In their most basic form,

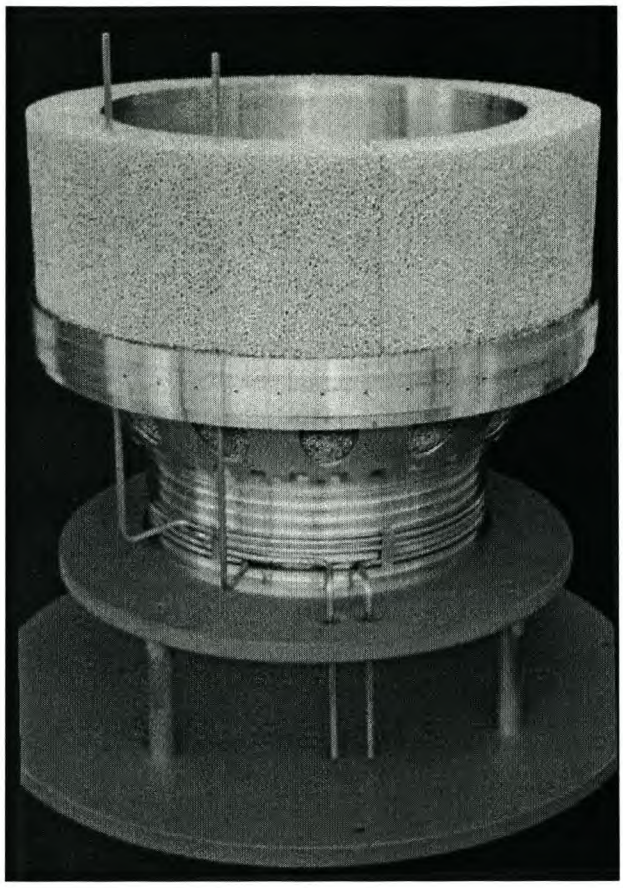

Figure 1.3 Metallic foam used in a cryogenic system (ERG Materials and Aerospace Corp.).

these models neglect the effect of thermal contact between the metallic foam and the solid wall, and consequently the existence of a thermal non-equilibrium region near the solid wall. They are furthermore limited to the steady state behaviour in two dimensions of a metallic foam of uniform porosity and cell size with a uniformly distributed thermal load along the full distance of one of its channel walls.

As can be seen from Figure 1.3 to Figure 1.5, metallic foams often find their application in the enhancement of heat transfer in cavities of arbitrary shape and under multi-dimensional distributed or localised thermal loading. Figure 1.6 shows a variety of metallic foam shapes and foam-substrate configurations. A universal model capable of predicting thermal behaviour for these types of applications will have its origin in a differential energy balance mathematical description of the transport of energy through the solid and the fluid phases.

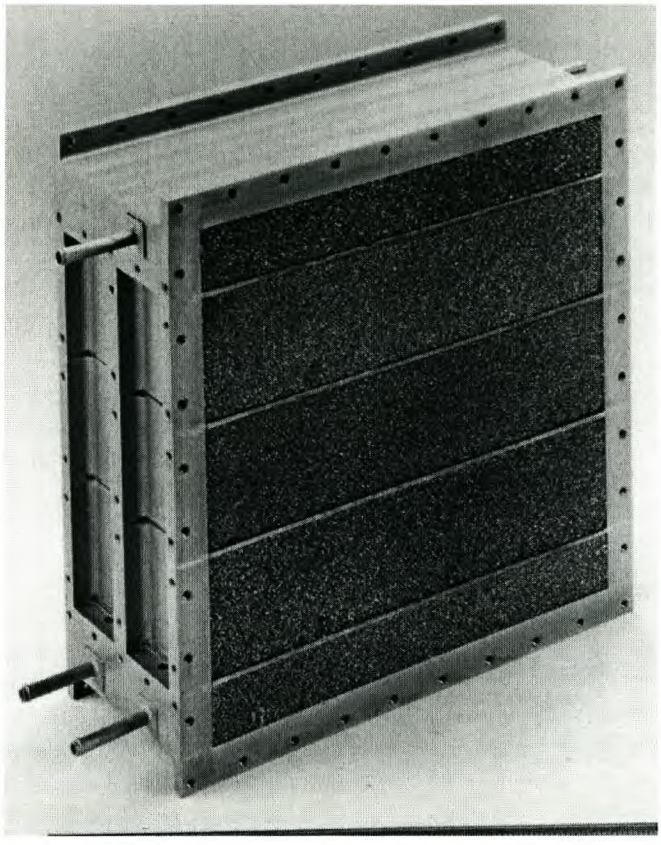

Figure 1.4 Metallic foam liquid heat exchanger (ERG Materials and Aerospace Corp.).

Only one approach towards the development of a thermal model of this kind is known to the author (Angirasa and Peterson, 1996). However, this model also neglects the effect of thermal contact between the metallic foam and the solid wall, leading to an assumption of thermal equilibrium between the solid and the fluid phases throughout the porous domain.

Following this assumption, a single representative temperature was used for both the solid and the fluid phases. Although this assumption greatly simplifies the analytical development of the energy balance model to a single governing equation, its underestimation of overall heat exchange where there is thermal contact between the metallic foam and a solid wall, severely limits its application.

Figure 1.5 Metallic foam heat pump (ERG Materials and Aerospace Corp.).

Even with only partial thermal contact between a metallic foam and a solid wall, measurements have shown the significance of heat exchange between the solid and the fluid phases in the region near the solid wall, where the phases are not in thermal equilibrium. Observations of metallic porous materials other than cellular foams, in thermal contact with a solid wall, also emphasise the importance of heat exchange in this region. Particle and gas temperature distributions in the vicinity of a water-cooled wall immersed in fixed and fluidised beds have indicated that wall-to-bed heat transfer and solid-gas heat exchange is significant near the wall (Flamant *et al.*, 1992). Dedicated heat transfer models for packed beds have been developed based on the existence of significant gas and solid temperature variations close to the wall (Mazza and Baretto, 1988).

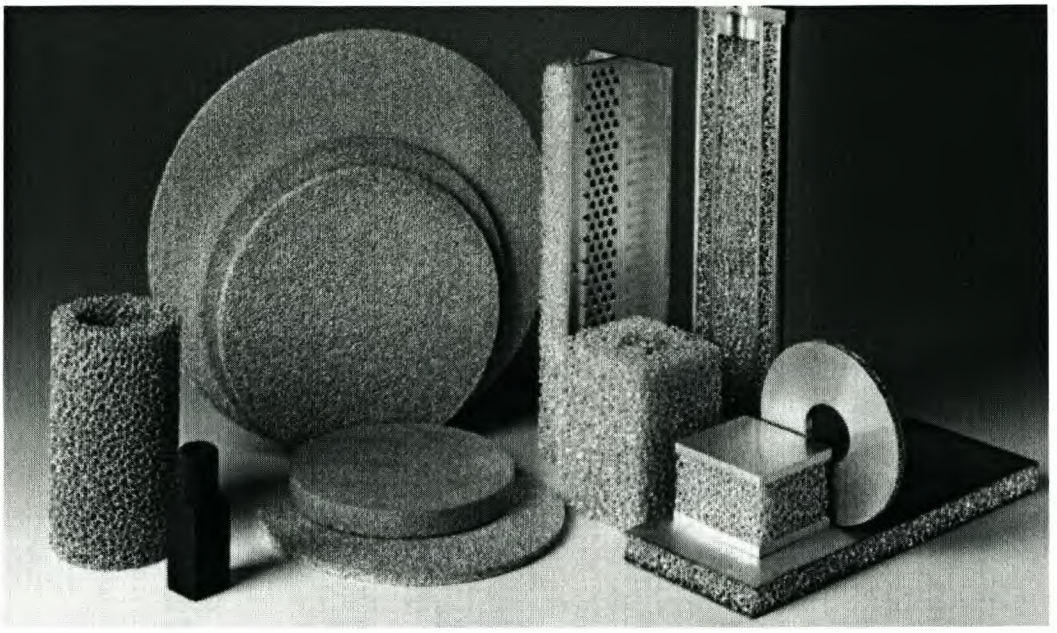

Figure 1.6 Metallic foams and substrates in a variety of shapes and configurations (ERG Materials and Aerospace Corp.).

As a result, the next step in the advancement of the thermal modelling of metallic foams was the inclusion of the effect of a thermal non-equilibrium layer created by thermal contact between the metallic foam and the solid wall. This advancement has been limited to empirical models only (Lu *et al.*, 1998b; Bastawros *et al.*, 1998). In one such model, a thermal non-equilibrium state is assumed throughout the porous domain. The model includes a relaxation factor, based on the Biot modulus, to account for a tendency towards thermal equilibrium between the phases in the far field away from the solid wall. The relaxation factor was derived from a bank-of-tubes analogy. In another model, the effect of the thermal non-equilibrium layer was considered by introducing an analytical expression for the temperature distribution of a single cylinder in cross flow. Both models are dedicated to the steady state behaviour in two dimensions of uniform porosity and cell size metallic foams and limited to a thermal load in the form of a uniformly distributed fixed temperature on one or both longitudinal channel walls.

1.6 Objectives of this study

This present study attempts to advance the thermal modelling of metallic foams one step further by including the effect of thermal non-equilibrium regions in the porous domain in an energy balance mathematical description of the transport of energy through the solid and the fluid phases.

The study has, as its goal, the development of a universally applicable model consisting of a set of differential governing equations. This set of equations, together with proper boundary conditions and a solution method, finds its application in predicting the thermal performance of metallic foams of arbitrary three dimensional shape with variable porosity and cell size, under multi-dimensional steady-state and dynamic thermal loading of a localised or distributed nature with fixed boundary temperatures or fixed boundary heat fluxes, and with variable fluid phase velocity distributions. A universal application requires that the thermal performance prediction does not rely on any calibration coefficients, which require *a priori* knowledge of the flow or thermal behaviour of the particular metallic foam.

Although there may be certain operating conditions that justify an independent evaluation of only certain heat transfer processes, it is highly desirable for such a model to be based on physically sound theory describing all the most relevant thermal processes in the solid and the fluid phases. These processes are described in the following section.

1.7 Relevant thermal and fluid flow processes in metallic foams

Assume for the moment that there is no thermal contact between the porous medium and the solid wall. The solid and the fluid phases will be in thermal equilibrium everywhere within the porous domain. The locally mean temperatures of the phases will be equal and thus no net exchange of heat between the phases occurs. If a gradient is introduced in

these equal locally mean temperatures, there will be a net conduction of heat through the phases, which is directly proportional to the gradient in the locally mean temperatures.

With thermal contact between the porous medium and the solid wall, conduction at any point in a particular phase within the thermal non-equilibrium region will consist of two components. One component is caused by the temperature gradient in that phase. The other component results from conduction in the other phase, taking "short cuts" through that phase. This "short cut" component is driven by the temperature gradient in the other phase. This phenomenon is reciprocal between the two phases.

Heat exchange between the two phases in the thermal non-equilibrium region is determined by the thermal resistance at the interface between the phases, which in turn depends on the hydrodynamics at the interface.

Under steady conditions, the thickness of the thermal non-equilibrium region is determined by the ratio of the relative magnitudes of thermal resistance between the two phases, to the resistance to internal conduction in the solid phase (generally referred to as the *Biot modulus*). Under transient thermal conditions, the difference between the convective heat transport rate in the fluid phase and the rate of conduction in the solid phase, is often the source of a temporal thermal non-equilibrium condition between the phases. This phenomenon is referred to in literature as the "hold-up" effect (Reis *et al.*, 1979) and is determined by the Fourier modulus, which compares a characteristic solid phase dimension to an approximate thermal penetration depth in the solid phase over a given time period.

Fluid flow through the porous medium affects that medium's thermal behaviour at two distinct length scale levels. At the porous domain length scale, a convective transport of heat is associated with the net fluid flow through the porous medium. At the pore length scale, as the fluid passes through the porous structure, interaction between the fluid and the complex structures of the solid phase introduces flow disturbance causing mixing and recirculation of local fluid streams (Koch and Brady, 1985; Fried, 1975; Dybbs and Edwards, 1984; Allen *et al.*, 1988). The convective heat transport associated with fluid flow at this level is referred to as *mechanical thermal dispersion*. Its effect on thermal

transport is comparable to that of molecular interaction, thereby enhancing the thermal transport characteristics of the fluid phase in the presence of a locally mean temperature gradient. The combination of mechanical thermal dispersion and thermal conduction is referred to as *hydrodynamic thermal dispersion.*

In addition, at the solid wall, the interaction of the fluid with the solid phase structures in the narrow region adjacent to the solid wall enhances heat transfer between the fluid phase and the wall by way of the continuous disruption of thermal boundary layer development on the wall.

At moderate temperatures, the effect of thermal radiation can be neglected (Lu *et al.*, 1998b).

1.8 Governing equations

A physically sound theory describing all these relevant thermal processes is available in the form of differential conservation of momentum and energy transport equations, balancing different momentum and heat transport processes described at a microscopic level. These equations are generally referred to as the momentum (or Navier-Stokes) equation and the energy equation, and can be derived by either a control volume approach or an integral approach. At this level, the attention is given to transfer processes within a single phase.

It would be routine to find the solution of transport equations at the microscopic level provided the conditions on the interfacial boundary and its geometric structure were known and not too complex. In that case, the transport of an extensive quantity could be depicted only by microscopic convection and conduction. However, because of the complexity and untraceability of the large number of intricate interfacial geometries encountered in metallic foams, it is nearly impossible to get the description and solution of a transport problem at that level. Furthermore, such microscopic details are rarely

needed in most engineering problems. The macroscopic aspects of transport processes are much more relevant and it is adequate to know only the locally mean values of intensive quantities, such as temperature, concentration and velocity. This means that another level of mathematical description, namely transport equations at a macroscopic level, is required.

In view of this, and since application to thermal non-equilibrium regions requires two separate energy balance equations for the solid and the fluid phases, a universally applicable set of governing equations consists of, firstly, a momentum balance in the fluid phase by the differential spatial distribution of its locally mean velocity, and secondly, an energy balance in the solid and the fluid phases, by the differential spatial and temporal distribution of their locally mean temperatures. For porous media in general, an approach to describe an energy balance separately for each of the two phases by the spatial and temporal distribution of their locally mean temperatures has also been widely recognised (Vortmeyer and Scheafer, 1974; Vortmeyer, 1975; Schlünder, 1975; Froment and Bischoff, 1979; Pereira Duarte *et al.*, 1984; Glatzmaier and Ramirez, 1988; Kaviany, 1995).

By including a momentum balance equation, the relevance of the model is extended to porous domains of variable locally mean fluid velocity distributions. There are two factors that can cause the locally mean velocity to vary in a porous domain. The first factor is a variation in the foam morphology and the second is in the narrow layer adjacent to a solid wall in contact with the porous domain, where the locally mean flow velocity is affected by viscous shear at the solid wall. In low porosity media, the momentum transfer to the narrow layer adjacent to a solid wall associated with viscous shear at that solid wall, is negligible when compared to the momentum transfer contribution of viscous shear at the interface between the solid and the fluid phases, in the same narrow layer adjacent to the solid wall. In that case, viscous shear at the solid wall will have a negligible deviating effect on the locally mean flow velocity.

1.9 Macroscopic description of heat transfer and fluid flow processes

The macroscopic description of conduction within the solid and the fluid phases, the net exchange of heat between the solid and the fluid phases (referred to as *interphasial heat transfer*), as well as convection and dispersion in the fluid phase, have largely been based on intuition.

In the case of conduction in the solid and the fluid phases, where the phases are in a thermal equilibrium state, a model referred to as the *one-equation model*, has independently been introduced by different researchers in a variety of forms. The one-equation model describes conduction in the solid and the fluid phases by a single locally mean representative temperature together with an *overall thermal conductivity* (Nozad *et al.*, 1985; Whitaker, 1980, Section III). Prediction methods for the overall thermal conductivity of metallic foams in thermal equilibrium states have received some attention (Bauer, 1993; Hsu, 1994; Mickley in Combarnous and Bories, 1975). Hunt and Tien (1988) and Calmidi and Mahajan (1998) have presented experimental results of the overall thermal conductivity of aluminium foam saturated by stagnant air or water.

Two approaches have been followed in literature to describe conduction in a porous domain consisting of regions of thermal equilibrium and regions of thermal non-equilibrium between the solid and the fluid phases. The first approach is referred to as a *two-region model* (Carberry, 1976) in which the regions of thermal equilibrium and thermal non-equilibrium are dealt with separately. In the thermal non-equilibrium region, heat transfer processes are separately described in each of the two phases. In the second approach, heat transfer processes are separately described in each of the two phases, both in the thermal equilibrium and thermal non-equilibrium regions. This approach is referred to as the *two-equation model.*

Using the two-region model, the one-equation model is applied in the thermal equilibrium region. These separate descriptions do not require compatibility with the region of thermal equilibrium. Application of the two-region model does however require identifying the location of the transition zone between the regions of thermal equilibrium and thermal non-equilibrium. By employing the method of estimates (Whitaker, 1983), a

series of constraints have been developed which must be satisfied for the principles of local thermal equilibrium to be acceptable (Whitaker, 1991). Although these constraints provide a consistent framework to identify the thermal equilibrium and non-equilibrium regions, the method of estimates is based on order-of-magnitude analysis and thus can provide only an indication to the validity of the principles of thermal equilibrium. In the two-equation model (as opposed to the two-region model), the separate description of heat transfer processes in each of the two phases requires compatibility with the one-equation model in the thermal equilibrium region.

A number of macroscopic level intuitive descriptions of the conduction terms in the microscopic energy equation have been proposed in literature (Vortmeyer and Scheafer, 1974; Vortmeyer, 1975; Schlünder, 1975; Glatzmaier and Ramirez, 1988; Vafai and Sözen, 1990). In these macroscopic descriptions, conduction in a phase is presented in terms of an effective thermal conductivity and the gradient of the locally mean temperature of that phase.

The initial intuitive developments toward the macroscopic description of dispersion dealt only with the dispersion of mass in the form of tracer elements in fluid flowing through a porous medium. However, by virtue of the convective nature of high Peclet mass number flow (where diffusive mass transfer can be neglected), momentum and thermal mechanical dispersion behaviour can be derived from the dispersion of mass, by the definition of a quantity introduced in the present study, referred to as the *dispersivity* (analogous to the definition of mass, momentum and thermal *diffusivity*).

Earlier models describing mass dispersion in porous media were purely geometric models representing a specific porous geometry. These geometric models, often referred to as *capillary models*, consisted of fixed capillaries that were either connected or independent. A "diffusion-like" conceptual representation of dispersion by a *dispersion coefficient*, together with the gradient of the locally mean concentration, was introduced from observations of the asymptotic behaviour of two miscible displacing fluids with molecular diffusion and velocity constraints on the cross-section of a single capillary (Taylor, 1953, 1954).

The next step was the introduction of *statistical* or *random capillary* dispersion models (Saffman, 1959a; De Josselin de Jong, 1958; Bear and Bachmat, 1967; Bear, 1972, p. 764). These models consisted of a network of straight tubes, distributed and oriented at random and connected together. Tube dimensions were of the order of actual pore dimensions. The distribution function of particle displacement after a given time period yields values for the dispersion coefficient. Bear (1988) gives a thorough review of the statistical treatments and the dispersion properties. Although straight tubes do not represent a general porous model, theoretical observations were sufficient to identify a difference between longitudinal dispersion and transverse dispersion and, based on previous work, a *longitudinal* and *transverse dispersion coefficient* in a "diffusion-like" conceptual representation, were defined.

Based on intuition, a description of interphasial heat transfer at a macroscopic level in terms of locally mean temperatures was proposed (Gray, 1975; Whitaker, 1977). The net interphasial heat transfer is directly proportional to the steady state locally mean temperature differential of the solid and the fluid phases. An *interphasial heat transfer coefficient* was defined as the ratio of the net exchange of heat between the solid and the fluid phases, and the locally mean temperature differential of the two phases. Auriault and Royer (1993) and Moyne (1997) proposed temporal convolutions for describing interphasial heat transfer under thermally unsteady state conditions. Auriault and Royer used the method of homogenisation and Moyne derived a temporal convolution using volume averaging. Moyne concluded that the steady state intuition-based approach of Gray and of Whitaker yields a satisfactory simplified model in most cases.

1.10 Analytical averaging techniques

Several analytical averaging procedures have been introduced in literature to transform, in a formal manner, the description of transport processes from a microscopic to a macroscopic level. Of these procedures, *statistical methods*, *homogenisation* and *volume averaging* are the most important and are therefore briefly discussed here.

In the statistical approach, averaging is performed over an ensemble of possible pore structures that are microscopically equivalent. One difficulty is that the statistical information about the ensemble must be based on a single sample, and this is usually only possible if statistical homogeneity is assumed. However, if one is concerned only with relationships between the space-averaged quantities and not with their fluctuation, then results obtained by statistical methods and volume averaging is essentially equivalent (Nield and Bejan, 1992).

If the porous medium has a periodic structure, then the homogenisation method may also be used to obtain mathematically rigorous results. This method is based on the study of periodic solutions of partial differential transport equations and the asymptotic behaviour of these equations, as the period tends to zero. The hypothesis of periodic structures allows for the rigorous treatment of problems such as fluid flow in porous media and other microscopically heterogeneous systems.

Although very similar to volume-averaging, the first development of the homogenisation method was very restrictive in its application and was only used for the macroscopic description of forced convection through porous media and heat transfer in a state of thermal equilibrium between the solid and the fluid phases (Sanchez-Palencia, 1980, p.129). At a later stage, the model was expanded and applied to a study of natural convection in porous media (Ene and Polisevski, 1987). A general discussion of the homogenisation method and the asymptotic analyses of periodic structures is given by Ene and Polisevski (1987) and Bensoussan *et al.* (1987).

Volume averaging, as well as variations thereof such as cellular averaging and configurational averaging, is the most commonly used of the three methods. It resides under the broader classification of Eulerian spatial and temporal averaging. Eulerian averaging provides the best framework to proceed in the understanding of transport in porous media in general. This is because the Eulerian spatial and temporal averaging procedure is closely related to physical observations and instrumentation data.

Eulerian averaging has appeared in literature for several decades to formulate theories of momentum, mass and energy transport, at a macroscopic level, in a wide variety of

engineering systems (Bear and Bachmat, 1984, 1986, 1991; Dobran, 1991; Zuber, 1964; Anderson and Jackson, 1967; Slattery, 1967; Bear, 1972; Whitaker, 1973; Gray, 1975; Hassanizadeh and Gray, 1979a, 1979b). Recently, extensive studies of fluid motions and energy transport behaviour in spatially periodic and disordered porous media have been done by using volume averaging (Nitsche and Brenner, 1989; Adler, 1992; Quintard and Whitaker, 1994a, 1994b). A thorough review of Eulerian averaging procedures was compiled by Nitche and Brenner (1989).

As a result, the analytical volume-averaging process was selected as the most appropriate and mathematically correct means for transforming the description level of transport processes in the present study.

1.11 Closure modelling

A useful set of governing transport equations at a macroscopic level requires momentum and energy balance descriptions in terms of volume-averaged velocities and temperatures only. However, applying the analytical volume-averaging process to the microscopic momentum equation yields certain viscous shear, pressure force and momentum dispersion processes, which are described as integrals of microscopic processes presented in terms of microscopic intensive quantities. The same predicament occurs in the application of volume averaging to the microscopic energy equation. In this case, thermal conduction, interphasial heat transfer and thermal dispersion processes are described as integrals of microscopic processes presented in terms of microscopic intensive quantities. In this study, closure is achieved by the transformation of these integrals of microscopic processes into a description in terms of volume-averaged intensive quantities.

The establishment of "diffusion-like" longitudinal and transverse dispersion behaviour was precedent to the development of analytical volume-averaging principles. This assumption was subsequently supported by concurrent theories developed by using the method of volume-averaging (Carbonell and Whitaker, 1983), the method of

configurational averaging over a set of media (Koch *et al.*, 1989), and the method of homogenisation (Rubinstein and Mauri, 1986; Mei, 1992) as technique to transform integrals describing momentum and thermal dispersion in terms of microscopic intensive quantities. It has therefore been used in the present study to transform the associated integrals into terms of volume-averaged intensive quantities only.

Similarly, the established intuition-based description of interphasial heat transfer at a macroscopic level in terms of volume-averaged temperatures and an interphasial heat transfer coefficient, discussed in Section 1.9, is used in the present study to transform integrals of microscopic interphasial heat transfer processes into a description in terms of volume-averaged temperatures only.

An analytical model has been introduced in literature which relates integrals of microscopic viscous shear and pressure force processes to the fluid viscosity and volume-averaged velocity, by a macroscopic transport parameter referred to as the *viscous shear factor* (Du Plessis, 1991a). This is the only model of its kind familiar to the author and was used in the present study.

Various theoretical methods have been proposed in literature for transforming the integral of microscopic conduction processes into terms of volume-averaged temperatures. The analytical processes of these methods have all shown that conduction within a phase described at a macroscopic level, is not just a function of the gradient of the volume-averaged temperature of that phase (as most intuitive models suggest), but also a function of the gradient of the volume-averaged temperature of the other phase. Theoretical methods therefore aim to present conduction in a phase in terms of an effective thermal conductivity and a volume-averaged temperature gradient of that phase, as well as a coupled thermal conductivity together with a volume-averaged temperature gradient of the other phase. In the macroscopic description of heat transfer in porous media in general, achieving this goal through a sound theoretical analysis has proved to be the single most challenging problem that has confronted researchers over the last few decades.

The first theoretical methods were dedicated in their application to specific porous media and were restricted to special cases only (Zanotti and Carbonel, 1984a, 1984b, 1984c; Whitaker, 1989; Carbonel and Whitaker, 1984; Levec and Carbonel, 1985a, 1985b; Kaviany, 1995). The most significant advancement towards the development of a universal model was the introduction of a weighting function (Marle, 1967; Quintard and Whitaker, 1993) that allows the microscopic temperature deviation field (Gray, 1975) to be mapped from the volume-averaged temperature field. This analytical process includes the steady-state closure of the temperature deviation field at a microscopic level. However, length and time scale constraints, based on order-of-magnitude estimates, had to be imposed for the application of this technique. Furthermore, essential simplifications could only be made by the neglect of higher order terms once these constrains were satisfied, despite the fact that order-of-magnitude estimates could not identify these terms as negligible. This approach was later extended by using an unsteady state closure at microscopic level in the analytical mapping process (Moyne, 1997). This led to the expression for the conductive terms as temporal convolutions. Only in the case of spatially periodic systems consisting of an array of symmetric unit cells, could further simplifications concerning the weighting function be made in the original model and the subsequent extension, to achieve closure. These models show various degrees of compatibility with the one-equation model under conditions of thermal equilibrium.

In the present study, the transformation of the integral describing conduction in terms of microscopic intensive quantities is accomplished by a novel approach (as introduced in the study) in the analytical volume-averaging process of the microscopic energy equation. This approach avoids the need to map the microscopic temperature deviation field from the volume-averaged temperature field. It also allows closure to be achieved for spatially periodic porous media consisting of symmetric and non-symmetric unit cells, as well as for symmetric and non-symmetric representative geometric models of disordered porous media. No constrains are placed on length or time scales and the analytical development does not require terms of any order to be neglected. The resulting formulation exhibits true two-equation model behaviour by reducing to the established one-equation model formulation under the conditions of thermal equilibrium between the solid and the fluid phases.

For the fluid phase, these transformations yield a momentum balance equation at macroscopic level in the form of an elliptic partial differential equation for the spatial and temporal volume-averaged velocity distribution. The transformations also yield two energy balance equations at macroscopic level in the form of elliptic partial differential equations for the spatial and temporal volume-averaged temperature distributions in the solid and the fluid phases. In this form, the present study refers to these equations as *transformed volume-averaged equations*. The transformed volume-averaged equations apply to any consolidated porous medium.

The transformation of integrals of microscopic processes presented in terms of microscopic intensive quantities into a description in terms of locally mean intensive quantities introduce a number of macroscopic transport parameters into the governing equations. These transport parameters essentially relate integrals of microscopic processes to their counterpart macroscopic descriptions in terms of volume-averaged intensive quantities, which are: the *viscous shear factor* from the transformation of integrals of microscopic viscous shear and pressure force processes; the *interphasial heat transfer coefficient* from the transformation of integrals of microscopic interphasial heat transfer processes, and; the *momentum* and *thermal dispersion tensors* (both with longitudinal and transverse components) from the transformation of integrals of microscopic momentum and thermal dispersion processes. The novel approach for the transformation of integrals of microscopic thermal conduction processes introduces two transport parameters in the form of an *effective* and a *coupled thermal conductivity*, which are defined directly from the formulation of the analytical process.

1.12 Metallic foam morphology modelling

The evaluation of surface and volume integrals in the definitions of the transport parameters is subject to a description of real velocity and temperature gradients within the solid and the fluid phases and at the pore surfaces. This in turn warrants an accurate description of the metallic foam morphology and its influence on momentum and energy transfer in the solid

and the fluid phases. Although the intricate interfacial geometries encountered in metallic foams are far too complex to accurately capture their nuances in every bit of detail, there is a fair degree of uniformity, which enables them to be treated in a semi-empirical manner.

Semi-empirical representations of porous media geometries in general have been classified in the present study as *geometric models* and *statistical models*. Geometric models are classified further into *morphological geometric models* and *representative geometric models*. Morphological geometric models not only realistically represent the morphology of the solid phase, but may also be used to characterise heat, mass and momentum transport behaviour in one or both phases. For cases where the complexity of morphological geometric models complicates their application in the characterisation of transfer behaviour, representative geometric models have been introduced in literature. As opposed to morphological geometric models, representative geometric models are often not realistic representations of the actual morphology of the solid phase, but more suited to providing a convenient facility for characterising transport behaviour.

Morphological models have a periodic nature, allowing the convenience of considering only one unit cell of an array to characterise transport behaviour in a medium. The fair degree of uniformity associated with cellular foam structures in general has inspired a number of morphological model presentations in literature. One such morphological model of significance presents the cellular configuration as an ordered array of tetrakaidecahedra (Gibson and Ashby, 1988). Each cell consists of eight hexagonal faces and six square faces. Other models include a configuration consisting of two-dimensional hexagonal arrays, lumped together at the points of intersection by square structures, into a three-dimensional array (Calmidi and Mahajan, 1999), and a model which shows the cellular configuration made up of uniformly distributed, equal-sized cubic cells consisting of three mutually perpendicular cylinders (Lu *et al.*, 1998b).

One example of representative geometric models used in literature is an ordered bank of cylindrical tubes in cross flow for investigating the large-scale thermal behaviour of metallic foams (Bastawros *et al.*, 1998). The thermal characteristics of metallic foams were modelled using a variation on the tube bank to predict the effect of varying foam morphologies. In another investigation, a single cylinder aligned transversely to the flow

and spanning over the entire porous medium domain was used as a representative geometric model to characterise the effect of thermal contact between a metallic foam and a duct wall (Lu *et al.*, 1998b).

A unique representative geometric model was introduced a few decades ago to develop an expression for the overall thermal conductivity of cellular foams under thermal equilibrium conditions (Mickley in Combarnous and Bories, 1975). This representative geometric model was later independently characterised in detail and its application successfully extended to model fluid flow in highly porous cellular foams (Du Plessis *et al.*, 1994). After attributing various properties to this model, it was introduced in literature as a *representative unit cell* (RUC) (Du Plessis and Masliyah, 1988; Du Plessis, 1991). The RUC can be considered as the most elementary volume, which satisfies a set of general criteria, stipulated in literature for the characterisation of a pore structure (Dullien, 1979, p. 90).

In statistical geometric models, rather than considering an actual random porous medium, an ensemble of porous media that are equivalent to each other, within limits, is considered. Geometric properties of the random porous medium are then related to some easily measurable statistical properties of that medium. The first attempt to describe the geometry of a solid phase statistically was limited to very specialised media. A more general statistical description was later proposed by defining a probabilistic function for the occurrence of void space and solid space along an arbitrarily chosen arc through the porous medium (Fara and Scheidegger, 1961). A brief overview of developments in statistical geometric modelling is given by Scheidegger (1974).

In the present study, a representative geometric model based on the RUC approach is used to characterise transport behaviour in metallic foams. The complete characterisation of an appropriate RUC relies on a morphologic geometric model presenting the metallic foam microstructure as an ordered array of tetrakaidecahedra. Each individual strand is represented in the morphological geometric model as a prism of triangular cross-sectional shape, flared at the ends to represent material clustering at the strand vertices.

1.13 Transport parameters

The transformed volume-averaged equations discussed in Section 1.11 apply to any consolidated porous medium. The flow and thermal behaviour of a specific porous medium, such as a metallic foams, is characterised by the values of the transport parameters, *i.e.*, the viscous shear factor and the momentum dispersion tensor in the transformed volume-averaged momentum equation, the solid phase effective and coupled thermal conductivities and the interphasial heat transfer coefficient in the transformed volume-averaged energy equation of the solid phase, and the fluid phase effective and coupled thermal conductivities, the interphasial heat transfer coefficient and the thermal dispersion tensor in the transformed volume-averaged energy equation of the fluid phase.

Mathematical relationships were developed for metallic foams in terms of the thermophysical properties of the solid and the fluid phases and the foam microstructure, which is morphologically completely defined by its porosity and cell size.

In the development of mathematical relationships for the viscous shear factor and the interphasial heat transfer coefficient, the RUC provides a facility to extrapolate established conceptual representations of momentum and heat transfer from common flow systems to the most elementary control volume of the metallic foam microstructure. For both the viscous shear factor and the interphasial heat transfer coefficient, separate expressions were developed from this approach for a viscous dominated flow range (low Reynolds number flow) as well as for an inertia dominated flow range (high Reynolds number flow). This analytical process introduces a conceptual dimension in the present study referred to as the *representative hydraulic diameter* (RHD). Using the RHD in the conceptual representation of momentum and heat transfer accounts for the effects of triangular cross-sectional shape of individual strands as well as material clustering at strand vertices. For both the viscous shear factor and the interphasial heat transfer coefficient, separate expressions for viscous and inertia dominated flows (also referred to in literature as the Darcy flow range and the Forchheimer flow range) are unified into single expressions by an established unification model.

Mathematical relationships for the effective and coupled thermal conductivities are derived from close observation of the relationship between microscopic and macroscopic

temperature distributions in the RUC. These temperature distributions are obtained from the computational solution of the three-dimensional conduction equation, with appropriate boundary conditions, in the RUC.

Advancements in the development of expressions for dispersion coefficients subsequent to the introduction of analytical averaging procedures were mostly concerned with specific porous media. These configurations include mechanical thermal dispersion, as well as two-dimensional and three-dimensional hydrodynamic thermal dispersion, primarily in spatially periodic systems (Carbonell and Whitaker, 1983; Sahraoui and Kaviany, 1995; Koch *et al.*, 1989). The author could not find any such developments dedicated to cellular foams.

Instead, a successful model which was developed to predict the dispersion coefficient of continuous randomly orientated fibres, using the method of configurational averaging over a set of media (Koch and Brady, 1985). This method was found to predict the transverse components of the dispersivity tensor of metallic foams sufficiently. In this study, the RHD of the metallic foam was used as a characteristic fibre diameter in the prediction model. Momentum and thermal dispersion tensors are derived from the dispersivity tensor.

1.14 Solution of governing equations

If analytical mathematical solution methods were to be used for solving the partial differential transformed volume-averaged momentum equation and the partial differential transformed volume-averaged energy equations for the solid and the fluid phases, only a tiny fraction of the range of practical problems could be solved in closed form. Analytical mathematical solutions are those given by a mathematical expression that yield the values of the desired volume-averaged temperatures and volume-averaged velocities at any location in the porous domain and are thus valid at an infinite number of locations in the porous domain.

For problems involving complicated domain geometries, it is generally not possible to obtain analytical mathematical solutions for these partial differential governing equations. For those cases, instead of solving the governing equations analytically over the entire porous domain in one operation, the development of computational methods allows for the equations to be formulated in terms of a set of simultaneous linear algebraic equations that are applied at a finite number of discrete grid points. The solution of the system of equations yields approximate values for the volume-averaged velocity and volume-averaged temperatures at a discrete number of points in the porous domain , which are then combined to obtain an approximate solution over the entire porous domain.

The process of modelling a domain by dividing it into an equivalent system of smaller units interconnected at surfaces common to two or more units together with the formulation of a set of equations is called *discretisation*. The development of discretisation processes has taken two paths: *finite elements* and *finite differences* (including the *finite volume* variation). A thorough evaluation and comparison of these methods are presented by Pepper and Baker (1988).

In this study, the transformed volume-averaged momentum equation and the transformed volume-averaged energy equations for the solid and the fluid phases are discretised using the established finite-volume method of Patankar (1980).

Using the finite-volume method, the coefficients of the discretised forms of the transformed volume-averaged momentum equation and the transformed volume-averaged energy equations for the solid and the fluid phases are written in matrix form, with all the non-zero coefficients aligned along three diagonals of the matrix. This particular configuration facilitates easy solutions by iterative procedures and direct solution methods. Iterative procedures include the Gauss-Seidel point-by-point method (Isaacson and Keller, 1966) and the Tri-Diagonal Matrix Algorithm (TDMA) method (Patankar, 1980). King (1976) developed a direct solution method for the case of a two-dimensional set of equations. Both the TDMA method and the direct solution method of King (1976) are used in this study.

1.15 Thesis layout

The application of the analytical volume-averaging process to the microscopic momentum equation and the microscopic energy equations of the solid and the fluid phases, as well as the subsequent transformation of integrals of microscopic processes into a description in terms of volume-averaged intensive quantities, can be regarded as the first of a three part composition of the thesis. The transformed volume-averaged equations apply to any consolidated porous medium. The flow and thermal behaviour of a specific porous medium are characterised by the transport parameter values. Developing mathematical relationships for the transport parameters of isotropic, highly porous, cellular metallic foams constitutes the subject of the second part of this study. The third and final part of the study deals with the application and computational solution of the governing equations.

Results obtained from the computational solution of the transformed volume-averaged momentum equation and the transformed volume-averaged energy equation for the solid and the fluid phases are compared to experimental results in Chapter 17.

A number of appendices are included. In Appendix I, the differential form of the microscopic continuity equation for the fluid phase, the microscopic continuity equation for an individual specie in a mixture, the microscopic momentum equation for the fluid phase and the microscopic energy equation for the solid and the fluid phases are derived. The principles, definitions, rules and theorems of the volume-averaging method are described in Appendix II, and a novel approach towards the application of the volume-averaging principles to the microscopic energy equation, developed in Part I, is qualified in Appendix III.

Two FORTRAN computer codes, called MacFlow and MacSolidFluid, are included on Compact Disc. One program solves the set of linear algebraic equations resulting from the discretisation of the two-dimensional, steady-state transformed volume-averaged momentum equation. The other program solves two sets of linear algebraic equations resulting from the discretisation of the two-dimensional, steady-state transformed volume-averaged energy equation of the solid and the fluid phases. Details of the programs and guidelines for their use are presented in Appendix IV.

PART I

Part I is devoted to the theoretical process of deriving the governing equations describing momentum and heat transfer in a porous medium at a macroscopic level. In Chapter 2 the volume averaging principles are applied to the microscopic momentum equation for the fluid phase, and the microscopic energy equation for the solid and the fluid phases. The analytical process yields certain momentum transfer processes, which are described as integrals of microscopic processes presented in terms of microscopic intensive quantities. The same occurs in the application of volume averaging to the microscopic energy equation. In this case, heat transfer processes are described as integrals of microscopic processes presented in terms of microscopic intensive quantities.

Chapter 3 to Chapter 7 involves the transformation of integrals of microscopic processes presented in terms of microscopic intensive quantities into a description in terms of locally mean intensive quantities. Substitution of these models into the volume-averaged forms of the microscopic momentum equation for the fluid phase, and the microscopic energy equation for the solid and the fluid phases, in Chapter 8, yields a macroscopic description of these heat transfer processes in terms of macroscopic quantities and appropriate proportionality coefficients.

CHAPTER 2

VOLUME-AVERAGED CONTINUITY, MOMENTUM AND ENERGY EQUATIONS

2.1 Overview

Applying the principles of volume averaging (discussed in Appendix II) to a microscopic momentum and energy equation in order to describe a momentum and energy balance at macroscopic level has formed part of numerous studies (*e.g.* Du Plessis and Masliyah, 1988; Carbonnel and Whitaker, 1984; Zanotti and Carbonnel, 1984a, 1984b, 1984c; Levec and Carbonnel, 1985a, 1985b; Quintard and Whitaker, 1993; Quintard *et al.*, 1997). The resulting volume-averaged equations are presented in many different forms, mainly due to various assumptions associated with the application of the resulting equations under different conditions (*e.g.* the assumption of constant porosity). For application to this study, the volume averaging process is applied in this chapter to the microscopic momentum equation for the fluid phase, and the microscopic energy equation for the solid and the fluid phases under the assumptions of constant thermophysical properties and variable porosity.

2.2 Volume-averaged continuity equation

The general continuity equation is derived in Appendix I as:

$$\frac{\mathrm{D}\rho}{\mathrm{D}t} = -\rho\nabla\cdot\boldsymbol{v}, \tag{I.11}$$

where ρ is the density, $\boldsymbol{v}$ is the velocity vector and t represents time. For a constant density fluid, Equation (I.11) reduces to:

$$\nabla \cdot \boldsymbol{v} = 0. \tag{2.1}$$

Integrating Equation (2.1) over the fluid phase of an REV (representative elementary volume, discussed in Section II.2), dividing by V_o and substituting Definition (II.3), yields:

$$\langle \nabla \cdot \boldsymbol{v} \rangle_f = 0. \tag{2.2}$$

Using Equation (II.10), Equation (2.2) can be written as:

$$\nabla \cdot \langle \boldsymbol{v} \rangle_f + \frac{1}{V_o} \int_{A_{sf}} \boldsymbol{v} \cdot \boldsymbol{n}_{fs} \, \mathrm{d}A = 0. \tag{2.3}$$

Substituting Equation (II.6) into Equation (2.3) and expanding the first term on the LHS, noting that $\boldsymbol{v} = 0$ at the interface A_{sf}, yields:

$$\varepsilon_f \nabla \cdot \langle \boldsymbol{v} \rangle_f^f + \langle \boldsymbol{v} \rangle_f^f \cdot \nabla \varepsilon_f = 0. \tag{2.4}$$

Dividing Equation (2.4) by ε_f and substituting Equation (II.6) again, yields the volume-averaged continuity equation:

$$\nabla \cdot \frac{\langle \boldsymbol{v} \rangle_f}{\varepsilon_f} + \frac{\langle \boldsymbol{v} \rangle_f}{\varepsilon_f^{\,2}} \cdot \nabla \varepsilon_f = 0. \tag{2.5}$$

The fluid phase volume fraction ε_f is also referred to as *porosity* in this study.

2.3 Volume-averaged momentum equation

The microscopic momentum is given by Equation (I.27) as:

$$\frac{\partial(\rho \boldsymbol{v})}{\partial t} + \nabla \cdot (\rho \boldsymbol{v}\boldsymbol{v}) = \rho \boldsymbol{B} - \nabla p - \nabla \cdot \boldsymbol{\tau}, \tag{I.27}$$

where ρ is the density, and $\boldsymbol{v}$ is the velocity vector, $\boldsymbol{B}$ denotes the body force vector per unit mass, p is the pressure and $\boldsymbol{\tau}$ is the viscous stress tensor.

Integrating Equation (I.27) over the fluid phase of a REV, dividing by V_o and substituting Definition (II.3), taking into account that the fluid density ρ_f is constant, yields:

$$\rho_f \left\langle \frac{\partial \boldsymbol{v}}{\partial t} \right\rangle_f + \rho_f \langle \nabla \cdot (\boldsymbol{v}\boldsymbol{v}) \rangle_f = \rho_f \langle \boldsymbol{B} \rangle_f - \langle \nabla p \rangle_f - \langle \nabla \cdot \boldsymbol{\tau} \rangle_f . \tag{2.6}$$

Consider the first term on the LHS of Equation (2.6). Using Equation (II.13), this term can be written as:

$$\rho_f \frac{\partial \langle \boldsymbol{v} \rangle_f}{\partial t} . \tag{2.7}$$

Consider the second term on the LHS of Equation (2.6). By using Equation (II.9) and taking into account that the fluid density ρ_f is constant, this term can be written as:

$$\rho_f \left[\nabla \cdot \left(\frac{1}{V_o} \int_{V_f} \boldsymbol{v}\boldsymbol{v} \, \mathrm{d}V \right) + \frac{1}{V_o} \int_{A_{sf}} (\boldsymbol{v}\boldsymbol{v}) \cdot \boldsymbol{n}_{fs} \, \mathrm{d}A \right] . \tag{2.8}$$

Noting that $\boldsymbol{v} = 0$ at the interface A_{sf}, and using Definition (II.1), Expression (2.8)

becomes:

$$\rho_f \nabla \cdot \left(\varepsilon_f \frac{1}{V_f} \int_{V_f} \boldsymbol{v}\boldsymbol{v}\, \mathrm{d}V \right). \tag{2.9}$$

Adding and subtracting the term:

$$\frac{1}{{V_f}^2} \int_{V_f} \boldsymbol{v}\, \mathrm{d}V \int_{V_f} \boldsymbol{v}\, \mathrm{d}V\,, \tag{2.10}$$

or:

$$\frac{1}{{V_f}^3} \int_{V_f} \boldsymbol{v}\, \mathrm{d}V \int_{V_f} \boldsymbol{v}\, \mathrm{d}V \int_{V_f} \mathrm{d}V \tag{2.11}$$

twice inside the parenthesis in Expression (2.9) and rearranging terms yields:

$$\rho_f \nabla \cdot \left[\varepsilon_f \left(\frac{1}{{V_f}^2} \int_{V_f} \boldsymbol{v}\, \mathrm{d}V \int_{V_f} \boldsymbol{v}\, \mathrm{d}V + \frac{1}{V_f} \int_{V_f} \boldsymbol{v}\boldsymbol{v}\, \mathrm{d}V - \frac{1}{{V_f}^2} \int_{V_f} \boldsymbol{v}\, \mathrm{d}V \int_{V_f} \boldsymbol{v}\, \mathrm{d}V - \right.\right.$$

$$\left.\left. \frac{1}{{V_f}^2} \int_{V_f} \boldsymbol{v}\, \mathrm{d}V \int_{V_f} \boldsymbol{v}\, \mathrm{d}V + \frac{1}{{V_f}^3} \int_{V_f} \boldsymbol{v}\, \mathrm{d}V \int_{V_f} \boldsymbol{v}\, \mathrm{d}V \int_{V_f} \mathrm{d}V \right) \right]. \tag{2.12}$$

Noting that a volume-averaged quantity in an REV is independent of the volume integral over that phase in the REV, the last three terms in the parenthesis in Expression (2.12) can

be manipulated to yield:

$$\rho_f \nabla\cdot\left\{\varepsilon_f\left[\frac{1}{{V_f}^2}\int_{V_f} v\,\mathrm{d}V\int_{V_f} v\,\mathrm{d}V+\frac{1}{V_f}\int_{V_f} vv\,\mathrm{d}V-\frac{1}{V_f}\int_{V_f}\left(v\frac{1}{V_f}\int_{V_f} v\,\mathrm{d}V\right)\mathrm{d}V-\right.\right.$$

$$\left.\left.\frac{1}{V_f}\int_{V_f}\left(v\frac{1}{V_f}\int_{V_f} v\,\mathrm{d}V\right)\mathrm{d}V+\frac{1}{V_f}\int_{V_f}\left(\frac{1}{V_f}\int_{V_f} v\,\mathrm{d}V\frac{1}{V_f}\int_{V_f} v\,\mathrm{d}V\right)\mathrm{d}V\right]\right\}. \quad (2.13)$$

Using Definition (II.4) in the last four terms in the square brackets, Expression (2.13) can be rewritten as:

$$\rho_f \nabla\cdot\left\{\varepsilon_f\left[\frac{1}{{V_f}^2}\int_{V_f} v\,\mathrm{d}V\int_{V_f} v\,\mathrm{d}V+\frac{1}{V_f}\int_{V_f}\left(vv-v\langle v\rangle_f^f-v\langle v\rangle_f^f+\langle v\rangle_f^f\langle v\rangle_f^f\right)\mathrm{d}V\right]\right\}, \quad (2.14)$$

or, after factorising the term in the parenthesis in Equation (2.14), it can be rewritten as:

$$\rho_f \nabla\cdot\left\{\varepsilon_f\left[\frac{1}{V_f}\int_{V_f} v\,\mathrm{d}V\frac{1}{V_f}\int_{V_f} v\,\mathrm{d}V+\frac{1}{V_f}\int_{V_f}\left(v-\langle v\rangle_f^f\right)\left(v-\langle v\rangle_f^f\right)\mathrm{d}V\right]\right\}. \quad (2.15)$$

Using Definition (II.4) and Definition (II.5), Expression (2.15) becomes:

$$\rho_f \nabla\cdot\left[\varepsilon_f\left(\langle v\rangle_f^f\langle v\rangle_f^f+\left\langle \overset{\circ}{v}\overset{\circ}{v}\right\rangle_f^f\right)\right], \quad (2.16)$$

or, expanding terms and using Equation (II.6), Expression (2.15) becomes:

$$\rho_f \nabla\cdot\left(\frac{1}{\varepsilon_f}\langle v\rangle_f\langle v\rangle_f\right)+\rho_f \nabla\cdot\left\langle \overset{\circ}{v}\overset{\circ}{v}\right\rangle_f. \quad (2.17)$$

Consider the second term on the RHS of Equation (2.6). With the fluid phase consolidated in all directions, using Equation (II.10), this term can be written as:

$$\nabla\langle p\rangle_f + \frac{1}{V_o}\int_{A_{sf}} p\boldsymbol{n}_{fs}\,\mathrm{d}A \tag{2.18}$$

or, using Equation (II.6), Expression (2.18) can be written as:

$$\nabla\left(\varepsilon_f\langle p\rangle_f^f\right) + \frac{1}{V_o}\int_{A_{sf}} p\boldsymbol{n}_{fs}\,\mathrm{d}A\,. \tag{2.19}$$

Applying the identity:

$$\nabla(ab) = (\nabla a)b + a(\nabla b), \tag{2.20}$$

where a and b are scalar quantities, to the first term in Expression (2.19) yields:

$$(\nabla\varepsilon_f)\langle p\rangle_f^f + \varepsilon_f\nabla\langle p\rangle_f^f + \frac{1}{V_o}\int_{A_{sf}} p\boldsymbol{n}_{fs}\,\mathrm{d}A\,. \tag{2.21}$$

Substituting Equation (II.15) and rearranging terms yields:

$$-\langle p\rangle_f^f\frac{1}{V_o}\int_{A_{sf}}\boldsymbol{n}_{fs}\,\mathrm{d}A + \varepsilon_f\nabla\langle p\rangle_f^f + \frac{1}{V_o}\int_{A_{sf}} p\boldsymbol{n}_{fs}\,\mathrm{d}A\,. \tag{2.22}$$

After rearranging terms and substituting Definition (II.5), noting that a volume-averaged quantity in an REV is independent of the volume integral over that phase in the REV, Expression (2.22) yields:

$$\varepsilon_f\nabla\langle p\rangle_f^f + \frac{1}{V_o}\int_{A_{sf}}{}^{\circ}p\boldsymbol{n}_{fs}\,\mathrm{d}A\,. \tag{2.23}$$

Consider the last term on the RHS of Equation (2.6). Substituting Newton's law of viscosity:

$$\boldsymbol{\tau} = -\mu \nabla \boldsymbol{v}, \tag{2.24}$$

where μ is the fluid viscosity, yields:

$$\left\langle \nabla \cdot \mu \nabla \boldsymbol{v} \right\rangle_f . \tag{2.25}$$

With both phases consolidated in all directions, using Equation (II.10) and taking into account that the fluid viscosity μ is constant, this term can be written as:

$$\nabla \cdot \left(\mu \left\langle \nabla \boldsymbol{v} \right\rangle_f \right) + \frac{1}{V_o} \int_{A_{sf}} \mu (\nabla \boldsymbol{v}) \cdot \boldsymbol{n}_{fs} \, \mathrm{d}A . \tag{2.26}$$

Another substitution of Equation (II.10) into the first term in Expression (2.26) yields:

$$\nabla \cdot \left[\mu \left(\nabla \left\langle \boldsymbol{v} \right\rangle_f + \frac{1}{V_o} \int_{A_{sf}} \boldsymbol{v} \cdot \boldsymbol{n}_{fs} \, \mathrm{d}A \right) \right] + \frac{1}{V_o} \int_{A_{sf}} \mu (\nabla \boldsymbol{v}) \cdot \boldsymbol{n}_{fs} \, \mathrm{d}A . \tag{2.27}$$

Noting that $\boldsymbol{v} = 0$ at the interface A_{sf}, it follows that:

$$\nabla \cdot \left(\mu \nabla \left\langle \boldsymbol{v} \right\rangle_f \right) + \frac{1}{V_o} \int_{A_{sf}} \mu (\nabla \boldsymbol{v}) \cdot \boldsymbol{n}_{fs} \, \mathrm{d}A . \tag{2.28}$$

Substituting Expression (2.7), Expression (2.17), Expression (2.23) and Expression (2.28) into Equation (2.6) yields:

$$\rho_f \frac{\partial \left\langle \boldsymbol{v} \right\rangle_f}{\partial t} + \rho_f \nabla \cdot \left(\frac{1}{\varepsilon_f} \left\langle \boldsymbol{v} \right\rangle_f \left\langle \boldsymbol{v} \right\rangle_f \right) + \rho_f \nabla \cdot \left\langle \overset{\circ}{\boldsymbol{v}} \overset{\circ}{\boldsymbol{v}} \right\rangle_f = \varepsilon_f \rho_f \left\langle \boldsymbol{B} \right\rangle_f -$$

$$\varepsilon_f \nabla \left\langle p \right\rangle_f^f - \frac{1}{V_o} \int_{A_{sf}} \overset{\circ}{p} \boldsymbol{n}_{fs} \, \mathrm{d}A + \nabla \cdot \left(\mu \nabla \left\langle \boldsymbol{v} \right\rangle_f \right) + \frac{1}{V_o} \int_{A_{sf}} \mu (\nabla \boldsymbol{v}) \cdot \boldsymbol{n}_{fs} \, \mathrm{d}A . \tag{2.29}$$

2.4 Volume-averaged energy equation

The microscopic energy equation is given in Equation (I.70) as:

$$\rho c_p \frac{\mathrm{D}T}{\mathrm{D}t} = -\nabla \cdot \boldsymbol{q} - \frac{1}{\rho}\left(\frac{\partial \rho}{\partial T}\right)_p T \frac{\mathrm{D}p}{\mathrm{D}t} - \boldsymbol{\tau} : \nabla \boldsymbol{v} + I, \tag{I.70}$$

where ρ is the density, c_p is the isobaric specific heat capacity, T is the temperature, $\boldsymbol{q}$ is the conductive heat transfer vector, p is the pressure, $\boldsymbol{\tau}$ is the viscous stress tensor and $\boldsymbol{v}$ is the velocity vector. Substituting the identity for the substantial derivative and Fourier's heat conduction law:

$$\boldsymbol{q} = -k\nabla T, \tag{2.30}$$

into Equation (I.70) yields, after rearranging terms:

$$\rho c_p \frac{\partial T}{\partial t} = \nabla \cdot (k \nabla T) - \rho c_p \boldsymbol{v} \cdot \nabla T - \frac{1}{\rho}\left(\frac{\partial \rho}{\partial T}\right)_p T \frac{\partial p}{\partial t} - \frac{1}{\rho}\left(\frac{\partial \rho}{\partial T}\right)_p T \boldsymbol{v} \cdot \nabla p - \boldsymbol{\tau} : \nabla \boldsymbol{v} + I. \tag{2.31}$$

For a rigid solid or a constant density fluid it follows that:

$$\frac{\partial \rho}{\partial T} = 0 \tag{2.32}$$

and for the fluid phase being displaced at moderate flow velocities:

$$\boldsymbol{\tau} : \nabla \boldsymbol{v} \approx 0. \tag{2.33}$$

Substituting Condition (2.32) and Condition (2.33) and utilising Identity (I.47):

$$\nabla \cdot (a\boldsymbol{b}) = (\nabla a) \cdot \boldsymbol{b} + a(\nabla \cdot \boldsymbol{b}), \tag{I.47}$$

where a is a scalar quantity and b is a vector quantity, to expand the second term on the RHS of Equation (2.31) yields:

$$\rho c_p \frac{\partial T}{\partial t} = \nabla \cdot (k \nabla T) - \rho c_p [\nabla \cdot (\boldsymbol{v} T) + T \nabla \cdot \boldsymbol{v}] + I . \tag{2.34}$$

Substituting Equation (I.11) and Identity (I.47) into Equation (2.4), noting that for a constant density fluid $\frac{\mathrm{D}\rho}{\mathrm{D}t} = 0$, yields the energy equation for a fluid with constant thermophysical properties, being displaced at moderate flow velocities as:

$$\rho c_p \frac{\partial T}{\partial t} = \nabla \cdot (k \nabla T) - \rho c_p \nabla \cdot (\boldsymbol{v} T) + I . \tag{2.35}$$

Substituting a zero velocity vector in Equation (2.35) yields the energy equation for a rigid solid with constant thermophysical properties:

$$\rho c_p \frac{\partial T}{\partial t} = \nabla \cdot (k \nabla T) + I . \tag{2.36}$$

Integrating Equation (2.36) over the solid phase of a REV, dividing by V_o and substituting Definition (II.3) yields:

$$\left\langle \rho_s c_{p,s} \frac{\partial T}{\partial t} \right\rangle_s = \left\langle \nabla \cdot (k_s \nabla T) \right\rangle_s + \left\langle I_s \right\rangle_s . \tag{2.37}$$

Similarly, integrating Equation (2.37) over the fluid phase of a REV, dividing by V_o and substituting Definition (II.3) yields:

$$\left\langle \rho_f c_{p,f} \frac{\partial T}{\partial t} \right\rangle_f = \left\langle \nabla \cdot (k_f \nabla T) \right\rangle_f - \left\langle \rho_f c_{p,f} \nabla \cdot (\boldsymbol{v} T) \right\rangle_f + \left\langle I_f \right\rangle_f . \tag{2.38}$$

Consider the terms on the LHS of Equation (2.37) and Equation (2.38). Using Equation (II.13), these terms can be written as:

$$\rho_\gamma c_{p,\gamma} \frac{\partial \langle T \rangle_\gamma}{\partial t}, \tag{2.39}$$

where $\gamma = s, f$.

Consider the first term on the RHS of Equation (2.37) and Equation (2.38). With both phases consolidated in all directions, using Equation (II.10) and taking into account that the thermal conductivities are constant, these terms can be written as:

$$\nabla \cdot \left(k_\gamma \langle \nabla T \rangle_\gamma \right) + \frac{1}{V_o} \int_{A_{sf}} k_\gamma \nabla T_\gamma \cdot \boldsymbol{n}_{\gamma\varphi} \mathrm{d}A, \tag{2.40}$$

where $\gamma = s$ and $\varphi = f$, or *vice versa*. Another substitution of Equation (II.10) into the first term in Expression (2.40) yields:

$$\nabla \cdot \left[k_\gamma \left(\nabla \langle T \rangle_\gamma + \frac{1}{V_o} \int_{A_{sf}} T \boldsymbol{n}_{\gamma\varphi} \, \mathrm{d}A \right) \right] + \frac{1}{V_o} \int_{A_{sf}} k_\gamma \nabla T_\gamma \cdot \boldsymbol{n}_{\gamma\varphi} \, \mathrm{d}A. \tag{2.41}$$

The temperature T in the surface integral in the parenthesis does not need a phase reference, since at the interface between the two phases $T_s = T_f$. Substituting Equation (II.6) into Expression (2.41) and expanding the partial derivative in the substituted term yields:

$$\nabla \cdot \left(k_\gamma \varepsilon_\gamma \nabla \langle T \rangle_\gamma^\gamma + k_\gamma \langle T \rangle_\gamma^\gamma \nabla \varepsilon_\gamma + \frac{1}{V_o} \int_{A_{sf}} k_\gamma T \boldsymbol{n}_{\gamma\varphi} \, \mathrm{d}A \right) + \frac{1}{V_o} \int_{A_{sf}} k_\gamma \nabla T_\gamma \cdot \boldsymbol{n}_{\gamma\varphi} \, \mathrm{d}A. \tag{2.42}$$

Substituting Equation (II.15) into the second term in the parenthesis in Expression (2.42) yields:

$$\nabla\cdot\left(k_\gamma\varepsilon_\gamma\nabla\langle T\rangle_\gamma^\gamma-k_\gamma\langle T\rangle_\gamma^\gamma\frac{1}{V_o}\int_{A_{sf}}\boldsymbol{n}_{\gamma\varphi}\,\mathrm{d}A+\frac{1}{V_o}\int_{A_{sf}}k_\gamma T\boldsymbol{n}_{\gamma\varphi}\,\mathrm{d}A\right)+\frac{1}{V_o}\int_{A_{sf}}k_\gamma\nabla T_\gamma\cdot\boldsymbol{n}_{\gamma\varphi}\,\mathrm{d}A. \tag{2.43}$$

Noting that $k_\gamma\langle T\rangle_\gamma^\gamma$ is independent of the surface integral in Expression (2.43), this expression can be written as:

$$\nabla\cdot\left(k_\gamma\varepsilon_\gamma\nabla\langle T\rangle_\gamma^\gamma\right)+\nabla\cdot\left[\frac{1}{V_o}\int_{A_{sf}}k_\gamma\left(T-\langle T\rangle_\gamma^\gamma\right)\boldsymbol{n}_{\gamma\varphi}\,\mathrm{d}A\right]+\frac{1}{V_o}\int_{A_{sf}}k_\gamma\nabla T_\gamma\cdot\boldsymbol{n}_{\gamma\varphi}\,\mathrm{d}A. \tag{2.44}$$

Substituting Definition (II.5) into the second term in Expression (2.44) yields:

$$\nabla\cdot\left(k_\gamma\varepsilon_\gamma\nabla\langle T\rangle_\gamma^\gamma\right)+\nabla\cdot\left(\frac{1}{V_o}\int_{A_{sf}}k_\gamma\,\mathring{T}\boldsymbol{n}_{\gamma\varphi}\,\mathrm{d}A\right)+\frac{1}{V_o}\int_{A_{sf}}k_\gamma\nabla T_\gamma\cdot\boldsymbol{n}_{\gamma\varphi}\,\mathrm{d}A. \tag{2.45}$$

Consider the second term on the RHS of Equation (2.38). Following the analytical procedure used from Expression (2.8) to Expression (2.17), this term can be written as:

$$\rho_f c_{p,f}\nabla\cdot\left(\frac{1}{\varepsilon_f}\langle\boldsymbol{v}\rangle_f\langle T\rangle_f\right)+\rho_f c_{p,f}\nabla\cdot\left\langle\mathring{\boldsymbol{v}}\mathring{T}\right\rangle_f. \tag{2.46}$$

Substituting Expression (2.39) and Expression (2.45) in Equation (2.37) yields for the

solid phase:

$$\rho_s c_{p,s} \frac{\partial \langle T \rangle_s}{\partial t} = \nabla \cdot \left(k_s \varepsilon_s \nabla \langle T \rangle_s^s \right) + \nabla \cdot \left(\frac{1}{V_o} \int_{A_{sf}} k_s \overset{\circ}{T}_s \boldsymbol{n}_{sf} \, \mathrm{d}A \right) + \frac{1}{V_o} \int_{A_{sf}} k_s \nabla T_s \cdot \boldsymbol{n}_{sf} \, \mathrm{d}A + \langle I_s \rangle_s . \tag{2.47}$$

Substituting Expression (2.39), Expression (2.45) and Expression (2.46) in Equation (2.38) yields for the fluid phase:

$$\rho_f c_{p,f} \frac{\partial \langle T \rangle_f}{\partial t} = \nabla \cdot \left(k_f \varepsilon_f \nabla \langle T \rangle_f^f \right) + \nabla \cdot \left(\frac{1}{V_o} \int_{A_{sf}} k_f \overset{\circ}{T}_f \boldsymbol{n}_{fs} \, \mathrm{d}A \right) +$$

$$\frac{1}{V_o} \int_{A_{sf}} k_f \nabla T_f \cdot \boldsymbol{n}_{fs} \, \mathrm{d}A - \rho_f c_{p,f} \nabla \cdot \left(\frac{1}{\varepsilon_f} \langle \boldsymbol{v} \rangle_f \langle T \rangle_f \right) - \rho_f c_{p,f} \nabla \cdot \left\langle \overset{\circ}{\boldsymbol{v}} \overset{\circ}{T} \right\rangle_f + \langle I_f \rangle_f . \tag{2.48}$$

2.5 Discussion

In Equation (2.29), Equation (2.47) and Equation (2.48), volume-averaged quantities are referred to as *macroscopic quantities* and terms containing them are classified as *macroscopic terms*. Terms containing microscopic quantities (including microscopic quantity deviations) are classified as *microscopic terms.*

In Equation (2.29), the macroscopic terms are, in the order in which they appear, referred to as the *transient term*, the *momentum convective term* the *body force term*, the *pressure term* and the *macroscopic viscous transfer term.* The microscopic terms are, in the order in which they appear, referred to as the *momentum dispersion term*, the *pressure deviation term* and the *microscopic viscous transfer term.*

In Equation (2.47) and Equation (2.48), the macroscopic terms are, in the order in which they appear, referred to as the *transient term*, the *conduction term* and the *source term*. Convective transport in the fluid phase yields an additional macroscopic term in Equation (2.48), referred to as the *thermal convective term*. The microscopic terms are, in the order in which they appear, referred to as the *temperature deviation term* and the *interphasial heat transfer term*. For the fluid phase, the additional microscopic convective term in Equation (2.48) is referred to as the *thermal dispersion term*.

Close observation reveals that the macroscopic terms in Equation (2.29), Equation (2.47) and Equation (2.48) correspond to a great degree with counterparts in the microscopic energy equation for the solid and the fluid phases. Microscopic terms in Equation (2.29), Equation (2.47) and Equation (2.48) deal with heat transfer phenomena that are introduced by the analytical process of raising the length scale level of description from microscopic to macroscopic level.

There is a distinct difference between macroscopic and microscopic terms. Although they both describe heat transfer processes at a macroscopic level, the microscopic terms still employ microscopic quantities, but in integral form. Since observations and measurements are restricted to macroscopic level, any further development towards the application and solution of Equation (2.29), Equation (2.47) and Equation (2.48) requires that the microscopic terms are transformed and rewritten in terms of macroscopic quantities. The success of any such effort relies on the correct physical interpretation of the microscopic terms.

CHAPTER 3

VISCOUS SHEAR MODEL

3.1 Overview

The *viscous shear model*, which transforms the microscopic viscous transfer term and the pressure deviation term in the volume-averaged momentum equation [Equation (2.29)] to a description in terms of the macroscopic velocity, is introduced in this chapter. Flow momentum change in the fluid phase, and viscous shear and form drag between the fluid and the foam microstructure are considered to relate the microscopic viscous transfer term and the pressure deviation term to a volume-averaged pressure gradient in the fluid phase. The volume-averaged pressure gradient is in turn related to a viscous shear factor introduced by Du Plessis (1991a).

3.2 Analysis

The drop in the mean microscopic pressure $\Delta\overline{p}$ experienced in a fluid flowing through an REV (representative elementary volume, discussed in Section II.2) will exert a drag force $\boldsymbol{F}$ on the REV in the main streamwise direction, according to:

$$\Delta\overline{p}\frac{\langle \boldsymbol{v} \rangle_f}{\langle v \rangle_f} = -\frac{\boldsymbol{F}}{\overline{A}_{pr}}, \tag{3.1}$$

where $\overline{A}_{pr}$ is the mean projected cross-flow area normal to the streamwise direction. The streamwise direction is given by the unit vector $\frac{\langle \boldsymbol{v} \rangle_f}{\langle v \rangle_f}$, where $\langle v \rangle_f$ is the magnitude of the phasial volume-averaged velocity vector $\langle \boldsymbol{v} \rangle_f$. The mean projected cross-flow area normal to the streamwise direction $\overline{A}_{pr}$ is given by:

$$\overline{A}_{pr} = -\frac{1}{l}\int_0^l A_{pr}\,\mathrm{d}m, \tag{3.2}$$

where l is the dimension across the REV, as shown in Figure II.1. Substituting Equation (3.2) into Equation (3.1) and rearranging terms, noting that the integral defines the volume of the fluid phase in the REV, yields:

$$\frac{\Delta \overline{p}}{l}\frac{\langle \boldsymbol{v} \rangle_f}{\langle v \rangle_f} = -\frac{\boldsymbol{F}}{V_f}. \tag{3.3}$$

Since the mean microscopic pressure $\Delta \overline{p}$ is with reference to an REV, the term on the LHS of Equation (3.3) can be approximated by $\nabla \langle p \rangle_f^f$ and, using Definition (II.1), the fluid phase volume V_f can be given in terms of the overall REV volume V_o and the porosity ε_f, to yield:

$$\nabla \langle p \rangle_f^f = -\frac{\boldsymbol{F}}{\varepsilon_f V_o}. \tag{3.4}$$

The total drag force vector $\boldsymbol{F}$ is due to flow momentum change, viscous shear and form drag. Flow momentum change is caused by change in the shape of velocity profiles in pore scale hydrodynamic entrance regions. Viscous shear is caused by the fluid viscosity and the no-slip condition at the interface between the solid and the fluid phases. At high Reynolds numbers, hydrodynamic boundary layer separation and flow recirculation will cause form drag on the streamwise lee-side surfaces, in addition to flow momentum change and viscous shear (White, 1991).

The viscous shear force in streamwise channels inside the REV can be written as:

$$-\int_{A_{sf}} \mu(\nabla \boldsymbol{v})\cdot \boldsymbol{n}_{fs}\,\mathrm{d}A\,. \tag{3.5}$$

Viscous shear stress in transverse channels causes axial pressure gradients over these channels. Drag forces caused by flow momentum change, form drag and, according to Du Plessis and Masliyah (1988), viscous shear forces in transverse channels, manifest themselves in a pressure deviation $\overset{\circ}{p}$ and can be written as:

$$\int_{A_{sf}} \overset{\circ}{p}\,\boldsymbol{n}_{fs}\,\mathrm{d}A\,. \tag{3.6}$$

Substituting Expression (3.5) and Expression (3.6), the pressure gradient in the streamwise direction, given by Equation (3.4), can be written as:

$$-\nabla\langle p\rangle_f^f = -\frac{1}{\varepsilon_f V_o}\int_{A_{sf}} \mu(\nabla \boldsymbol{v})\cdot \boldsymbol{n}_{fs}\,\mathrm{d}A + \frac{1}{\varepsilon_f V_o}\int_{A_{sf}} \overset{\circ}{p}\,\boldsymbol{n}_{fs}\,\mathrm{d}A\,. \tag{3.7}$$

The terms on the RHS of Equation (3.7) correspond to the surface integral terms in Equation (2.29). Du Plessis (1991a) defined a rearranged version of Equation (3.7) in terms of a viscous shear factor $\boldsymbol{f}$, given here implicitly in the form of a diagonal tensor as:

$$\mu \boldsymbol{f}\cdot\langle \boldsymbol{v}\rangle_f \equiv -\frac{1}{V_o}\int_{A_{sf}} \mu(\nabla \boldsymbol{v})\cdot \boldsymbol{n}_{fs}\,\mathrm{d}A + \frac{1}{V_o}\int_{A_{sf}} \overset{\circ}{p}\,\boldsymbol{n}_{fs}\,\mathrm{d}A\,. \tag{3.8}$$

Definition (3.8) is referred to as the *viscous shear model.*

CHAPTER 4

EQUILIBRIUM AND NON-EQUILIBRIUM TEMPERATURE DISTRIBUTIONS

4.1 Overview

The approach towards transforming the temperature deviation terms in the volume-averaged energy equation for the solid and the fluid phases [Equation (2.47) and Equation (2.48)], to a description in terms of macroscopic temperature gradients, somewhat resembles the approach followed in Fourier's conduction law. In that approach, diffusive transport of heat in a substance is conceptually represented by a temperature gradient together with a proportionality coefficient referred to as thermal conductivity. Fourier's conduction law elevates the distribution of energy content in random molecular motion in a substance, to a higher measurable averaging level in the form of the substance's microscopic temperature gradient. In order to describe conduction at a macroscopic level in terms of macroscopic temperatures gradients only, microscopic heat conduction described by the microscopic temperature gradients, needs to be elevated to a higher averaging level where they could be related to measurable macroscopic temperature gradients. This is achieved by the introduction of certain proportionality coefficients in Chapter 6, which are defined at a macroscopic level.

As a first step, it is necessary to identify well defined and measurable building blocks amounting to observed microscopic conductive heat transfer in a two-phase system where the phases are not in thermal equilibrium with each other, in such a way that they could be conceptually presented in the form suggested above. These building blocks are identified by characteristic temperature distributions in consolidated two-phase systems (see Section 4.2), referred to as *equilibrium*, *directional non-equilibrium* and *non-directional non-equilibrium* temperature distributions, and which are defined in this chapter.

The analysis of this chapter is restricted to conduction only. According to Fourier's law, the conceptual representation of conduction is the same in solids and fluids. Therefore the analysis applies to any two-phase system. The phases will not be identified as the solid phase and the fluid phase. Instead, the two phases are identified by generic designations, namely the *α-phase* and the *β-phase*.

4.2 Consolidated and non-consolidated phases

Whenever a domain of a phase is connected with reference to a particular direction (*i.e.* if any two points aligned in the particular direction, belonging to that phase, can be connected by a curve that lies completely within it), the phase is said to be *consolidated* with reference to that direction. If a phase is not connected with reference to a particular direction, then the phase is said to be *non-consolidated* with reference to that direction. Flow through a porous medium is only possible in a direction in which the fluid phase is consolidated. Figure 4.1 shows a fibrous porous medium of which the solid phase is consolidated with reference to the *y*-direction and the fluid phase is consolidated with reference to all three principle directions.

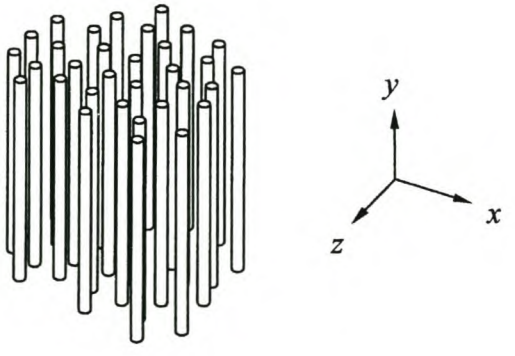

Figure 4.1 A fibrous porous medium with different consolidation characteristics in the two phases.

4.3 Microscopic temperature distributions

Consider the representative elementary volume (REV) of a two-phase porous medium shown in Figure II.1. For the purpose of this theoretical process, locally constant porosity is assumed within the REV. Figure 4.2 shows the upper half of the REV placed in a coordinate system with a microscopic temperature distribution T at centreline AA. Let the centreline AA corresponds to a principal direction of the coordinate system, referred to as the direction m. If a thermal non-equilibrium state prevails throughout the REV, let the microscopic temperature T at any point within the REV be a linear combination of an *equilibrium* microscopic temperature distribution T_e and a *non-equilibrium* microscopic temperature distribution T_n that is:

$$T = T_e + T_n \,. \tag{4.1}$$

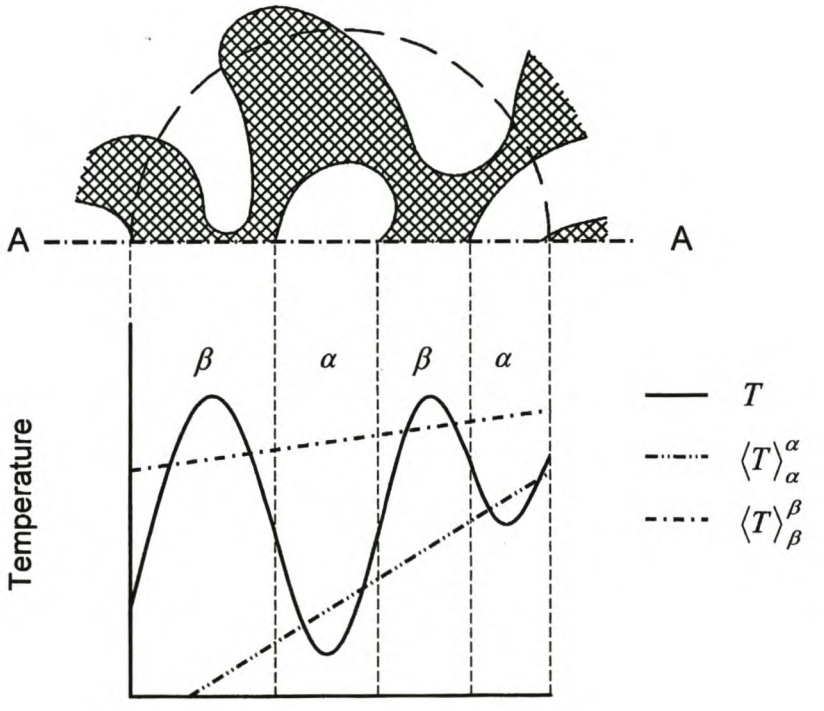

Figure 4.2 Temperature distribution through an REV.

With the equilibrium microscopic temperature distribution T_e, the phases are in thermal equilibrium everywhere within the two-phase system. The choice of such a single temperature, which describes the conservation of heat under thermal equilibrium conditions, is not necessarily obvious. Nozad *et al.* (1985) suggested that the overall volume-averaged temperature, as defined by Definition (II.2), is the most likely candidate.

In the present approach though, an equilibrium microscopic temperature distribution T_e is selected such that it accounts for directional heat transfer within the REV. The non-equilibrium microscopic temperature distribution T_n then represents a temperature distribution which accounts for the net exchange of heat between the phases with a zero net directional heat transfer in the principle direction m within the REV. Figure 4.3 and Figure 4.4 show the decomposition of the microscopic temperature distribution T into temperature distributions T_e and T_n.

Further, let the non-equilibrium microscopic temperature distribution T_n, at any point within an REV, be a linear combination of a *directional non-equilibrium* microscopic temperature distribution T_{nd} and a *non-directional non-equilibrium* microscopic temperature distribution T_{nn}, that is:

$$T_n = T_{nd} + T_{nn}\,, \tag{4.2}$$

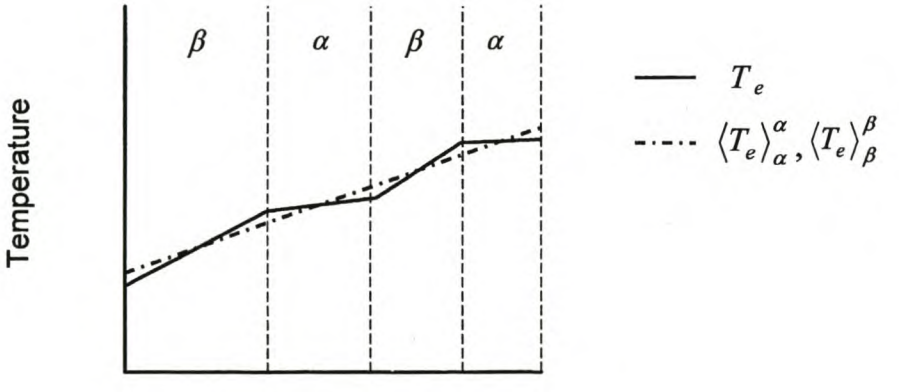

Figure 4.3 Equilibrium temperature distribution T_e through an REV.

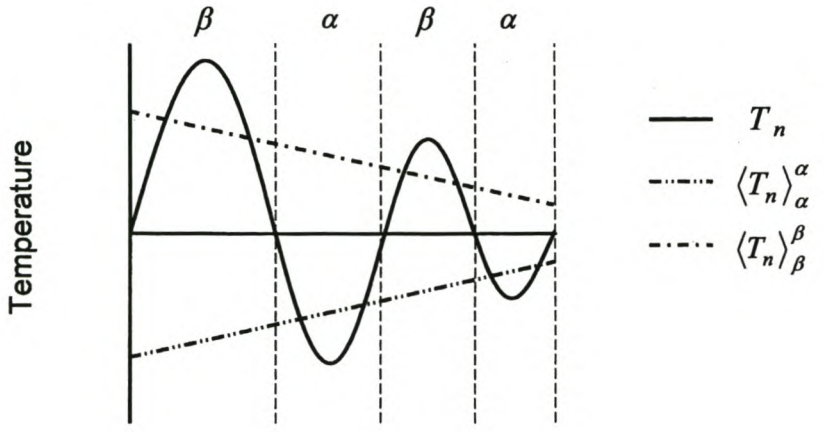

Figure 4.4 Non-equilibrium temperature distribution T_n through an REV.

as shown by Figure 4.5 and Figure 4.6. The directional non-equilibrium microscopic temperature distribution T_{nd} accounts for the directional heat transfer in the principle direction in each phase within the REV, while the net heat transfer across the interface between the two phases is zero within the REV. The non-directional non-equilibrium microscopic temperature distribution T_{nn} then accounts only for the net exchange of heat between the phases, with a zero net directional heat transfer in the principle direction in each phase within the REV.

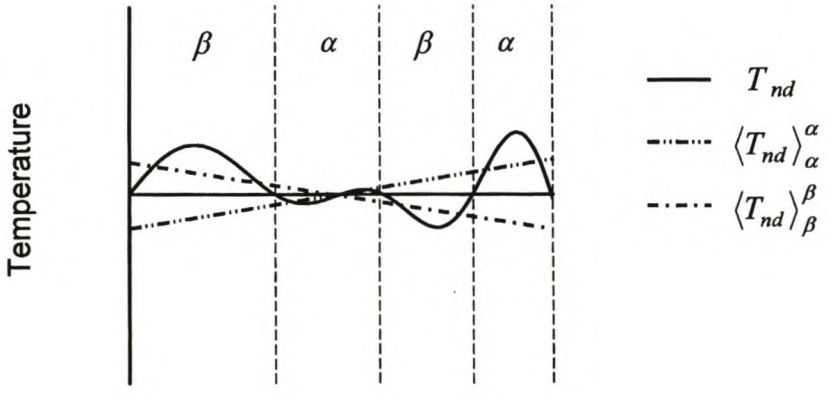

Figure 4.5 Directional non-equilibrium temperature distribution T_{nd} through an REV.

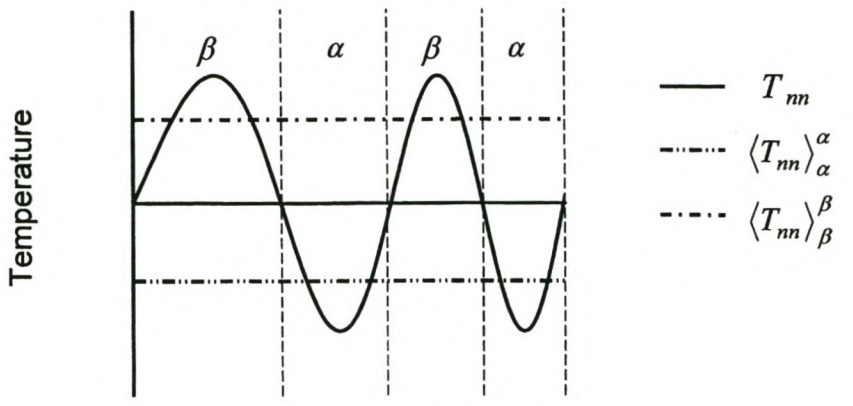

Figure 4.6 Non-directional non-equilibrium temperature distribution T_{nn} through an REV.

4.4 Equilibrium microscopic temperature distribution

With the two phases in equilibrium, the net heat transferred across the interface between the two phases is zero:

$$\int_{A_{\alpha\beta}} \left(k \nabla T_e\right)_{\gamma} \cdot \boldsymbol{n}_{\gamma\varphi} \, \mathrm{d}A = 0 \,, \tag{4.3}$$

where $\gamma = \alpha$ and $\varphi = \beta$, or *vice versa*. The intrinsic volume-averaged equilibrium temperature of the α-phase is equal to that of the β-phase everywhere within the REV, that is:

$$\langle T_e \rangle_{\alpha}^{\alpha} = \langle T_e \rangle_{\beta}^{\beta} \,, \tag{4.4}$$

and, with reference to the direction m:

$$\frac{\partial}{\partial m} \langle T_e \rangle_{\alpha}^{\alpha} = \frac{\partial}{\partial m} \langle T_e \rangle_{\beta}^{\beta} \,. \tag{4.5}$$

Considering the hypothesis of a locally constant porosity within the REV, substituting Equation (II.6) into Condition (4.5) yields:

$$\frac{1}{\varepsilon_\alpha}\frac{\partial}{\partial m}\langle T_e\rangle_\alpha = \frac{1}{\varepsilon_\beta}\frac{\partial}{\partial m}\langle T_e\rangle_\beta \,. \tag{4.6}$$

4.5 Non-equilibrium microscopic temperature distribution

With a zero net directional heat transfer with reference to the *m*-direction within the REV, it follows that:

$$k_\alpha\left\langle\frac{\partial T_n}{\partial m}\right\rangle_\alpha = -k_\beta\left\langle\frac{\partial T_n}{\partial m}\right\rangle_\beta \,. \tag{4.7}$$

4.6 Directional non-equilibrium microscopic temperature distribution

With a zero net heat transfer across the interface between the two phases, it follows that:

$$\int_{A_{\alpha\beta}} \left(k\nabla T_{nd}\right)_\gamma \cdot \boldsymbol{n}_{\gamma\varphi}\,\mathrm{d}A = 0 \,. \tag{4.8}$$

The intrinsic volume-averaged directional non-equilibrium temperatures $\langle T_{nd}\rangle_\alpha^\alpha$ and $\langle T_{nd}\rangle_\beta^\beta$ are equal at the centre of the REV, that is:

$$\langle T_{nd}\rangle_\alpha^\alpha = \langle T_{nd}\rangle_\beta^\beta \,. \tag{4.9}$$

The gradients in the intrinsic volume-averaged directional non-equilibrium temperatures $\frac{\partial}{\partial m}\langle T_{nd}\rangle_{\gamma}^{\gamma}$ are equal to the gradients in the intrinsic non-equilibrium temperatures $\frac{\partial}{\partial m}\langle T_{n}\rangle_{\gamma}^{\gamma}$ at the centre of the REV, that is:

$$\frac{\partial}{\partial m}\langle T_{nd}\rangle_{\gamma}^{\gamma} = \frac{\partial}{\partial m}\langle T_{n}\rangle_{\gamma}^{\gamma} . \tag{4.10}$$

4.7 Non-directional non-equilibrium microscopic temperature distribution

Substituting Equation (4.2) into Condition (4.10) yields, at the centre of the REV:

$$\frac{\partial}{\partial m}\langle T_{nn}\rangle_{\gamma}^{\gamma} = 0 . \tag{4.11}$$

Considering the hypothesis of a locally constant porosity within the REV, substituting Equation (II.6) into Condition (4.11) yields:

$$\frac{\partial}{\partial m}\langle T_{nn}\rangle_{\gamma} = 0 . \tag{4.12}$$

Substituting Equation (4.2) and Condition (4.12) into Condition (4.7) yields:

$$k_{\alpha}\left\langle \frac{\partial T_{nd}}{\partial m}\right\rangle_{\alpha} = -k_{\beta}\left\langle \frac{\partial T_{nd}}{\partial m}\right\rangle_{\beta} . \tag{4.13}$$

CHAPTER 5

INTERPHASIAL HEAT TRANSFER MODEL

5.1 Overview

The *interphasial heat transfer model*, which transforms the interphasial heat transfer terms in the volume-averaged energy equation of the solid and the fluid phases [Equation (2.47) and Equation (2.48)] to a description in terms of the macroscopic temperature and velocity, is introduced in this chapter. A hypothesis is presented which relates interphasial heat transfer to the difference between a particular volume–averaged temperature of each phase. The microscopic form of this temperature distribution is discussed in Chapter 4. It is also shown that this hypothesis reduces to a formulation for interphasial heat transfer proposed by Gray (1975) and Whitaker (1977).

5.2 Analysis

In Equation (2.47) and Equation (2.48), consider the interphasial heat transfer term:

$$\frac{1}{V_o}\int_{A_{sf}} k_\gamma \nabla T_\gamma \cdot \boldsymbol{n}_{\gamma\varphi}\, \mathrm{d}A, \tag{5.1}$$

where $\gamma = \alpha$ and $\varphi = \beta$, or *vice versa*. Expression (5.1) describes the net heat flux across the interface between the solid and the fluid phases whenever the two phases are not in thermal equilibrium.

In analogy to the general conceptual representation of heat flux between a rigid stationary surface and an adjacent moving fluid, it is proposed that the net exchange of heat between

the phases is directly proportional to the intrinsic volume-averaged temperature difference between the phases, that is:

$$\frac{1}{A_{sf}}\int_{A_{sf}}\left(k\nabla T_{nn}\right)_{\gamma}\cdot\boldsymbol{n}_{\gamma\varphi}\,\mathrm{d}A=-h_{sf}\left(\left\langle T_{nn}\right\rangle_{\gamma}^{\gamma}-\left\langle T_{nn}\right\rangle_{\varphi}^{\varphi}\right), \tag{5.2}$$

where T_{nn} is a non-directional non-equilibrium microscopic temperature distribution defined in Equation (4.1) and Equation (4.2), and h_{sf} is a proportionality coefficient referred to as the *interphasial heat transfer coefficient*, which is independent of $\left\langle T_{nn}\right\rangle_{\gamma}^{\gamma}-\left\langle T_{nn}\right\rangle_{\varphi}^{\varphi}$. This hypothesis relates the macroscopic description of the interphasial heat transfer process, given as an integral of a microscopic process, to a macroscopic description of the process in terms of macroscopic quantities.

Substituting Equation (4.1) and Equation (4.2), and then Condition (4.3) and Condition (4.8) into the term on the LHS of Assumption (5.2), and substituting Equation (4.1) and Equation (4.2), and then Condition (4.4) and Condition (4.9) into the term on the RHS of Assumption (5.2) yields:

$$\frac{1}{A_{sf}}\int_{A_{sf}}k_{\gamma}\nabla T_{\gamma}\cdot\boldsymbol{n}_{\gamma\varphi}\,\mathrm{d}A=-h_{sf}\left(\left\langle T\right\rangle_{\gamma}^{\gamma}-\left\langle T\right\rangle_{\varphi}^{\varphi}\right), \tag{5.3}$$

which corresponds to the proposal of Gray (1975) and Whitaker (1977). Substituting Equation (II.6) into Equation (5.3) and rearranging terms yields:

$$\frac{1}{A_{sf}}\int_{A_{sf}}k_{\gamma}\nabla T_{\gamma}\cdot\boldsymbol{n}_{\gamma\varphi}\,\mathrm{d}A=-\frac{h_{sf}}{\varepsilon_{\gamma}}\left(\left\langle T\right\rangle_{\gamma}-\frac{\varepsilon_{\gamma}}{1-\varepsilon_{\gamma}}\left\langle T\right\rangle_{\varphi}\right), \tag{5.4}$$

which is referred to as the *interphasial heat transfer model.*

The interphasial heat transfer model is qualified for the case of conduction heat transfer in both phases, in Appendix III.

CHAPTER 6

CONDUCTION MODEL

6.1 Overview

The *conduction model*, which transforms the temperature deviation terms in the volume-averaged energy equation for the solid and the fluid phases [Equation (2.47) and Equation (2.48)], in order to describe them in terms of macroscopic temperatures only, is introduced in this chapter. The manner in which this is done distinguishes the present approach from previous work.

The analytical process of the transformation introduces a novel approach in the volume averaging process, which avoids the mapping of the microscopic temperature deviation field from the intrinsic volume-averaged temperature field (Carbonel and Whitaker, 1984; Zanotti and Carbonel, 1984a, 1984b, 1984c; Quintard and Whitaker, 1993; Moyne, 1997). An effective thermal conductivity and a coupled thermal conductivity are introduced, defined from the formalism of the analytical process. This approach allows closure of spatially periodic and random porous media. No constraints are placed on length and time scales and the analytical process does not require the neglect of higher order terms (Quintard and Whitaker, 1993; Moyne, 1997).

A rigorous physical interpretation of the temperature deviation terms distinguishes this study from previous work and sets the stage for their successful transformation in terms of macroscopic quantities.

The analysis of this chapter is restricted to conduction only and the phases will not be identified as the solid phase or the fluid phase, but are identified by generic designations, namely the *α-phase* and the *β-phase*.

6.2 Physical interpretation of the temperature deviation terms

Consider Figure 6.1, which shows an enlargement of part of the REV shown in Figure II.1, where a section of the solid phase extends into the fluid phase. In the absence of a thermal contact resistance between the phases, conduction caused by an x-direction macroscopic temperature gradient in the fluid phase takes a "short cut" route through the extended region of the solid. This effect causes the microscopic temperature to deviate from the intrinsic volume-averaged temperature in that phase in the extended region of the solid phase. The complete conduction process in the extended region of the solid phase can therefore not be described by only the intrinsic or phasial volume-averaged temperature distribution in the solid phase, but must include the conduction contribution of the deviation from the intrinsic volume-averaged temperature. From Definition (II.5) it follows that the temperature deviation is relative to the macroscopic temperature and therefore the expression:

$$k\nabla \overset{\circ}{T} \tag{6.1}$$

describes conduction relative to that described by the intrinsic volume-averaged temperature distribution.

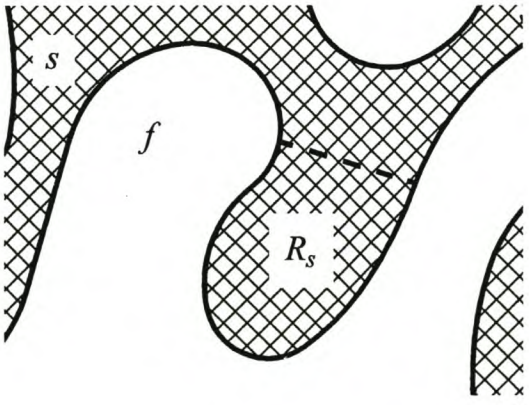

Figure 6.1 Temperature deviation in a representative elementary volume (REV).

The broken line in Figure 6.1, together with the interface between the two phases, encloses the region in the solid phase in which the microscopic temperature deviates from the intrinsic volume-averaged temperature. Let this region be referred to as R_s, as shown in Figure 6.1. The expression:

$$\int_{R_S} k_s \nabla \overset{\circ}{T}_s \, \mathrm{d}V \tag{6.2}$$

therefore describes the total amount of conduction occurring in region R_s, relative to that described by the intrinsic volume-averaged temperature distribution. Applying the Divergence Theorem (Kreyszig, 1993, p. 545) to Expression (6.2), noting that $\overset{\circ}{T} = 0$ at the boundary indicated by the broken line, yields:

$$\int_{R_S} k_s \nabla \overset{\circ}{T}_s \, \mathrm{d}V = \int_{A_{sf}} k_s \overset{\circ}{T}_s \, \boldsymbol{n}_{sf} \, \mathrm{d}A . \tag{6.3}$$

The right hand side of Equation (6.3) corresponds to the surface integral contained in the temperature deviation term. Therefore, the temperature deviation term describes the secondary conduction within the solid phase in the REV as a result of a non-zero temperature deviation occurring within the solid phase. The secondary conduction is relative to that described by the volume-averaged temperature distribution.

The same argument applies to sections of the fluid phase extending into the solid phase.

The physical interpretation of the temperature deviation terms justifies an attempt to incorporate them into the conduction terms in Equation (2.47) and Equation (2.48).

6.3 Analysis

Substituting Equation (4.2) into Equation (4.1), integrating the α- and the β-phase respectively within an REV, dividing by the overall volume V_o and substituting Definition (II.3) yields:

$$\langle T \rangle_\gamma = \langle T_e \rangle_\gamma + \langle T_{nd} \rangle_\gamma + \langle T_{nn} \rangle_\gamma , \tag{6.4}$$

where $\gamma = \alpha$ or β. Similarly, substituting Equation (4.2) into Equation (4.1), integrating its derivative with respect to the m-direction in the α-phase and the β-phase within an REV, dividing by V_o and substituting Definition (II.3), yields:

$$\left\langle \frac{\partial T}{\partial m} \right\rangle_\gamma = \left\langle \frac{\partial T_e}{\partial m} \right\rangle_\gamma + \left\langle \frac{\partial T_{nd}}{\partial m} \right\rangle_\gamma + \left\langle \frac{\partial T_{nn}}{\partial m} \right\rangle_\gamma . \tag{6.5}$$

For a continuous distribution of T_{nn}, it follows from Condition (4.12) that:

$$\left\langle \frac{\partial T_{nn}}{\partial m} \right\rangle_\gamma = 0 . \tag{6.6}$$

Substituting Condition (6.6) into Equation (6.5), the one-dimensional form of the first two terms on the RHS of Equation (2.47) and Equation (2.48) can be written as:

$$\frac{\partial}{\partial m}\left(k_\gamma \varepsilon_\gamma \frac{\partial}{\partial m} \langle T \rangle_\gamma^\gamma \right) + \frac{\partial}{\partial m}\left(\frac{1}{V_o} \int_{A_{sf}} k_\gamma \overset{\circ}{T}_\gamma \boldsymbol{n}_{\gamma\varphi,m} \, \mathrm{d}A \right) = \frac{\partial}{\partial m}\left(k_\gamma \left\langle \frac{\partial T_e}{\partial m} \right\rangle_\gamma \right) + \frac{\partial}{\partial m}\left(k_\gamma \left\langle \frac{\partial T_{nd}}{\partial m} \right\rangle_\gamma \right), \tag{6.7}$$

where $\gamma = s$ and $\varphi = f$, or *vice versa*.

Define an *equilibrium thermal conductivity* as:

$$k_{e,\gamma,m} \equiv \frac{k_\gamma \left\langle \frac{\partial T_e}{\partial m} \right\rangle_\gamma}{\frac{\partial}{\partial m}\langle T_e \rangle_\gamma} \tag{6.8}$$

and a *non-equilibrium thermal conductivity* as:

$$k_{nd,\gamma,m} \equiv \frac{k_\gamma \left\langle \frac{\partial T_{nd}}{\partial m} \right\rangle_\gamma}{\frac{\partial}{\partial m}\langle T_{nd} \rangle_\gamma}. \tag{6.9}$$

Substituting Definition (6.8) and Definition (6.9), the RHS of Equation (6.7) is given as:

$$\frac{\partial}{\partial m}\left(k_{e,\gamma,m} \frac{\partial}{\partial m}\langle T_e \rangle_\gamma \right) + \frac{\partial}{\partial m}\left(k_{nd,\gamma,m} \frac{\partial}{\partial m}\langle T_{nd} \rangle_\gamma \right). \tag{6.10}$$

Substituting Equation (6.4) into the second term of Expression (6.10) yields:

$$\frac{\partial}{\partial m}\left(k_{e,\gamma,m} \frac{\partial}{\partial m}\langle T_e \rangle_\gamma \right) + \frac{\partial}{\partial m}\left[k_{nd,\gamma,m}\left(\frac{\partial}{\partial m}\langle T \rangle_\gamma - \frac{\partial}{\partial m}\langle T_e \rangle_\gamma - \frac{\partial}{\partial m}\langle T_{nn} \rangle_\gamma \right) \right]. \tag{6.11}$$

Substituting Condition (4.12) into Expression (6.11) and rearranging terms yields:

$$\frac{\partial}{\partial m}\left[\left(k_{e,\gamma,m} - k_{nd,\gamma,m} \right) \frac{\partial}{\partial m}\langle T_e \rangle_\gamma \right] + \frac{\partial}{\partial m}\left(k_{nd,\gamma,m} \frac{\partial}{\partial m}\langle T \rangle_\gamma \right). \tag{6.12}$$

In order to derive an expression for the volume-averaged equilibrium temperature $\langle T_e \rangle_\gamma$ in terms of the volume-averaged temperature $\langle T \rangle_\gamma$, substitute Definition (6.9) into

Condition (4.13) to give:

$$k_{nd,\alpha,m}\frac{\partial}{\partial m}\langle T_{nd}\rangle_{\alpha} = -k_{nd,\beta,m}\frac{\partial}{\partial m}\langle T_{nd}\rangle_{\beta}. \tag{6.13}$$

Substituting Equation (4.1), Equation (4.2) and Condition (4.12) into Condition (6.13) yields:

$$k_{nd,\alpha,m}\left(\frac{\partial}{\partial m}\langle T\rangle_{\alpha} - \frac{\partial}{\partial m}\langle T_e\rangle_{\alpha}\right) = -k_{nd,\beta,m}\left(\frac{\partial}{\partial m}\langle T\rangle_{\beta} - \frac{\partial}{\partial m}\langle T_e\rangle_{\beta}\right). \tag{6.14}$$

Substituting Condition (4.6) into Condition (6.14) yields after rearranging terms:

$$\frac{\partial}{\partial m}\langle T_e\rangle_{\gamma} = \frac{k_{nd,\gamma,m}}{k_{nd,\gamma,m} + \dfrac{\varepsilon_{\varphi}}{\varepsilon_{\gamma}}k_{nd,\varphi,m}}\frac{\partial}{\partial m}\langle T\rangle_{\gamma} + \frac{k_{nd,\varphi,m}}{k_{nd,\gamma,m} + \dfrac{\varepsilon_{\varphi}}{\varepsilon_{\gamma}}k_{nd,\varphi,m}}\frac{\partial}{\partial m}\langle T\rangle_{\varphi}. \tag{6.15}$$

Substituting Equation (6.15) into Expression (6.12) yields:

$$\frac{\partial}{\partial m}\left[\left(k_{e,\gamma,m} - k_{nd,\gamma,m}\right)\left(\frac{k_{nd,\gamma,m}}{k_{nd,\gamma,m} + \dfrac{\varepsilon_{\varphi}}{\varepsilon_{\gamma}}k_{nd,\varphi,m}}\frac{\partial}{\partial m}\langle T\rangle_{\gamma} + \frac{k_{nd,\varphi,m}}{k_{nd,\gamma,m} + \dfrac{\varepsilon_{\varphi}}{\varepsilon_{\gamma}}k_{nd,\varphi,m}}\frac{\partial}{\partial m}\langle T\rangle_{\varphi}\right)\right] + \frac{\partial}{\partial m}\left(k_{nd,\gamma,m}\frac{\partial}{\partial m}\langle T\rangle_{\gamma}\right). \tag{6.16}$$

After rearranging terms in Expression (6.16) and substituting back into Equation (6.7), that equation can be written as:

$$\frac{\partial}{\partial m}k_{\gamma}\varepsilon_{\gamma}\frac{\partial}{\partial m}\langle T\rangle_{\gamma}^{\gamma} + \frac{\partial}{\partial m}\frac{1}{V_o}\int_{A_{sf}} k_{\gamma}\,\mathring{T}\,\boldsymbol{n}_{\gamma\varphi,m}\,\mathrm{d}A = \frac{\partial}{\partial m}\left(k_{\gamma\gamma,m}\frac{\partial}{\partial m}\langle T\rangle_{\gamma}\right) + \frac{\partial}{\partial m}\left(k_{\gamma\varphi,m}\frac{\partial}{\partial m}\langle T\rangle_{\varphi}\right), \tag{6.17}$$

with $k_{\gamma\gamma}$ defined as:

$$k_{\gamma\gamma,m} \equiv \frac{k_{nd,\gamma,m}k_{e,\gamma,m} + \frac{\varepsilon_\varphi}{\varepsilon_\gamma}k_{nd,\varphi,m}k_{nd,\gamma,m}}{k_{nd,\gamma,m} + \frac{\varepsilon_\varphi}{\varepsilon_\gamma}k_{nd,\varphi,m}} \tag{6.18}$$

and $k_{\gamma\varphi}$ defined as:

$$k_{\gamma\varphi,m} \equiv \frac{k_{nd,\varphi,m}\left(k_{e,\gamma,m} - k_{nd,\gamma,m}\right)}{k_{nd,\gamma,m} + \frac{\varepsilon_\varphi}{\varepsilon_\gamma}k_{nd,\varphi,m}}. \tag{6.19}$$

Equation (6.17) defines the *conduction model*, which in three dimensions is given as:

$$\nabla\cdot\left(k_\gamma\varepsilon_\gamma\nabla\langle T\rangle_\gamma^\gamma\right)+\nabla\cdot\left(\frac{1}{V_o}\int_{A_{sf}}k_\gamma\,\overset{\circ}{T}_\gamma\,\boldsymbol{n}_{\gamma\varphi}\mathrm{d}A\right) = \nabla\cdot\left(\boldsymbol{k}_{\gamma\gamma}\cdot\nabla\langle T\rangle_\gamma\right)+\nabla\cdot\left(\boldsymbol{k}_{\gamma\varphi}\cdot\nabla\langle T\rangle_\varphi\right). \tag{6.20}$$

For the α-phase, the RHS of Equation (6.20) is:

$$\nabla\cdot\left(\boldsymbol{k}_{\alpha\alpha}\cdot\nabla\langle T\rangle_\alpha\right)+\nabla\cdot\left(\boldsymbol{k}_{\alpha\beta}\cdot\nabla\langle T\rangle_\beta\right) \tag{6.21}$$

and for the β-phase:

$$\nabla\cdot\left(\boldsymbol{k}_{\beta\beta}\cdot\nabla\langle T\rangle_\beta\right)+\nabla\cdot\left(\boldsymbol{k}_{\beta\alpha}\cdot\nabla\langle T\rangle_\alpha\right). \tag{6.22}$$

In Expression (6.21), $\boldsymbol{k}_{\alpha\alpha}$ is referred to as the *α-phase effective thermal conductivity tensor* and $\boldsymbol{k}_{\alpha\beta}$ is referred to as the *α-phase coupled thermal conductivity tensor*. Similarly, in Expression (6.22), $\boldsymbol{k}_{\beta\beta}$ is referred to as the *β-phase effective thermal conductivity tensor* and $\boldsymbol{k}_{\alpha\beta}$ is referred to as the *β-phase coupled thermal conductivity tensor*.

6.4 Discussion

The effect of the gradient of the α-phase volume averaged temperature on an energy balance in the β-phase and *vice versa* can be explained by considering a control volume in the porous domain of constant porosity, an order of magnitude larger than the pore scale dimension. Conduction in the α-phase crossing the boundaries of the control volume consists of a component caused by the gradient in the volume-averaged temperature of the α-phase, as well as a "short cut" component caused by the volume-averaged temperature gradient of the β-phase. If the volume-averaged temperature gradient of the β-phase were constant throughout the control volume, then the "short cut" component of conduction will introduce and remove the same amounts of heat to and from the control volume. However, with a change in the gradient of the β-phase volume-averaged temperature (*i.e.* the second spatial derivative of the volume-averaged temperature being unequal to zero), then the "short cut" component of conduction will either introduce heat into, or remove heat from the control volume. Therefore, an energy balance description at a macroscopic level in the α-phase represents the effect of a changing gradient in the volume-averaged temperature of the β-phase, on the energy balance. The same argument applies to an energy balance description at a macroscopic level in the β-phase.

The "short cut" component of conduction is associated with regions where two phases are geometrically arranged in series with respect to the direction of heat conduction. In an expression for the overall thermal conductivity of two dissimilar materials geometrically arranged in series, the volume fraction of each material appears in the denominator [see *e.g.* Equation (15.11)]. Therefore, when a phase has a high volume fraction, its coupled thermal conductivity will be a much stronger function of its own thermal conductivity than the thermal conductivity of the other phase. Conversely, when a phase has a low volume fraction, its coupled thermal conductivity will be a stronger function of the thermal conductivity of the other phase than that of its own.

The conduction model is qualified in Appendix III.

6.5 Compatibility with the classic one equation model

Under the conditions of thermal equilibrium:

$$\frac{1}{\varepsilon_\alpha}\langle T\rangle_\alpha = \frac{1}{\varepsilon_\beta}\langle T\rangle_\beta = \langle T\rangle . \tag{6.23}$$

After substituting Condition (6.23) into Expression (6.21) and Expression (6.22), the addition of Expression (6.21) and Expression (6.22) yields:

$$\nabla\cdot\left[\left(\varepsilon_\alpha \boldsymbol{k}_{\alpha\alpha} + \varepsilon_\beta \boldsymbol{k}_{\alpha\beta} + \varepsilon_\beta \boldsymbol{k}_{\beta\beta} + \varepsilon_\alpha \boldsymbol{k}_{\beta\alpha}\right)\cdot\nabla\langle T\rangle\right]. \tag{6.24}$$

Consider the contents of the parenthesis in Expression (6.24). Substituting Definition (6.18) and Definition (6.19) into Expression (6.24) yields after rearrangement and cancellation of terms:

$$\varepsilon_\alpha \boldsymbol{k}_{\alpha,e} + \varepsilon_\beta \boldsymbol{k}_{\beta,e} \ . \tag{6.25}$$

Substituting Definition (II.1) and Definition (6.8) into Expression (6.25) yields:

$$\frac{\frac{V_\alpha}{V_o}k_\alpha\langle\nabla T_e\rangle_\alpha}{\nabla\langle T_e\rangle_\alpha} + \frac{\frac{V_\beta}{V_o}k_\beta\langle\nabla T_e\rangle_\beta}{\nabla\langle T_e\rangle_\beta}. \tag{6.26}$$

For constant thermal conductivity, using Equation (II.6) and the hypothesis of local uniform porosity in an REV, Expression (6.26) can be written as:

$$\frac{\varepsilon_\alpha\langle k_\alpha\nabla T_e\rangle_\alpha}{\nabla\langle T_e\rangle_\alpha^\alpha} + \frac{\varepsilon_\beta\langle k_\beta\nabla T_e\rangle_\beta}{\nabla\langle T_e\rangle_\beta^\beta}. \tag{6.27}$$

When the phases are in thermal equilibrium, as is the case with the equilibrium temperature distribution T_e, then:

$$\langle T_e \rangle_\alpha^\alpha = \langle T_e \rangle_\beta^\beta = \langle T_e \rangle . \tag{6.28}$$

Substituting Condition (6.28) and rearranging terms, Expression (6.27) can be written as:

$$\frac{\langle k \nabla T_e \rangle}{\nabla \langle T_e \rangle} . \tag{6.29}$$

Substituting Definition (II.2) and dropping the subscript e under the condition of thermal equilibrium between the phases yields:

$$\frac{\int_{V_o} k \nabla T \, \mathrm{d}V}{\nabla \int_{V_o} T \, \mathrm{d}V} . \tag{6.30}$$

Expression (6.30) is the classic definition of the overall thermal conductivity $\boldsymbol{k}_o$ of a two-phase system with thermal equilibrium between the two phases (Nozad *et. al.*, 1985), which proves that Expression (6.21) and Expression (6.22) are compatible with the classic one-equation model.

CHAPTER 7

DISPERSION MODEL

7.1 Overview

The *dispersion model*, which transforms the momentum and thermal dispersion terms in the volume-averaged momentum equation [Equation (2.29)] and the volume-averaged energy equation of the fluid phase [Equation (2.48)], to descriptions in terms of the macroscopic temperatures and velocities, is introduced in this chapter. The model is based on empirical formulations derived from experimental observations and incorporates the definition of a dispersion parameter, which relates mass, momentum and thermal dispersion. The difference between longitudinal and transverse dispersion is also addressed.

7.2 Conceptual representation of mass dispersion

In Equation (2.29) and Equation (2.48), mechanical momentum and mechanical thermal dispersion are respectively represented by:

$$\rho_f \nabla \cdot \left\langle \mathring{\boldsymbol{v}} \right\rangle_f \tag{7.1}$$

and:

$$\rho_f c_{p,f} \nabla \cdot \left\langle \mathring{\boldsymbol{v}} \mathring{T} \right\rangle_f . \tag{7.2}$$

Dispersive transport of momentum, heat and mass are all due to the same microscopic convective process. The dispersion of mass is easily observable and has therefore mostly been used for the development of conceptual representations of dispersion.

As far as this study is concerned, the two most important contributions towards the modelling of dispersion are that of Baron (1952) and Taylor (1953), who introduced the concept of a *dispersion coefficient*, and de Josselin de Jong (1958), who found that there is a difference between *longitudinal* and *transverse* dispersion.

Taylor used a bundle of capillary tubes as a simple model for a porous medium. His approach is based on the analogies between porous media and bundles of capillaries and between dispersion and diffusion. Taylor used two miscible liquids and investigated the displacement of one liquid by the other in a straight capillary tube. Both liquids had the same density and viscosity. Due to the parabolic velocity distribution across the tube, a group of marked fluid particles, initially on a plane perpendicular to the tube's axis, will eventually lie on a parabolic surface. This means that particles from both fluids continuously spread along the tube as flow continuous, even in the absence of molecular diffusion.

Taylor argued that dispersive transfer of mass in a porous medium obeys Fick's law for the molecular diffusion of mass, namely:

$$\boldsymbol{j} = -D_M \nabla c_A, \tag{7.3}$$

where $\boldsymbol{j}$ is the mass flux vector (mass transfer rate per unit area) and c_A is the mass fraction of a miscible fluid A. D_M is a proportionality coefficient referred to as the *mass dispersion coefficient*. [Note that when Fick's law applies to only the diffusional transfer of mass, then the proportionality coefficient in Equation (7.3) is generally referred to as the *diffusional mass transfer coefficient.*]

De Josselin de Jong visualised a porous medium model composed of a network of interconnecting straight channels of equal length, orientated at random, but uniformly distributed in all directions. Ignoring molecular diffusion, it was assumed that particles

would move through the porous medium with a uniform velocity within each channel. This uniform velocity was assumed to vary with the direction of the channels. Each particle would therefore undergo a different number of displacements in a given time interval. The probability of a particle arriving at a given point and time, after a large number of displacements, was determined. The result was a normal distribution in three dimensions. For one-dimensional flow, dispersive mass flux in the longitudinal direction is given by:

$$j_l = -D_{M,l} \frac{\partial c_A}{\partial m_l} \tag{7.4}$$

and in the transverse direction by:

$$j_t = -D_{M,t} \frac{\partial c_A}{\partial m_t}. \tag{7.5}$$

$D_{M,l}$ and $D_{M,t}$ are referred to as the *longitudinal* and the *transverse mass dispersion coefficients* and m_l and m_t are linear dimensions directed in the longitudinal and transverse directions respectively.

This "diffusion-like" behaviour of dispersion was later supported by concurrent theories developed by using the method of volume averaging (Carbonell and Whitaker, 1983), the method of homogenisation (Rubinstein and Mauri, 1986; Mei, 1992) and the method of configurational averaging over a set of media (Koch *et al.*, 1985).

7.3 Dispersivity

In order for the modelling equations presented here to apply to heat, mass and momentum transfer, it is more convenient to refer to a *dispersivity D* in analogy with molecular diffusivity (Brodkey and Hershey, 1988). Using this analogy, the dispersivity is defined

in this study as:

$$D \equiv \frac{D_M}{\rho_f} = \frac{D_P}{\rho_f} = \frac{D_T}{\rho_f c_{pf}}, \tag{7.6}$$

where D_P and D_T are proportionality coefficients referred to as the *momentum and the thermal dispersion coefficienst* respectively. Definition (7.6) is not valid when the dispersion coefficients D_M, D_P and D_T include transport by molecular diffusion (in which case the coefficients should be referred to as *hydrodynamic* dispersion coefficients).

Using Definition (7.6), Equation (7.4) and Equation (7.5) are written as:

$$j_l = -\rho_f D_l \frac{\partial c_A}{\partial m_l} \tag{7.7}$$

and:

$$j_t = -\rho_f D_t \frac{\partial c_A}{\partial m_t}. \tag{7.8}$$

D_l and D_t are the *longitudinal* and the *transverse dispersivities* respectively.

The corresponding dispersive momentum transfer is represented by:

$$P_{t,l} = -\rho_f D_l \frac{\partial v}{\partial m_l} \tag{7.9}$$

and:

$$P_{t,t} = -\rho_f D_t \frac{\partial v}{\partial m_t}, \tag{7.10}$$

and the corresponding dispersive heat flux is represented by:

$$q_l = -\rho_f c_{pf} D_l \frac{\partial T}{\partial m_l} \tag{7.11}$$

and:

$$q_t = -\rho_f c_{p,f} D_t \frac{\partial T}{\partial m_t}. \tag{7.12}$$

From Definition (7.6), Equation (7.9) and Equation (7.10) can be written as:

$$P_{t,l} = -D_{P,l} \frac{\partial v}{\partial m_l} \tag{7.13}$$

and:

$$P_{t,t} = -D_{P,t} \frac{\partial v}{\partial m_t}, \tag{7.14}$$

where $D_{P,l}$ and $D_{P,t}$ are the *longitudinal* and the *transverse momentum dispersion coefficients*, and Equation (7.11) and Equation (7.12) can be written as:

$$q_l = -D_{T,l} \frac{\partial T}{\partial m_l} \tag{7.15}$$

and:

$$q_t = -D_{T,t} \frac{\partial T}{\partial m_t}, \tag{7.16}$$

where $D_{T,l}$ and $D_{T,t}$ are the *longitudinal* and the *transverse thermal dispersion coefficients*.

Expression (7.1) can now be represented as:

$$\rho_f \nabla \cdot \left\langle \overset{\circ}{\boldsymbol{v}} \overset{\circ}{\boldsymbol{v}} \right\rangle_f = -\nabla \cdot \left(\boldsymbol{D}_P \cdot \nabla \langle \boldsymbol{v} \rangle_f \right), \tag{7.17}$$

where $\boldsymbol{D}_P$ is the *momentum dispersion tensor*, and Expression (7.2) as:

$$\rho_f c_{p,f} \boldsymbol{\nabla} \cdot \left\langle \mathring{\boldsymbol{v}} \mathring{T} \right\rangle_f = -\boldsymbol{\nabla} \cdot \left(\boldsymbol{D}_T \cdot \boldsymbol{\nabla} \langle T \rangle_f \right), \tag{7.18}$$

where $\boldsymbol{D}_T$ is the *thermal dispersion tensor*.

The components of the momentum dispersion tensor $\boldsymbol{D}_P$ and the thermal dispersion tensor $\boldsymbol{D}_T$ are given in terms of their transverse and longitudinal components respectively as (Bear and Bachmat, 1991, p. 403):

$$\boldsymbol{D}_P = D_{P,t} \boldsymbol{u} + \left(D_{P,l} - D_{P,t} \right) \frac{\langle \boldsymbol{v} \rangle_f \langle \boldsymbol{v} \rangle_f}{\langle v \rangle_f^{\,2}} \tag{7.19}$$

and:

$$\boldsymbol{D}_T = D_{T,t} \boldsymbol{u} + \left(D_{T,l} - D_{T,t} \right) \frac{\langle \boldsymbol{v} \rangle_f \langle \boldsymbol{v} \rangle_f}{\langle v \rangle_f^{\,2}}, \tag{7.20}$$

where $\boldsymbol{u}$ is a unit diagonal tensor and $\langle v \rangle_f$ is the magnitude of the phasial volume-averaged velocity vector $\langle \boldsymbol{v} \rangle_f$.

CHAPTER 8

TRANSFORMED VOLUME-AVERAGED MOMENTUM AND ENERGY EQUATIONS

8.1 Overview

In the first part of this chapter, models developed in Chapter 3 to Chapter 7 to transform integrals of microscopic processes presented in terms of microscopic intensive quantities are substituted in the volume-averaged momentum equation for the fluid phase [Equation (2.29)] and the volume-averaged energy equations for the solid and the fluid phases [Equation (2.47) and Equation (2.48) respectively]. This substitution yields a set of governing equations at macroscopic level, referred to as *transformed volume-averaged equations*, which are presented in terms of volume-averaged velocities and temperatures only. Analytical expressions for phasial volume-averaged heat and momentum transfer across a reference plane in the porous domain are derived in the last part of the chapter.

8.2 Transformed volume-averaged momentum equation

The volume-averaged momentum equation for a rigid solid with constant thermophysical properties states that:

$$\rho_f \frac{\partial \langle \boldsymbol{v} \rangle_f}{\partial t} + \rho_f \nabla \cdot \left(\frac{1}{\varepsilon_f} \langle \boldsymbol{v} \rangle_f \langle \boldsymbol{v} \rangle_f \right) + \rho_f \nabla \cdot \left\langle \mathring{\boldsymbol{v}} \mathring{\boldsymbol{v}} \right\rangle_f = \varepsilon_f \rho_f \langle \boldsymbol{B} \rangle_f - \varepsilon_f \nabla \langle p \rangle_f^f - \frac{1}{V_o} \int_{A_{sf}} \mathring{p} \boldsymbol{n}_{fs} \, \mathrm{d}A + \nabla \cdot \left(\mu \nabla \langle \boldsymbol{v} \rangle_f \right) + \frac{1}{V_o} \int_{A_{sf}} \mu \left(\nabla \boldsymbol{v} \right) \cdot \boldsymbol{n}_{fs} \, \mathrm{d}A, \quad (2.29)$$

where ρ_f is the fluid density, μ is the kinematic viscosity of the fluid phase, $\langle \boldsymbol{v} \rangle_f$ is the phasial volume-averaged velocity vector for the fluid phase, ε_f is the fluid phase volume fraction [defined by Definition (II.1)] and $\boldsymbol{n}_{fs}$ is a local unit vector normal to the interface between the two phases. $\langle \boldsymbol{B} \rangle_f$ is a phasial volume-averaged body force and $\langle p \rangle_f^f$ is the intrinsic volume averaged pressure in the fluid. $\overset{\circ}{\boldsymbol{v}}$ and $\overset{\circ}{p}$ are velocity and pressure deviations as defined by Definition (II.5).

Substituting the viscous shear model:

$$\mu \boldsymbol{f} \cdot \langle \boldsymbol{v} \rangle_f \equiv \left(-\frac{1}{V_o} \int_{A_{sf}} \mu (\nabla \boldsymbol{v}) \cdot \boldsymbol{n}_{fs} \, \mathrm{d}A + \frac{1}{V_o} \int_{A_{sf}} \overset{\circ}{p} \boldsymbol{n}_{fs} \, \mathrm{d}A \right) \tag{3.8}$$

and the dispersion model for momentum transport:

$$\rho_f \nabla \cdot \left\langle \overset{\circ}{\boldsymbol{v}} \overset{\circ}{\boldsymbol{v}} \right\rangle_f = -\nabla \cdot \left(\boldsymbol{D}_P \cdot \nabla \langle \boldsymbol{v} \rangle_f \right), \tag{7.17}$$

into Equation (2.29) yields:

$$\rho_f \frac{\partial \langle \boldsymbol{v} \rangle_f}{\partial t} + \rho_f \nabla \cdot \left(\frac{1}{\varepsilon_f} \langle \boldsymbol{v} \rangle_f \langle \boldsymbol{v} \rangle_f \right) - \nabla \cdot \left(\mu \nabla \langle \boldsymbol{v} \rangle_f \right) + \varepsilon_f \nabla \langle p \rangle_f^f -$$

$$\varepsilon_f \rho_f \langle \boldsymbol{B} \rangle_f - \nabla \cdot \left(\boldsymbol{D}_P \cdot \nabla \langle \boldsymbol{v} \rangle_f \right) + \mu \boldsymbol{f} \cdot \langle \boldsymbol{v} \rangle_f = 0, \tag{8.1}$$

or:

$$\rho_f \frac{\partial \langle \boldsymbol{v} \rangle_f}{\partial t} + \rho_f \nabla \cdot \left(\frac{1}{\varepsilon_f} \langle \boldsymbol{v} \rangle_f \langle \boldsymbol{v} \rangle_f \right) - \nabla \cdot \left[(\mu \boldsymbol{u} + \boldsymbol{D}_P) \cdot \nabla \langle \boldsymbol{v} \rangle_f \right] +$$

$$\varepsilon_f \nabla \langle p \rangle_f^f - \varepsilon_f \rho_f \langle \boldsymbol{B} \rangle_f + \mu \boldsymbol{f} \cdot \langle \boldsymbol{v} \rangle_f = 0. \tag{8.2}$$

where $\boldsymbol{u}$ is a unit diagonal tensor.

8.3 Transformed volume-averaged energy equations

The volume-averaged energy equation for a rigid solid with constant thermophysical properties states that:

$$\rho_s c_{p,s} \frac{\partial \langle T \rangle_s}{\partial t} = \nabla \cdot \left(k_s \varepsilon_s \nabla \langle T \rangle_s^s \right) + \nabla \cdot \left(\frac{1}{V_o} \int_{A_{sf}} k_s \overset{\circ}{T}_s \boldsymbol{n}_{sf} \, \mathrm{d}A \right) + \frac{1}{V_o} \int_{A_{sf}} k_s \nabla T_s \cdot \boldsymbol{n}_{sf} \, \mathrm{d}A + \langle I_s \rangle_s \tag{2.47}$$

and the volume-averaged energy equation for a fluid with constant thermophysical properties flowing at moderate temperatures states that:

$$\rho_f c_{p,f} \frac{\partial \langle T \rangle_f}{\partial t} = \nabla \cdot \left(k_f \varepsilon_f \nabla \langle T \rangle_f^f \right) + \nabla \cdot \left(\frac{1}{V_o} \int_{A_{sf}} k_f \overset{\circ}{T}_f \boldsymbol{n}_{fs} \, \mathrm{d}A \right) +$$

$$\frac{1}{V_o} \int_{A_{sf}} k_f \nabla T_f \cdot \boldsymbol{n}_{fs} \, \mathrm{d}A - \rho_f c_{p,f} \nabla \cdot \left(\frac{1}{\varepsilon_f} \langle \boldsymbol{v} \rangle_f \langle T \rangle_f \right) - \rho_f c_{p,f} \nabla \cdot \left\langle \overset{\circ}{\boldsymbol{v}} \overset{\circ}{T} \right\rangle_f + \langle I_f \rangle_f, \tag{2.48}$$

where, in Equation (2.47) and Equation (2.48), t represents time, ρ_s and ρ_f, k_s and k_f, $c_{p,s}$ and $c_{p,f}$, are constant densities, constant thermal conductivities, and constant isobaric specific heat capacities for the solid and the fluid phases respectively, $\langle T \rangle_s$ and $\langle T \rangle_f$, and $\langle I_s \rangle_s$ and $\langle I_f \rangle_f$, are phasial volume-averaged temperatures and phasial volume-averaged internal heat sources for the solid and the fluid phases respectively, $\langle \boldsymbol{v} \rangle_f$ is the phasial volume-averaged velocity vector for the fluid phase, ε_s and ε_f are volume fractions for the solid and the fluid phases respectively, as defined by Definition (II.1), $\boldsymbol{n}_{sf}$ and $\boldsymbol{n}_{fs}$ are local unit vectors normal to the interface between the two phases, and $\overset{\circ}{\boldsymbol{v}}$ and $\overset{\circ}{T}$ are velocity and temperature deviations as defined by Definition (II.5).

Substituting the conduction model:

$$\nabla\cdot\left(k_\gamma\varepsilon_\gamma\nabla\langle T\rangle_\gamma^\gamma\right)+\nabla\cdot\left(\frac{1}{V_o}\int_{A_{sf}}k_\gamma\,\overset{\circ}{T}_\gamma\,\boldsymbol{n}_{\gamma\varphi}\mathrm{d}A\right)=\nabla\cdot\left(\boldsymbol{k}_{\gamma\gamma}\cdot\nabla\langle T\rangle_\gamma\right)+\nabla\cdot\left(\boldsymbol{k}_{\gamma\varphi}\cdot\nabla\langle T\rangle_\varphi\right), \tag{6.20}$$

the interphasial heat transfer model:

$$\frac{1}{A_{sf}}\int_{A_{sf}}k_\gamma\nabla T_\gamma\cdot\boldsymbol{n}_{\gamma\varphi}\,\mathrm{d}A=-\frac{h_{sf}}{\varepsilon_\gamma}\left(\langle T\rangle_\gamma-\frac{\varepsilon_\gamma}{1-\varepsilon_\gamma}\langle T\rangle_\varphi\right), \tag{5.4}$$

and the dispersion model:

$$\rho_f c_{p,f}\nabla\cdot\left\langle\overset{\circ}{\boldsymbol{v}}\overset{\circ}{T}\right\rangle_f=-\nabla\cdot\left(\boldsymbol{D}_T\cdot\nabla\langle T\rangle_f\right) \tag{7.18}$$

in the first and second terms respectively, on the RHS of Equation (2.47) and Equation (2.48), the third terms on the RHS of Equation (2.47) and Equation (2.48), and the last term on the RHS of Equation (2.48), yields a transformed volume-averaged energy equation for the solid phase:

$$\rho_s c_{p,s}\frac{\partial\langle T\rangle_s}{\partial t}=\nabla\cdot\left(\boldsymbol{k}_{ss}\cdot\nabla\langle T\rangle_s\right)+\nabla\cdot\left(\boldsymbol{k}_{sf}\cdot\nabla\langle T\rangle_f\right)-\frac{h_{sf}}{\varepsilon_s}\frac{A_{sf}}{V_o}\left(\langle T\rangle_s-\frac{\varepsilon_s}{1-\varepsilon_s}\langle T\rangle_f\right)+\langle I_s\rangle_s, \tag{8.3}$$

and for the fluid phase:

$$\rho_f c_{p,f}\frac{\partial\langle T\rangle_f}{\partial t}=\nabla\cdot\left(\boldsymbol{k}_{ff}\cdot\nabla\langle T\rangle_f\right)+\nabla\cdot\left(\boldsymbol{k}_{fs}\cdot\nabla\langle T\rangle_s\right)-\frac{h_{sf}}{\varepsilon_f}\frac{A_{sf}}{V_o}\left(\langle T\rangle_f-\frac{\varepsilon_f}{1-\varepsilon_f}\langle T\rangle_s\right)-$$

$$\rho_f c_{p,f}\nabla\cdot\left(\frac{1}{\varepsilon_f}\langle\boldsymbol{v}\rangle_f\langle T\rangle_f\right)+\nabla\cdot\left(\boldsymbol{D}_T\cdot\nabla\langle T\rangle_f\right)+\langle I_f\rangle_f, \tag{8.4}$$

or:

$$\rho_f c_{p,f} \frac{\partial \langle T \rangle_f}{\partial t} = \nabla \cdot \left[\left(\boldsymbol{k}_{ff} + \boldsymbol{D}_T \right) \cdot \nabla \langle T \rangle_f \right] + \nabla \cdot \left(\boldsymbol{k}_{fs} \cdot \nabla \langle T \rangle_s \right) -$$

$$\frac{h_{sf}}{\varepsilon_f} \frac{A_{sf}}{V_o} \left(\langle T \rangle_f - \frac{\varepsilon_f}{1-\varepsilon_f} \langle T \rangle_s \right) - \rho_f c_{p,f} \nabla \cdot \left(\frac{1}{\varepsilon_f} \langle \boldsymbol{v} \rangle_f \langle T \rangle_f \right) + \langle I_f \rangle_f . \quad (8.5)$$

8.4 Discussion

Equation (8.2) describes a momentum balance in the fluid phase and Equation (8.3) and Equation (8.4) describe an energy balance in the solid and the fluid phases respectively, all in terms of macroscopic quantities. The three equations apply to any consolidated porous medium.

The transformation process that yielded the complete description of a momentum and energy balance in terms of macroscopic quantities only, also introduces a number of proportionality coefficients, referred to as *transport parameters*.

The behaviour of momentum and energy transport in a specific porous medium is characterised by the values of the transport parameters.

8.5 Phasial volume-averaged momentum transfer in the fluid phase

The microscopic momentum transfer in the fluid phase normal to an incremental reference plane δA_{ff} consists of a diffusive (viscous) and a convective component and is given by the momentum transfer vector $\delta \boldsymbol{P}_t$ as:

$$\delta \boldsymbol{P}_t \equiv \left(-\mu \nabla \boldsymbol{v} + \rho_f \boldsymbol{v} \boldsymbol{v} \right) \cdot \boldsymbol{n}_{ff} \ , \quad (8.6)$$

where $\boldsymbol{n}_{ff}$ is a unit normal surface vector to the incremental surface δA_{ff}. The mean momentum transfer normal to a reference plane A_{ff} is given by:

$$\frac{1}{A_{ff}} \int_{A_{ff}} \left(-\mu \nabla \boldsymbol{v} + \rho_f \boldsymbol{v}\boldsymbol{v} \right) \cdot \boldsymbol{n}_{ff} \, \mathrm{d}A \,. \tag{8.7}$$

With reference to the overall surface A_o, defined as:

$$A_o \equiv A_{ss} + A_{ff} \,, \tag{8.8}$$

the mean normal momentum transfer in the fluid phase is:

$$\frac{1}{A_o} \int_{A_{ff}} \left(-\mu \nabla \boldsymbol{v} + \rho_f \boldsymbol{v}\boldsymbol{v} \right) \cdot \boldsymbol{n}_{ff} \, \mathrm{d}A \,. \tag{8.9}$$

From Bear and Bachmat (1991, p.37) it follows that the surface average in Expression (8.9) can be substituted by a volume average to give the mean normal momentum transfer in the fluid phase as:

$$\frac{1}{V_o} \int_{V_f} \left(-\mu \nabla \boldsymbol{v} + \rho_f \boldsymbol{v}\boldsymbol{v} \right) \cdot \boldsymbol{n}_{ff} \, \mathrm{d}V \,. \tag{8.10}$$

Substituting Definition (8.6) into Expression (8.10) and using Definition (II.3) yields an expression for the phasial volume-averaged momentum transfer in the fluid phase normal to a reference plane A_o, which is given as:

$$\langle \boldsymbol{P}_t \rangle_f = \frac{1}{V_o} \int_{V_f} \left(-\mu \nabla \boldsymbol{v} + \rho_f \boldsymbol{v}\boldsymbol{v} \right) \cdot \boldsymbol{n}_{ff} \, \mathrm{d}V \,. \tag{8.11}$$

Consider the first term in the parenthesis on the RHS of Equation (8.11). With the fluid phase consolidated in all directions, using Equation (II.10) and taking into account that the viscosity μ is constant, the phasial volume-averaged form of this term can be written as:

$$\langle -\mu\nabla\boldsymbol{v}\rangle_f = -\mu\left(\nabla\langle\boldsymbol{v}\rangle_f + \frac{1}{V_o}\int_{A_{sf}} \boldsymbol{v}\cdot\boldsymbol{n}_{ff}\,\mathrm{d}A\right). \tag{8.12}$$

Noting that $v = 0$ at the interface A_{sf}, it follows that:

$$\langle -\mu\nabla\boldsymbol{v}\rangle_f = -\mu\nabla\langle\boldsymbol{v}\rangle_f. \tag{8.13}$$

Consider the second term in the parenthesis on the RHS of Equation (8.11). By using Equation (II.6) and taking into account that the fluid density ρ_f is constant, the phasial volume-averaged form of this term can be written as:

$$\langle \rho_f \boldsymbol{v}\boldsymbol{v}\rangle_f = \frac{\rho_f}{\varepsilon_f}\frac{1}{V_f}\int_{V_f} \boldsymbol{v}\boldsymbol{v}\,\mathrm{d}V. \tag{8.14}$$

Following the analytical process used between Equation (2.4) and Equation (2.11), Equation (8.14) can be written as:

$$\langle \rho_f \boldsymbol{v}\boldsymbol{v}\rangle_f = \frac{\rho_f}{\varepsilon_f}\langle\boldsymbol{v}\rangle_f\langle\boldsymbol{v}\rangle_f + \rho_f\left\langle \mathring{\boldsymbol{v}}\mathring{\boldsymbol{v}}\right\rangle_f^f. \tag{8.15}$$

Substituting Equation (8.13) and Equation (8.15) into Equation (8.11) yields:

$$\langle \boldsymbol{P}_t\rangle_f = \left(-\mu\nabla\langle\boldsymbol{v}\rangle_f + \frac{\rho_f}{\varepsilon_f}\langle\boldsymbol{v}\rangle_f\langle\boldsymbol{v}\rangle_f + \rho_f\left\langle \mathring{\boldsymbol{v}}\mathring{\boldsymbol{v}}\right\rangle_f^f\right)\cdot\boldsymbol{n}_{ff}. \tag{8.16}$$

By substituting the dispersion model, described for momentum transfer by Equation (7.17), and rearranging terms, Equation (8.16) can be written as:

$$\langle \boldsymbol{P}_t \rangle_f = \left[-(\mu \boldsymbol{u} + \boldsymbol{D}_P) \cdot \nabla \langle \boldsymbol{v} \rangle_f + \frac{\rho_f}{\varepsilon_f} \langle \boldsymbol{v} \rangle_f \langle \boldsymbol{v} \rangle_f \right] \cdot \boldsymbol{n}_{ff} \ , \tag{8.17}$$

where $\boldsymbol{u}$ is a unit diagonal tensor.

If the reference surface A_o corresponds to a closed system boundary (see Section 14.2), then the phasial volume-averaged velocity normal to the closed system boundary is zero, reducing Equation (8.17) to:

$$\langle \boldsymbol{P}_t \rangle_f = \left[-(\mu \boldsymbol{u} + \boldsymbol{D}_P) \cdot \nabla \langle \boldsymbol{v} \rangle_f \right] \cdot \boldsymbol{n}_{ff} \tag{8.18}$$

or:

$$\langle P_t \rangle_{f,m} = -(\mu + D_{P,m}) \frac{\partial}{\partial m} \langle v \rangle_f \ , \tag{8.19}$$

where m in Equation (8.19) is a direction index normal to the closed system boundary and $D_{P,m}$ is the component of the tensor quantity $\boldsymbol{D}_P$ in the direction m. In the absence of the macroscopic convection, the RHS of Equation (8.19) can be regarded as a macroscopic viscous shear stress, which includes the effects of diffusive (viscous) and dispersive momentum transfer.

Transverse dispersion and its effect on the transport of momentum reduce to zero in a confined narrow region near the solid wall. However, when viewed at a macroscopic level, the thickness of the region is an order of magnitude smaller than the minimum REV diameter (see Section II.2), shown in Figure 14.1. It is therefore assumed that Equation (8.19) applies up to the closed system boundary.

If the reference plane A_o corresponds to an open system boundary, it is assumed that the dispersive transport of momentum does not extend beyond the open system boundary.

Dispersion at the open system boundary is limited to the porous domain by assuming that only diffusive (viscous) momentum transfer occurs at the system boundary. Therefore, at the open system boundary, the phasial volume-averaged momentum transfer in the fluid phase normal to the system boundary is given as:

$$\langle \boldsymbol{P}_t \rangle_f = \left(-\mu \nabla \langle \boldsymbol{v} \rangle_f + \frac{\rho_f}{\varepsilon_f} \langle \boldsymbol{v} \rangle_f \langle \boldsymbol{v} \rangle_f \right) \cdot \boldsymbol{n}_{ff} \ . \tag{8.20}$$

(This assumption is particularly true for the longitudinal component of momentum dispersion, which is considered zero in this study anyhow.)

8.6 Phasial volume-averaged heat transfer in the solid phase

The microscopic heat transfer component normal to an incremental reference plane δA_{ss} is defined by the scalar quantity δq_s as:

$$\delta q_s \equiv \left(-k \nabla T \right)_s \cdot \boldsymbol{n}_{ss} \, . \tag{8.21}$$

The mean heat transfer in the solid phase normal to a reference plane A_{ss} is given as:

$$\frac{1}{A_{ss}} \int_{A_{ss}} \left(-k \nabla T \right)_s \cdot \boldsymbol{n}_{ss} \, \mathrm{d}A \, . \tag{8.22}$$

With reference to the overall surface area A_o, defined by Definition (8.8), the mean heat transfer in the solid phase normal to the overall surface area A_o is given as:

$$\frac{1}{A_o} \int_{A_{ss}} \left(-k \nabla T \right)_s \cdot \boldsymbol{n}_{ss} \, \mathrm{d}A \, . \tag{8.23}$$

From Bear and Bachmat (1991, p.37) it follows that the surface average in Expression (8.23) can be substituted by a volume average to yield:

$$\frac{1}{V_o}\int_{V_S}\left(-k\nabla T\right)_s \cdot \boldsymbol{n}_{ss}\,\mathrm{d}V\,. \tag{8.24}$$

Substituting Definition (8.21) into Expression (8.24), and using Definition (II.3) yields an expression for the phasial volume-averaged heat transfer in the solid phase normal to a reference plane A_o, which is given as:

$$\langle q\rangle_s = \frac{1}{V_o}\int_{V_S}\left(-k\nabla T\right)_s \cdot \boldsymbol{n}_{ss}\,\mathrm{d}V\,. \tag{8.25}$$

Repeating the analytical process demonstrated between Equation (2.40) and Equation (2.45), the RHS of Equation (8.25) can be written as:

$$\langle q\rangle_s = \left[-k_s\varepsilon_s\nabla\langle T\rangle_s^s - \left(\frac{1}{V_o}\int_{A_{sf}} k_s\,\overset{\circ}{T}\boldsymbol{n}_{sf}\,\mathrm{d}A\right)\right]\cdot\boldsymbol{n}_{ss}\,. \tag{8.26}$$

Substituting the conduction model described by Equation (6.20), it follows that:

$$\langle q\rangle_s = \left[-\left(\boldsymbol{k}_{ss}\cdot\nabla\langle T\rangle_s\right)-\left(\boldsymbol{k}_{sf}\cdot\nabla\langle T\rangle_f\right)\right]\cdot\boldsymbol{n}_{ss} \tag{8.27}$$

or:

$$\langle q\rangle_s = -k_{ss,m}\frac{\partial}{\partial m}\langle T\rangle_s - k_{sf,m}\frac{\partial}{\partial m}\langle T\rangle_f\,, \tag{8.28}$$

where m is a direction index normal to the reference plane A_o, and $k_{ss,m}$ and $k_{sf,m}$ are the components of the tensor quantities $\boldsymbol{k}_{ss}$ and $\boldsymbol{k}_{sf}$ respectively in the direction m.

8.7 Phasial volume-averaged heat transfer in the fluid phase

The microscopic heat transfer component normal to an incremental reference plane δA_{ff} is defined by the scalar quantity δq_f as:

$$\delta q_f \equiv \left[\left(-k\nabla T\right)_f + \rho_f c_{p,f} \boldsymbol{v} T_f\right] \cdot \boldsymbol{n}_{ff} . \tag{8.29}$$

The mean heat transfer in the fluid phase normal to a reference plane A_{ff} is given as:

$$\frac{1}{A_{ff}} \int_{A_{ff}} \left[\left(-k\nabla T\right)_f + \rho_f c_{p,f} \boldsymbol{v} T_f\right] \cdot \boldsymbol{n}_{ff} \, \mathrm{d}A . \tag{8.30}$$

Applying the same arguments as those used between Equation (8.21) and Equation (8.26), Expression (8.30) can be written in a phasial volume-averaged form as:

$$\langle q \rangle_f = \left(-k_f \varepsilon_f \nabla \langle T \rangle_f^f - \frac{1}{V_o} \int_{A_{sf}} k_f \overset{\circ}{T} \boldsymbol{n}_{fs} \, \mathrm{d}A + \rho_f c_{p,f} \frac{1}{\varepsilon_f} \langle \boldsymbol{v} \rangle_f \langle T \rangle_f + \rho_f c_{p,f} \left\langle \overset{\circ}{\boldsymbol{v}} \overset{\circ}{T} \right\rangle_f^f \right) \cdot \boldsymbol{n}_{ff} . \tag{8.31}$$

Substituting the conduction model described by Equation (6.20) and the dispersion model described by Equation (7.18), Equation (8.31) can be written as:

$$\langle q \rangle_f = \left[-\left(\boldsymbol{k}_{ff} + \boldsymbol{D}_T\right) \cdot \nabla \langle T \rangle_f - \boldsymbol{k}_{fs} \cdot \nabla \langle T \rangle_s + \rho_f c_{p,f} \frac{1}{\varepsilon_f} \langle \boldsymbol{v} \rangle_f \langle T \rangle_f \right] \cdot \boldsymbol{n}_{ff} . \tag{8.32}$$

The quantity $\boldsymbol{k}_{ff} + \boldsymbol{D}_T$ can be regarded as a total heat transfer coefficient [see Definition (15.50)].

If the reference surface A_o corresponds to a closed system boundary (see Section 14.2), then the phasial volume-averaged velocity normal to the closed system boundary is zero, reducing Equation (8.32) to:

$$\langle q \rangle_f = \left[-\left(\boldsymbol{k}_{ff} + \boldsymbol{D}_T \right) \cdot \nabla \langle T \rangle_f - \boldsymbol{k}_{fs} \cdot \nabla \langle T \rangle_s \right] \cdot \boldsymbol{n}_{ff} \tag{8.33}$$

or:

$$\langle q \rangle_f = -\left(k_{ff,m} + D_{T,m} \right) \frac{\partial}{\partial m} \langle T \rangle_f - k_{fs,m} \frac{\partial}{\partial m} \langle T \rangle_s , \tag{8.34}$$

where m is a direction index normal to the reference plane A_o, and $k_{ff,m}$, $k_{\gamma\tau,m}$ and $D_{T,m}$ are the components of the tensor quantities $\boldsymbol{k}_{\gamma\gamma}$, $\boldsymbol{k}_{\gamma\tau}$ and $\boldsymbol{D}_T$ respectively in the direction m.

As mentioned previously for the case of momentum transfer, when heat transfer at the solid wall is considered, it is assumed that Equation (8.34) applies up to the closed system boundary. This assumption is made regardless of the fact that the effect of dispersion reduces to zero in a confined narrow region near the solid wall.

Also, at an open system boundary the effect of thermal dispersion is limited to the porous domain, by assuming that at the open system boundary only conductive heat transfer occurs. Secondary heat transfer caused by a gradient in the phasial volume-averaged temperature of the solid phase also does not extend beyond an open system boundary. Therefore, at an open system boundary the phasial volume-averaged heat transfer given by Equation (8.34) reduces to:

$$\langle q \rangle_f = -k_{ff,m} \frac{\partial}{\partial m} \langle T \rangle_f . \tag{8.35}$$

PART II

The transformed volume-averaged momentum equation and the transformed volume-averaged energy equations for the solid and the fluid phases, derived in Part I, are universal in their application to consolidated porous media. The behaviour of momentum and energy transport in a specific porous medium is characterised by the values of the transport parameters. Finding relations for the transport parameters for a highly porous, cellular foam medium constitutes the subject of Part II.

A geometric model of the REV (representative elementary volume, discussed in Section II.2) in the cellular foam structure is developed in Chapter 9. This is required for the theoretical development of relationships to quantify the viscous shear factor in Chapter 10, the effective and coupled thermal conductivities in Chapter 11, the interphasial heat transfer coefficient in Chapter 12 and the momentum and thermal dispersion coefficients in Chapter 13. In Chapter 14, relationships are developed for modelling momentum transfer in the fluid phase at a system boundary as well as heat transfer in the solid and the fluid phases at a system boundary.

CHAPTER 9

GEOMETRIC MODEL

9.1 Overview

The theoretical development of relationships to quantify the transport parameters of metallic foams requires a geometric model of the REV (Representative Elementary Volume, discussed in Appendix II) in the cellular foam structure. A geometric model is introduced in this chapter, which consists of a representative geometric model (see Section 1.12) based on the RUC (representative unit cell) approach that is used to characterise transport behaviour in the cellular foam, as well as a morphologic geometric model (see Section 1.12) that is used to completely characterise the RUC in terms of measurable morphological quantities.

A thorough discussion of the characteristics of an RUC is presented, followed by a rigorous mathematical characterisation of the RUC for cellular foams introduced by Du Plessis (1991a) and the morphological representation introduced by Gibson and Ashby (1988). A number of geometric parameters at a system boundary are also introduced in this chapter.

9.2 General characteristics of the RUC

From its first introduction, Du Plessis and co-workers have formulated several characteristics of the RUC (Du Plessis, 1989, 1991a, 1991b; Du Plessis and Van der Westhuizen, 1993; Du Plessis *et al.*, 1994; Du Plessis and Diedericks, 1997). Important characteristics pertaining to the application of the RUC as a representative geometric model for heat transfer analysis are repeated here.

Whereas an REV is large enough to give reasonable statistical representative averages, an RUC is the minimum size into which the statistical average geometry, as found in its corresponding REV, can be incorporated. The RUC provides a facility to consider flow and heat transfer conditions within the most elementary control volume of a particular porous medium. The RUC is positioned with its volumetric centroid collocated with that of the corresponding REV. Whenever the analysis is limited to isotropic porous media, as is true in this study, the RUC may be simplified into a cubic representative unit cell yielding identical properties in each of its three geometric principal directions.

The volume V_s of solid material present in the RUC of overall volume V_o is chosen to reflect the correct porosity, as defined by Definition (II.1). This solid material is then arranged in rectangular fashion within the RUC to conform to the basic geometric features of the original porous matrix it is meant to represent. Due to the adopted rectangular arrangement within the RUC, the solid-fluid interface A_{sf} will provide pair-wise sets of equal parallel surfaces, possibly with some lateral displacement. Any particular arrangement of the solid is required to provide mutually perpendicular duct sections for fluid discharge and the direction of such sections are, for the sake of convenience, called the principal directions of the RUC.

An evaluation of surface and volume integrals is subject to a description of real velocity and temperature gradients within the solid and the fluid phases. This, in turn, warrants an accurate description of the porous microstructure and its influence on momentum and energy transfer. To facilitate such an analysis, a further requirement is imposed, namely that the RUC is oriented in such a manner that one of its principal axes is collinear with the average transport velocity as obtained from the REV, *i.e.* one channel section is orientated in the streamwise direction. Since unwanted directional priorities may be induced by the particular channels created in a single RUC, it may be necessary to consider the average of several RUC's, each of which is exhibiting a different permutation of directional changes.

This presentation steers away from a simple pore or particle approach towards periodic porous media modelling and should rather be interpreted as a certain arrangement of solid material to fulfil the basic requirements of the actual porous structure it resembles. It also

should be noted that an RUC is not the same as a repetitive building block of the material as it appears in network theory, since it is impossible to construct an isotropic structure with identical building blocks. An RUC is also not a unit cell that contains only a small portion of the material as introduced by Quintard and Whitaker (1994a) as the same problem will arise.

When dealing with isotropic (random) media, the internal channel sections are arranged in such a manner that the fluid forced through an RUC is displaced laterally, to the maximum within the cell, before it exits. This implies that internally the relative positioning of material is subjected to both maximum staggering and maximum interconnection of duct sections and ensures that no passive regions or dead ends are present.

9.3 RUC for cellular foams

Figure 9.1 shows an RUC for a consolidated, cellular foams, as proposed by Du Plessis (1991a). It consists of three mutually perpendicular solid square prisms representing the strands of the cellular foams. The square shape of the prisms allows applicability to the total porosity range. The arrangement automatically creates three mutually orthogonal duct sections of square cross-section.

In order to conform to geometric isotropy, the arrangement of the solid phase within the RUC exhibits geometric similarity in the three principal directions of the cubic RUC, together with maximum possible staggering of the pore sections and maximum pore interconnectivity.

The size and shape of the RUC is identified by the *characteristic dimension d*, and the *characteristic prism width* d_s. The ratio $\frac{d_s}{d}$ characterises the porosity ε_f. Due to the isotropy requirement, all the parallel surface pairs will be an equal distance d_p apart, where d_p is referred to as the *characteristic pore width*.

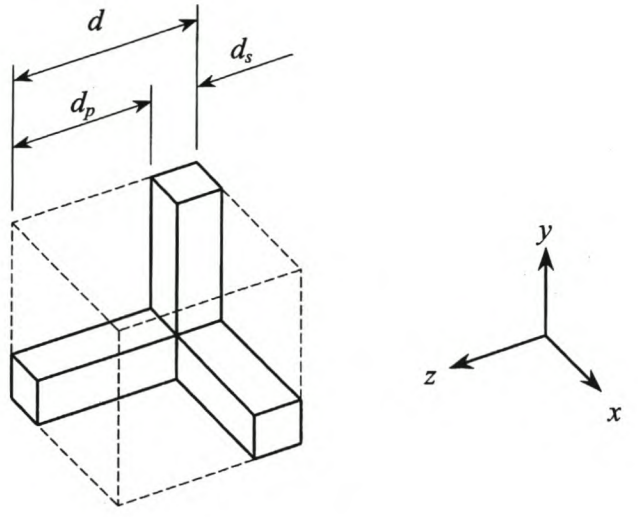

Figure 9.1 Representative unit cell for cellular foams.

The RUC shown in Figure 9.1 induces an unwanted directional priority by converging flow from an upward channel and a lateral channel from the left into a streamwise channel. This effect may be eliminated by considering three complementary RUC's: one in which the flow converges from a downward channel and a lateral channel from the right into a streamwise channel, one in which a streamwise channel splits into a lateral channel to the right and an upward channel, and one in which a streamwise channel splits into a lateral channel to the left and a downward channel.

The RUC geometry shown in Figure 9.1, together with its application requirements discussed above, satisfy three criteria specified by Dullien (1979, p. 90) for characterising a pore structure, namely the dimensionality of the network (three dimensional in the case of cellular foams), pore coordinate number (the number of connections made to a pore volume) and the microscopic topology of the network (given by parameters such as shape, structure and connectivity).

9.4 Application of the RUC for cellular foams

In this study, it will be assumed that the porosity ε_f and the RUC characteristic dimension d, are spatially variable functions to be specified at each location within the porous domain. Therefore, conceptually an RUC is defined at each location in the porous domain, is stationary, and consists of a volume V_o of the real porous medium inclusive of the pores.

From Figure 9.1 it follows that the overall volume of the RUC is:

$$V_o = d^3 \tag{9.1}$$

and the void part of the RUC can be written in terms of the RUC characteristic dimension d and the characteristic pore width d_p, as:

$$V_f = 3{d_p}^2 d - 2{d_p}^3 . \tag{9.2}$$

Dividing Equation (9.2) by Equation (9.1) yields the porosity as:

$$\varepsilon_f = 3\left(\frac{d_p}{d}\right)^2 - 2\left(\frac{d_p}{d}\right)^3 . \tag{9.3}$$

The tortuosity χ of the porous medium is defined as:

$$\chi \equiv \frac{d_e}{d}, \tag{9.4}$$

where d_e is the total path length within the RUC available for flow under the constant cross-section ${d_p}^2$, given as:

$$d_e \equiv \frac{V_f}{{d_p}^2} . \tag{9.5}$$

The tortuosity of the porous microstructure is a measure of the tortuous pore length per length of porous medium. Smit and Du Plessis (1999) presented the tortuosity of the porous medium in terms of the porosity ε_f as:

$$\chi = 2 + 2\cos\left[\frac{4\pi}{3} + \frac{1}{3}\cos^{-1}\left(2\varepsilon_f - 1\right)\right]. \tag{9.6}$$

From Equation (9.1) and Definition (II.1), Definition (9.4) and Definition (9.5) it follows that:

$$\frac{d_p}{d} = \sqrt{\frac{\varepsilon_f}{\chi}}. \tag{9.7}$$

Substituting Equation (9.7) into Equation (9.3) and rearranging terms yields:

$$\varepsilon_f = \chi\left(\frac{3-\chi}{2}\right)^2. \tag{9.8}$$

Substituting Equation (9.8) into Equation (9.7) yields:

$$\frac{d_p}{d} = \frac{3-\chi}{2}. \tag{9.9}$$

Also, noting that:

$$d_s = d - d_p, \tag{9.10}$$

where d_s is the characteristic prism width, it follows from Equation (9.9) that:

$$\frac{d_s}{d} = \frac{\chi - 1}{2}. \tag{9.11}$$

Allowing for a solid-solid interface A_{ss} of equal area d_s^2 on all six sides of the RUC, the total wetted surface within the RUC is given by:

$$A_{sf} = 12 d_p d_s. \tag{9.12}$$

Dividing Equation (9.12) by Equation (9.1) and substituting Equation (9.9) and Equation (9.11) yields the specific volume $\frac{A_{sf}}{V_o}$ of the RUC as:

$$\left(\frac{A_{sf}}{V_o}\right)_{RUC} = \frac{3}{d}(3-\chi)(\chi-1). \tag{9.13}$$

9.5 Metallic foam morphology

If a metallic foam microstructure is geometrically well defined in relation to an RUC model, then the characteristic dimension d can be related to some physically measurable pore scale dimension.

From a geometric definition point of view it is helpful to think of a cellular structure as *vertices*, joined by *edges*, which surround *faces*, which enclose *cells*. The number of edges that meet at a vertex is the edge connectivity Z_e, which is usually four. The number of faces that meet at an edge is the face connectivity Z_f that is usually three. The number of vertices v, edges e, faces f, and cells c are related by Euler's law (Lakatos, 1976), which for a large aggregate of cells states that:

$$-c + f - e + v = 1. \tag{9.14}$$

For an isolated cell (c = 1), the average number of edges per face $\overline{n}$ is related to the number of faces f according to (Gibson and Ashby, 1988):

$$\overline{n} = \frac{Z_e Z_f}{Z_e - 2}\left(1 - \frac{2}{f}\right). \tag{9.15}$$

In general, for cellular foams, $f \approx 14$ and $\overline{n} \approx 5$ (Gibson and Ashby, 1988) but, as Weaire and Rivier (1984) and Fortes (1986) emphasised, both f and $\overline{n}$ depend on the method of manufacture and on the forces which shape the cells.

The morphological characteristics of metallic foams are usually specified by their manufacturers in terms of a cell size designation and foam porosity [or sometimes by the solid phase volume fraction defined by Definition (II.1), also referred to as the *specific density*]. Cell size designations have been found to be very subjective.

In this study, a representation of the cellular configuration is based on a morphological model consisting of an ordered array of tetrakaidecahedra (Gibson and Ashby, 1988). The geometry of a single tetrakaidecahedron is shown in Figure 9.2 and an array of three tetrakaidecahedra is shown in Figure 9.3. Each cell consists of eight hexagonal faces and six square faces. Therefore, f = 14 and, from Equation (9.15), $\overline{n}$ = 5.14, which corresponds to that of cellular foams in general. There are 24 vertices and 36 edges per unit cell. A unit cell volume is $11.31t^3$, where t is the edge length. In an infinitely packed array of tetrakaidecahedra, every edge is shared between three faces, leaving 12 edges associated with every cell.

The characteristic dimension a, representing cell size, is taken as the mean of the distance between two parallel square faces ($2.83t$) and the distance between two opposing edges where two hexagonal faces meet in a tetrakaidecahedron ($3.0t$) (Bastawros *et al.*, 1998), given as:

$$a = 2.9t\,. \tag{9.16}$$

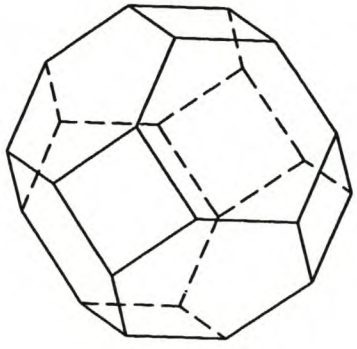

Figure 9.2 Geometry of a single tetrakaidecahedron.

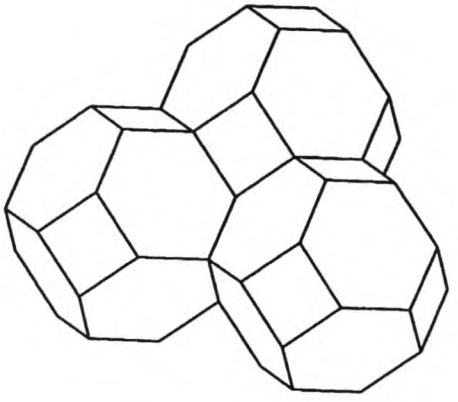

Figure 9.3 An array of three tetrakaidecahedra.

9.6 Strand model

Now consider that a solid strand substitutes every edge of an array of tetrakaidecahedra. In the manufacturing of metallic foams, surface tension during solidification of the superheated metal in a liquidus state causes material clustering at strand vertices and also causes the strand to have a non-cylindrical cross-sectional shape. The triangular cross-section corresponds geometrically to the cell face connectivity Z_f of three. In order to simplify volume and surface area calculations, the geometry of a single strand is approximated by that of a prism of uniform, triangular cross-section, flared and finished off on both ends to fit into a three-dimensional lattice structure. This geometry is shown in Figure 9.4. With an edge connectivity Z_e of four, the geometry of the finished-off ends was selected to fit into an evenly spaced tetragon, shown in Figure 9.5. Each strand is orientated in the tetrakaidecahedronal lattice such that the axis of symmetry of the cross-sectional triangle coincides with the plane shared by the axis of adjacent strands, as shown in Figure 9.5. The angle between any two axes in an evenly spaced tetragon is 109.47°. The maximum flare angle that allows smooth transition from one strand to another is 109.47° - 90.0° = 19.47°.

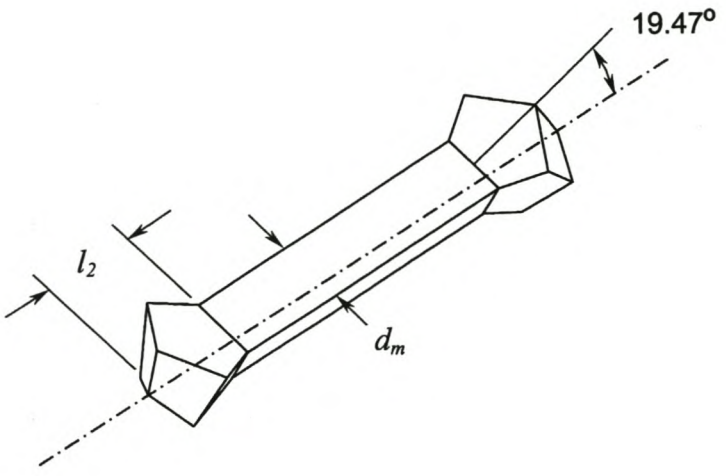

Figure 9.4 Representative geometry of a single strand.

Close observation of metallic foams of various porosities and cell sizes has revealed that a fixed ratio can be assumed between the side-length d_m of the triangular prismatic cross-section and the flare length l_2. In that case a given cell size a with porosity ε_f yields a single value for the side-length d_m. An approximate ratio between side-length d_m and flare length l_2 can be determined from the work of Bastawros *et al.* (1998) who measured cell morphology in the porosity range 0.915 to 0.936. Using optical microscopy and approximating the cross-sectional shape of a strand as circular, Bastawros *et al.* observed that:

$$\frac{d_\phi}{d_{\phi m}} = 1.24 , \tag{9.17}$$

where d_ϕ is the diameter of a cylinder of uniform cross-sectional surface area and $d_{\phi m}$ is the observed minimum circular strand diameter, measured in the region around the midpoint between two vertices.

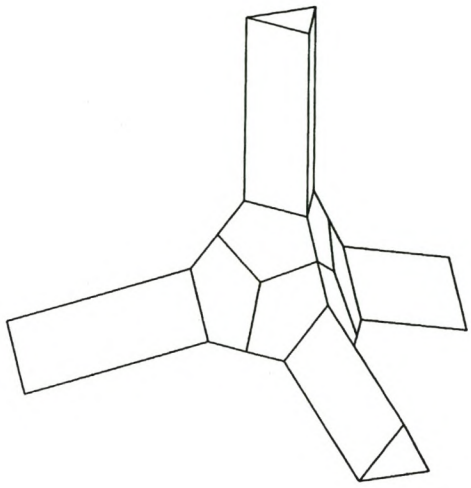

Figure 9.5 Strand ends flared and finished off to fit into a three-dimensional evenly-spaced tetragon.

Using 0.925 (the average of 0.915 and 0.936) as a reference porosity at which Equation (9.17) applies, it follows that:

$$\frac{d_{\phi m}}{t} = 0.2418. \tag{9.18}$$

Substituting the circular cross-sectional shape by a triangular cross-sectional shape of equal cross-sectional surface area, Equation (9.18) becomes:

$$\frac{d_m}{t} = 0.3257, \tag{9.19}$$

where d_m is the triangle side-length. The reference porosity applies when the ratio

between the side-length d_m and the flare length l_2 is:

$$\frac{d_m}{l_2} = 0.8714. \tag{9.20}$$

Based on this ratio, the volume of a single strand can be expressed in terms of the strand length t and the triangular prismatic cross section side-length d_m as:

$$V_{strand} = 0.4330\, d_m^2 t + 0.7146\, d_m^3 \tag{9.21}$$

and the exposed surface area as:

$$A_{strand} = 3.0\, d_m t - 0.5748\, d_m^2. \tag{9.22}$$

Since 12 edges are associated with every cell of volume $11.3\, t^3$, it follows from Equation (9.16) and Equation (9.21) that the porosity ε_f of an array of tetrakaidecahedra in which solid strands substitute the vertices as shown in Figure 9.4, is given as:

$$\varepsilon_f = 1 - 3.867\left(\frac{d_m}{a}\right)^2 - 18.51\left(\frac{d_m}{a}\right)^3 \tag{9.23}$$

and from Equation (9.16) and Equation (9.22), the specific surface area $\frac{A_{sf}}{V_o}$ is:

$$\left(\frac{A_{sf}}{V_o}\right)_{mor} = 26.79\frac{d_m}{a^2} - 14.89\frac{d_m^2}{a^3}. \tag{9.24}$$

Figure 9.6 graphically relates strand triangular side-length d_m to cell size a at four different porosities. Figure 9.7 shows the relation between specific surface area $\frac{A_{sf}}{V_o}$ and cell size a at four different porosities.

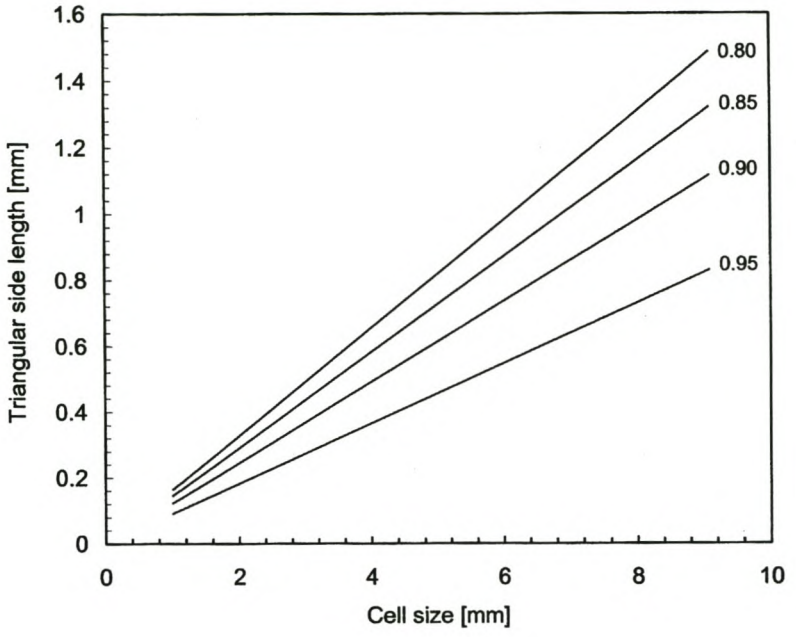

Figure 9.6 The strand triangular side length d_m as a function of the cell size a at four different porosities. Each curve represents the porosity ε_f indicated next to the curve.

9.7 Characteristic dimension

Equating the right hand sides of Equation (9.13) and Equation (9.24) yields, after rearranging terms:

$$d = \frac{3(3-\chi)(\chi-1)}{26.79\frac{d_m}{a^2} - 14.89\frac{{d_m}^2}{a^3}}. \tag{9.25}$$

Equation (9.25), together with Equation (9.6) and Equation (9.23), forms an expression for the RUC characteristic dimension d as a function of the cell size a and the porosity ε_f. This relationship is shown graphically in Figure 9.8.

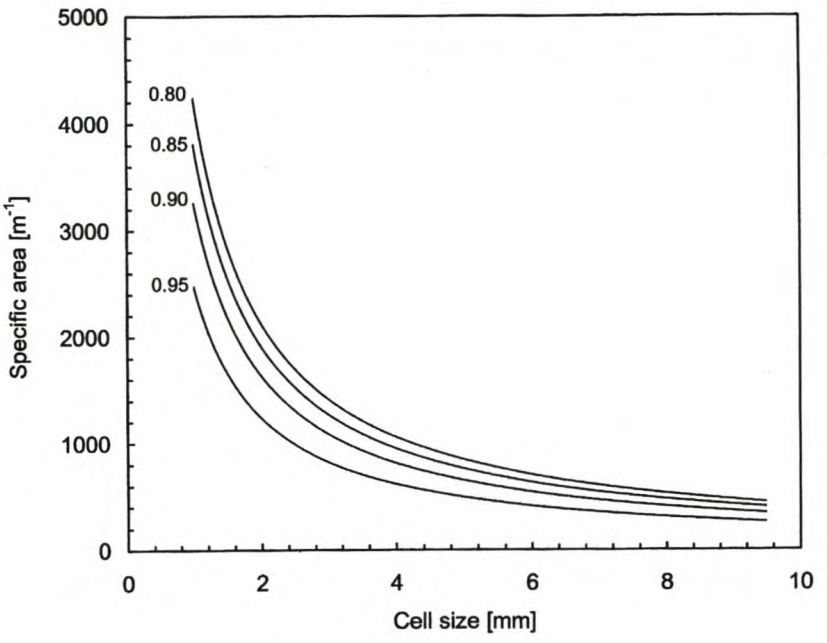

Figure 9.7 The specific surface area $\frac{A_{sf}}{V_o}$ as a function of the cell size a at four different porosities. Each curve represents the porosity ε_f indicated next to the curve.

9.8 Mean linear distances

Two other useful geometric parameters for analysing fluid flow and heat transfer along a system boundary (*i.e.* the porous domain boundary) are the mean linear distance $\bar{d}_{ss}$ across a solid phase element intersected by the system boundary and the mean linear distance $\bar{d}_{ff}$ between solid phase elements at the system boundary. In order to determine these quantities, an expression is required for the average cross-sectional surface area size $A_{ss,average}$ of solid phase elements at the system boundary.

The system boundary intersects strands between vertices, where the cross-sectional surface area is relatively small, as well as in regions near vertices where the cross-sectional area is larger. However, from close observation it was determined that in low

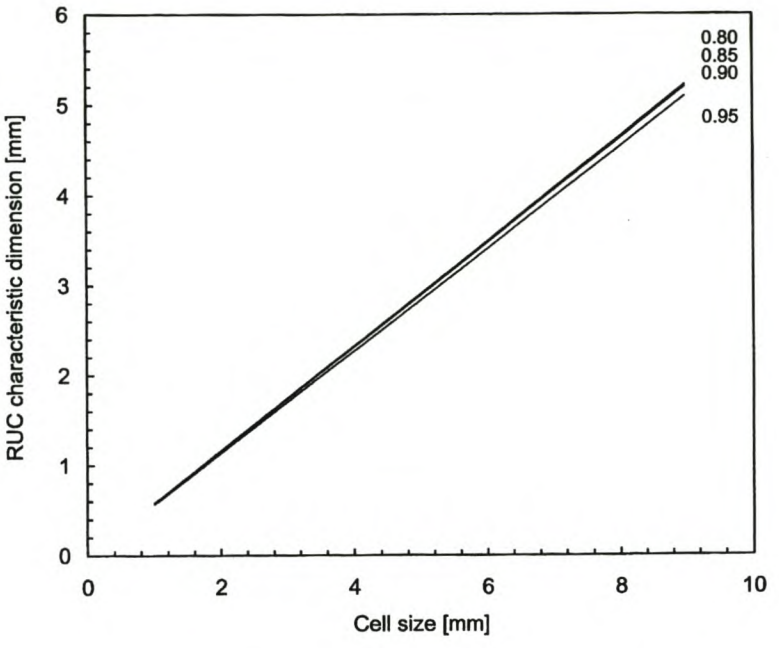

Figure 9.8 The RUC characteristic dimension d as a function of the cell size a at four different porosities. Each curve represents the porosity ε_f indicated next to the curve.

porosity metallic foams, the system boundary intersections are mostly near vertices, resulting in larger cross-sectional areas. In metallic foams of higher porosities, it was observed that a greater number of relatively small cross-sections of strands intersecting between vertices are present, reducing the average cross-sectional surface area size. This observation supports the assumption of a fixed ratio between the strand cross-sectional dimension in the region between vertices, and the flare length, where these geometries are represented by d_m and l_2 respectively in the simplified geometry shown in Figure 9.4.

A cross-sectional area size parameter is defined in this study as:

$$\eta \equiv \frac{A_{ss,average}}{d_m^{\,2}}, \tag{9.26}$$

where the square of the strand side-length d_m is used as the reference strand surface area.

An approximate distribution of the cross-sectional area size parameter η is determined as a function of porosity ε_f using a unit cell configuration. The unit cell consists of four strands connected at a vertex, as shown in Figure 9.9. Various strand lengths were used to represent a range of porosities. Using 3D solid modelling computer software, each unit cell was intersected at regular vertical intervals from which an average cross-sectional surface area size $A_{ss,average}$ and the area size parameter η were determined. Figure 9.10 shows a number of area size parameter data points with a curve fit through the data points. The equation for the curve is:

$$\eta = 2.47 - 0.08\left(\frac{\varepsilon_f}{0.988 - \varepsilon_f}\right)^{0.61}. \tag{9.27}$$

Equation (9.27) is only valid in the range $0.8 < \varepsilon_f < 0.97$.

If it is assumed that the average cross-sectional surface area is of square shape with two sides transverse and two sides longitudinal to the direction of the linear distance of interest, then it follows that:

$$\bar{d}_{ss} \equiv \sqrt{\eta}\, d_m. \tag{9.28}$$

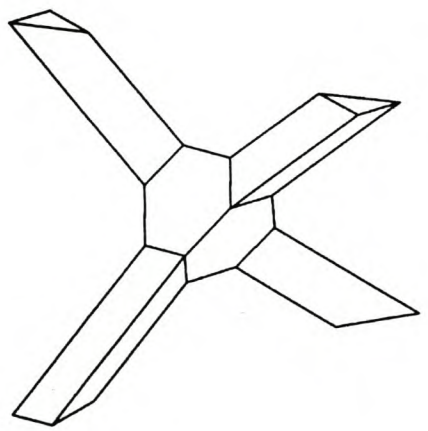

Figure 9.9 A unit cell consisting of four strands connected at a vertex.

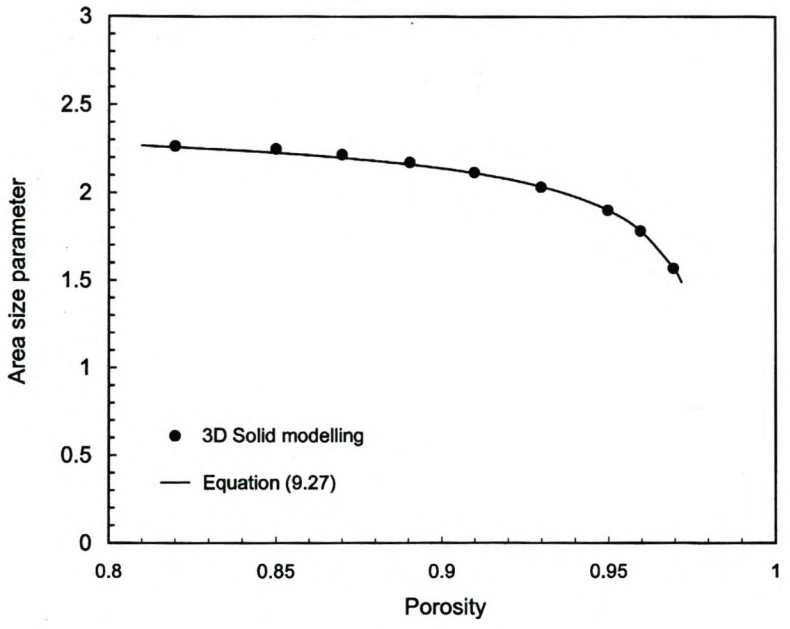

Figure 9.10 The cross-sectional area size parameter η as a function of porosity ε_f.

Bear and Bachmat (1991) showed that the two-dimensional surface plane distribution density of the solid and the fluid phases is the same as their three-dimensional volumetric counterparts, *i.e.*:

$$A_{ss} = (1 - \varepsilon_f) A_o \tag{9.29}$$

and:

$$A_{ff} = \varepsilon_f \, A_o, \tag{9.30}$$

where A_o is the overall system boundary surface area, and A_{ss} and A_{ff} are the total cross-sectional surface area of solid phase elements and the fluid phase respectively at the system boundary. The same approach may be followed to show that this argument can be extended to the one-dimensional linear distribution density of the solid and the fluid

phases, to yield:

$$\frac{d_{ss}}{d_{ff}} = \frac{(1-\varepsilon_f)}{\varepsilon_f}, \tag{9.31}$$

or, when divided by the number of solid phase elements encountered along the linear dimension:

$$\frac{\bar{d}_{ss}}{\bar{d}_{ff}} = \frac{(1-\varepsilon_f)}{\varepsilon_f}. \tag{9.32}$$

Substituting Equation (9.28) into Equation (9.32) and rearranging terms yields:

$$\bar{d}_{ff} = \frac{\varepsilon_f}{(1-\varepsilon_f)} \sqrt{\eta}\, d_m. \tag{9.33}$$

CHAPTER 10

VISCOUS SHEAR FACTOR

10.1 Overview

In this chapter, the viscous shear factor (introduced by the viscous shear model in Section 3.2) is quantified for metallic foams in terms of flow parameters, fluid phase thermophysical properties and metallic foam morphological parameters. The viscous shear factor retains its diagonal tensor form (as introduced in Section 3.2) even for isotropic metallic foams, since its component values in the principal directions are a function of the directional volume-averaged velocity vector $\langle \boldsymbol{v} \rangle_f$. Expressions are derived for low Reynolds number flow where viscous shear in the fluid is predominant, as well as for high Reynolds number flow where form drag on the foam microstructure is predominant. These expressions are unified into a single expression which applies to low and high Reynolds number flow. In the formulation of these expressions, general flow patterns on a solid body are considered in the modelling of viscous shear stress and form drag. Other related topics such as permeability and pressure gradient in metallic foams are also addressed in this chapter.

10.2 Analysis

The viscous shear model discussed in Section 3.2 states that:

$$\mu \boldsymbol{f} \cdot \langle \boldsymbol{v} \rangle_f \equiv \left(-\frac{1}{V_o} \int_{A_{sf}} \mu (\nabla \boldsymbol{v}) \cdot \boldsymbol{n}_{fs} \, \mathrm{d}A + \frac{1}{V_o} \int_{A_{sf}} {}^{\circ}_{p} \boldsymbol{n}_{fs} \, \mathrm{d}A \right). \tag{3.8}$$

Substituting Equation (3.7) into Definition (3.8) yields:

$$\mu \boldsymbol{f} \cdot \langle \boldsymbol{v} \rangle_f = -\varepsilon_f \nabla \langle p \rangle_f^f . \tag{10.1}$$

Equation (10.1) also follows directly from the steady-state version of the transformed volume-averaged momentum equation [Equation (8.2)] with a uniform volume-averaged velocity distribution and in the absence of a body force.

From Equation (10.1) it follows that quantifying the surface integrals in Definition (3.8) is subject to a description of the actual velocity and pressure distributions at the interface between the two phases in the metallic foam. Velocity and pressure distributions on any solid body in cross flow depend on the local flow regime existing on the body. Several types of flow regimes can be distinguished, characterised by their Reynolds number. The Reynolds number is defined as the ratio of inertial to viscous forces in the fluid, with reference to an identifiable characteristic dimension of the solid body. The following section gives a brief description of flow regimes and their relation to the Reynolds number.

10.3 General flow patterns on a solid body in cross flow

Because of viscosity of real fluids, laminar hydraulic boundary layers are formed on the front portion of a body, the thickness of which increases downstream. At $Re < 1$, where the Reynolds number is based on a characteristic cross-sectional dimension of the body, inertial forces are negligibly small compared to viscous forces, and if the body is streamlined, the laminar hydraulic boundary layer separates from the surface at the rear stagnation point.

With increasing Reynolds number, the influence of inertial forces increases and eventually, at $Re > 5$, the hydraulic laminar boundary layer separates from the body's surface without reaching the rear stagnation point. A thorough description of the

separation phenomenon is given by Schlichting (1979, p. 28). Behind the object there appears recirculation vortices, which form a circulation region confined by flow lines. With further increase in Reynolds number the vortices become extended downstream. In the case of a cylinder in cross flow, the region shows a stable circulation pattern up to $Re = 40$. Beyond this, the stability of the movement in the recirculation region is lost.

With even further increase of the Reynolds number, the boundary layers gradually become turbulent and receive additional kinetic energy from the main flow through turbulent fluctuations. On streamlined bodies, the turbulent part of the boundary layer and the separation point are shifted downstream.

In a porous medium, hydrodynamic behaviour in the low Reynolds number range shows a linear relationship between experimental pressure gradient data and the locally mean flow velocity through a porous medium. Darcy (1856) first made this observation. The flow regime corresponding to this hydrodynamic behaviour has consequently been referred to as the *Darcy* flow regime.

At higher Reynolds number flow, where recirculation behind individual strands becomes predominant, experimental pressure gradient data shows a clear deviation from linear behaviour toward higher-pressure gradients. Forchheimer (1901) proposed an additional non-linear term to a purely linear mathematical description of the relationship between the pressure gradient and the locally mean flow velocity. Hydrodynamic behaviour associated with higher Reynolds number flow has therefore been referred to as *Forchheimer* flow.

10.4 Modelling the viscous shear factor in the RUC

The RUC for cellular foams, shown in Figure 9.1, provides a facility to extrapolate momentum transport knowledge from common flow systems to the microstructure of the metallic foam. Two prisms in cross flow represent the random inclination of strands to the mean flow direction and one prism aligned with the mean flow direction. When applied to

the RUC geometry, the viscous shear factor in Definition (3.8) can be rewritten in a simple deterministic manner in terms of a friction coefficient $C_{D,v}$ in the Darcy flow regime and a form drag coefficient $C_{D,f}$ in the Forchheimer flow regime.

The friction coefficient, defined as (White, 1991, p.119):

$$C_{D,v} \equiv \frac{F_v}{\frac{1}{2}\rho_f v_p^{\,2} A_{sf}}, \tag{10.2}$$

accounts for viscous shear stress in the longitudinal and transverse channels in the RUC, the predominant process causing a drag force F_v in the Darcy flow regime. The form drag coefficient accounts for drag force F_f caused by hydrodynamic boundary layer separation and flow recirculation, which are predominant in Forchheimer flow (Bennethum and Giorgi, 1997), and is defined as (White, 1991, p.119):

$$C_{D,f} \equiv \frac{F_f}{\frac{1}{2}\rho_f v_p^{\,2} A_{fr}}. \tag{10.3}$$

In Definition (10.2) and Definition (10.3), v_p is the mean pore velocity and ρ_f is the fluid density. In Definition (10.2) A_{sf} is the total wetted surface and in Definition (10.3) A_{fr} is the frontal area subjected to recirculation.

Within the RUC, the mean velocity v_p denotes the area average pore velocity in a longitudinally oriented pore. The longitudinal direction is defined by the main flow direction represented by the local volume-averaged velocity vector $\langle \boldsymbol{v} \rangle_f$. With a cross-section area A_p ($= d_p^{\,2}$) of a longitudinally oriented pore, it follows that:

$$v_p = \frac{1}{A_p} \int_{A_p} v \, \mathrm{d}A. \tag{10.4}$$

The volumetric flow rate through the RUC is given by $v_p d_p^{\,2}$. Since the volumetric flow

rate is also equal to $\langle \boldsymbol{v} \rangle_f d^2$, it follows that:

$$v_p = \langle v \rangle_f \left(\frac{d}{d_p} \right)^2 . \tag{10.5}$$

Substituting Equation (9.7) into Equation (10.5) and rearranging terms yields:

$$v_p = \langle v \rangle_f \frac{\chi}{\varepsilon_f} . \tag{10.6}$$

The drag force F in an RUC of frontal area size d^2 and depth d is given as:

$$F = -\varepsilon_f \nabla \langle p \rangle_f^f d^3 . \tag{10.7}$$

Substituting Equation (10.7) into Definition (10.2) and then substituting Equation (10.1), Equation (10.6) and Equation (9.13), noting that the overall RUC volume V_o (= d^3) yields the viscous shear factor in a diagonal tensor form in the Darcy flow regime as:

$$\boldsymbol{f} = (3-\chi)(\chi-1) \frac{3\rho_f \chi^2}{2\mu \varepsilon_f{}^2 d} C_{D,v} \delta_{ij} \boldsymbol{i} \langle \boldsymbol{v} \rangle_f \tag{10.8}$$

and in the Forchheimer flow regime as:

$$\boldsymbol{f} = (3-\chi)(\chi-1) \frac{A_{fr}}{A_{sf}} \frac{3\rho_f \chi^2}{2\mu \varepsilon_f{}^2 d} C_{D,f} \delta_{ij} \boldsymbol{i} \langle \boldsymbol{v} \rangle_f , \tag{10.9}$$

where $\boldsymbol{i}$ is a unit vector δ_{ij} is the Kronecker delta ($\delta_{ij} = 1$ for $i = j$, $\delta_{ij} = 0$ for $i \neq j$).

In the RUC for cellular foams, the contribution to drag force from one prism aligned with the mean flow direction can be neglected. Two thirds of the interface area A_{sf} is subjected to cross flow and the frontal area A_{fr} subjected to recirculation, is one sixth of the interface

area A_{sf}, or:

$$\frac{A_{fr}}{A_{sf}} = \frac{1}{6}. \tag{10.10}$$

Equation (10.8) and Equation (10.9) are predominant in the limits of low and high Reynolds number flow respectively. Solutions for intermediate Reynolds numbers are determined by a superposition technique described by Churchill and Usagi (1972). Substituting Equation (10.10) and selecting a shifting exponent of one in the superposition technique (Du Plessis *et al.*, 1994), leads to a general expression for the viscous shear factor as the simple addition of Equation (10.8) and Equation (10.9):

$$\boldsymbol{f} = (3-\chi)(\chi-1)\frac{\rho_f \chi^2}{\mu \varepsilon_f{}^2 d}\left(\frac{3C_{D,v}}{2} + \frac{C_{D,f}}{4}\right)\delta_{ij}\boldsymbol{i}\langle \boldsymbol{v}\rangle_f . \tag{10.11}$$

10.5 Modelling the friction coefficient in the RUC

In the Darcy flow regime, following the work of Du Plessis *et al.* (1994) and Du Plessis and Van der Westhuizen (1993), it is assumed that hydrodynamic stresses at the solid-fluid interface of the RUC comply to Poiseuille flow at a mean RUC velocity v_p, between parallel surfaces at a distance apart, which equals the characteristic pore width d_p. The friction coefficient for Poiseuille flow is given as:

$$C_{D,v} = \frac{12\mu}{\rho_f v_p d_p}. \tag{10.12}$$

Substituting Equation (10.6) and Equation (9.9) into Equation (10.12) yields:

$$C_{D,v} = \frac{24\varepsilon_f \mu}{\rho_f \chi(3-\chi) d \langle v\rangle_f}. \tag{10.13}$$

10.6 Modelling the form drag coefficient in the RUC

In order to model flow across the strand geometries shown in Figure 1.2, it is assumed that at sufficiently high Reynolds numbers where hydraulic boundary layer separation and recirculation occur behind strands, the flow behaviour is approximately equivalent to that on a cylinder in cross flow. The effect on the hydrodynamic behaviour of non-cylindrical cross sections and material clustering at the vertices of strands is accounted for by a cylinder diameter referred to as the *representative hydraulic diameter* (RHD).

In order to illustrate the concept of the RHD hypothesis, consider Figure 10.1 showing flow through a bundle of parallel square bars of varying square dimensions (from bar to bar and along the length of each bar), with their cross sections orientated randomly to the direction of flow. According to the RHD hypothesis, the overall form drag caused by the randomly aligned square bars, equals that of a bundle of the same number of similar cylindrical bars of diameters equal to the RHD of the bundle of square bars. Although a square cross section is used in the description and illustration, the concept applies to any cross-sectional geometry that promote high Reynolds number recirculation on its lee side at any alignment to the direction of flow (therefore excluding geometries such as airfoils).

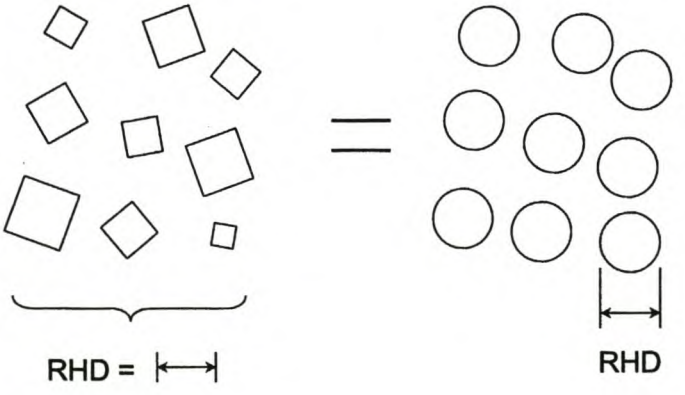

Figure 10.1 Basic concept of the representative hydraulic diameter (RHD).

It is now assumed that in the Forchheimer flow region, the RUC for cellular foams, shown in Figure 9.1, together with the representative hydraulic diameter (RHD) hypothesis, relates hydrodynamic stresses and flow recirculation in a metallic foam, to that on a cylinder of diameter equal to the RHD of the metallic foam. It is further assumed that the RHD is equal to the characteristic strand width d_s of the RUC, which is determined by the characteristic dimension d of the RUC and the porosity ε_f of the porous medium.

White (1991, p. 183) proposed the following expression for the drag coefficient of a cylinder in cross flow:

$$C_{D,f} = 1 + \frac{10}{Re^{0.667}}, \tag{10.14}$$

where the Reynolds number Re, relates diffusive and hydrodynamic momentum transport in a fluid and is defined as:

$$Re \equiv \frac{\rho_f v d_h}{\mu}. \tag{10.15}$$

In Definition (10.15), ρ_f is the fluid density, v is the mean flow velocity, d_h is a characteristic hydraulic dimension and μ is the dynamic viscosity of the fluid. For the application of the RHD hypothesis, it is further assumed that the pore velocity v_p is the most appropriate velocity representation in the Reynolds number definition. Based on these assumptions and substituting Equation (9.11) and Equation (10.6), Equation (10.14) can be written as:

$$C_{D,f} = 1 + 10\left(\frac{\rho_f \langle v \rangle_f d\,(\chi - 1)}{2\mu\varepsilon_f}\right)^{-0.667}. \tag{10.16}$$

Equation (10.11), together with Equation (10.13) and Equation (10.16), gives the viscous shear factor in terms of the overall characteristic dimension d and the tortuosity χ, which is given in terms of the porosity ε_f by Equation (9.6).

10.7 Pressure gradient

With a uniform volume-averaged velocity distribution and in the absence of a body force, the substitution of Equation (10.1) into Equation (10.11) yields the following equation for the pressure gradient in metallic foams:

$$\nabla\langle p\rangle_f^f = -(3-\chi)(\chi-1)\frac{\rho_f \chi^2 \langle v\rangle_f \langle \boldsymbol{v}\rangle_f}{\varepsilon_f{}^3 d}\left(\frac{3C_{D,v}}{2}+\frac{C_{D,f}}{4}\right). \tag{10.17}$$

Figure 17.2 to Figure 17.4 compare results from Equation (10.17) to experimentally determined pressure gradient data of three different metallic foams (Bastawros *et al.*, 1998).

10.8 Permeability

Permeability has often been used as a flow parameter in the quantitative evaluation of pressure gradient in porous media. The Ergun equation relates pressure gradient to flow velocity and geometric parameters as:

$$-\nabla\overline{p} = \frac{\mu \boldsymbol{v}}{K}+\frac{\rho_f C_E \boldsymbol{v}v}{\sqrt{K}}, \tag{10.18}$$

where $\overline{p}$ is the mean pressure, K is the permeability and C_E is an inertial coefficient. After rearranging terms, Equation (10.18) may be written in terms of a *reduced pressure gradient*, as:

$$-\frac{\nabla\overline{p}}{\mu v} = \frac{1}{K}\frac{\boldsymbol{v}}{v}+\rho_f \frac{C_E}{\sqrt{K}}\frac{\boldsymbol{v}}{\mu}. \tag{10.19}$$

10.9 Analytical models for predicting permeability

Spielman and Goren (1986) developed an expression for continuous randomly orientated fibres, given in an implicit form as:

$$K^{-1} = \frac{1-\varepsilon_f}{\pi {d_\phi}^2 \mu}\left(\frac{1}{3} f_{||} + \frac{2}{3} f_{\perp}\right), \tag{10.20}$$

where:

$$f_{||} = \frac{-2\mu d_\phi}{\sqrt{K}} \frac{\mathrm{K}_1\left(\frac{d_\phi}{\sqrt{K}}\right)}{\mathrm{K}_0\left(\frac{d_\phi}{\sqrt{K}}\right)} \tag{10.21}$$

and:

$$f_{\perp} = \frac{-4\mu d_\phi}{\sqrt{K}}\left[\frac{d_\phi}{\sqrt{K}} \frac{\mathrm{K}_1\left(\frac{d_\phi}{\sqrt{K}}\right)}{\mathrm{K}_0\left(\frac{d_\phi}{\sqrt{K}}\right)} + \frac{{d_\phi}^2}{2\sqrt{K}}\right], \tag{10.22}$$

and K_0 and K_1 are the modified Bessel functions of the order zero and one. In their development, Spielman and Goren associated the geometry of randomly orientated fibres with one fibre aligned with the direction of flow and two fibres orientated transverse to the direction of flow. This association corresponds to that implied by the geometry of the RUC for cellular foams, shown in Figure 9.1.

Koch and Brady (1986) simplified the expression given in Equation (10.20) to an explicit form given as:

$$K = \frac{3{d_\phi}^2}{20} \frac{\ln\left(\frac{1}{1-\varepsilon_f}\right)}{1-\varepsilon_f}, \tag{10.23}$$

where d_ϕ is the fibre diameter. Angirasa and Peterson (1996) (see Section 1.5 for a brief discussion of their work) applied Equation (10.23) directly to predict the permeability of metallic foams.

The simplification of Brady and Koch introduces an error of the order:

$$\frac{1-\varepsilon_f}{{d_\phi}^2}\frac{\ln\left[\ln\left(\frac{1}{1-\varepsilon_f}\right)\right]}{\ln\left(\frac{1}{1-\varepsilon_f}\right)}, \tag{10.24}$$

which decreases with increasing porosity.

Comparing Equation (10.17) and Equation (10.18), assuming that $\overline{p} = \langle p \rangle_f^f$, and using Equation (10.12) yields:

$$K = \frac{{\varepsilon_f}^2 d^2}{36(\chi - 1)\chi} \tag{10.25}$$

and:

$$C_E = (3-\chi)(\chi-1)\frac{C_{D,f}\,\chi^{1.5}}{24{\varepsilon_f}^2}\ . \tag{10.26}$$

Figure 10.2 graphically compares the permeabilities predicted by Equation (10.23) and Equation (10.25) over a range of porosities. The cell size a was arbitrarily selected as 3.0 mm and the fibre diameter d_ϕ in Equation (10.23) was set equal to the RHD of the corresponding foam.

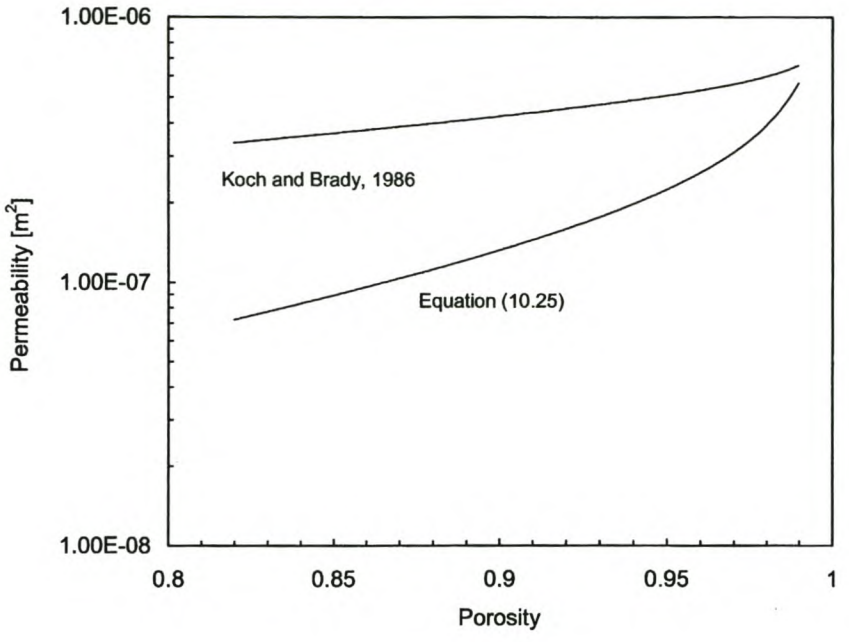

Figure 10.2 Comparison between permeability models.

10.10 Experimental methods for predicting permeability

If Equation (10.19) sufficiently correlated experimentally determined pressure gradient data then the straight-line curve fit yields the inverse of the permeability at its intersection with the *y*-axis. Hunt and Tien (1988) used this technique to determine the permeability of two metallic foam samples from their pressure gradient data. The porosity of one sample is 0.97 and that of the other is 0.94. Both samples have a pore density of 25 ppi. For both samples the pressure gradient data is from a limited range of Reynolds numbers. Fitting a straight-line curve on the pressure gradient data presented in terms of the reduced pressure gradient [defined by the LHS of Equation (10.19)], yields a permeability of 8×10^{-8} m^2 for the 0.94 porosity sample and a permeability of 5.3×10^{-8} m^2 for the 0.97 porosity sample.

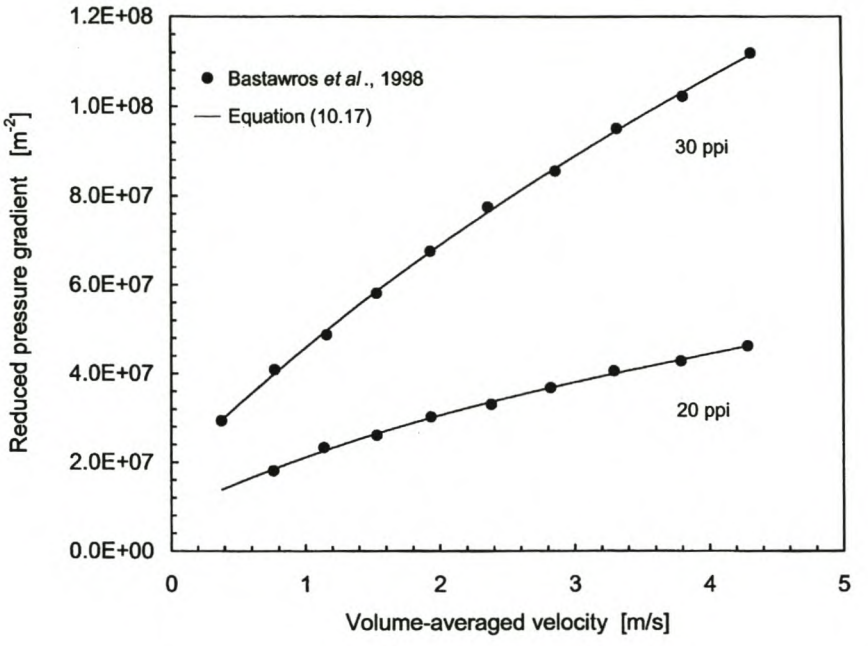

Figure 10.3 Non-linear behaviour of the reduced pressure gradient with flow Reynolds number.

However, when the pressure gradient data of Bastawros *et al.* (1998) shown in Figure 17.3 and Figure 17.4 is presented in terms of the reduced pressure gradient, it reveals a non-linear behaviour with the velocity v, as shown in Figure 10.3. The inertial coefficient C_E in Equation (10.19) therefore shows a Reynolds number dependency instead of constant-value behaviour over the Reynolds number range of interests.

This tendency is also observed in pressure drop across tube bundles. Zukauskas and Uliskas (1983, p. 2.2.4-1) found that the pressure drop data across a tube bundle is well correlated by the relation:

$$\Delta p = Eu \frac{\rho_f v^2}{2} n, \tag{10.27}$$

where v is a representative velocity and n is the number of tube rows. The Euler number

in Equation (10.27) is related to the Reynolds number *Re* by a relation of the form:

$$Eu = a\,Re^{b}, \tag{10.28}$$

where b is determined by the tube bank configuration and geometry, and is not zero as is expected for the linear behaviour of the reduced pressure gradient.

The non-linear behaviour of the reduced pressure gradient results in the under-prediction of the permeability by Equation (10.19). The under-prediction is less when pressure gradient data from the lower range of Reynolds numbers is used for a straight-line curve fit. *E.g.* from the pressure gradient data of Bastawros *et al.* (1998) for the 20 ppi metallic foam sample shown in Figure 10.3, using the upper three data points, a straight-line curve fit yields a permeability of 4.626×10^{-8} m^2. Using the middle three data points yields a permeability of 6.346×10^{-8} m^2 and using the lower three data points, a permeability of 9.342×10^{-8} m^2. Using Equation (10.25), the foam morphological data of the 20 ppi metallic foam sample yields a permeability of 3.771×10^{-8} m^2.

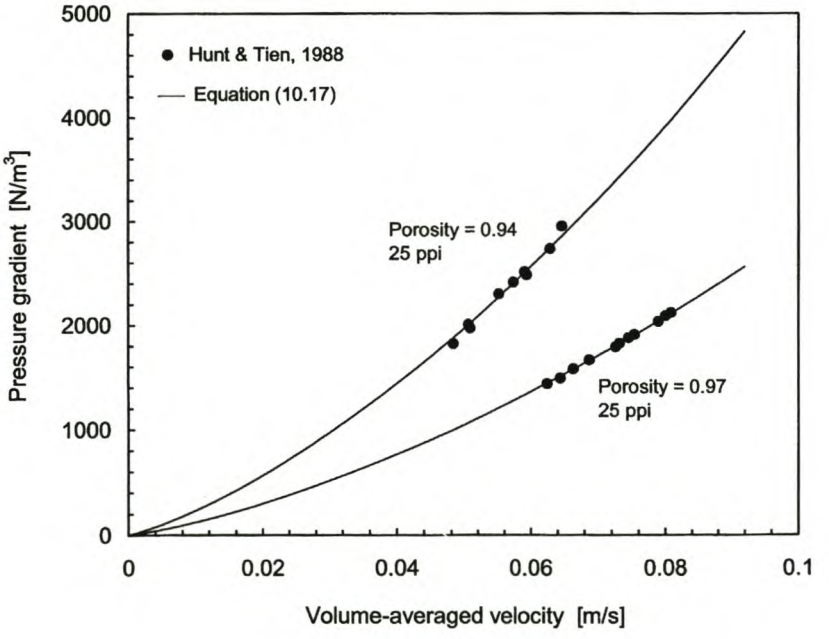

Figure 10.4 Model fit to pressure gradient data of Hunt and Tien (1988).

Figure 10.4 shows the fits of Equation (10.17) on the pressure gradient data of Hunt and Tien (1988). A cell size a of 2.518 mm (d = 1.447 mm) was used for the 0.97 porosity metallic foam sample. For this sample, Equation (10.25) yields a permeability of 2.187×10^{-7} m^2.

The cell size a used for the curve fit on the pressure gradient data of the 0.94 porosity sample is 2.093 mm (d = 1.233 mm) yielding a permeability of 9.639×10^{-8} m^2.

It therefore follows that the method of determining the permeability of a metallic foam from a straight-line curve fit through experimentally determined reduced pressure gradient data, yields inconsistent results.

CHAPTER 11

EFFECTIVE AND COUPLED THERMAL CONDUCTIVITIES

11.1 Overview

The conduction model, discussed in Section 6.3, introduced the effective thermal conductivity tensor $\boldsymbol{k}_{\gamma\gamma}$ and the coupled thermal conductivity tensor $\boldsymbol{k}_{\gamma\tau}$ into the volume-averaged energy equations of the solid and the fluid phases. In this chapter, the components of these tensors are quantified for cellular foams in terms of the solid and the fluid phase thermal conductivities and foam morphological parameters. Note that the term "cellular foam" is used instead of "metallic foam", since the analysis in this chapter applies to any foam-like medium that could be geometrically represented by the RUC for cellular foams.

The conduction model defines the effective and coupled thermal conductivities as functions of the equilibrium thermal conductivity tensor $\boldsymbol{k}_{e,\gamma}$ and the non-equilibrium thermal conductivity tensor $\boldsymbol{k}_{nd,\gamma}$ [Definition (6.8) and Definition (6.9)].

The equilibrium thermal conductivity tensor and the non-equilibrium thermal conductivity tensor are symmetric tensors with components in each of the principal directions. The RUC for isotropic cellular foams is geometrically similar in its principal directions. The components of the equilibrium thermal conductivity tensor and the non-equilibrium thermal conductivity tensor are therefore respectively equal, reducing the tensors to scalar quantities, simply referred to as the equilibrium thermal conductivity and the non-equilibrium thermal conductivity.

The equilibrium and the non-equilibrium thermal conductivities are defined with particular temperature distributions within the REV (representative elementary volume, discussed in Section II.2). These temperature distributions are discussed in Chapter 4.

With these temperature distributions established within the RUC, the equilibrium and non-equilibrium thermal conductivities are determined from analysing the microscopic temperature distributions in the phases of the RUC. Porosity is the only morphologically variable parameter in this analysis.

11.2 Microscopic temperature analysis

For a two-phase system of specific geometry and thermal conductivities, the components of the equilibrium thermal conductivities, $k_{e,s}$ and $k_{e,f}$, and the non-equilibrium thermal conductivities, $k_{nd,s}$ and $k_{nd,f}$ are all defined by a fixed relation within an REV between the phasial volume-averaged temperature gradient $\langle \nabla T \rangle_\gamma$ and the gradient in the phasial volume-averaged temperature $\nabla \langle T \rangle_\gamma$, where $\gamma = s$ or f. The equilibrium thermal conductivities, $k_{e,s}$ and $k_{e,f}$, are defined with an equilibrium temperature distribution T_e within the REV and the non-equilibrium thermal conductivities, $k_{nd,s}$ and $k_{nd,f}$, are defined with a directional, non-equilibrium temperature distribution T_{nd} within the REV. The phases are in a thermal equilibrium state with the T_e and T_{nd} temperature distributions and there is a non-zero gradient in the phasial volume-averaged temperature of each phase within the REV.

The T_e and T_{nd} temperature distributions in the RUC were obtained from the computational solution of the steady-state energy equation in both phases. With steady-state conduction as the predominant means of heat transfer, Equation (I.70) reduces to [see Equation (2.36)]:

$$\nabla \cdot (k \nabla T) + I = 0 . \tag{11.1}$$

Thermal boundary conditions were specified in the RUC in a way that the conditions for the T_e and T_{nd} temperature distributions discussed in Chapter 4, are satisfied.

The RUC for cellular foams is rotationally invariant and can always be orientated with one of its principal axis parallel to the local flow velocity. Therefore, an analysis of the microscopic temperature gradient under the condition of a gradient in the phasial volume-averaged temperatures is only required in one of the principal directions. In this study, the analysis was done with the gradient in the phasial intrinsic volume-averaged temperature in the y-direction in Figure 9.1. The definition of the equilibrium thermal conductivity therefore becomes:

$$k_{e,\gamma} = \frac{k_\gamma \left\langle \frac{\partial T_e}{\partial y} \right\rangle_\gamma}{\frac{\partial \langle T_e \rangle_\gamma}{\partial y}}, \tag{11.2}$$

and that of the non-equilibrium thermal conductivity becomes:

$$k_{nd,\gamma} = \frac{k_\gamma \left\langle \frac{\partial T_{nd}}{\partial y} \right\rangle_\gamma}{\frac{\partial \langle T_{nd} \rangle_\gamma}{\partial y}}. \tag{11.3}$$

The computational solution of Equation (11.1) yields temperature values at discrete grid points in the RUC. The equilibrium and non-equilibrium thermal conductivities were therefore determined from discretised forms of Equation (11.2) and Equation (11.3), while satisfying the discretised forms of the equilibrium and non-equilibrium temperature distribution conditions outlined in Chapter 4.

11.3 Geometric quantities

The discretised forms of Equation (11.2) and Equation (11.3) as well as the discretised forms of the equilibrium and non-equilibrium temperature distribution conditions include certain geometric quantities, which are given here for a Cartesian coordinate grid layout.

The geometric parameters are: the interface area, given as:

$$A_{sf} = \sum_{A_{sf}} \Delta y \Delta z + \sum_{A_{sf}} \Delta x \Delta z + \sum_{A_{sf}} \Delta x \Delta y ; \tag{11.4}$$

the phasial volume, given as:

$$V_\gamma = \sum_{V_\gamma} \Delta x \Delta y \Delta z , \tag{11.5}$$

and; the overall volume, given as:

$$V_o = \sum_{s} \Delta x \Delta y \Delta z + \sum_{f} \Delta x \Delta y \Delta z . \tag{11.6}$$

All geometric quantities refer to a single RUC, where Δx, Δy and Δz are the overall dimensions of the three dimensional finite volume shown in Figure 11.1.

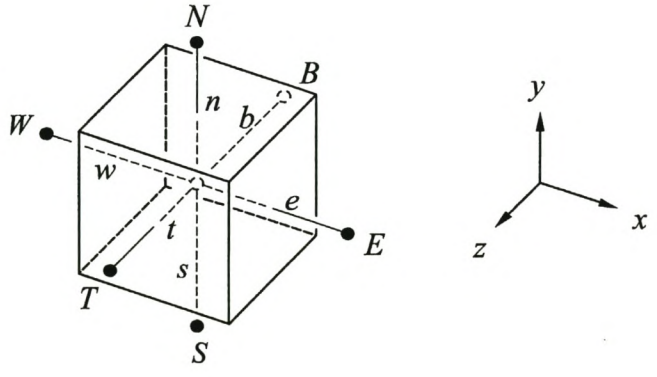

Figure 11.1 Three-dimensional finite volume.

11.4 Thermal quantities

Substituting the definition of an integral into the volume integral of a temperature and dropping the limits $\Delta x \to 0$, $\Delta y \to 0$ and $\Delta z \to 0$, yields:

$$\int_{V_\gamma} T \, \mathrm{d}V = \sum_{V_\gamma} T \Delta x \Delta y \Delta z \, . \tag{11.7}$$

Evaluating the y-direction spatial temperature derivative from a piecewise linear temperature profile between grid points yields:

$$\frac{\partial T}{\partial y} = \frac{1}{2}\left(\frac{T_N - T_P}{\delta y_n} + \frac{T_P - T_S}{\delta y_s} \right), \tag{11.8}$$

where subscripts N and S refer to neighbouring grid points and δy_n and δy_s are the one-dimensional finite volume dimensions, as shown in the one-dimensional finite volume in Figure 11.2. Substituting Equation (11.8) and the definition of an integral into the volume integral of the temperature spatial derivative, and dropping the limits $\Delta x \to 0$, $\Delta y \to 0$ and $\Delta z \to 0$ yields:

$$\int_{V_\gamma} \frac{\partial T}{\partial y} \, \mathrm{d}V = \frac{1}{2} \sum_{V_\gamma} \left(\frac{T_N - T_P}{\delta y_n} + \frac{T_P - T_S}{\delta y_s} \right) \Delta x \Delta y \Delta z \, . \tag{11.9}$$

Using Equation (11.9), heat flux across the interface between the two phases is given by:

$$\int_{A_{sf}} \left(k \nabla T \right)_\gamma \cdot \boldsymbol{n}_{\gamma\varphi} \, \mathrm{d}A = \sum_{A_{sf}} \left[\frac{k_{12}}{\delta x} (T_1 - T_2) \Delta y \Delta z \right] + \sum_{A_{sf}} \left[\frac{k_{12}}{\delta y} (T_1 - T_2) \Delta x \Delta z \right] + \sum_{A_{sf}} \left[\frac{k_{12}}{\delta z} (T_1 - T_2) \Delta x \Delta y \right] , \tag{11.10}$$

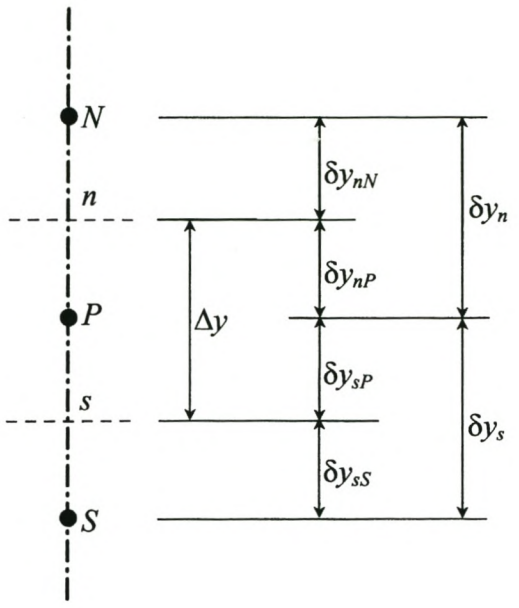

Figure 11.2 One-dimensional finite volume.

where $\gamma = s$ and $\varphi = f$, or *vice versa*, and where the grid points 1 and 2 are as shown in Figure 11.3 to be on either side of the interface. Depending on the orientation of the interface, grid point 1 is on the eastern, southern or bottom side and grid point 2 is respectively on the western, northern or top side. The thermal conductivity k_{12} at the interface is given in terms of the thermal conductivities at grid points 1 and 2 by:

$$k_{12} = \frac{\delta m}{\frac{\delta m_1}{k_1} + \frac{\delta m_2}{k_2}}, \tag{11.11}$$

where $m = x$, y or z.

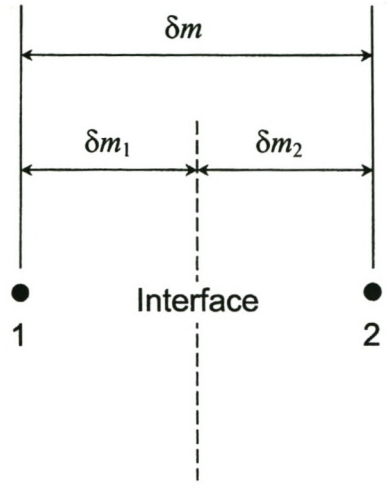

Figure 11.3 Grid points at the interface between two phases.

11.5 Temperature distribution conditions

Substituting Equation (11.10) into Condition (4.3) yields:

$$\sum_{A_{sf}}\left[\frac{k_{12}}{\delta x}\left(T_{e,1}-T_{e,2}\right)\Delta y\,\Delta z\right]+\sum_{A_{sf}}\left[\frac{k_{12}}{\delta y}\left(T_{e,1}-T_{e,2}\right)\Delta x\,\Delta z\right]+$$

$$\sum_{A_{sf}}\left[\frac{k_{12}}{\delta z}\left(T_{e,1}-T_{e,2}\right)\Delta x\,\Delta y\right]=0\,. \qquad (11.12)$$

Substituting Equation (11.7) into Condition (4.4) yields:

$$\sum_{V_s}T_e\,\Delta x\,\Delta y\,\Delta z=\sum_{V_f}T_e\,\Delta x\,\Delta y\,\Delta z\,. \qquad (11.13)$$

Substituting Equation (11. 10) into Condition (4.8) yields:

$$\sum_{A_{sf}}\left[\frac{k_{12}}{\delta x}\left(T_{nd,1}-T_{nd,2}\right)\Delta y\,\Delta z\right]+\sum_{A_{sf}}\left[\frac{k_{12}}{\delta y}\left(T_{nd,1}-T_{nd,2}\right)\Delta x\,\Delta z\right]+$$

$$\sum_{A_{sf}}\left[\frac{k_{12}}{\delta z}\left(T_{nd,1}-T_{nd,2}\right)\Delta x\,\Delta y\right]=0. \qquad (11.14)$$

Substituting Equation (11.7) into Condition (4.9) yields:

$$\sum_{V_s}T_{nd}\,\Delta x\,\Delta y\,\Delta z=\sum_{V_f}T_{nd}\,\Delta x\,\Delta y\,\Delta z. \qquad (11.15)$$

Substituting Equation (11.9) into Condition (4.13), where $m = y$ yields:

$$k_s\sum_{V_s}\left[\left(\frac{T_{nd,N}-T_{nd,P}}{\delta y_n}+\frac{T_{nd,P}-T_{nd,S}}{\delta y_s}\right)\Delta x\,\Delta y\,\Delta z\right]=$$

$$-k_f\sum_{V_f}\left[\left(\frac{T_{nd,N}-T_{nd,P}}{\delta y_n}+\frac{T_{nd,P}-T_{nd,S}}{\delta y_s}\right)\Delta x\,\Delta y\,\Delta z\right]. \qquad (11.16)$$

11.6 Equilibrium and non-equilibrium thermal conductivities

The gradients in the phasial volume-averaged temperature in Equation (11.2) and Equation (11.3) are approximated by:

$$\frac{\partial\langle T\rangle_\gamma}{\partial y}=\frac{\varepsilon_\gamma\left(\overline{T}_{\gamma,n}-\overline{T}_{\gamma,s}\right)}{d}, \qquad (11.17)$$

where $\gamma = s$ or f, d is the characteristic dimension of the RUC shown in Figure 9.1, and $\overline{T}_{\gamma,n}$ and $\overline{T}_{\gamma,s}$ are the mean boundary temperatures specified at the northern and southern boundaries respectively of the RUC.

Substituting the definition for a phasial volume-averaged quantity [Definition (II.3)] and the discretised form of the volume integral of a temperature spatial derivative [Equation (11.9)] into the numerators of Equation (11.2) and Equation (11.3) and substituting Equation (11.17) into the denominators of Equation (11.2) and Equation (11.3), yields the discretised form of the equilibrium thermal conductivity:

$$k_{\gamma,e} = \frac{d\,k_\gamma \sum_{V_\gamma} \left[\left(\frac{T_{e,N} - T_{e,P}}{\delta y_n} + \frac{T_{e,P} - T_{e,S}}{\delta y_s} \right) \Delta x \, \Delta y \, \Delta z \right]}{2 \left(\sum_s \Delta x \, \Delta y \, \Delta z + \sum_f \Delta x \, \Delta y \, \Delta z \right) \varepsilon_\alpha \left(\overline{T}_{e,\gamma,n} - \overline{T}_{e,\gamma,s} \right)} \tag{11.18}$$

and the non-equilibrium thermal conductivity:

$$k_{\gamma,nd} = \frac{d\,k_\gamma \sum_{V_\gamma} \left[\left(\frac{T_{nd,N} - T_{nd,P}}{\delta y_n} + \frac{T_{nd,P} - T_{nd,S}}{\delta y_s} \right) \Delta x \, \Delta y \, \Delta z \right]}{2 \left(\sum_s \Delta x \, \Delta y \, \Delta z + \sum_f \Delta x \, \Delta y \, \Delta z \right) \varepsilon_\alpha \left(\overline{T}_{nd,\gamma,n} - \overline{T}_{nd,\gamma,s} \right)}. \tag{11.19}$$

11.7 Grid layout

A length of one unit was arbitrarily selected for the RUC characteristic length d, shown in Figure 9.1. The volume of the RUC was divided into 8000 (20 × 20 × 20) finite volumes of similar dimensions.

11.8 Thermal boundary conditions

In order to create a one-dimensional phasial volume-averaged temperature gradient in the y-direction within the RUC, boundary temperatures were specified along the boundaries of the RUC normal to the y-direction while boundaries normal the x- and the z-directions were thermally insulated (zero heat flux across these boundaries).

The equilibrium temperature distribution in Equation (11.18) was established in the RUC by specifying two different arbitrarily selected uniform temperature distributions at the northern and southern boundaries respectively of the RUC. The mean boundary temperatures at the northern boundary in Equation (11.18), namely $\overline{T}_{e,s,n}$ and $\overline{T}_{e,f,n}$, are equal to the specified uniform temperature at that boundary. Similarly, the mean boundary temperatures at the southern boundary, $\overline{T}_{e,s,s}$ and $\overline{T}_{e,f,s}$, are equal to the specified uniform temperature at that boundary.

For determining the non-equilibrium thermal conductivity, linear temperature distributions were specified in each phase. Figure 11.4 shows the temperature distributions at the northern boundary of the RUC. The distributions apply from the edges where they are indicated, to the diagonal broken line (*i.e.* the distribution has a mirror image about a vertical plane through the broken line). The mean boundary temperatures at the northern boundary, $\overline{T}_{nd,s,n}$ and $\overline{T}_{nd,f,n}$, in Equation (11.19) were determined by:

$$\overline{T}_{nd,\gamma,n} = \frac{\sum_{A_{\gamma,n}} T_{nd} \Delta x \Delta z}{\sum_{A_{\gamma,n}} \Delta x \Delta z}, \tag{11.20}$$

where $\gamma = s$ and f respectively, and $A_{s,n}$ and $A_{f,n}$ represent the surfaces of the solid and the fluid phases respectively at the northern boundary of the RUC.

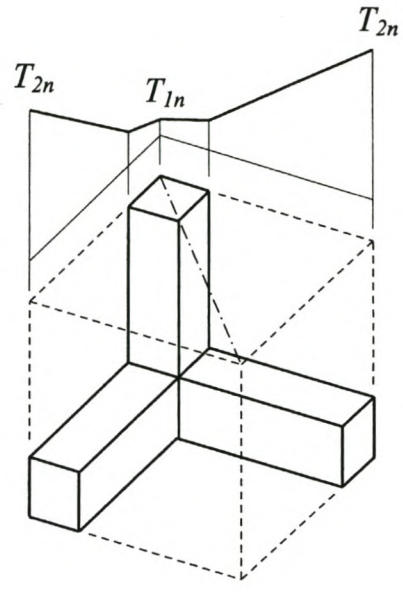

Figure 11.4 Northern boundary temperature on the RUC.

Figure 11.5 shows the temperature distributions at the southern boundary of the RUC. Similar to those at the northern boundary, the temperature distributions at the southern boundary apply from the edges where they are indicated, to the diagonal broken line. The mean boundary temperatures at the southern boundary, $\overline{T}_{nd,s,s}$ and $\overline{T}_{nd,f,s}$, in Equation (11.19) were determined by:

$$\overline{T}_{nd,\gamma,s} = \frac{\sum_{A_{\gamma,s}} T_{nd} \Delta x \Delta z}{\sum_{A_{\gamma,s}} \Delta x \Delta z}, \tag{11.21}$$

where $\gamma = s$ or f respectively, and $A_{s,s}$ and $A_{f,s}$ represent the surfaces of the solid and the fluid phases respectively at the southern boundary of the RUC.

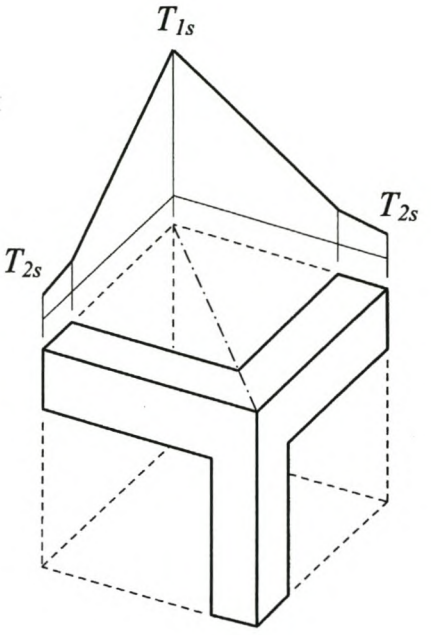

Figure 11.5 Southern boundary temperature on the RUC.

The gradients of the linear temperature distributions in Figure 11.4 and Figure 11.5 are inversely proportional to the thermal conductivity of the corresponding phases. Temperatures $T_{1,n}$ and $T_{1,s}$ in Figure 11.4 and Figure 11.5 were arbitrarily selected. Temperatures $T_{2,n}$ and $T_{2,s}$ were selected such that the solution of Equation (11.1) will satisfy Condition (11.14) to Condition (11.16).

11.9 Solution method

Equation (11.1) is discretised at the grid points using the finite volume method for conduction heat transfer of Patankar (1980). The direct solution algorithm presented by King (1976) was used to solve the temperature at each grid point.

11.10 Results

Multiple sets of data for the equilibrium and non-equilibrium thermal conductivities were obtained from Equation (11.18) and Equation (11.19), following the computational solution of Equation (11.1) with RUC properties in the range: $0.8 < \varepsilon_f < 0.98$ and $0.0001 < \frac{k_f}{k_s} < 0.1$. Using Definition (6.18) and Definition (6.19), Figure 11.6 to Figure 11.9 respectively show curves representing the calculated solid phase effective thermal conductivity k_{ss} relative to the solid phase thermal conductivity k_s, the solid phase coupled thermal conductivity k_{sf} relative to the solid phase thermal conductivity k_s, the fluid phase effective thermal conductivity k_{ff} relative to the fluid phase thermal conductivity k_f and the fluid phase coupled thermal conductivity k_{fs} relative to the fluid phase thermal conductivity k_f. Each of the relative effective and coupled thermal conductivities are shown as a function of porosity ε_f at four different thermal conductivity ratios. Each curve represents the thermal conductivity ratio $\frac{k_f}{k_s}$ indicated next to the curve.

The curves in Figure 11.6 to Figure 11.9 are sufficiently correlated by the following empirical relations:

$$k_{ss} = 0.5593 k_s \left(1.64 - \varepsilon_f\right) + 0.5618 k_f \left(\frac{\varepsilon_f}{1-\varepsilon_f}\right)^{0.2349}, \tag{11.22}$$

$$k_{sf} = \left(1.181 \varepsilon_f{}^2 - 2.505 \varepsilon_f + 1.315\right) k_f{}^{0.996} k_s{}^{0.004}, \tag{11.23}$$

$$k_{ff} = 0.6445 \frac{k_f{}^2}{k_s} \left(\varepsilon_f - 0.9610\right) + 1.816 k_f \varepsilon_f{}^2 - 3.285 k_f \varepsilon_f + 2.431 k_f \tag{11.24}$$

and:

$$k_{fs} = \left(-14.23 \varepsilon_f{}^2 + 22.64 \varepsilon_f - 9.615\right) \frac{k_f{}^2}{k_s} + 0.3277 k_f \left(\frac{\varepsilon_f}{1-\varepsilon_f}\right)^{0.5385}, \tag{11.25}$$

where thermal conductivities are in W/m·°C.

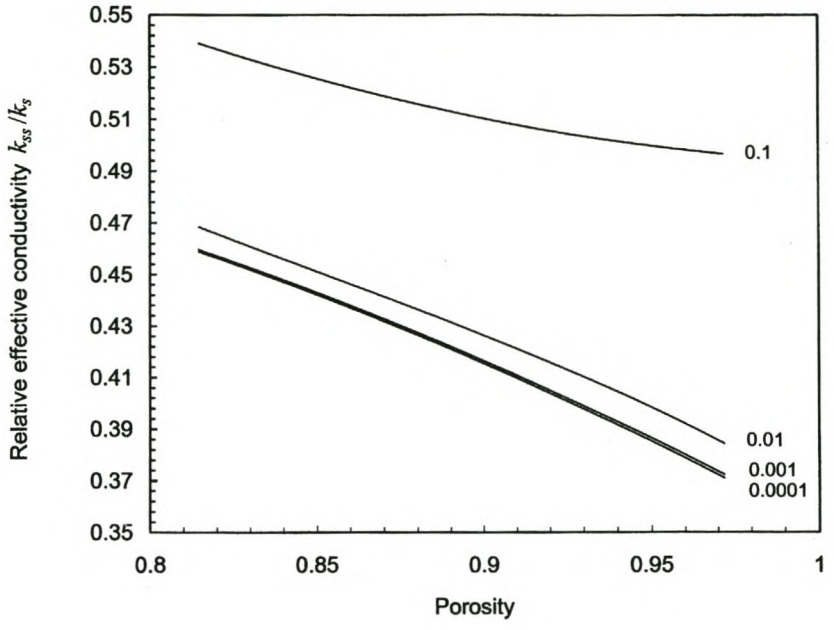

Figure 11.6 Solid phase effective thermal conductivity k_{ss} relative to the solid phase thermal conductivity k_s as a function of porosity ε_f at four different thermal conductivity ratios.

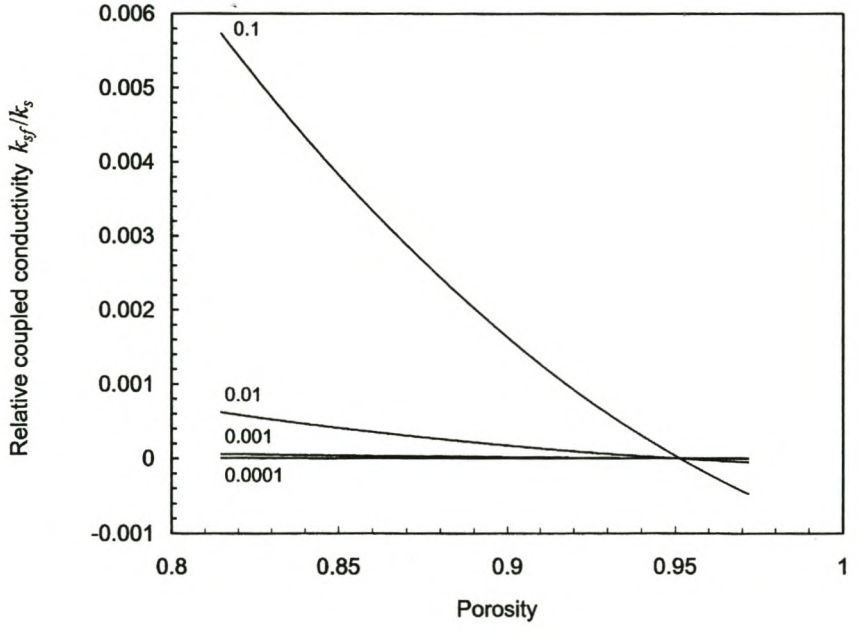

Figure 11.7 Solid phase coupled thermal conductivity k_{sf} relative to the solid phase thermal conductivity k_s as a function of porosity ε_f at four different thermal conductivity ratios.

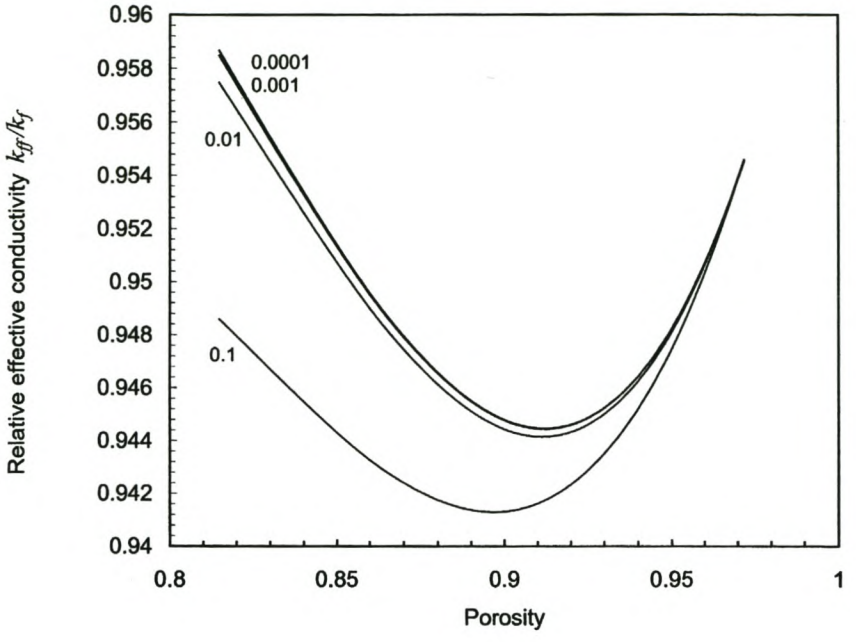

Figure 11.8 Fluid phase effective thermal conductivity k_{ff} relative to the fluid phase thermal conductivity k_f as a function of porosity ε_f at four different thermal conductivity ratios.

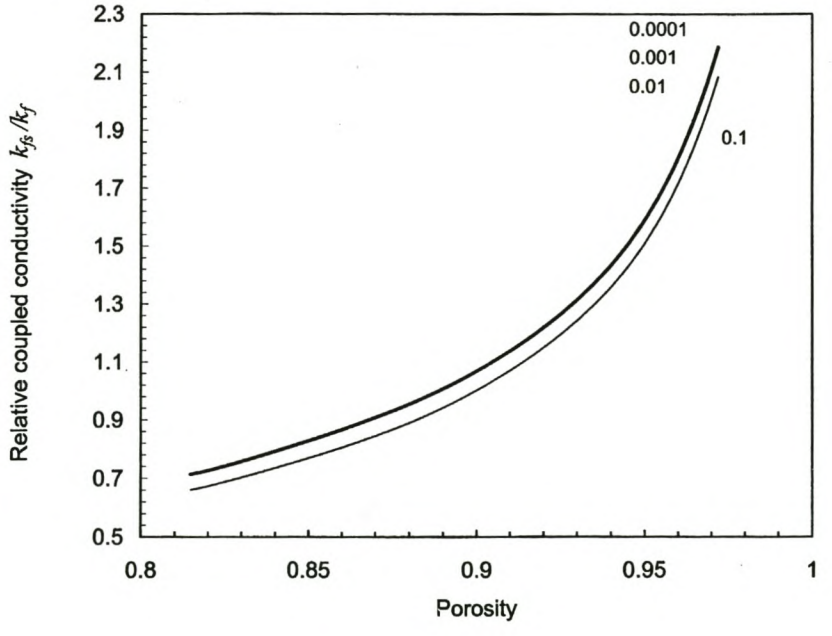

Figure 11.9 Fluid phase coupled thermal conductivity k_{fs} relative to the fluid phase thermal conductivity k_f as a function of porosity ε_f at four different thermal conductivity ratios.

Tendencies shown by the curves in Figure 11.7 and Figure 11.9 are consistent with comments made in the Section 6.4. Since these curves present the coupled thermal conductivities at high porosities only (*i.e.* high fluid phase volume fraction ε_f or low solid phase volume fraction ε_s), the solid phase and the fluid phase coupled thermal conductivities, respectively shown in Figure 11.7 and Figure 11.9, both show weak dependency on the solid phase thermal conductivity. In fact, Equation (11.23) describes the ratio $\frac{k_{sf}}{k_f}$ as being completely independent of the solid phase thermal conductivity.

Figure 11.10 to Figure 11.17 show the correlations between data from the solutions of Equation (11.18) and Equation (11.19), presented by dots, and that predicted by Equation (11.22) to Equation (11.25), presented by lines. The figures show the effective and coupled thermal conductivities of 6061 aluminium foam and air, and 6061 aluminium foam and water, as functions of the porosity ε_f. The thermal conductivity of 6061 aluminium foam, air and water is 156.0 W/m·°C, 0.026 W/m·°C and 0.6 W/m·°C respectively.

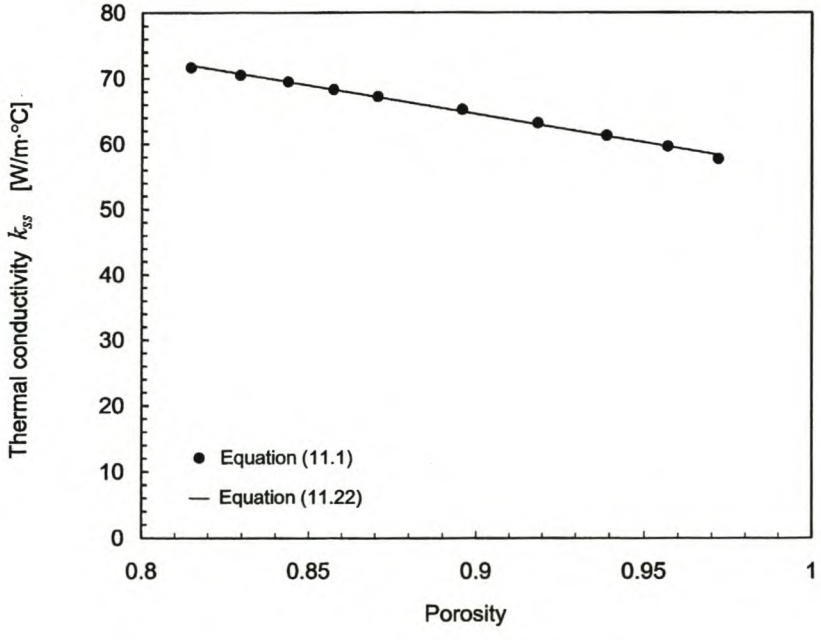

Figure 11.10 Solid phase effective thermal conductivity k_{ss} for 6061 aluminium foam and air.

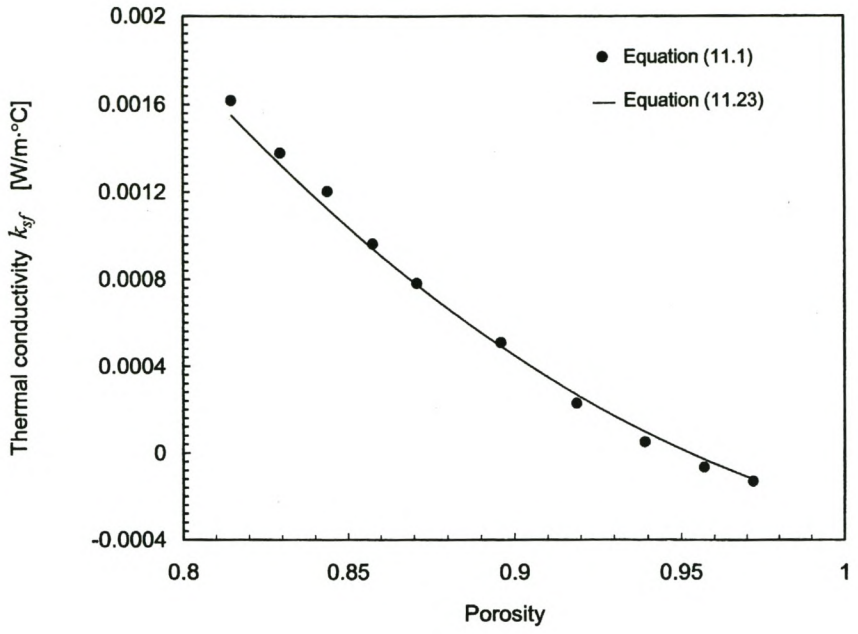

Figure 11.11 Solid phase coupled thermal conductivity k_{sf} for 6061 aluminium foam and air.

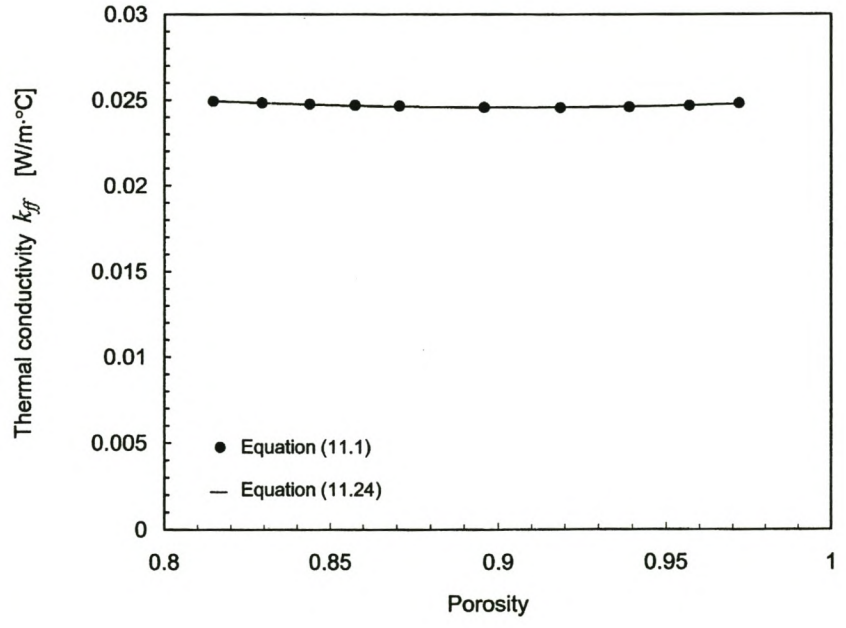

Figure 11.12 Fluid phase effective thermal conductivity k_{ff} for 6061 aluminium foam and air.

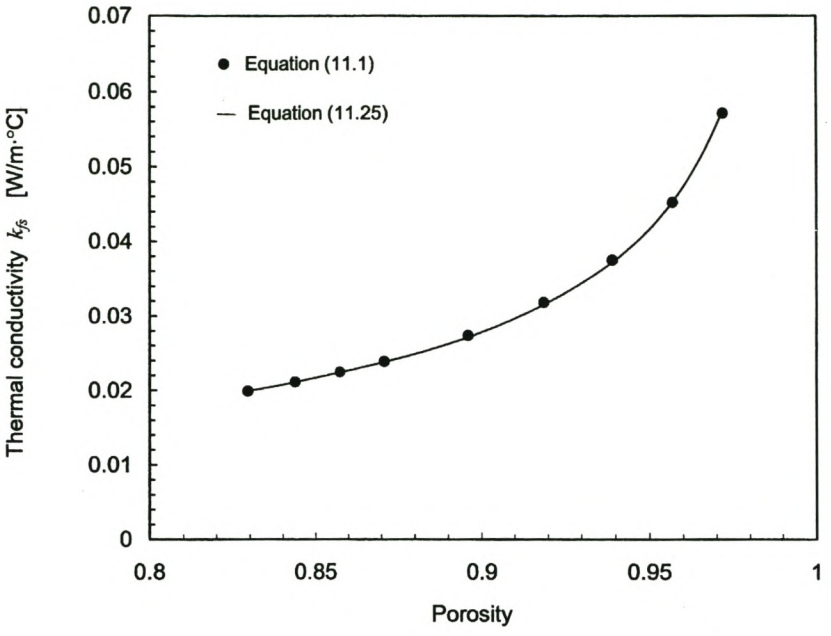

Figure 11.13 Fluid phase coupled thermal conductivity k_{fs} for 6061 aluminium foam and air.

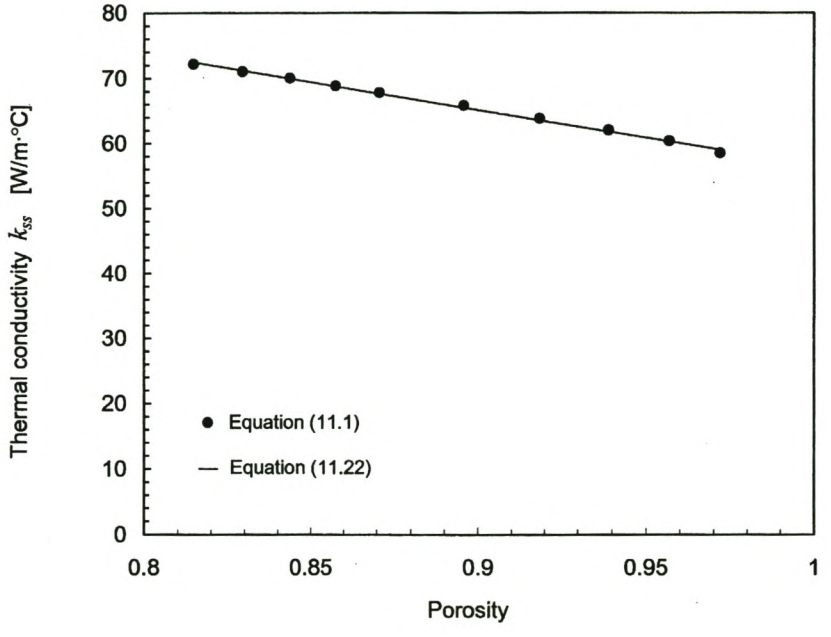

Figure 11.14 Solid phase effective thermal conductivity k_{ss} for 6061 aluminium foam and water.

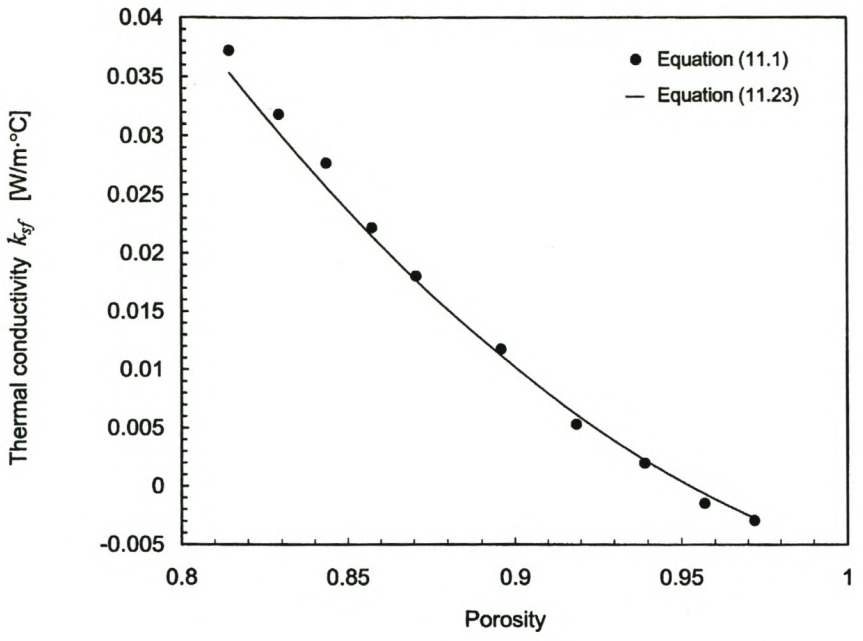

Figure 11.15 Solid phase coupled thermal conductivity k_{sf} for 6061 aluminium foam and water.

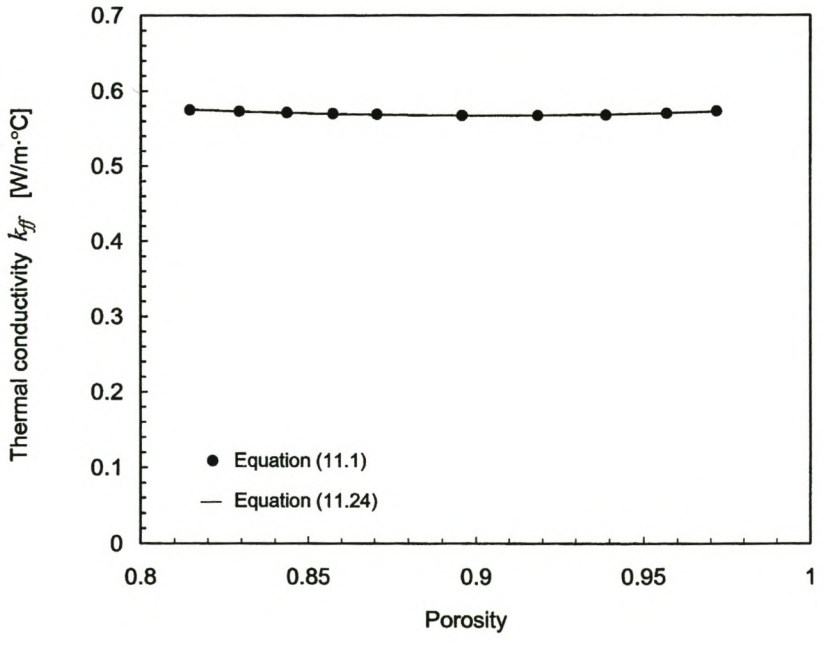

Figure 11.16 Fluid phase effective thermal conductivity k_{ff} for 6061 aluminium foam and water.

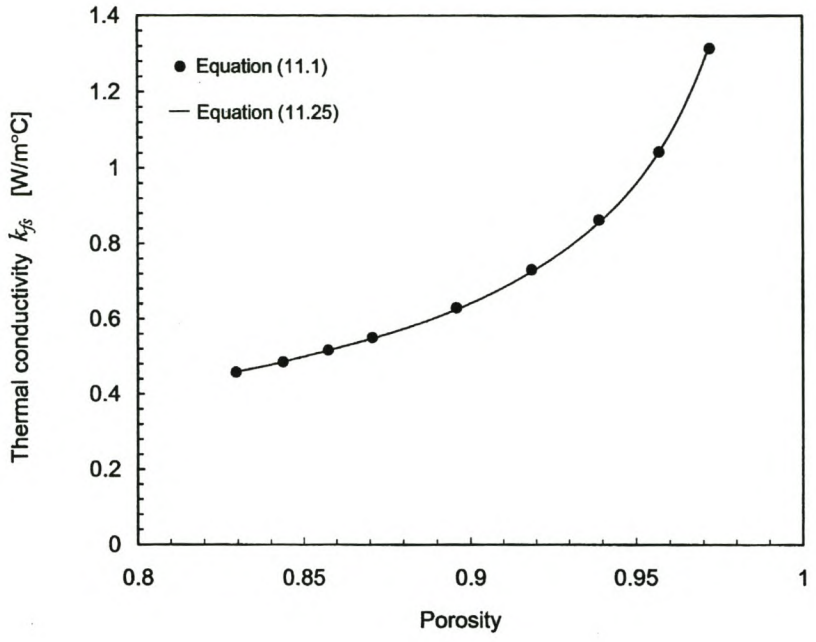

Figure 11.17 Fluid phase coupled thermal conductivity k_{fs} for 6061 aluminium foam and water.

11.11 Evaluation

The conduction model, together with the definitions for the equilibrium and non-equilibrium thermal conductivities, and the definitions for the effective and coupled thermal conductivities, is a novel approach introduced in this study. No other attempts have been made to determine these quantities by analytical, experimental or computational methods.

However, consider for now the scalar version of the expression within the parenthesis of Expression (6.24):

$$\varepsilon_s k_{ss} + \varepsilon_f k_{sf} + \varepsilon_f k_{ff} + \varepsilon_s k_{fs} . \tag{11.26}$$

Expression (6.30) shows that Expression (11.26) is the classic definition of the overall thermal conductivity k_o of a two-phase system with the phases in thermal equilibrium (Nozad *et. al.*, 1985).

The overall thermal conductivity k_o was determined experimentally for T6201 aluminium foam (Calmidi and Mahajan, 1999) and theoretically for high thermal conductivity fibrous materials (Bauer, 1993) and cellular foams (Hsu, 1994). These results were compared to values for Expression (11.26). Figure 11.18 shows the comparison for T6201 aluminium foam and air, as a function of porosity ε_f. Figure 11.19 shows the same comparison for T6201 aluminium foam and water. The thermal conductivity of T6201 aluminium foam, air and water is 218.0 W/m·°C, 0.026 W/m·°C and 0.6 W/m·°C respectively.

Figure 11.18 and Figure 11.19 also show a curve representing an analytical expression developed by Mickley in Combarnous and Bories (1975) for a two-phase geometric configuration similar to the RUC for cellular foams shown in Figure 9.1. That expression

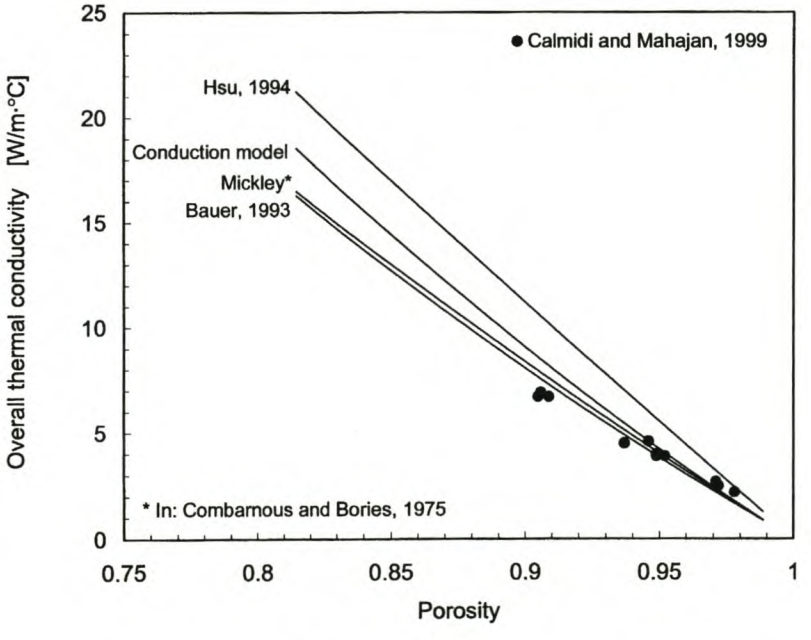

Figure 11.18 Overall thermal conductivity k_o for T6201 aluminium foam and air.

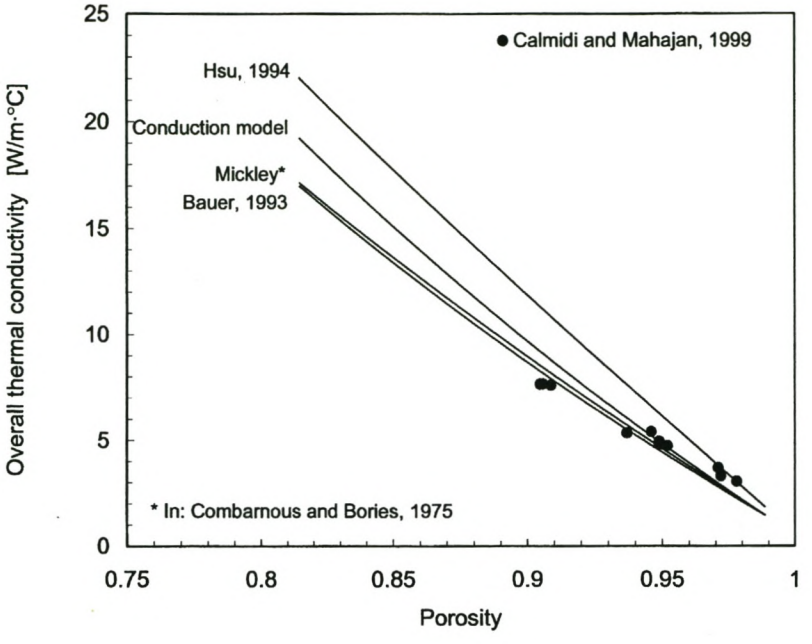

Figure 11.19 Overall thermal conductivity k_o for T6201 aluminium foam and water.

is based on the hypothesis of parallel local heat fluxes. The expression was incorrectly quoted by Combarnous and Bories (1975) where it should read:

$$k_o = k_f\left(\frac{f}{d}\right)^2 + k_s\left(1-\frac{f}{d}\right)^2 + \frac{2k_f k_s \frac{f}{d}\left(1-\frac{f}{d}\right)}{k_s\frac{f}{d} + k_f\left(1-\frac{f}{d}\right)}. \qquad (11.27)$$

CHAPTER 12

INTERPHASIAL HEAT TRANSFER COEFFICIENT

12.1 Overview

In this chapter, the interphasial heat transfer coefficient h_{sf} (introduced by the interphasial heat transfer model in Section 5.2) is quantified for metallic foams in terms of flow parameters, fluid phase thermophysical properties and metallic foam morphological parameters. Expressions are derived for low Reynolds number flow where conductive heat transfer in the fluid is predominant, as well as for high Reynolds number flow where heat transfer associated with flow recirculation is predominant. The expressions are unified into a single expression which applies to low and high Reynolds number flow. In the formulation of these expressions, general flow patterns on a solid body are considered in heat transfer modelling between the fluid and the foam microstructure.

12.2 Heat transfer associated with general flow patterns on a solid body in cross flow

The interphasial heat transfer coefficient h_{sf} is defined in Equation (5.4) as the ratio between the net heat transfer per interface area between two phases in an REV (representative elementary volume, discussed in Section II.2), and the difference between the intrinsic volume-averaged temperatures of each phase. This ratio is in a fixed relation for a two-phase system of specific geometry and thermal conductivities.

In quantifying the interphasial heat transfer coefficient h_{sf}, an evaluation of the surface integral in Equation (5.4) is subject to a description of actual temperature gradients at the

interface between the two phases in the metallic foam. Similar to velocity distributions on solid bodies in cross flow, temperature gradients depend on the local flow regime existing on the body, discussed in Section 10.3.

In low Reynolds number flow, heat transfer rates between a single solid body and a fluid are exclusively determined by the thermal conductivity of the fluid. Heat transfer on the upstream side of the body is generally higher than on the downstream side (Eckert and Soengen, 1952). In the case of multiple solid bodies in close proximity of each other, the flow area between the bodies also affects heat transfer rates.

In high Reynolds number flow, stable recirculation vortices forming behind the solid body facilitate access of fluid from outside the thermal boundary layer to the surface, increasing heat transfer sharply in the rear portion. With an even further increase of the Reynolds number, the variation of heat transfer acquires a new character under the influence of the transition from laminar to turbulent flow in the boundary layer.

Heat transfer is also influenced by turbulence of the main flow, mostly at the front of a body (Zukauskas, A. and Ziugzda, J., 1985, p. 208).

12.3 Modelling heat transfer in the RUC

The RUC for cellular foams (shown in Figure 9.1) provides a facility to extrapolate heat transfer knowledge from common flow systems to the microstructure of the metallic foam. The RUC shows the random inclination of strands to the mean flow direction represented by two prisms in cross flow and one prism aligned with the mean flow direction.

In the Darcy flow regime, where heat transfer is exclusively determined by fluid thermal conductivity and flow channel size, an equal contribution of all three prisms to the overall interphasial heat transfer is assumed. Following the work of Du Plessis *et al.* (1994) and Du Plessis and Van der Westhuizen (1993), it is assumed that heat transfer at the interface

between the phases complies with constant heat flux experienced in Poiseuille flow at a mean RUC velocity v_p, between parallel surfaces at a distance apart, which is equal to the characteristic pore width d_p.

In the Forchheimer flow regime (Forchheimer, 1901) it is assumed that the mean interphasial heat transfer on the prism aligned with the mean flow direction complies with laminar developing flow on a flat plate over a distance equal to the characteristic pore width d_p, under a mean velocity equal to the pore velocity v_p.

The largest contribution to heat transfer in Forchheimer flow comes from the two prisms in cross flow. It is assumed that heat transfer behaviour on these two prisms is equivalent to that on a cylinder in cross flow. A corresponding flow regime is represented by a cylinder diameter referred to as the *representative hydraulic diameter* (RHD). The effect on heat transfer of non-cylindrical cross sections and material clustering at the vertices of strands is accounted for by the RHD.

In order to assess the validity of this assumption, a general discussion on the conceptual representation of heat transfer on solid bodies, with reference to heat transfer on a cylinder, is presented.

The following power equation based on a functional dimensionless relation is commonly used for the generalisation of experimental heat transfer data on solid bodies in high Reynolds number cross flow (Holman, 1980):

$$Nu = cRe^m Pr^n. \tag{12.1}$$

This expression has been useful for quantifying heat transfer on objects of many different shapes, including prismatic bodies and cylinders aligned perpendicular and inclined to the flow direction. The equation applies for most ordinary gasses and liquids, except for liquid metals.

The onset of a specific flow regime is reflected in Equation (12.1) by a change in the value of the Reynolds number power index m. For a cylinder in cross flow, numerous

experimental results suggest m = 0.5 for a laminar boundary layer at low levels of turbulence (Tu < 1%) in the front part of the cylinder (Zukauskas, 1987). For the rear part, the value of m varies from 0.5 to 0.8. Zukauskas and Ziugzda (1985) suggest an average value of m = 0.73 to be assumed for the rear part throughout.

When the cross-sectional shape of a prismatic body deviates from cylindrical, then the relative contributions of heat transfer associated with hydrodynamic behaviour at the front and the rear parts of a cylinder, also change. A change in these relative contributions manifests itself in the change of the mean value of the Reynolds number exponent m in Equation (12.1). This is evident from the findings of Jacob (1949) who reported a different value for m for a square bar in cross flow with two of the square sides aligned with the flow direction, and the same square bar in cross flow with a diagonal between two opposing corners aligned with the direction of flow. In general, the Reynolds number power index m varies between 0.59 and 0.78 for prismatic bodies of different cross-sectional shapes and orientations to the direction of flow.

An increase in turbulence involves an increase in the value of m in the front part of the cylinder and a decrease of m in the rear part of the cylinder. Zukauskas and Ziugzda (1985) report that at Tu > 12%, a practical constant value of m = 0.66 was observed for the whole circumference of a cylinder.

Most of the fluids used in practice have Prandtl numbers ranging from 1 to 1000. This means that in calculations of heat transfer, a wrong choice of the Prandtl number power index n may lead to considerable errors. A value of n varying between 0.31 and 0.33 for most commonly shaped objects is mostly accepted. This value is suggested by theoretical investigations of heat transfer in a laminar boundary layer on a plate. However, later calculations and experimental measurements have revealed the dependence of n on the flow regime in the boundary layer (Zukauskas, 1987). For a laminar boundary layer on a plate n = 0.33, but for a turbulent boundary layer it can amount up to 0.43.

Investigations also suggest certain changes in the value of the power index with large variations of Prandtl number. Numerical solutions of heat transfer in the region of the front stagnation point, performed by Zukauskas (1987), gave n = 0.37 for Pr < 10, and

$n = 0.35$ for $Pr > 10$. In later investigations of local heat transfer from a tube at a constant heat flux, it was determined that n varies along the tube perimeter, reaching a value of 0.39 in the rear (Katinas *et al.*, 1971). Detailed studies by Zukauskas (1987) of the mean heat transfer from a tube at constant wall temperature, in cross flow of oil, water and air, yielded an approximate value of n between 0.37 and 0.38. Further investigations by Zukauskas (1987) of heat transfer in 27 banks of tubes of different arrangements in flow of various fluids in the Prandtl number range from 0.7 to 500 suggest that, for the mean heat transfer of all sorts of banks, $n = 0.36$.

The value of n does not appear to vary with the degree of turbulence in the boundary layer (Zukauskas, 1987).

In flows of viscous fluids, the intensity of heat transfer markedly depends on physical property variations in the boundary layer. This is caused by the temperature difference between the main flow stream and the wall. Additional terms have been added to equations of the form of Equation (12.1) to compensate for property variation (*e.g.* Zukauskas and Ziugzda, 1985). However, since this study is limited to fluids of constant property, these terms will not be included. Furthermore, the relatively small amounts of heat conduction possible in the strands of metallic foams limit this temperature difference so that the effect of property variations can be neglected. This assumption is in agreement with Lu *et al.* (1998b) who concluded from the thermophysical property values of common fluids (*e.g.* air and water), that the heat transfer coefficient depends weakly on temperature.

The above suggests that in the Forchheimer flow region, the RUC for cellular foams, shown in Figure 9.1, together with the representative hydraulic diameter (RHD) hypothesis, is sufficient to relate interphasial heat transfer in a metallic foam to that on a cylinder of diameter equal to the RHD of that metallic foam.

As in the case of quantifying the viscous shear factor, it is assumed that the RHD is equal to the characteristic strand width d_s of the RUC, which is determined by the characteristic dimension d of the RUC and the porosity ε_f of the porous medium.

12.4 Dimensionless groups

The mean Nusselt number Nu is used as a dependent dimensionless parameter to present the heat flux and is defined as:

$$Nu \equiv \frac{h d_h}{k_f}, \tag{12.2}$$

where d_h is a characteristic dimension and k_f is the fluid thermal conductivity. The coefficient h is defined as:

$$h \equiv -\frac{1}{A_{sf}} \int_{A_{sf}} \frac{k_f \nabla T_f \cdot \boldsymbol{n}_{fs}}{\overline{T}_f - \overline{T}_s} \mathrm{d}A, \tag{12.3}$$

where A_{sf} is the interface area, $\boldsymbol{n}_{fs}$ is a normal surface unit vector, and $\overline{T}_f$ and $\overline{T}_s$ are mean fluid and solid temperatures respectively.

The Reynolds number Re, defined in Definition (10.15), relates diffusive and convective momentum transport in a fluid as:

$$Re \equiv \frac{\rho_f v d_h}{\mu}, \tag{10.15}$$

where ρ_f is the fluid density, v is the mean flow velocity and μ is the dynamic viscosity of the fluid.

The Prandtl number Pr, which relates diffusive momentum and heat transport in a fluid, is defined as:

$$Pr \equiv \frac{c_{p,f} \mu}{k_f}, \tag{12.4}$$

where $c_{p,f}$ is the isobaric specific heat capacity of the fluid.

12.5 Low Reynolds number heat transfer modelling in Poiseuille flow

For constant heat flux in Poiseuille flow, Shah and London (1978) proposed that:

$$Nu = 8.24, \tag{12.5}$$

where the Nusselt number Nu is based on the hydraulic dimension d_h for two parallel surfaces, given as:

$$d_h = 2\, d_p. \tag{12.6}$$

12.6 High Reynolds number laminar flow heat transfer modelling on a flat surface

Polhausen (1921) used the well-known Blasius solution (White, 1991, p. 234) to generate temperature profiles for various Prandtl numbers in laminar boundary layers. Deriving heat flux in the boundary layer from these profiles, the following correlation is a good curve fit for the local Nusselt number Nu_x at the downstream distance x from the leading edge, in the Prandtl number range $10^{-1} < \mathrm{Pr} < 10^4$ (White, 1991, p. 241):

$$Nu_x = 0.332\, Re_x^{0.5} Pr^{0.33}. \tag{12.7}$$

The average Nusselt number Nu over the range from $x = 0$ to $x = L$ is obtained by integrating the local Nusselt number over that range, yielding:

$$Nu = 2Nu_{x=L} = 0.664\, Re_L^{0.5} Pr^{0.33}. \tag{12.8}$$

Although free stream turbulence influences the transition from a laminar to a turbulent boundary layer it does not affect heat transfer within a laminar boundary layer.

12.7 High Reynolds number heat transfer modelling on a cylinder in cross flow

Zukauskas and Ziugzda (1985) recommended the following correlation for predicting the Nusselt number on a cylinder in crossflow in the range $40 < Re < 1000$:

$$Nu = 0.52\, Re^{0.5}\, Pr^{0.37}, \tag{12.9}$$

where the Nusselt number Nu and the Reynolds number Re are based on a hydraulic dimension equal to the cylinder diameter.

The original expression for predicting the Nusselt number includes a term that accounts for thermophysical fluid property variation in the boundary layer, caused by the temperature difference between the main flow stream and the wall. That term is not included here for reasons discussed in Section 12.3.

12.8 Turbulence enhancement of heat transfer in cross flow

Turbulence intensity in flow through a metallic foam has its origin in the vortex shedding behind the strands of the solid structure. Since turbulence intensity enhances heat transfer, it can be assumed that at the leading strands of a porous domain (*i.e.* at the entry of streamlined flow), the average heat transfer is less than on downstream strands. Similar observations were made by Zukauskas (1987) regarding heat transfer from the leading tube rows in a bank of tubes, at $Re > 10^4$. A relationship proposed by Gnielinski *et al.* (1987, p. 2.5.3-1) for predicting the enhancing effect of turbulence on heat transfer in a staggered tube bundle is used here to predict the turbulence enhancement in metallic foams.

For the staggered tube bundle arrangement shown in Figure 12.1, a turbulence enhancement factor f_t is given as:

$$f_t = 1 + \frac{2d_t}{3s}. \tag{12.10}$$

In the application of Equation (12.10) to a metallic foam microstructure, the tube diameter d_t is substituted by the RHD and the ratio $\frac{d_t}{s}$ is varied to match the porosity of the metallic foam. It is however important to note that the RUC for cellular foams (shown in Figure 9.1) shows only two thirds of the solid phase volume fraction [defined by Definition (II.1)] contributing to vortex shedding. Substituting the RHD by the characteristic strand width d_s and using Equation (9.11), it follows that:

$$f_t = 1 + \frac{32}{9\pi}\frac{1-\varepsilon_f}{\chi - 1}. \tag{12.11}$$

Figure 12.2 shows the turbulence enhancement factor f_t as a function of porosity ε_f.

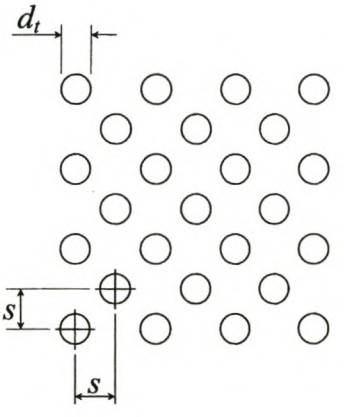

Figure 12.1 Geometry in a staggered tube arrangement.

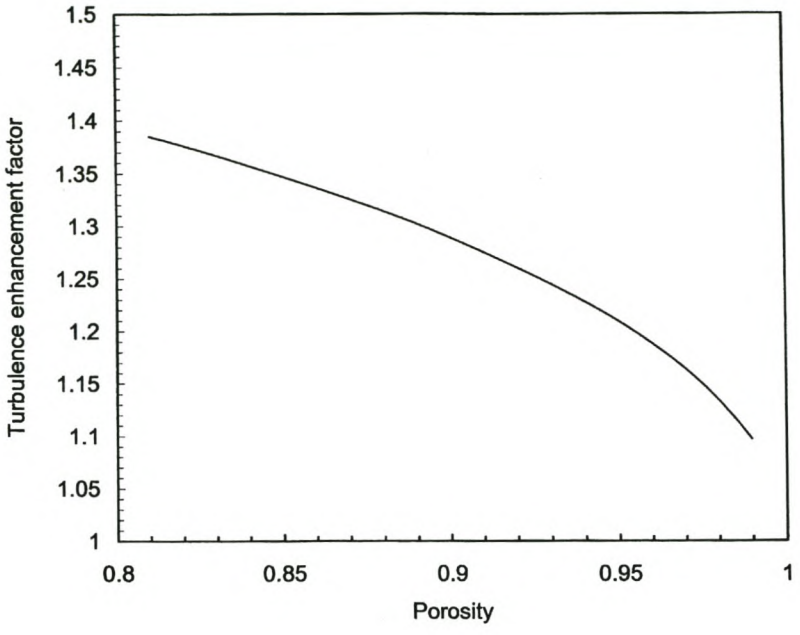

Figure 12.2 Turbulence enhancement factor f_t.

12.9 Interphasial heat transfer coefficient in the Darcy flow regime

Substituting Definition (12.3) into Equation (5.4), assuming that the mean fluid and solid temperatures, $\overline{T}_f$ and $\overline{T}_s$ are respectively represented by their intrinsic volume-averaged temperatures, and then substituting Equation (12.2), Equation (12.5), Equation (12.6) and Equation (9.9), yields the interphasial heat transfer coefficient h_{sf} in terms of the RUC characteristic dimension d and the tortuosity χ:

$$h_{sf,low\,Re} = \frac{8.24 k_f}{d(3-\chi)}. \tag{12.12}$$

At low Reynolds number flow, the effect of turbulence caused by recirculation and vortex shedding can be neglected.

12.10 Interphasial heat transfer coefficient in the Forchheimer flow regime

Observation of the RUC for cellular foams, shown in Figure 9.1, suggests that the mean interphasial heat transfer coefficient in the Forchheimer flow regime can be given as:

$$h_{sf} = \frac{1}{3} h_{sf||} + \frac{2}{3} h_{sf\perp}, \tag{12.13}$$

where $h_{sf\,||}$ is the mean heat transfer coefficient on the prism aligned with the flow direction and $h_{sf\perp}$ is the mean heat transfer coefficient on the prisms perpendicular to the flow direction.

Substituting Definition (12.3) into Equation (5.4), assuming that the mean fluid and solid temperatures, $\overline{T}_f$ and $\overline{T}_s$ are respectively represented by their intrinsic volume-averaged temperatures, and then substituting Equation (12.8) and Equation (12.9) into Equation (12.13) together with Equation (12.11), and using Definition (10.15), Definition (12.4) and Equation (9.7), yields the following expression for the interphasial heat transfer coefficient h_{sf} at high Reynolds number flow:

$$h_{sf,high\,Re} = \left[0.49 \left({k_f}^{0.63} {c_{p,f}}^{0.37} \mu^{-0.13} \right) \left(1 + \frac{32}{9\pi} \frac{1-\varepsilon_f}{\chi - 1} \right) \sqrt{\frac{1}{\chi - 1}} + 0.313 \left({k_f}^{0.67} {c_{p,f}}^{0.33} \mu^{-0.17} \right) \sqrt{\frac{1}{3-\chi}} \right] \sqrt{\frac{\rho_f \chi \langle v \rangle_f}{\varepsilon_f d}}. \tag{12.14}$$

12.11 Unified model

Equation (12.12) and Equation (12.14) are predominant in the limits of low and high Reynolds number flow respectively. Solutions for intermediate Reynolds numbers between the limiting cases are determined by a superposition technique described by

Churchill and Usagi (1972). Visual inspection has revealed that a shifting exponent of two in the superposition technique yields a unified model for the interphasial heat transfer coefficient h_{sf} over the entire Reynolds number range of application, with a truthful transition between the Darcy and Forchheimer flow regimes, as shown in Figure 12.3. With a shifting exponent of two the unified model is given as:

$$h_{sf} = \sqrt{h_{sf,low\,Re}{}^2 + h_{sf,high\,Re}{}^2}\,. \tag{12.15}$$

Equation (12.15), together with Equation (12.12), and Equation (12.14) presents the interphasial heat transfer coefficient h_{sf} in terms of the thermophysical fluid properties, the phasial volume-averaged velocity $\langle v \rangle_f$, the porosity ε_f and the RUC characteristic dimension d.

Figure 12.3 shows the interphasial heat transfer coefficient h_{sf} for a metallic foam of porosity $\varepsilon_f = 0.9$ and characteristic RUC length $d = 5$ mm, in cross flow with air at STP (25 °C, 101325 N/m^2). At STP, $k_f = 0.026$ W/m·°C, $c_{p,f} = 1007$ J/kg·°C, $\rho_f = 1.184$ kg/m^3 and $\mu = 1.838\times10^{-5}$ kg/m·s. Figure 12.3 shows Equation (12.12), Equation (12.14) and the unified model given by Equation (12.15).

12.12 Evaluation

An evaluation of Equation (12.15) by a comparison to experimentally determined interphasial heat transfer coefficient values was considered. From its definition it follows that interphasial heat transfer coefficient values can be determined experimentally if the phasial volume-averaged temperatures of the solid and the fluid phases could be isolated. The spatial distribution of the microscopic solid phase temperature can be monitored through infrared imaging. A temperature resolution of 0.1 °C and spatial resolution of 0.175 mm/pixel are possible. Such fine resolution allows for a post-processing averaging procedure to be applied. The fluid phase volume-averaged temperature can be accurately determined from embedded thermocouples.

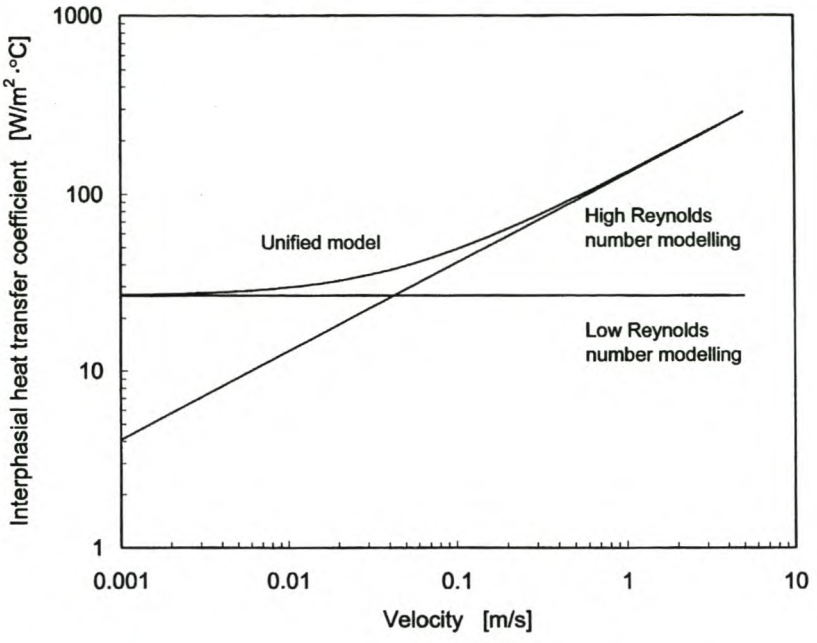

Figure 12.3 Interphasial heat transfer coefficient prediction at low Reynolds number flow, high Reynolds number flow, and the unified model for intermediate Reynolds number flow.

If conduction to or from a wall is used to create a non-equilibrium state (a transfer thermal non-equilibrium condition, as defined in Section III.2) then the contribution of the interphasial heat transfer component must be isolated from that of other heat transfer processes such as radiation, dispersion and conduction. This could be accomplished theoretically if reliable mathematical models existed for these processes. The effect of these processes could also be limited by using a source thermal non-equilibrium condition (as defined in Section III.2) instead of a transfer thermal non-equilibrium condition. Furthermore, using moderate heat loads limits temperatures and temperature gradients experienced in the experiment. This reduces radiation and conduction within the phases. Flow at sufficiently high Peclét numbers also reduces the effect of molecular thermal action in the fluid phase.

Two methods of applying a source thermal non-equilibrium condition by uniform heat generation in the solid phase of metallic foam samples were considered, namely induction heating and electrical resistance heating. Induction heating relies on electrical currents that are induced internally in the material to be heated. The so-called eddy currents dissipate energy and bring about heating. The basic components of an induction heating system are an induction coil, an alternating-current (ac) power supply and the work piece itself. The flow of ac current through the coil generates an alternating magnetic field, which cuts through the work piece. It is this alternating magnetic field, which induces the eddy currents that heat the work piece. However, because the magnitude of the eddy currents decreases from the surface of the work piece, uniform heating cannot be established throughout the metallic foam sample.

When an electrical potential difference is applied across a metallic foam sample, then strands longitudinal to the direction of the applied potential will be subjected to higher potential differences across their ends, than those oriented transverse to the direction of the applied potential, thereby creating locally non-uniform heating in the metallic foam sample.

From the outcome of these investigations the idea of an evaluation of Equation (12.15) by comparison to experimentally determined interphasial heat transfer coefficient values was abandoned.

However, the order of magnitude of results from Equation (12.15) is verified by a comparison to the heat transfer coefficient of a cylindrical tube bundle. The tube bundle heat transfer coefficient is predicted using the correlations of Zukauskas (1987), given as:

$$Nu = 1.04 n_g \, Re^{0.4} \, Pr^{0.36} \tag{12.16}$$

for $1.6 < Re < 40$ and as :

$$Nu = 0.71 n_g \, Re^{0.5} \, Pr^{0.37}, \tag{12.17}$$

for $40 < Re < 1000$, where n_g is a correction factor for the angle of inclination of the tube bundle.

The Nusselt numbers *Nu* and Reynolds numbers *Re* are based on the tube diameter. The Reynolds numbers *Re* is also based on a reference flow velocity given by:

$$v_{ref} = v_o \frac{1-\left(\frac{d_t}{w}\right)^2}{1-\frac{\pi}{4}\frac{d_t}{w}}. \tag{12.18}$$

The ratio $\frac{d_t}{w}$ relates the tube diameter d_t to a representative channel width w, which can be approximated by:

$$\frac{d_t}{w} \approx \varepsilon_s. \tag{12.19}$$

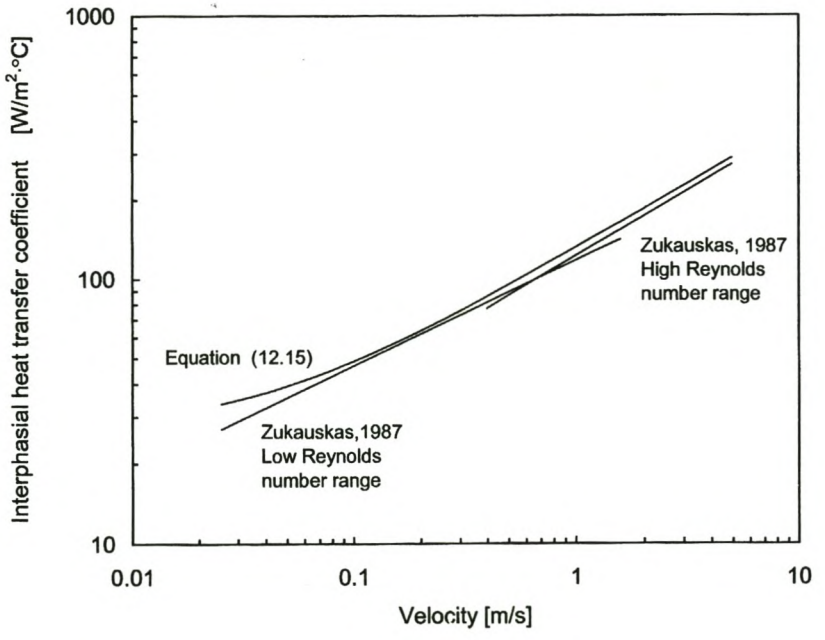

Figure 12.4 Comparison between the interphasial heat transfer coefficient prediction for a metallic foam, and that of a tube bundle.

Figure 12.4 shows good order of magnitude agreement between Equation (12.15) and the low and high Reynolds number correlations of Zukauskas. The foam morphological parameters, and thermophysical and flow parameters are the same as those used in Figure 12.3. The tube diameter that was used is equal to the RHD of the metallic foam, namely 0.979 mm. For a random orientation, the statistical mean angle of attack is 60° (90° being the angle of attack when the tubes are aligned perpendicular to the flow stream). At a 60° angle of attack, Zukauskas (1987) suggests $n_g = 0.89$.

CHAPTER 13

MOMENTUM AND THERMAL DISPERSION COEFFICIENTS

13.1 Overview

In this chapter, the momentum and thermal dispersion tensors (introduced by the dispersion model in Section 7.3) are quantified for metallic foams in terms of flow parameters, fluid phase thermophysical properties and foam morphology parameters. Deriving expressions for longitudinal and transverse dispersion of momentum and energy from the RUC for cellular foams (shown in Figure 9.1) has proved to be too challenging for this study. Instead, empirical expressions for longitudinal and transverse dispersion in continuous randomly orientated fibres, obtained from literature, are evaluated for application to metallic foams. Evaluation is done by comparing experimentally measurement dispersion parameters for metallic foams of various porosity and cell size configurations, to those predicted by the empirical expressions.

The momentum and thermal dispersion tensors retain their diagonal tensor form (as introduced in Section 7.3) even for isotropic metallic foams, since their component values in the principal directions are functions of the directional phasial volume-averaged velocity vector $\langle \boldsymbol{v} \rangle_f$.

13.2 Transverse and longitudinal dispersion components

Although generally accepted in literature (Kaviany, 1995), the 'diffusion-like' conceptual representation of longitudinal dispersion is somewhat misleading. Firstly, in an Eulerian coordinate system, the effect of longitudinal dispersion can only be observed under

transient conditions. The longitudinal dispersion coefficient therefore reduces to zero under steady-state conditions.

Secondly, consider Figure 13.1 showing the transient diffusion-like behaviour in a La Grange coordinate system (moving with the flow) of an intensive quantity ϕ (velocity, temperature or concentration). The flow direction is from left to right through a stationary porous medium. It shows the transport of the corresponding extensive quantity (momentum, energy or mass) in an upstream direction (to the left) and in a downstream direction (to the right).

However, true transient behaviour of the same initial distribution of the intensive quantity moving through a porous medium resembles more the kind of behaviour shown in Figure 13.2. In view of the behaviour shown in Figure 13.2, the mechanism of mechanical dispersion cannot transport the corresponding extensive quantity (momentum, energy or mass) in a downstream direction (to the right). Furthermore, in an upstream direction (to

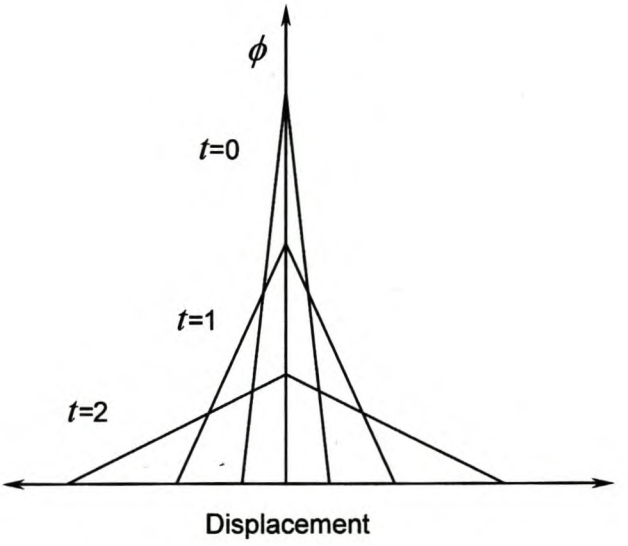

Figure 13.1 'Diffusion-like' transient behaviour of an intensive quantity ϕ in a La Grange coordinate system during flow through a porous medium.

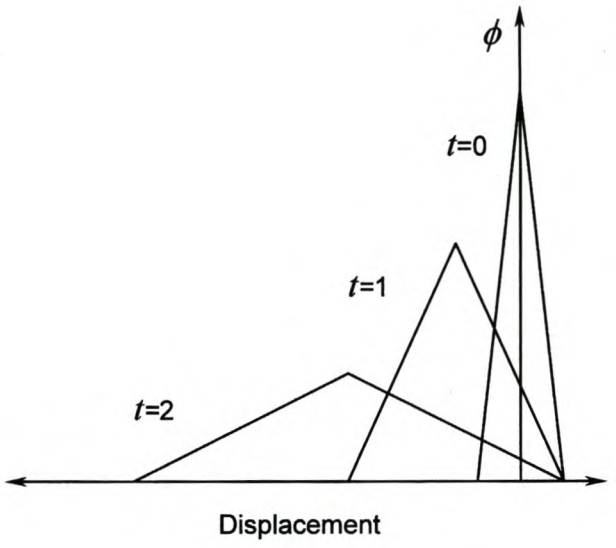

Figure 13.2 True 'convection-like' transient behaviour of an intensive quantity ϕ in a La Grange coordinate system.

the left), the rate of transport of the extensive quantity is limited to that of the flow velocity through the porous medium.

Therefore, transient behaviour of the extensive quantity resembles that of convection, in a direction opposite to the main flow direction. In this 'convection-like' behaviour, fluid particles have some statistical distribution in their velocities, which is determined by the porous medium, and have a maximum velocity limited by that of the main flow. The statistical velocity distribution is not necessarily symmetric, as evidenced by the results from the experimental investigation of Didierjean *et al.* (1997).

The development of a conceptual model for a convection-like representation of longitudinal dispersive transport under transient conditions is beyond the scope of this thesis. For all practical purposes, the longitudinal dispersion coefficient is assumed to be zero under steady state and transient conditions in the present study.

It is furthermore assumed that the cross components of the momentum dispersion tensor $\boldsymbol{D}_P$ and the thermal dispersion tensor $\boldsymbol{D}_T$, given respectively by Equation (7.19) and Equation (7.20), can be neglected.

13.3 Empirical expression

Koch and Brady (1986) used the method of configurational averaging over a set of media to develop an expression for the transverse mass dispersion coefficient of continuous randomly orientated fibres of uniform diameter at high Peclét number flow. Using Definition (7.6), their expression yields the following equation for the transverse dispersity D_t:

$$D_t = \frac{9\pi^3}{6400} \frac{{d_\phi}^2 v}{\sqrt{K}\,\varepsilon_s}, \tag{13.1}$$

where d_ϕ is the fibre diameter, K is the permeability and v is the mean bulk flow velocity. It is assumed that the mean bulk flow velocity v is best characterised the intrinsic volume-averaged velocity $\langle v \rangle_f^f$. The fibre diameter is assumed to be equal to the RHD, which is equal to the characteristic prism width d_s (see Section 10.6). Substituting Equation (II.6) into Equation (13.1) yields:

$$D_t = \frac{9\pi^3}{6400} \frac{{d_s}^2 \langle v \rangle_f}{\sqrt{K}\,\varepsilon_s\,\varepsilon_f}. \tag{13.2}$$

From Definition (7.6), the transverse momentum dispersion coefficient $D_{P,t}$ is given as:

$$D_{P,t} = \rho_f \frac{9\pi^3}{6400} \frac{{d_s}^2 \langle v \rangle_f}{\sqrt{K}\,\varepsilon_s\,\varepsilon_f} \tag{13.3}$$

and the transverse thermal dispersion coefficient $D_{T,t}$ is given as:

$$D_{T,t} = \rho_f c_{p,f} \frac{9\pi^3}{6400} \frac{d_s^{\,2} \langle v \rangle_f}{\sqrt{K}\, \varepsilon_s\, \varepsilon_f}. \tag{13.4}$$

13.4 Experimental evaluation

The objective of this section is to experimentally validate the application of Equation (13.2) for determining the transverse dispersivity D_t of metallic foams. Transverse dispersivity values obtained from Equation (13.2) for three different morphological configurations are compared to corresponding experimentally determined values.

Experimental transverse dispersion data was obtained from the observation of the macroscopic spreading of a neutrally buoyant tracer introduced into water flowing through a metallic foam sample. In a water tunnel built for this purpose, a tracer was added to water flowing towards a metallic foam sample occupying the entire cross section of the flow tunnel. Images of the tracer distribution in the water entering and exiting the metallic foam sample were recorded and analysed. At the flow Peclét numbers of interest, the contribution of molecular diffusion to the spreading of the tracer element is negligible. The transverse dispersivity was extracted from this data by a comparison to data obtained from the numerical solution of the differential equations governing the dispersive behaviour of the tracer.

13.5 Experimental apparatus

An experimental set-up for determining the transverse dispersivity is shown in Figure 13.3. A horizontally mounted water tunnel (A) of internal dimensions 50.8 mm × 50.8 mm × 600 mm houses metallic foam samples (B). The water tunnel has two opposing walls made of transparent Lexan™. The other two walls of the tunnel compose of aluminium channel sections. The end caps of the water tunnel are also aluminium and have tapped inlet and outlet holes to accommodate rubber hose fittings. One of the transparent Lexan™ tunnel walls could be removed from the assembly to access the metallic foam samples. The water supply for the tunnel from the city water line (C) can be controlled upstream with an adjustable valve (D). The water flow rate is determined by a flow gauge (E) in the water outlet line. To minimise inlet and outlet turbulence effects and to level out minor pressure fluctuations from the water supply, porous flow stabilisers (F) were placed in the water tunnel upstream and downstream of the test samples.

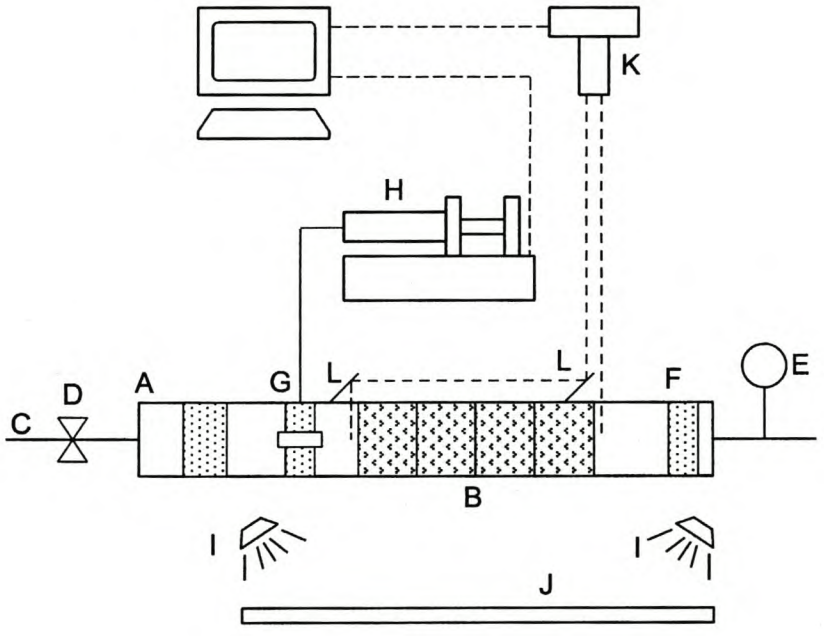

Figure 13.3 The experimental apparatus and set-up.

Three different metallic foam samples, referred to as Sample 1, Sample 2 and Sample 3, were tested. Figure 13.4 to Figure 13.6 show a 2.4 times magnified view of the morphological structure of each sample. A graduated millimetre scale is shown next to the magnified view. The morphological parameters of each structure are given in Table 13.1. The cell sizes given in Table 13.1 were visually measured and confirmed with a pressure gradient test, using Equation (10.1) together with Equation (10.11) to Equation (10.13). The samples were supplied by ERG Materials and Aerospace Corp. of Oakland CA, USA.

For each of the three metallic foam samples, four blocks (dimensions 50.8 mm × 50.8 mm × 38.1 mm) were placed end-to-end in the flow tank, making a metallic foam sample of overall dimension of 50.8 mm × 50.8 mm × 152.4 mm. The ratio of the longitudinal sample length to the transverse sample width is large enough to disperse the injected dye over a large part of the water tunnel cross sectional area. All the metallic foam samples were electro-discharge machined to avoid cell damage.

Water (as opposed to air) was selected as a working medium because of its ability to carry a variety of tracer mediums at sufficiently high concentrations. Furthermore, at

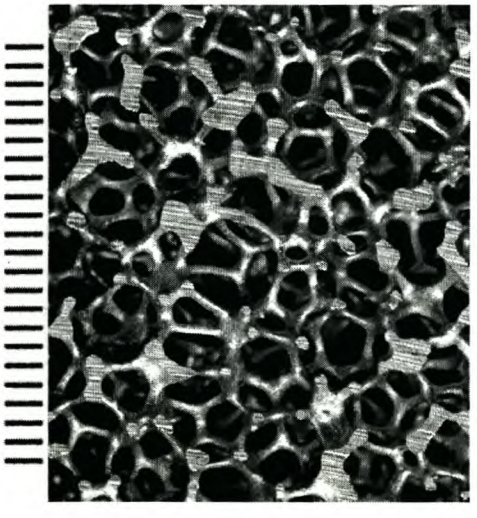

Figure 13.4 2.4 Times magnified view of the morphological structure of Sample 1.

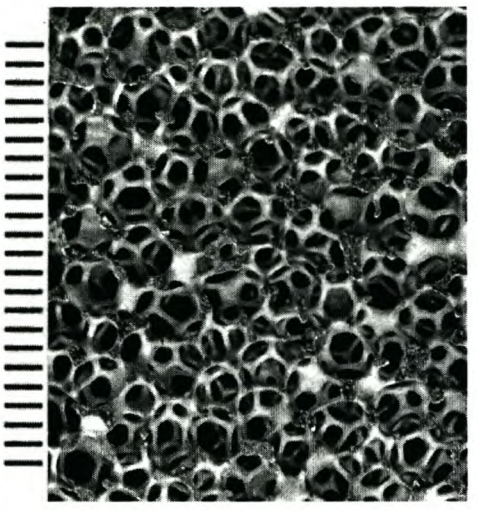

Figure 13.5 2.4 Times magnified view of the morphological structure of Sample 2.

sufficiently high mass Peclét numbers, mechanical dispersion depends only on the flow hydrodynamics, which is characterised by the flow Reynolds number. At STP conditions (25 °C, 101325 N/m^2) the same flow Reynolds number requires the volumetric flow rate of air to be 17 times higher than that of water, requiring much more volume of tracer medium.

Figure 13.6 2.4 Times magnified view of the morphological structure of Sample 3.

Sample	1	2	3
Measured cell size a [mm]	3.8	2.7	2.0
Measured porosity ε_f	0.8874	0.8874	0.9081
Tortuosity χ	1.418	1.418	1.374
Overall characteristic dimension d [mm]	2.278	1.618	1.194
Characteristic strand width d_s [mm]	0.4756	0.3379	0.2235

Table 13.1 Morphological parameters of metallic foam samples.

An aqueous solution of methylene blue dye was selected. The molecular mass diffusion coefficient of methylene blue in water is 4×10^{10} m^2/s. This is a few orders of magnitude less that the transverse dispersivity in the mass Peclét number range of interest. Dye is injected into the flow via an injector (G). Figure 13.7 shows a cut-away image of the injector. The injector is made up of two metallic tubes (G1), each with an outer diameter of 0.6 mm. The tips of the metallic tubes are embedded in a crossed pattern into a nylon

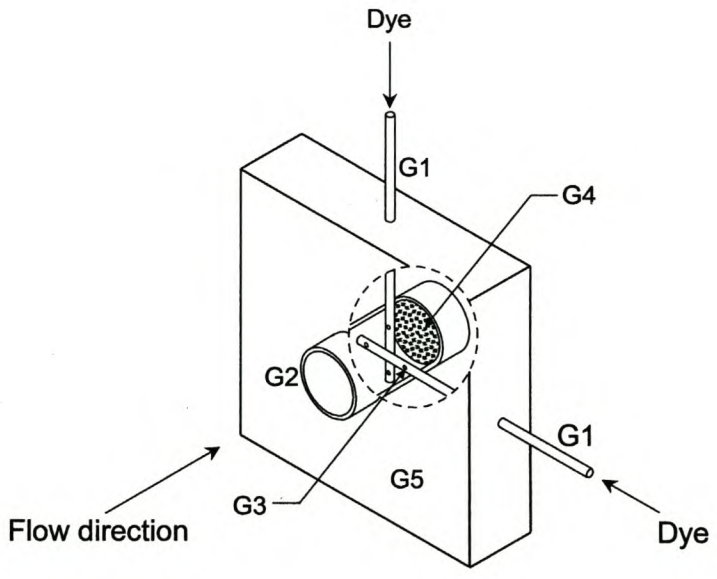

Figure 13.7 Dye injector.

tube (G2), 6 mm in diameter and 10 mm long, which confines the injected dye to a cylindrical stream along the longitudinal tank centreline. Four holes in the metallic tubes (G3) are arranged in a square pattern around the centreline. The holes face the upstreamflow direction. A porous flow stabiliser is inserted into the nylon tube (G4), downstream of the crossed metallic tubes. The upstream facing holes in the metallic tubes, together with vortices shed from the cylindrical metallic tubes and the flow stabiliser, encouraged mixing of dye with water within the nylon tube. The nylon tube is secured in the channel by a thin porous block (G5), yielding the same flow resistance as the flow stabiliser inserted into the nylon tube.

The injector aims to dispense a dye solution into the water flow stream in a form closest achievable to a cylindrical stream of uniformly concentrated dye solution, with a sharp transition at the cylindrical stream boundary between the dye solution and the surrounding fluid. A well-defined injected dye solution stream was essential for an accurate comparison to data obtained from the numerical solution of the differential equations governing the dispersive behaviour of the dye solution. Other simpler injection systems were unable to produce clearly defined injected dye solution shapes.

The rate of injected dye was controlled by a computerised syringe pump (H).

Transparency of the water tunnel made it possible to observe the dye solution in the flow stream, just before entering the metallic foam sample and immediately after leaving the metallic foam sample. For this purpose, the water tunnel was lit from behind by two halogen flood lights (I) illuminating a diffuse white backdrop (J), providing a near-uniform white light distribution.

A computerised digital CCD camera (K) was used to capture images of the dye solution at the inlet and the exit of the metallic foam sample. The digital camera set-up is also shown in Figure 13.8. The camera was positioned approximately 2m from the water tunnel. At this distance perspective distortion is minimised, while a clear picture is still obtained. In order to capture images of the dye solution at both positions in a single camera field of view, two mirrors (L) were attached to the tank, as shown in Figure 13.3.

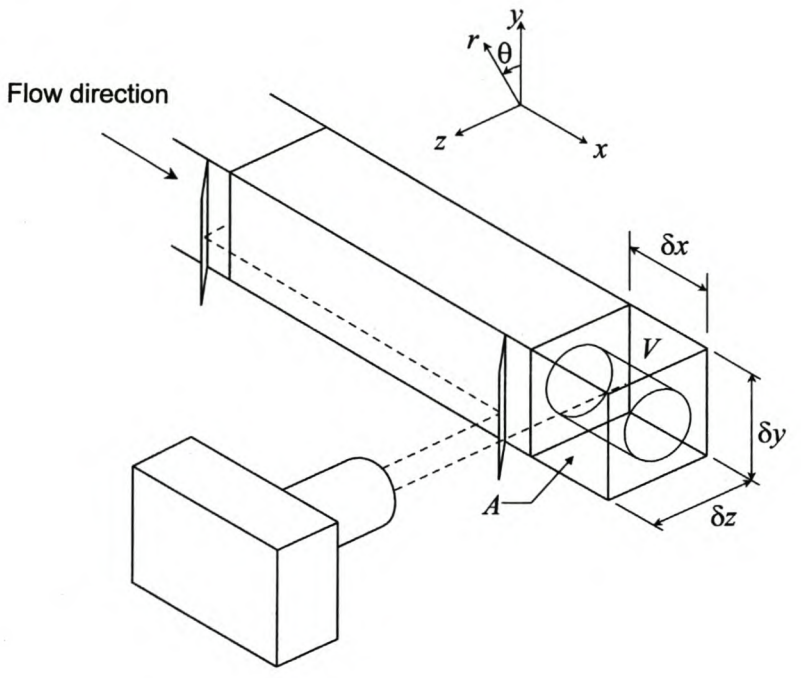

Figure 13.8 Digital camera set-up and coordinate system.

Using a spectrophotometer, the wavelength for maximum dye absorption was determined to be λ_{max} = 664 nm. A 660 – 670 nm bandpass filter was used with the camera to obtain a maximum dynamic range from the CCD camera. That way, for a fixed background light intensity, using the bandpass filter increases the light absorption of the dye solution per dye concentration. It therefore reduces the overall concentration of methylene blue dye required, which in turn reduces light scattering and limits the alteration of fluid properties from that of water.

13.6 Experimental procedure

Images of the dye solution at the inlet and exit of the metallic foam sample were captured at five flow rates, for each of the three morphological configurations tested. The CCD camera exports a 752 × 240 pixels array image in an *x-y* coordinate plane in a *tagged*

image file (tif) format. The coordinate arrangement is shown in Figure 13.8. Each pixel has a 1024 (10 bit) shade-of-grey reading, which represents an integral of light absorption through a concentric mass fraction distribution of dye solution.

An imaged two-dimensional light intensity distribution is designated as $I(x, y)$. For a clear flow field (*i.e.* no dye tracers present), an image of the light intensity distribution, designated as $I_o(x, y)$, was also captured. The $I(x, y)$ and $I_o(x, y)$ light intensity distributions were processed numerically to yield a relative intensity field $I/I_o\,(x, y)$ at the exit distributions of the dye.

A typical dye solution image exported by the CCD camera is shown in Figure 13.9. The LHS of Figure 13.9 shows a view of dye solution flowing from the injector, mounted on the LHS of the figure, and entering the metallic foam sample. The RHS of Figure 13.9 shows a corresponding view of dispersed dye solution exiting the metallic foam sample and continuing to flow toward the RHS of the figure. Figure 13.10 shows the corresponding clear image used in the data processing, with the injector clearly visible in the view on the LHS.

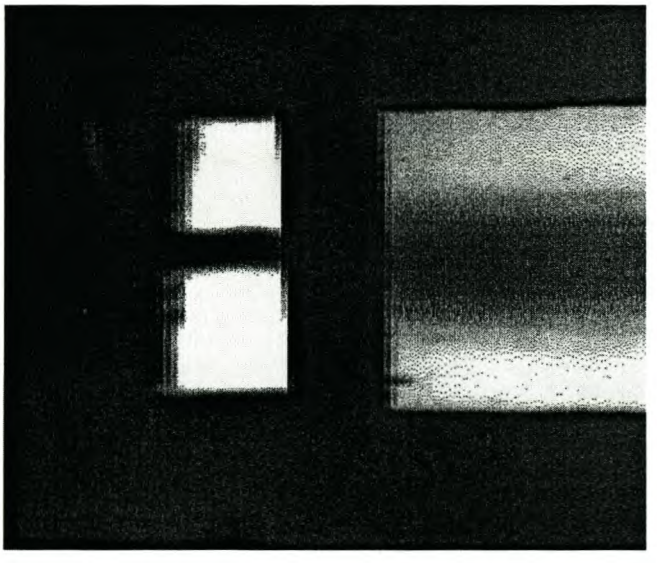

Figure 13.9 Typical image exported by the CCD camera.

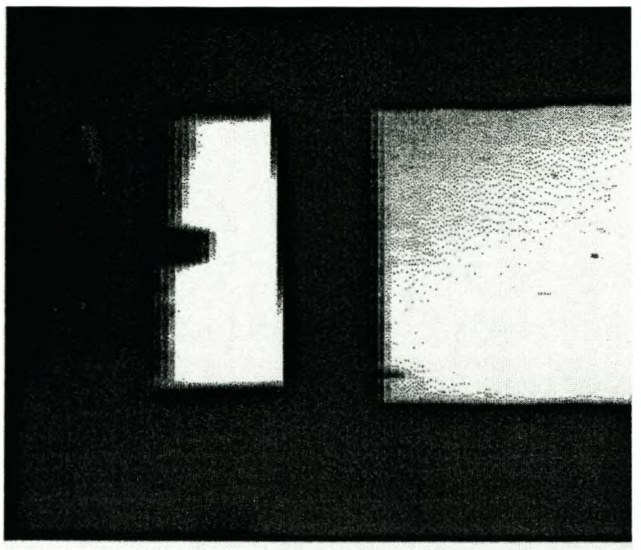

Figure 13.10 Clear image (no dye injected) used for data processing.

An image of the dye solution at the inlet of the metallic foam sample was only required as a measure of the diameter of an assumed cylindrically shaped dye solution stream.

13.7 Microscopic governing equation

Equation (I.19) gives the mass conservation of an individual specie A in a mixture in terms of its mass fraction c_A, as:

$$\rho \frac{\mathrm{D}c_A}{\mathrm{D}t} = -\nabla \cdot \boldsymbol{j}_A, \tag{I.19}$$

where ρ is the density of the solution, c_A is the mass fraction of the specie A in the solution and $\boldsymbol{j}_A$ is the mass transfer rate of the specie A per unit area.

In this section a subscript '*M*' is used to refer to an individual specie of methylene blue, instead of the '*A*' used in Equation (I.19).

A relative mass fraction $c_{M,r}$ is defined as:

$$c_{M,r} \equiv \frac{c_M}{c_{M,o}}, \tag{13.5}$$

where $c_{M,o}$ is a reference dye mass fraction. In the experimental set-up shown in Figure 13.3, the dye (methylene blue) mixes with water in an injector at introduction into the flow stream. It is then assumed to have a uniform mass fraction distribution within defined boundaries in the flow stream when it enters the porous medium. Taking this uniform mass fraction as the reference mass fraction $c_{M,o}$ in Definition (13.5), yields a unit value for the relative mass fraction of the dye ($c_{M,r}$ = 1) at the point of entry into the metallic foam sample.

By dividing Equation (I.19) by the reference mass fraction $c_{M,o}$, the mass conservation equation for the methylene blue in solution can be written in terms of the relative mass fraction $c_{M,r}$:

$$\rho \frac{\mathrm{D}c_{M,r}}{\mathrm{D}t} = -\nabla \cdot \boldsymbol{j}_{M,r}, \tag{13.6}$$

where $\boldsymbol{j}_{M,r}$ represents the transfer of a reference mass fraction $c_{M,o}$. Substituting the identity for the substantial derivative and introducing Fick's law for diffusive mass transfer, which states that:

$$\boldsymbol{j}_{M,r} = -d_{m,M} \nabla c_{M,r}, \tag{13.7}$$

where $d_{m,M}$ is the diffusive mass transfer coefficient of methylene blue in water, into

Equation (13.6) yields, after rearranging terms:

$$\rho\frac{\partial c_{M,r}}{\partial t} = \nabla\cdot\left(d_{m,M}\nabla c_{M,r}\right) - \rho\boldsymbol{v}\cdot\left(\nabla c_{M,r}\right). \tag{13.8}$$

Utilising Identity (I.47), which states that:

$$\nabla\cdot(a\boldsymbol{b}) = (\nabla a)\cdot\boldsymbol{b} + a(\nabla\cdot\boldsymbol{b}), \tag{I.47}$$

where a is a scalar quantity and $\boldsymbol{b}$ is a vector quantity, to expand the second term on the RHS of Equation (13.8) yields:

$$\rho\frac{\partial c_{M,r}}{\partial t} = \nabla\cdot\left(d_{m,M}\nabla c_{M,r}\right) - \rho\left[\nabla\cdot\left(\boldsymbol{v}c_{M,r}\right) - c_{M,r}\nabla\cdot\boldsymbol{v}\right]. \tag{13.9}$$

The continuity equation is given by Equation (I.10) as:

$$\frac{\partial\rho}{\partial t} + \boldsymbol{v}\cdot\nabla\rho = -\rho\nabla\cdot\boldsymbol{v}. \tag{I.10}$$

For a constant fluid density, it follows from Equation (I.10) that:

$$\nabla\cdot\boldsymbol{v} = 0. \tag{13.10}$$

Substituting Equation (13.10) into Equation (13.9) yields the mass conservation equation for methylene blue in solution, of constant thermophysical properties, as:

$$\rho\frac{\partial c_{M,r}}{\partial t} = \nabla\cdot\left(d_{m,M}\nabla c_{M,r}\right) - \rho\nabla\cdot\left(\boldsymbol{v}c_{M,r}\right). \tag{13.11}$$

13.8 Volume-averaged governing equation

Following the analytical volume averaging procedure used from Equation (2.38) to Equation (2.48), Equation (13.11) can be written at a macroscopic level as:

$$\rho_f \frac{\partial \langle c_{M,r} \rangle_f}{\partial t} = \nabla \cdot \left(d_{m,M} \varepsilon_f \nabla \langle c_{M,r} \rangle_f^f \right) + \nabla \cdot \left(\frac{1}{V_o} \int_{A_{sf}} d_{m,M} \overset{\circ}{c}_{M,r} \, \boldsymbol{n}_{fs} \, \mathrm{d}A \right) +$$

$$\frac{1}{V_o} \int_{A_{sf}} d_{m,M} \nabla c_{M,r} \cdot \boldsymbol{n}_{fs} \, \mathrm{d}A - \rho_f \nabla \cdot \left(\frac{1}{\varepsilon_f} \langle \boldsymbol{v} \rangle_f \langle c_{M,r} \rangle_f \right) - \rho_f \nabla \cdot \left\langle \overset{\circ}{\boldsymbol{v}} \overset{\circ}{c}_{M,r} \right\rangle_f , \quad (13.12)$$

where ρ_f is the density of the solution. The effect of the water tank boundaries on the flow velocity distribution in the metallic foam samples was assumed negligible, justifying an assumption of a uniform volume-averaged velocity in the positive x-direction.

The last term on the RHS of Equation (13.12) describes mechanical mass dispersion. According to the dispersion model discussed in Chapter 7, the mass dispersion term can be represented as:

$$\rho_f \nabla \cdot \left\langle \overset{\circ}{\boldsymbol{v}} \overset{\circ}{c}_{M,r} \right\rangle_f = -\nabla \cdot \left(\rho_f \boldsymbol{D} \cdot \nabla \langle c_{M,r} \rangle_f \right), \quad (13.13)$$

where $\boldsymbol{D}$ is the tensor form of the dispersivity defined in Definition (7.6). Under steady-state conditions, it follows that:

$$\frac{\partial \langle c_{M,r} \rangle_f}{\partial t} = 0 \quad (13.14)$$

and in the absence of molecular diffusion, it follows that:

$$d_{m,M} = 0. \quad (13.15)$$

Substituting Equation (II.6) and Equation (13.13) to Condition (13.15) into Equation (13.12), and rearranging terms, noting that the thermophysical properties of the solution are constant, yields:

$$\nabla \cdot \left(\boldsymbol{D} \cdot \nabla \left\langle c_{M,r} \right\rangle_f - \left\langle \boldsymbol{v} \right\rangle_f^f \left\langle c_{M,r} \right\rangle_f \right) = 0 . \tag{13.16}$$

In a cylindrical coordinate system, shown in Figure 13.8, Equation (13.16) is given as:

$$\frac{1}{r}\frac{\partial}{\partial r}\left(r D_r \frac{\partial \left\langle c_{M,r} \right\rangle_f}{\partial r} \right) + \frac{1}{r^2}\frac{\partial}{\partial \theta}\left(D_\theta \frac{\partial \left\langle c_{M,r} \right\rangle_f}{\partial \theta} \right) + \frac{\partial}{\partial x}\left(D_x \frac{\partial \left\langle c_{M,r} \right\rangle_f}{\partial x} \right) -$$

$$\frac{\partial}{\partial r}\left(\left\langle v_r \right\rangle_f^f \left\langle c_{M,r} \right\rangle_f \right) - \frac{1}{r}\frac{\partial}{\partial \theta}\left(\left\langle v_\theta \right\rangle_f^f \left\langle c_{M,r} \right\rangle_f \right) - \frac{\partial}{\partial x}\left(\left\langle v_x \right\rangle_f^f \left\langle c_{M,r} \right\rangle_f \right) = 0 . \tag{13.17}$$

The phasial volume-averaged mass fraction $\left\langle c_{M,r} \right\rangle_f$ is invariable in the tangential and longitudinal directions, therefore:

$$\frac{\partial \left\langle c_{M,r} \right\rangle_f}{\partial \theta} = 0 \tag{13.18}$$

and:

$$\frac{\partial \left\langle c_{M,r} \right\rangle_f}{\partial x} = 0 . \tag{13.19}$$

The tangential intrinsic volume-averaged velocity component is zero:

$$\left\langle v_\theta \right\rangle_f^f = 0 \tag{13.20}$$

and the radial intrinsic volume-averaged velocity component is zero:

$$\left\langle v_r \right\rangle_f^f = 0 . \tag{13.21}$$

Condition (13.18) and Condition (13.20) reduce the phasial volume-averaged mass fraction distribution to a quasi two-dimensional field, $\langle c_{M,r} \rangle_f = f(r,x)$.

With the volume-averaged flow only in the positive x-direction, the radial dispersivity D_r in Equation (13.17) becomes the transverse dispersivity D_t, and the dispersivity in the x-direction D_x becomes the longitudinal dispersivity D_l. Since the phasial volume-averaged mass fraction $\langle c_{M,r} \rangle_f$ is invariable in the tangential direction, there is no dispersivity component in that direction, or:

$$D_\theta = 0, \tag{13.22}$$

and the longitudinal dispersivity D_l is assumed zero (see Section 13.2):

$$D_l = 0. \tag{13.23}$$

Substituting Condition (13.18) to Condition (13.23) into Equation (13.17) yields:

$$\frac{1}{r}\frac{\partial}{\partial r}\left(r D_t \frac{\partial \langle c_{M,r} \rangle_f}{\partial r} \right) - \frac{\partial}{\partial x}\left(\langle v_x \rangle_f^f \langle c_{M,r} \rangle_f \right) = 0. \tag{13.24}$$

13.9 Discretisation

Integrating the first term on the RHS of Equation (13.24) over the finite volume shown in the Figure 13.11 yields:

$$\int_w^e \int_i^o \frac{1}{r}\frac{\partial}{\partial r}\left(r D_t \frac{\partial \langle c_{M,r} \rangle_f}{\partial r} \right) r \, dr \, dx =$$

$$\left[D_t \frac{r_o}{\delta r_o}\left(\langle c_{M,r} \rangle_{f,O} - \langle c_{M,r} \rangle_{f,P} \right) - D_t \frac{r_i}{\delta r_i}\left(\langle c_{M,r} \rangle_{f,P} - \langle c_{M,r} \rangle_{f,I} \right) \right] \Delta x. \tag{13.25}$$

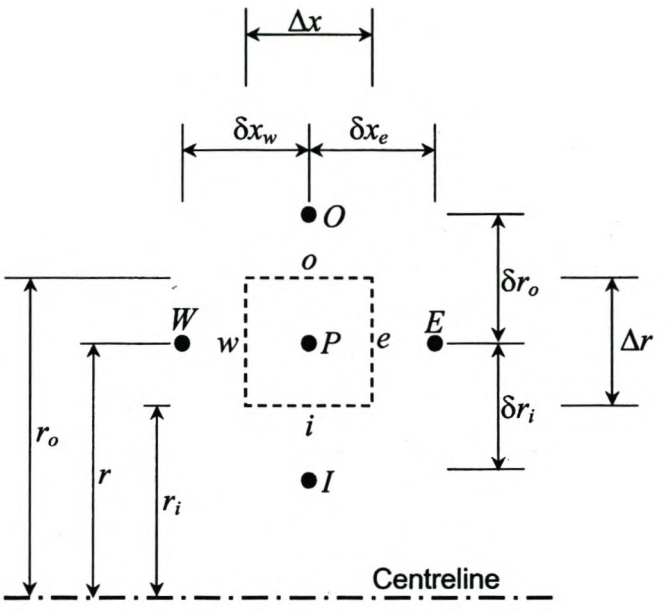

Figure 13.11 Finite volume in a cylindrical coordinate system.

Integrating the second term on the RHS of Equation (13.24) over the finite volume yields:

$$\int_w^e \int_i^o \frac{\partial}{\partial x}\left(\langle v_x\rangle_f^f \langle c_{M,r}\rangle_f\right) r \, dr \, dx = \left[\left(\langle v_x\rangle_f^f \langle c_{M,r}\rangle_f\right)_e - \left(\langle v_x\rangle_f^f \langle c_{M,r}\rangle_f\right)_w\right] r \, \Delta r \, . \tag{13.26}$$

According the *upwind scheme* (Patankar, 1980), the value of $\langle c_{M,r}\rangle_f$ at an interface is equal to the value of $\langle c_{M,r}\rangle_f$ at the grid point on the upwind side of that interface. Implementing the upwind scheme in Equation (13.26) and substituting Equation (13.25) and Equation (13.26) into Equation (13.24) yields, after rearranging terms:

$$\left(\langle v_x\rangle_f^f \, r\,\Delta r + D_t \frac{r_o \Delta x}{\delta r_o} + D_t \frac{r_i \Delta x}{\delta r_i}\right)\langle c_{M,r}\rangle_{f,P} =$$

$$\langle v_x\rangle_f^f \, r\,\Delta r \langle c_{M,r}\rangle_{f,W} + D_t \frac{r_o \, \Delta x}{\delta r_o}\langle c_{M,r}\rangle_{f,O} + D_t \frac{r_i \, \Delta x}{\delta r_i}\langle c_{M,r}\rangle_{f,I} \, , \tag{13.27}$$

where, through continuity, Equation (13.20) and Equation (13.21) suggest that for a constant density fluid the axial intrinsic volume-averaged velocity component $\langle v_x \rangle_f^f$ is constant. Equation (13.27) can be written in a general form:

$$a_P \langle c_{M,r} \rangle_{f,P} = a_W \langle c_{M,r} \rangle_{f,W} + a_O \langle c_{M,r} \rangle_{f,O} + a_I \langle c_{M,r} \rangle_{f,I} + b \tag{13.28}$$

with:

$$a_W = \langle v \rangle_f^f r \Delta r , \tag{13.29}$$

$$a_O = D_t \frac{r_o \Delta x}{\delta r_o} , \tag{13.30}$$

$$a_I = D_t \frac{r_i \Delta x}{\delta r_i} , \tag{13.31}$$

$$a_P = a_W + a_O + a_I \tag{13.32}$$

and:

$$b = 0 . \tag{13.33}$$

13.10 Boundary conditions

Equation (13.24) was solved at the grid points of a two-dimensional rectangular grid in the domain occupied by the metallic foam sample. The grid is in the *x*-*y* plane of the coordinate system that is shown in Figure 13.8. Figure 13.12 shows the two-dimensional solution domain with system boundary conditions.

The mass fraction values at the boundary finite volumes at the flow inlet system boundary are known. At each grid point *P* along the inflow system boundary, Equation (13.29) to

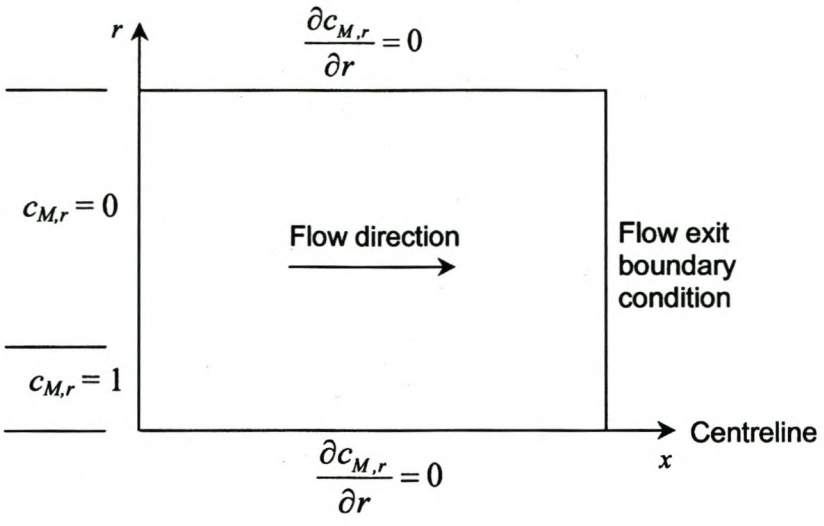

Figure 13.12 Two-dimensional solution domain with boundary conditions.

Equation (13.33) then become:

$$a_W = a_O = a_I = 0, \tag{13.34}$$

$$a_P = 1 \tag{13.35}$$

and:

$$b = \langle c_{M,r} \rangle_f, \tag{13.36}$$

where $\langle c_{M,r} \rangle_f$ in Equation (13.36) is the known phasial volume-averaged relative mass fraction at the flow inlet system boundary. Since the relative mass fraction in the cylindrical stream of dye solution approaching the metallic foam sample is one, it follows that in flow inlet system boundary finite volumes traversed by the cylindrical stream of dye solution, the intrinsic volume-averaged relative mass fraction $\langle c_{M,r} \rangle_f^f$ is one. From

Equation (II.6) it then follows that:

$$b = \varepsilon_f . \tag{13.37}$$

For the rest of the grid points along the inflow system boundary, the relative mass fraction is zero, yielding:

$$b = 0 . \tag{13.38}$$

Along the outflow system boundary, where fluid exits the domain, it is assumed that the phasial volume-averaged mass fraction at each grid point is equal to that at the grid point on the upstream side. Therefore, for each grid point P along the outflow system boundary, Equation (13.29) to Equation (13.34) then become:

$$a_P = 1, \tag{13.39}$$

$$a_W = 1 \tag{13.40}$$

and:

$$b = a_O = a_I = 0. \tag{13.41}$$

Along the system boundaries corresponding to the channel walls, there is no transfer of mass across the boundary. Therefore, along the outer boundary it follows that:

$$\left[\frac{\partial \langle c_{M,r} \rangle_f}{\partial r} \right]_o = 0 \tag{13.42}$$

and along the inner boundary it follows that:

$$\left[\frac{\partial \langle c_{M,r} \rangle_f}{\partial r} \right]_i = 0 . \tag{13.43}$$

Substituting Condition (13.42) into Equation (13.24) yields the same coefficients as those given by Equation (13.29) to Equation (13.33), except that :

$$a_O = 0. \tag{13.44}$$

Similarly, substituting Condition (13.43) into Equation (13.24) yields the same coefficients as those given by Equation (13.29) to Equation (13.33), except that:

$$a_I = 0. \tag{13.45}$$

13.11 Solution of volume-averaged governing equation

Equation (13.27) was solved, using the direct solution method of King (1976), at the grid points of a 52 × 52 grid in the domain enclosed by the metallic foam sample. Grid points were evenly spaced in the domain.

13.12 Light intensity ratio

Consider a volume V of dimensions $\delta x \times \delta y \times \delta z$ in the water tank at the exit of the metallic foam sample, as shown in Figure 13.8. This volume has a projected area A of dimensions $\delta x \times \delta y$ in the direction of the imaging camera.

The microscopic relative mass fraction $c_{M,r}$ in the volume V can be determined from the calculated phasial volume-averaged relative mass fraction $\langle c_{M,r} \rangle_f$ distribution in the metallic foam sample by using Equation (II.6). It is assuming that the microscopic relative mass fraction $c_{M,r}$ immediately behind the metallic foam sample is equal to the intrinsic volume-averaged relative mass fraction $\langle c_{M,r} \rangle_f^f$ just before exiting from the metallic foam sample.

At every point on the area A, the relative intensity field I/I_o is given as (Carlson, 1977):

$$\frac{I}{I_o} = \mathrm{e}^{-\int_{\delta z} \sigma \, \mathrm{d}z}, \tag{13.46}$$

where σ is the absorption coefficient of the methylene blue solution, which is a function of its mass fraction c_M, and the integral is along an observer's line of sight. It is assumed that the absorption coefficient σ is directly proportional to the mass fraction of methylene blue in the solution, or:

$$\sigma = \alpha \, c_M, \tag{13.47}$$

where α is a constant proportionality coefficient. Using Definition (13.5), Equation (13.47) can be given in terms of the relative mass fraction as:

$$\sigma = \alpha \, c_{M,o} \, c_{M,r}. \tag{13.48}$$

Substituting Equation (13.48) into Equation (13.46) and rearranging terms yields:

$$\ln \frac{I}{I_o} = -\alpha \, c_{M,o} \int_{\delta z} c_{M,r} \, \mathrm{d}z. \tag{13.49}$$

Integrating Equation (13.49) over the area A in Figure 13.8 yields:

$$\int_A \ln \frac{I}{I_o} \, \mathrm{d}A = -\alpha \, c_{M,o} \int_V c_{M,r} \, \mathrm{d}V. \tag{13.50}$$

Consider for a moment Equation (13.46) to Equation (13.50). These equations apply to the relative mass fraction $c_{M,r}$ distribution obtained from the solution of Equation (13.24) as well as to the imaged dye solution. However, the distribution of the relative mass

fraction $c_{M,r}$ in the volume V in the term on the RHS of Equation (13.50) is known from the solution of Equation (13.24), and the distribution of the intensity ratio I/I_o over the area A in the term on the LHS of Equation (13.50) is known in the imaged dye solution. Furthermore, since Equation (13.24) is solved for the same methylene blue mass fraction distribution entering the metallic foam sample, as that observed by the imaging camera, the conservation of mass requires that:

$$\left[\int_V c_{M,r}\,\mathrm{d}V\right]_{\text{imaged}} = \left[\int_V c_{M,r}\,\mathrm{d}V\right]_{\text{Equation(13.24)}}, \tag{13.51}$$

irrespective of whether Equation (13.24) was solved with an appropriate transverse dispersivity value.

When Equation (13.50) is applied to the imaged dye solution, the substitution of Equation (13.51) yields, after rearranging terms:

$$-\alpha c_{M,o} = \frac{\left[\int_A \ln\frac{I}{I_o}\,\mathrm{d}A\right]_{\text{imaged}}}{\left[\int_V c_{M,r}\,\mathrm{d}V\right]_{\text{Equation(13.24)}}}. \tag{13.52}$$

When Equation (13.49) is applied to the imaged dye solution, the substitution of Equation (13.52) yields:

$$\left[\ln\frac{I}{I_o}\right]_{\text{Equation(13.24)}} = \left[\int_A \ln\frac{I}{I_o}\,\mathrm{d}A\right]_{\text{imaged}} \left[\frac{\int_{\delta z} c_{M,r}\,\mathrm{d}z}{\int_V c_{M,r}\,\mathrm{d}V}\right]_{\text{Equation(13.24)}}. \tag{13.53}$$

By using Equation (13.53), the intensity ratio I/I_o at a locations that correspond to the pixel positions of the camera image, can be determined from the calculated relative mass fraction distribution in the volume V and the imaged intensity ratio distribution over the area A. Equation (13.53) reveals that no knowledge is required of the reference mass fraction $c_{M,o}$ or the constant proportionality coefficient α. The *Sum of Squares Error* (*SSE*), defined as:

$$SSE \equiv \sum_{i=1}^{n} \left(1 - \frac{\left[\frac{I}{I_o} \right]_{\text{Equation (13.24)}}}{\left[\frac{I}{I_o} \right]_{\text{imaged}}} \right)^2 , \qquad (13.54)$$

where n is the total number of pixels, quantifies the degree of agreement between calculated and imaged intensity ratios.

Distributions of $c_{M,r}$ were obtained using various values for the transverse dispersivity D_t in Equation (13.24). The transverse dispersivity value yielding the smallest *SSE* value was assumed to apply to the particular porous medium and flow rate.

13.13 Results

The flow Peclét number in the metallic foam samples was high enough to ignore the contribution of molecular diffusion to the transport of dye solution. In that case, dispersivity is a flow hydrodynamic phenomenon only, which is most appropriately presented as a function of Reynolds number.

Table 13.2 gives the imaged dispersivity for each of the three samples as a function of Reynolds number. The Reynolds numbers are based on the RHD.

Sample	Re	D_t [m^2/s]
1	8.604	7.56×10^{-7}
1	15.02	2.11×10^{-6}
1	22.84	4.24×10^{-6}
1	29.53	6.08×10^{-6}
1	68.49	2.37×10^{-5}
2	5.851	5.75×10^{-7}
2	11.70	2.25×10^{-6}
2	16.22	4.66×10^{-6}
2	20.98	7.41×10^{-6}
2	46.80	2.08×10^{-5}
3	3.692	5.09×10^{-7}
3	7.347	1.05×10^{-6}
3	11.07	2.06×10^{-6}
3	16.73	5.27×10^{-6}
3	30.24	1.56×10^{-5}

Table 13.2 Imaged dispersivity as a function of Reynolds number.

Figure 13.13 to Figure 13.27 show correlations between imaged and calculated intensity ratio values for each of the three metallic foam samples at various Reynolds numbers. Only one halve of the intensity distribution is shown. The vertical axes represent radial distance from the centreline and the horizontal axes represent the intensity ratio. This axis arrangement corresponds to that of the camera image, as shown by the image in Figure 13.9. The imaged intensity ratio values presented on the graph are averages of values on either side of the centreline.

Figure 13.28 compares all the imaged transverse dispersivity data to the prediction of Equation (13.2). A direct comparison of all the imaged data on a single graph is done in terms of a dimensionless reduced dispersivity parameter (*RDP*) defined as:

$$RDP \equiv \frac{\rho_f \varepsilon_s \sqrt{K}\, D_t}{\mu d_s}. \tag{13.55}$$

The Reynolds numbers in Figure 13.13 to Figure 13.28 are all based on the RHD.

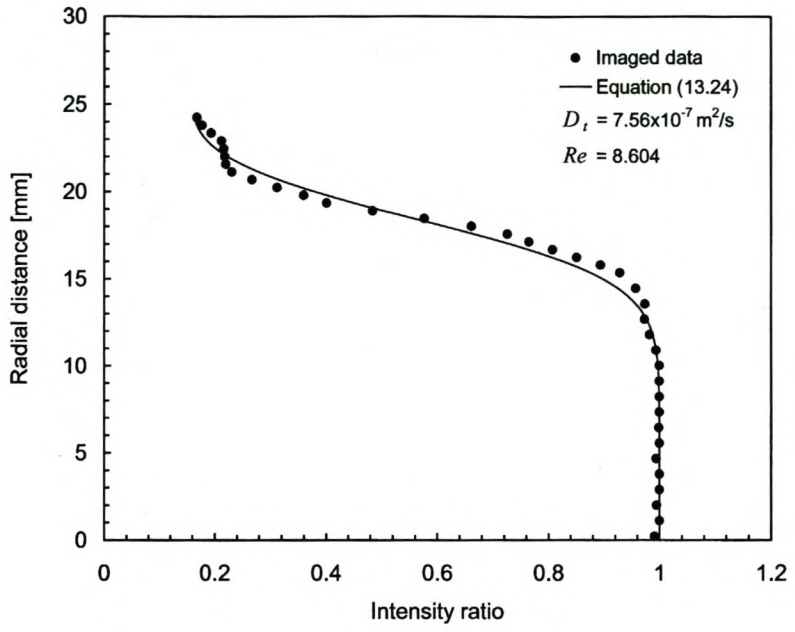

Figure 13.13 Comparison between imaged and calculated intensity ratio values for Sample 1 at Re = 8.604, using a dispersivity value of 7.56×10^{-7} m^2/s.

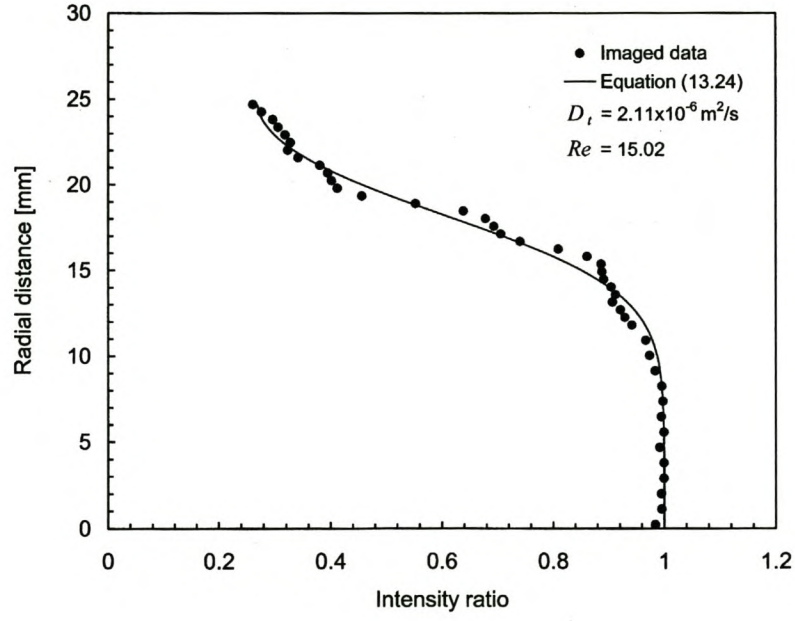

Figure 13.14 Comparison between imaged and calculated intensity ratio values for Sample 1 at Re = 15.02, using a dispersivity value of 2.11×10^{-6} m^2/s.

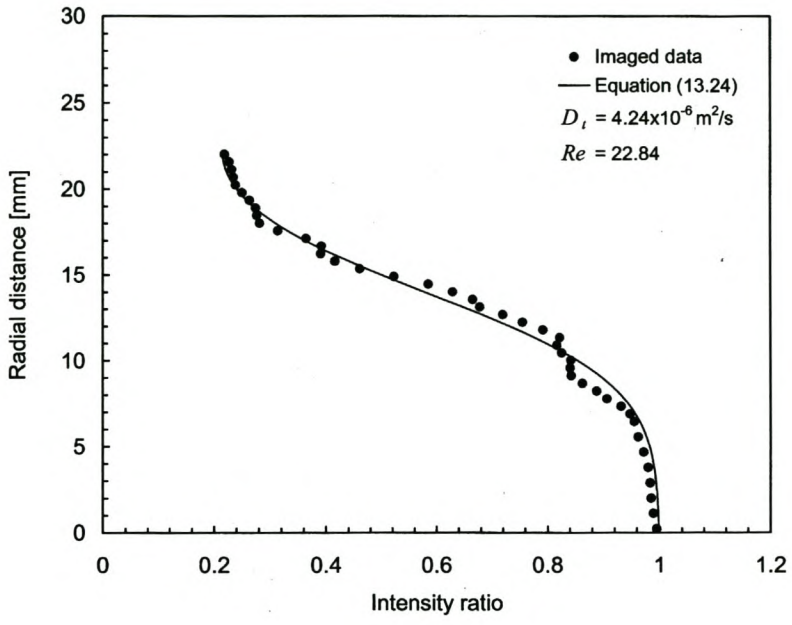

Figure 13.15 Comparison between imaged and calculated intensity ratio values for Sample 1 at Re = 22.84, using a dispersivity value of 4.24×10^{-6} m^2/s.

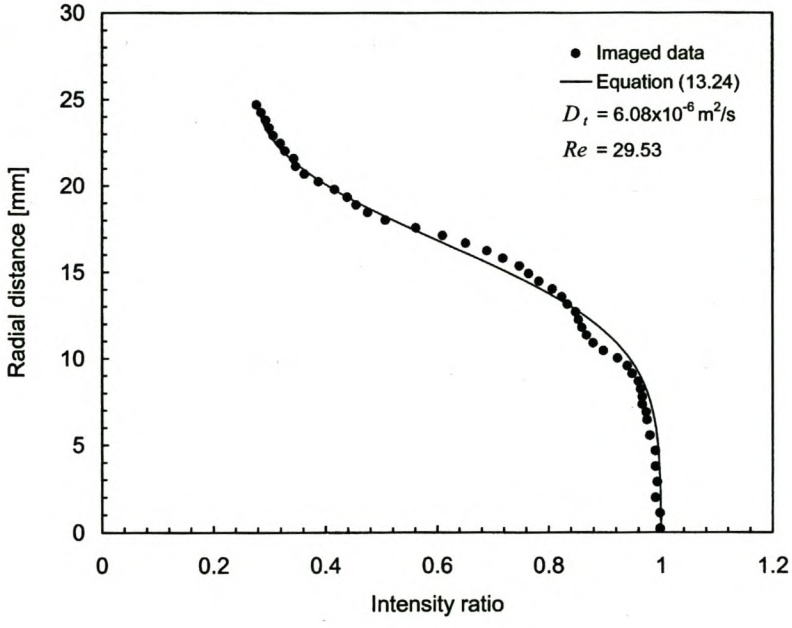

Figure 13.16 Comparison between imaged and calculated intensity ratio values for Sample 1 at Re = 29.53, using a dispersivity value of 6.08×10^{-6} m^2/s.

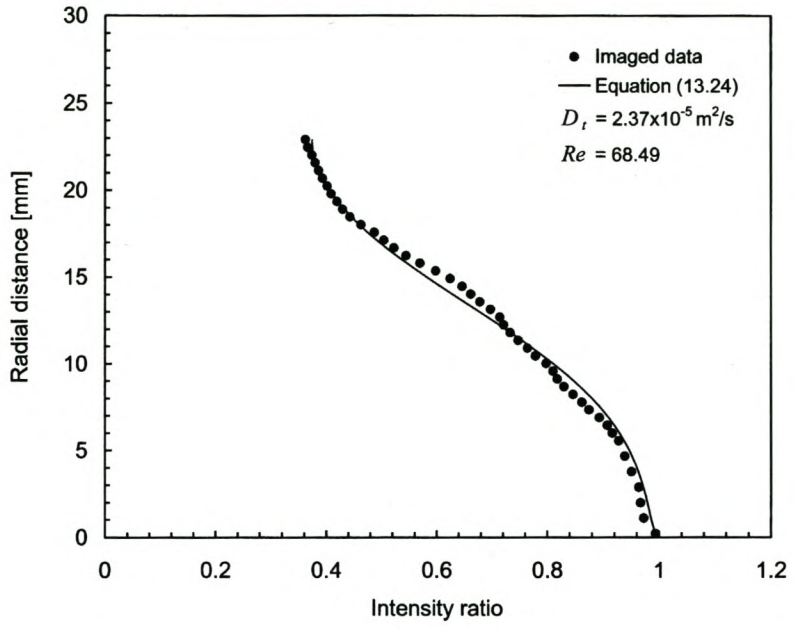

Figure 13.17 Comparison between imaged and calculated intensity ratio values for Sample 1 at Re = 68.49, using a dispersivity value of 2.37×10^{-5} m^2/s.

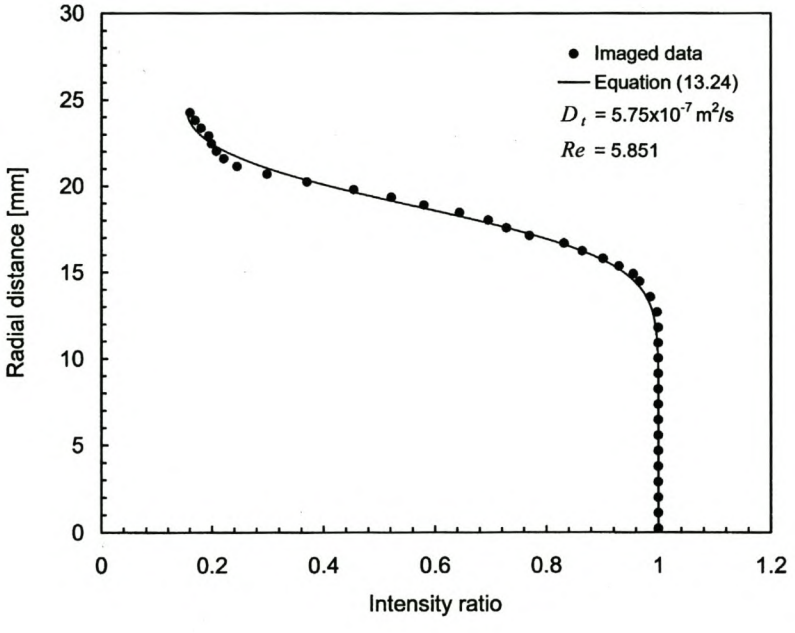

Figure 13.18 Comparison between imaged and calculated intensity ratio values for Sample 2 at Re = 5.851, using a dispersivity value of 5.75×10^{-7} m^2/s.

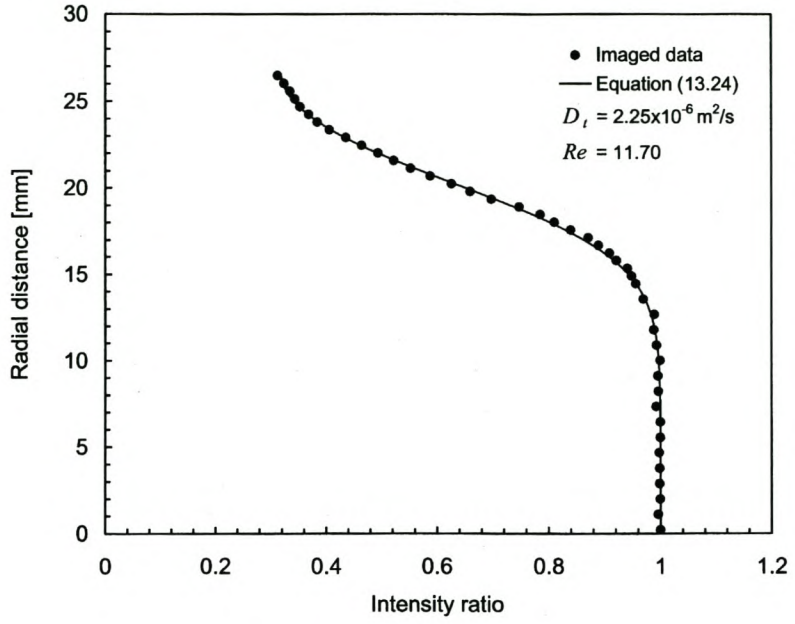

Figure 13.19 Comparison between imaged and calculated intensity ratio values for Sample 2 at Re = 11.70, using a dispersivity value of 2.25×10^{-6} m^2/s.

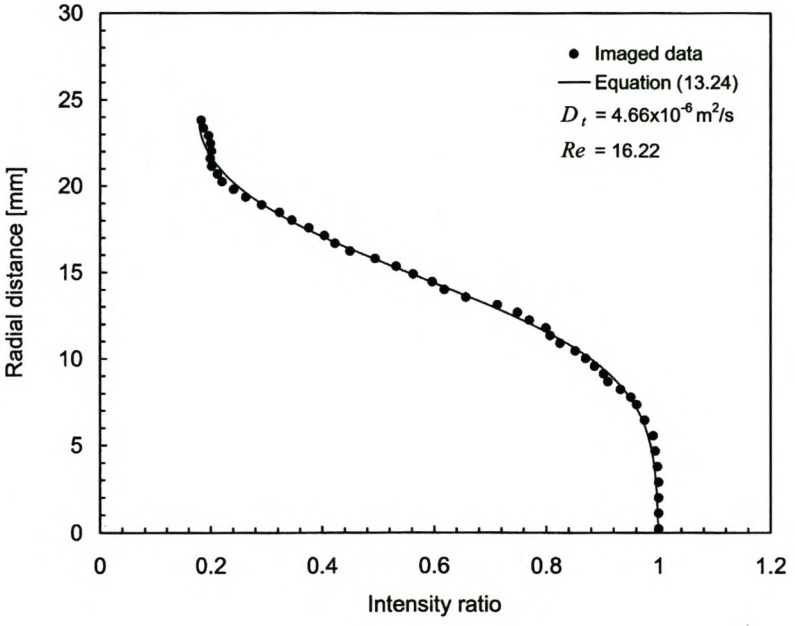

Figure 13.20 Comparison between imaged and calculated intensity ratio values for Sample 2 at Re = 16.22, using a dispersivity value of 4.66×10^{-6} m^2/s.

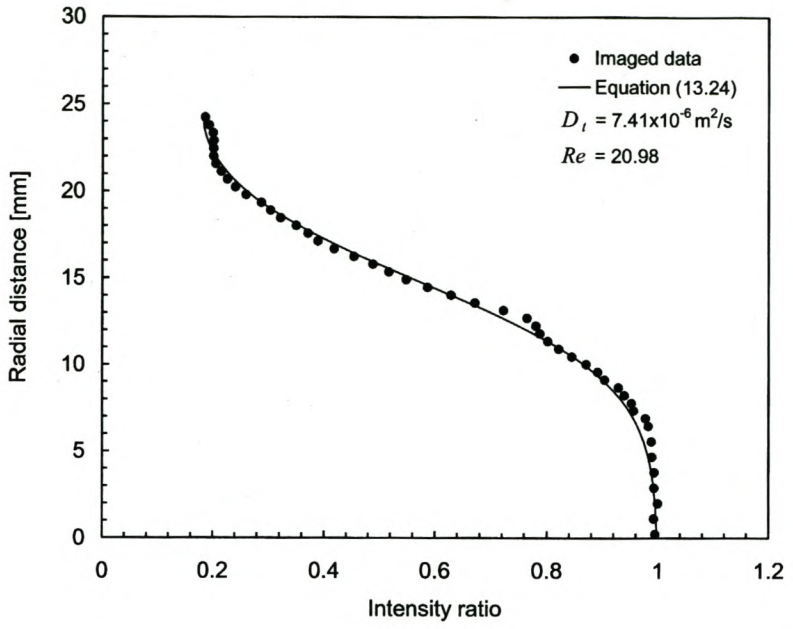

Figure 13.21 Comparison between imaged and calculated intensity ratio values for Sample 2 at Re = 20.98, using a dispersivity value of 7.41×10^{-6} m^2/s.

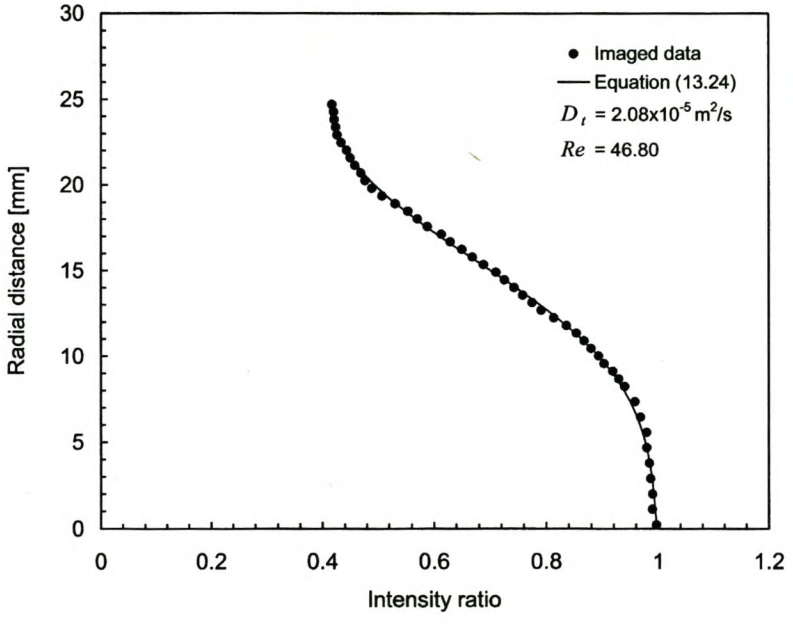

Figure 13.22 Comparison between imaged and calculated intensity ratio values for Sample 2 at Re = 46.80, using a dispersivity value of 2.08×10^{-5} m^2/s.

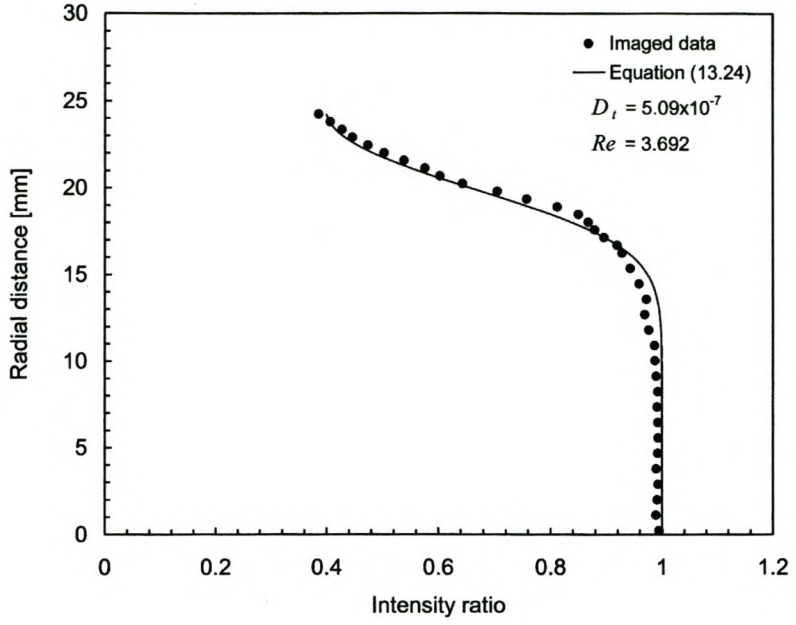

Figure 13.23 Comparison between imaged and calculated intensity ratio values for Sample 3 at Re = 3.692, using a dispersivity value of 5.09×10^{-7} m^2/s.

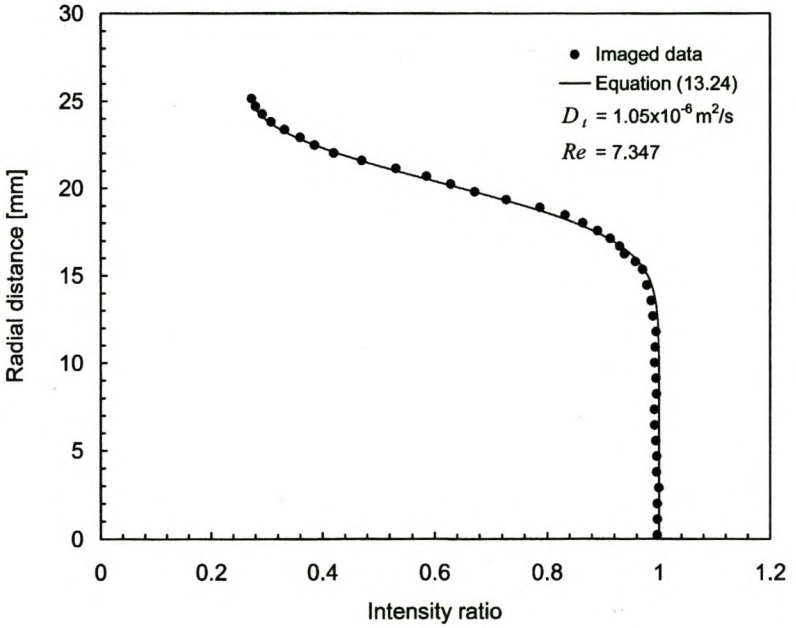

Figure 13.24 Comparison between imaged and calculated intensity ratio values for Sample 3 at Re = 7.347, using a dispersivity value of 1.05×10^{-6} m^2/s.

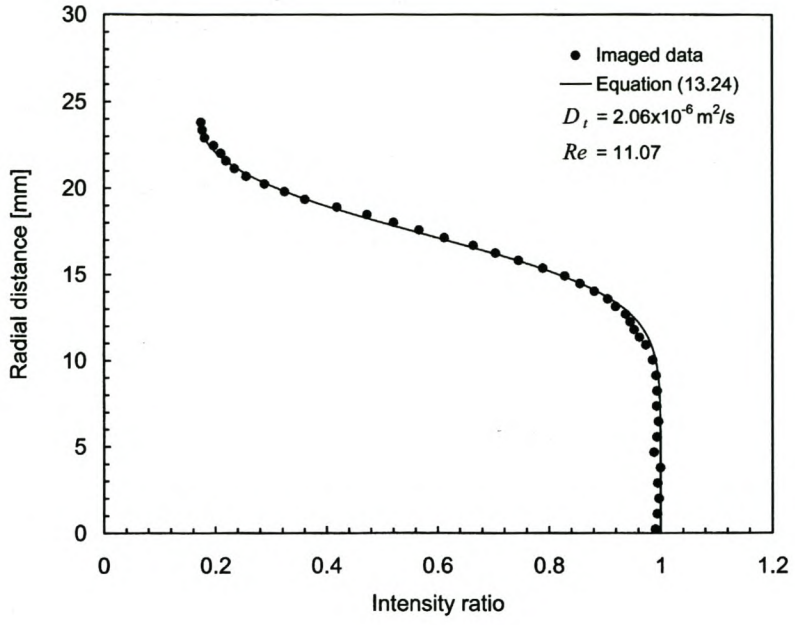

Figure 13.25 Comparison between imaged and calculated intensity ratio values for Sample 3 at Re = 11.07, using a dispersivity value of 2.06×10^{-6} m^2/s.

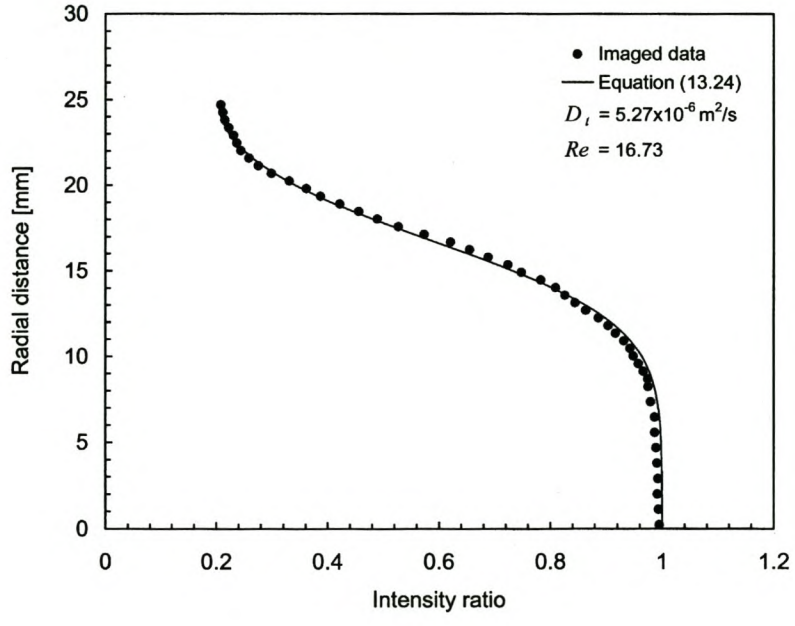

Figure 13.26 Comparison between imaged and calculated intensity ratio values for Sample 3 at Re = 16.73, using a dispersivity value of 5.27×10^{-6} m^2/s.

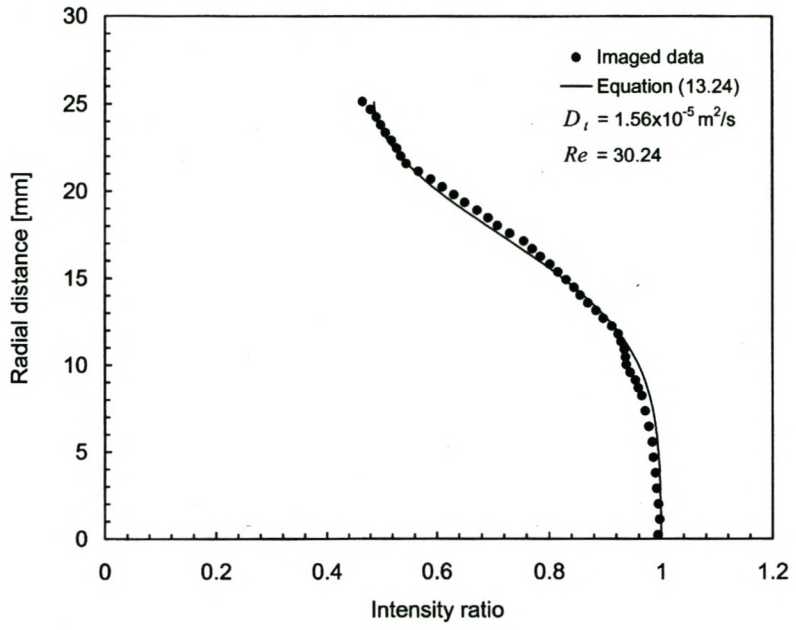

Figure 13.27 Comparison between imaged and calculated intensity ratio values for Sample 3 at Re = 30.24, using a dispersivity value of 1.56×10^{-5} m^2/s.

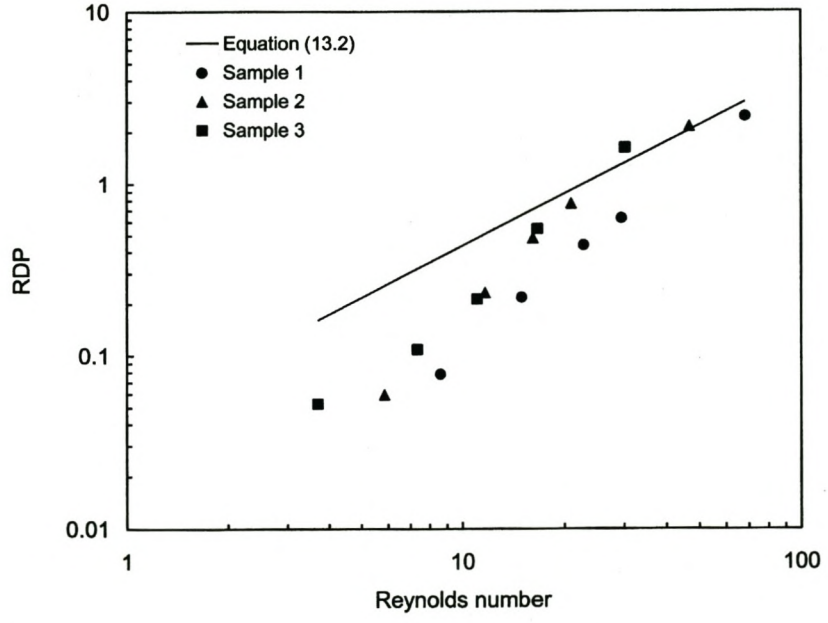

Figure 13.28 Comparison between imaged transverse dispersivity data.

13.14 Conclusion

In a heat exchange system consisting of a porous medium in thermal contact with a substrate material and saturated with a moving fluid, the contribution of transverse thermal dispersion to the overall heat exchange between the substrate material and the fluid is mostly affected by the Biot modulus. The Biot modulus compares the relative magnitudes of thermal resistance between the two phases to the resistance to internal conduction in the solid phase. At a high Biot modulus, where heat exchange is mostly limited in the narrow region adjacent to the substrate material, dispersion will contribute more to the overall heat exchange than at a low Biot modulus, where heat exchange is more evenly distributed between the substrate material and the outer boundary of the heat exchanger.

In general, the Biot modulus is defined as:

$$Bi \equiv \frac{hd}{k}, \tag{13.56}$$

where h is the convection coefficient between a solid and fluid, d is a characteristic dimension and k is the thermal conductivity of the solid. For application to metallic foam heat exchangers, the convection coefficient h is substituted by the interphasial heat transfer coefficient h_{sf}, d is characterized by the heat exchanger height and the thermal conductivity k is substituted by the solid phase effective thermal conductivity k_{ss} of the metallic foam.

The interphasial heat transfer coefficient h_{sf} in the Biot modulus definition increases with increasing Reynolds number (see Section 12.6). It therefore follows that the contribution of dispersion to the overall heat exchange increases with increasing Reynolds number.

Consider for a moment a typical metallic foam heat exchanger, such as that shown in Figure 17.1, with length L = 40 mm and height H = 10 mm. With air as a fluid medium at a flow Reynolds number of 20 ($\langle v \rangle_f$ = 1.08 m/s), the Biot modulus is 0.039, where the interphasial heat transfer coefficient h_{sf} is based on a uniform volume-averaged velocity in

the metallic foam sample. The solution of Equation (8.3) and Equation (8.5) revealed that the contribution of thermal dispersion to the overall heat exchange is less than 0.4%. When water is used as a fluid medium under the same operating conditions and flow Reynolds number ($\langle v \rangle_f$ = 0.06 m/s), the Biot modulus is 1.89. In this case, the contribution of thermal dispersion to the overall heat exchange is less than 24%. The air and water inlet temperatures were taken as 20 °C and the substrate temperature as 93 °C.

Therefore, from Figure 13.28 it follows that at $Re < 20$, where Equation (13.2) shows little agreement with experimental results, the contribution of thermal dispersion to the overall heat exchange is of less significance.

CHAPTER 14

HEAT AND MOMENTUM TRANSFER AT SYSTEM BOUNDARIES

14.1 Overview

In this chapter, different types of momentum and thermal boundary conditions at open and closed system boundaries are discussed. (For a definition of open and closed system boundaries, see Section 14.2.) Expressions are derived for heat and momentum transfer at a system boundary. Boundary conditions are modelled by defining certain momentum and heat transfer parameters, which are then quantified in terms of fluid thermophysical properties and metallic foam morphological parameters.

14.2 Open and closed system boundaries

The nature of a system boundary condition depends on its system boundary geometry. If an impermeable, solid wall forms a system boundary of a porous domain, then the boundary is referred to as a *closed system boundary*. On the other hand, if a system boundary is an open end, then the boundary is referred to as an *open system boundary*.

14.3 Momentum system boundary conditions at a closed system boundary

Angirasa and Peterson (1996) solved a simplified version of the transformed volume-averaged momentum equation in metallic foams by specifying a zero volume-averaged

velocity at a closed system boundary (in analogy to a zero microscopic velocity at the closed system boundary). However, the volume-averaged velocity is with reference to an REV (representative elementary volume, discussed in Section II.2) of which the minimum size is limited by geometric considerations of the porous medium (Bear and Bachmat, 1991). Furthermore, since there is no flow beyond the solid boundary, the border of the REV cannot extend beyond the solid boundary. It is therefore not possible for an REV with its origin located at the wall, to yield a zero volume-averaged velocity value, despite the fact that the microscopic velocity is zero at the solid wall. Figure 14.1 shows the location of an REV in relation to a closed system boundary.

From a macroscopic point of view, microscopic flow considerations can predict the transport of momentum between the solid wall and the REV neighbouring the solid wall. Instead of specifying a volume-averaged velocity value at the solid wall, the volume-averaged velocity at the wall can be determined by the volume-averaged velocity in the far field way from the solid wall, and the momentum transfer between the solid wall and the fluid.

Predicting the volume-averaged velocity at the wall is important since it affects the direct exchange of heat between the solid wall and the fluid phase, as well as heat transfer between strands neighbouring the solid wall, and the fluid phase. The contribution of heat transfer in these regions is of more interest at a high Biot modulus (see Section 13.14).

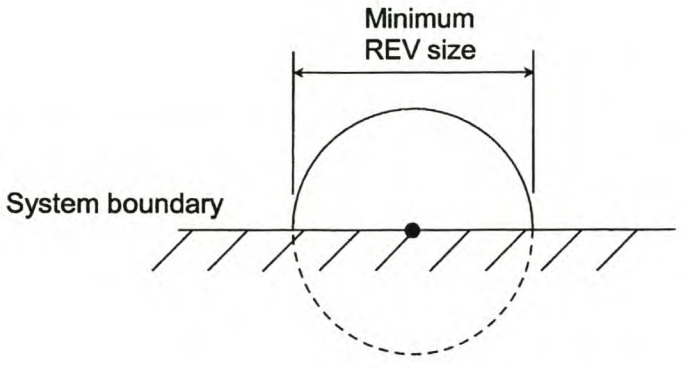

Figure 14.1 Location of an REV in relation to a closed system boundary.

14.4 Momentum system boundary conditions at an open system boundary

The solution of the transformed volume-averaged momentum equation requires that the fluid phase volume-averaged velocity be available at an open system boundary where fluid enters the porous domain. At an open system boundary where fluid leaves the porous domain, high Reynolds number flow behaviour (*i.e.* ignoring diffusive momentum transfer along the flow direction) is assumed along the system boundary. That way, the volume-averaged velocity at the system boundary is only determined by upstream flow conditions in the porous domain.

14.5 Thermal system boundary conditions at a closed system boundary for the solid and the fluid phases

At a closed system boundary a metallic foam could be in complete, partial or no thermal contact with the solid wall. Complete thermal contact is achieved when the metallic foam is braised to the wall, yielding a continuous temperature distribution across the interface between the porous domain and the solid wall. Other methods of binding, such as high thermal conductivity epoxy adhesives form a thermal contact resistance and creating only partial thermal contact between the solid phase and the wall. When the metallic foam is not bonded to the wall in any way, no thermal contact can be assumed.

The two most common types of boundary conditions that are found at a closed system boundary are a specified wall temperature and a specified wall heat flux.

When there is complete thermal contact between the porous domain and the solid wall (*i.e.* the metallic foam is braised to the wall), the temperature in the solid phase at the system boundary is at the specified wall temperature. If there is only partial thermal contact at the interface between the porous domain and the solid wall, the solid phase

system boundary temperature is determined by the specified wall temperature, the thermal contact resistance and heat transfer between the phases within the porous domain. With no thermal contact at the interface between the porous domain and the solid wall, the solid phase can be regarded as insulated (zero heat transfer) at the interface between the porous domain and the solid wall.

With a specified wall temperature, the fluid phase system boundary is a function of the specified wall temperature and heat transfer coefficient between the fluid phase and the solid wall. The heat transfer coefficient is determined by fluid thermophysical properties, flow velocity and morphological parameters.

When there is a specified heat transfer through the wall, a fraction of the total heat transfer through the wall is exchanged directly between the fluid and the solid wall. The rest of the heat is conducted between the wall and the solid phase of the porous medium. The relative amounts of heat exchanged between the fluid and the wall, and that conducted between the wall and the solid phase, are determined by the thermal contact resistance in the solid phase at the interface between the porous domain and the solid wall and the heat transfer coefficient between the fluid phase and the wall. The solid phase system boundary temperature is determined by the fraction of heat transfer that is conducted between the wall and the solid phase, and the thermal contact resistance at the interface. The fluid phase system boundary temperature is determined by heat that is exchanged directly between the fluid and the wall.

When there is a specified heat transfer through the wall, the specification of the system boundary conditions for the solution of the model is often done by trial-and-error. The magnitude of a specified wall temperature is varied until the resulting heat transfer in the solid phase and the fluid phase add up to the specified heat transfer through the wall.

14.6 Thermal system boundary conditions at an open system boundary for the solid and the fluid phases

At an open system boundary, fluid could either enter or leave the porous domain. In both cases, heat is exchanged between the exposed cross-section of the solid strands and the fluid. The amount of heat exchanged depends on the fluid phase volume-averaged temperature and a heat transfer coefficient between the fluid phase and the solid wall. The heat transfer coefficient is determined by fluid thermophysical properties, flow velocity and orientation of the mean flow direction relative to the system boundary. The amount of heat exchanged is also determined by geometric parameters such as the exposed cross-sectional area per strand at the open system boundary.

The heat exchanged between the exposed cross-section of the solid strands and the fluid determines the volume-averaged temperature gradient in the solid phase at the system boundary.

The volume-averaged fluid phase temperature at the system boundary is essentially the volume-averaged temperature of the fluid within the pores immediately adjacent to the system boundary. The heat exchanged between the exposed cross-section of the strands and fluid entering the porous domain creates a change in the measurable fluid temperature from before entering the porous domain, to becoming the fluid phase system boundary temperature. The same can be said about fluid leaving the porous domain. At exiting the porous domain, heat exchanged between the exposed cross-section of the solid strands at the outflow system boundary and the fluid creates a change in the measurable fluid temperature from the volume-averaged fluid phase system boundary temperature, to the fluid temperature in the exit free stream.

At an open system boundary where the fluid leaves the porous domain, high Peclét number flow behaviour (*i.e.* ignoring fluid phase conduction along the flow direction) is assumed. This assumption assists in the computational solution of the volume-averaged energy equation for the fluid phase (see Section 15.3).

14.7 Modelling momentum transfer at a system boundary

A wall momentum transfer coefficient c is defined such that:

$$c \equiv \frac{\langle P_t \rangle_f^f}{\mu \langle v \rangle_f^f} \tag{14.1}$$

or, using Equation (II.6), as:

$$c \equiv \frac{\langle P_t \rangle_f}{\mu \langle v \rangle_f}, \tag{14.2}$$

where P_t is defined by Equation (8.18) for a closed system boundary and Equation (8.20) for an open system boundary.

It is assumed that at a closed system boundary, where the volume-averaged momentum transfer can be considered a macroscopic viscous shear stress, momentum transfer at the interface between the fluid phase and the wall complies to a mean viscous shear stress in laminar flow on a flat surface over a flow length equal to the fluid phase mean linear distance $\overline{d}_{ff}$ of a fluid particle next to the solid wall (see Section 9.8 for a definition of the fluid phase mean linear distance).

At a microscopic level, viscous shear stress between a fluid and a stationary wall is generally presented in terms of a friction coefficient C_f, defined as (White, 1990):

$$C_f \equiv \frac{2\tau}{\rho_f v^2}. \tag{14.3}$$

In a developing laminar boundary layer, τ is a function of the distance x along the flow direction, so that:

$$C_{f,x} = \frac{2\tau_x}{\rho_f v^2}. \tag{14.4}$$

The drag coefficient C_d is then defined as the mean drag caused by viscous shear stress from the start of boundary layer development to the position $x = L$, given as:

$$C_{d,L} \equiv \frac{1}{L}\int_0^L C_f \, dx \tag{14.5}$$

or:

$$C_{d,L} = \frac{4\tau_L}{\rho_f v^2}. \tag{14.6}$$

Imai (1957) presented the following correlation for the drag coefficient $C_{d,L}$ on a flat surface in a laminar developing boundary layer:

$$C_{d,L} = \frac{1.382}{\sqrt{Re_L}} + \frac{2.3}{Re_L}. \tag{14.7}$$

It is now assumed that the Reynolds number Re is best characterised by the intrinsic volume-averaged velocity $\langle v \rangle_f^f$, that the boundary layer develops over the fluid phase mean linear distance $\bar{d}_{ff}$, and that the averaging nature of the drag coefficient qualifies it as a good representation of the intrinsic volume-averaged viscous shear stress in Definition (14.2). Using Equation (II.6), it follows from Definition (14.2), Equation (14.6) and Equation (14.7), that the wall momentum transfer coefficient c can be written as:

$$c = 0.332\sqrt{\frac{\rho_f \langle v \rangle_f}{\mu \bar{d}_{ff} \varepsilon_f}} + 0.575\frac{1}{\bar{d}_{ff}}. \tag{14.8}$$

14.8 Modelling heat transfer in the solid and the fluid phases at a system boundary

At a closed system boundary condition the thermal contact resistance at the interface between the solid phase and the wall $R_{ss,closed}$ is defined as:

$$R_{ss,closed} \equiv \left| \frac{T_{wall} - \langle T \rangle_s^s}{\langle q \rangle_s^s} \right| \tag{14.9}$$

or, using Equation (II.6), as:

$$R_{ss,closed} \equiv \left| \frac{\varepsilon_s T_{wall} - \langle T \rangle_s}{\langle q \rangle_s} \right|, \tag{14.10}$$

where T_{wall} is the specified wall temperature, $\langle T \rangle_s$ is the solid phase phasial volume-averaged system boundary temperature and $\langle q \rangle_s$ is the phasial volume-averaged heat transfer in the solid phase, defined by Equation (8.28).

The heat transfer coefficient between the fluid phase and the wall is defined as:

$$h_{sf,closed} \equiv \left| \frac{\langle q \rangle_f^f}{T_{wall} - \langle T \rangle_f^f} \right| \tag{14.11}$$

or, using Equation (II.6), as:

$$h_{sf,closed} \equiv \left| \frac{\langle q \rangle_f}{\varepsilon_f T_{wall} - \langle T \rangle_f} \right|, \tag{14.12}$$

where $\langle T \rangle_f$ is the fluid phase phasial volume-averaged system boundary temperature and $\langle q \rangle_f$ is the phasial volume-averaged heat transfer in the fluid phase, defined by Equation (8.34).

It is assumed that the heat transfer coefficient between the fluid phase and the wall comply to the mean heat transfer in laminar flow on a flat surface over a flow length equal to the fluid phase mean linear distance $\bar{d}_{ff}$ of a fluid particle next to the solid wall. Assuming that the intrinsic volume-averaged velocity $\langle v \rangle_f^f$ is the best candidate on which to base the Reynolds number, then it follows from Equation (12.8) and Equation (II.6) that the mean heat transfer coefficient over the fluid phase mean linear distance $\bar{d}_{ff}$ is given by:

$$h_{sf,closed} = 0.664 \left({k_f}^{0.67} {c_{p,f}}^{0.33} \mu^{-0.17} \right) \sqrt{\frac{\rho_f \langle v \rangle_f}{\bar{d}_{ff} \varepsilon_f}} . \tag{14.13}$$

At an open system boundary where fluid enters the porous domain, the fluid temperature is T_f is known. Here, the heat transfer coefficient between the solid phase and the fluid phase is defined as:

$$h_{sf,open,in} \equiv \left| \frac{\langle q \rangle_s^s}{T_f - \langle T \rangle_s^s} \right| \tag{14.14}$$

or, using Equation (II.6), as:

$$h_{sf,open,in} \equiv \left| \frac{\langle q \rangle_s}{\varepsilon_s T_f - \langle T \rangle_s} \right| , \tag{14.15}$$

where T_f is the fluid temperature immediately outside the porous domain.

At an open system boundary where the fluid enters the porous domain perpendicular to the boundary, heat transfer can be characterised by that near the stagnation point of axi-symmetric flow. White (1991) recommends the following relationship for heat transfer at a distance x from the stagnation point:

$$Nu_x = 0.762 {Re_x}^{0.5} Pr^{0.4} . \tag{14.16}$$

The mean heat transfer follows from the integration:

$$Nu_L = \int_0^L Nu_x \, dx \tag{14.17}$$

or:

$$Nu_L = 1.524 \, Re_L^{0.5} \, Pr^{0.4}. \tag{14.18}$$

Assuming that the phasial volume-averaged velocity $\langle v \rangle_f$ is the best candidate to be used in the Nusselt and Reynolds numbers, and that hydrodynamic and thermal boundary layer development occurs over a flow distance $L = \frac{d_{ss}}{2}$, the heat transfer coefficient is given by:

$$h_{sf,open,in} = 1.524 \left(k_f^{0.6} \, c_{p,f}^{0.4} \, \mu^{-0.1} \right) \sqrt{\frac{2 \rho_f \langle v \rangle_f}{\bar{d}_{ss}}}. \tag{14.19}$$

If high Peclét number flow behaviour (*i.e.* ignoring fluid phase conduction along the flow direction) is assumed at an inflow open system boundary, the fluid phase intrinsic volume-averaged system boundary temperature is given by:

$$\langle T \rangle_f^f = T_{f,in} + \frac{\delta A_{ss}}{\delta \dot{m} \, c_{p,f}} h_{sf,open,in} \left(\langle T \rangle_s^s - T_f \right), \tag{14.20}$$

where $T_{f,in}$ is the fluid temperature before entering the porous domain, δA_{ss} is the solid phase surface exposed at the open system boundary and $\delta \dot{m}$ is the mass flow rate of the fluid phase associated with the open boundary area δA_{ss}. The mass flow rate $\delta \dot{m}$ is given as:

$$\delta \dot{m} = \rho_f \langle \boldsymbol{v} \rangle_f \, \delta A_{ss} \cdot \boldsymbol{n}_{fs}, \tag{14.21}$$

where $\boldsymbol{n}_{sf}$ is a normal unit surface vector to the surface δA_{ss}.

Substituting Equation (14.21) and Equation (II.6) into Equation (14.20), rearranging terms and noting that according to Bear and Bachmat (1991, p.37):

$$\frac{\delta A_{ss}}{\delta A_o} = \varepsilon_s , \tag{14.22}$$

yields:

$$\langle T \rangle_f = \varepsilon_f T_{f,in} + \frac{\varepsilon_f h_{sf,open,in}}{\rho_f c_{p,f} \left| \langle \boldsymbol{v} \rangle_f \cdot \boldsymbol{n}_{fs} \right|} \left(\langle T \rangle_s - \varepsilon_s T_f \right) . \tag{14.23}$$

At an open system boundary where fluid leaves the porous domain, the fluid temperature is not known. Instead, the fluid phase volume-averaged temperature just before exiting the porous domain is used as a reference fluid temperature to characterise heat transfer at the exposed surfaces. The heat transfer coefficient between the solid phase and the fluid phase at the outflow system boundary is then defined as:

$$h_{sf,open,out} \equiv \left| \frac{\langle q \rangle_s^s}{\langle T \rangle_f^f - \langle T \rangle_s^s} \right| \tag{14.24}$$

or, using Equation (II.6), as:

$$h_{sf,open,out} \equiv \left| \frac{\langle q \rangle_s}{\frac{\varepsilon_s}{\varepsilon_f} \langle T \rangle_f - \langle T \rangle_s} \right| . \tag{14.25}$$

At an outflow open boundary, it is assumed that the heat transfer is characterised by laminar developing flow on a flat plate. Using Equation (12.9) in which the Reynolds number is based on the intrinsic volume-averaged velocity $\langle v \rangle_f^f$ developing over a

distance $L = \frac{d_{ss}}{2}$ it follows that:

$$h_{sf,open,out} = 0.664\left(k_f{}^{0.67}\, c_{p,f}{}^{0.33}\, \mu^{-0.17}\right)\sqrt{\frac{2\,\rho_f \langle v\rangle_f}{\varepsilon_f\, \bar{d}_{ss}}}\,. \tag{14.26}$$

Assuming high Peclét number thermal behaviour (*i.e.* ignoring fluid phase conduction along the direction of flow), the fluid temperature immediately beyond the outflow open system boundary is given by:

$$T_{f,out} = \langle T\rangle_f^f + \frac{\delta A_{ss}}{\delta \dot{m}\, c_{p,f}}\, h_{sf,open,out}\left(\langle T\rangle_s^s - \langle T\rangle_f^f\right). \tag{14.27}$$

Substituting Equation (14.21), Equation (14.22) and Equation (II.6) into Equation (14.27) yields after rearranging terms:

$$T_{f,out} = \frac{\langle T\rangle_f}{\varepsilon_f} + \frac{h_{sf,open,in}}{\rho_f\, c_{p,f}\left|\langle \boldsymbol{v}\rangle_f \cdot \boldsymbol{n}_{fs}\right|}\left(\langle T\rangle_s - \frac{\varepsilon_s}{\varepsilon_f}\langle T\rangle_f\right). \tag{14.28}$$

PART III

Part III deals with the computational solution of the transformed volume-averaged momentum equation for the fluid phase and the transformed volume-averaged energy equations for the solid and the fluid phases. These equations are discretised in Chapter 15. Chapter 16 presents techniques and algorithms to assist in the computational solution of the discretised forms of the transformed volume-averaged momentum equation and the transformed volume-averaged energy equations for the solid and the fluid phases.

CHAPTER 15

DISCRETISED FORMS OF THE VOLUME-AVERAGED CONTINUITY EQUATION, THE TRANSFORMED VOLUME-AVERAGED MOMENTUM EQUATION AND THE TRANSFORMED VOLUME-AVERAGED ENERGY EQUATIONS

15.1 Overview

In this chapter, a discretisation process is carried out on the transformed volume-averaged momentum equation for the fluid phase and the transformed volume-averaged energy equations for the solid and the fluid phases, yielding three sets of linear algebraic equations.

The discretisation process of the transformed volume-averaged momentum equation and the transformed volume-averaged energy equation for the fluid phase requires the volume-averaged form of the continuity equation (derived in Appendix I).

In thermal systems that employ metallic foams to enhance heat transfer, the flow is hardly ever regulated, even under dynamic thermal loading, and never undergoes rapid changes for practical reasons. Therefore, only the steady-state version of the transformed volume-averaged momentum equation is considered.

Although the effective and coupled thermal conductivity tensors reduce to scalar form for isotropic metallic foams (see Section 11.1), they retain their diagonal tensor form in this analysis.

For a set of discrete grid points in a porous domain, certain grid points are located on the outer surface of a three-dimensional domain or along the perimeter of a two-dimensional domain. These points are referred to as *system boundary grid points*, all others being referred to as *internal grid points*. Finite volumes associated with system boundary grid points are referred to as system boundary finite volumes. It is through special algebraic treatment of the discretised form of the transformed volume-averaged momentum equation and the transformed volume-averaged energy equation for the solid and the fluid phases at these system boundary grid points that different options for momentum and thermal boundary conditions are introduced into the numerical solution scheme.

Boundary conditions for the solution of the transformed volume-averaged momentum equation include the influx of fluid into the porous domain, the efflux of fluid out of the porous domain, and flow along a solid wall bordering the porous domain. Boundary conditions for the transformed volume-averaged energy equation of the solid phase include: a specified solid phase phasial volume-averaged temperature; a specified heat transfer in the solid phase, and; a specified solid wall temperature together with a thermal contact resistance. Boundary conditions for the transformed volume-averaged energy equation of the fluid phase correspond to those of the solid phase, except that a thermal contact resistance is not specified between the fluid phase and a solid wall at a specified temperature.

15.2 Solid phase transformed volume-averaged energy equation

Section 8.3 gives the transformed volume-averaged energy equation for the solid phase as:

$$\rho_s c_{p,s} \frac{\partial \langle T \rangle_s}{\partial t} = \nabla \cdot \left(\boldsymbol{k}_{ss} \cdot \nabla \langle T \rangle_s \right) + \nabla \cdot \left(\boldsymbol{k}_{sf} \cdot \nabla \langle T \rangle_f \right) - \frac{h_{sf}}{\varepsilon_s} \frac{A_{sf}}{V_o} \left(\langle T \rangle_s - \frac{\varepsilon_s}{1-\varepsilon_s} \langle T \rangle_f \right) + \langle I_s \rangle_s , \tag{8.3}$$

where ρ_s is a constant solid phase density, $c_{p,s}$ is a constant isobaric specific heat capacity, $\langle T \rangle_s$ and $\langle T \rangle_f$ are the phasial volume-averaged temperatures for the solid and the fluid phases respectively, t represents time, $\boldsymbol{k}_{ss}$ and $\boldsymbol{k}_{sf}$ are the effective thermal conductivity and the coupled thermal conductivity respectively of the solid phase, h_{sf} is the interphasial heat transfer coefficient, ε_s is the solid phase volume fraction, as defined by Definition (II.1), and $\langle I_s \rangle_s$ is the phasial volume-averaged internal heat source. The solid phase density and the isobaric specific heat capacity are assumed constant.

In a three-dimensional Cartesian coordinate system, Equation (8.3) becomes:

$$\rho_s c_{p,s} \frac{\partial \langle T \rangle_s}{\partial t} - \frac{\partial}{\partial x}\left(k_{ss,x} \frac{\partial \langle T \rangle_s}{\partial x} \right) - \frac{\partial}{\partial y}\left(k_{ss,y} \frac{\partial \langle T \rangle_s}{\partial y} \right) - \frac{\partial}{\partial z}\left(k_{ss,z} \frac{\partial \langle T \rangle_s}{\partial z} \right) - \frac{\partial}{\partial x}\left(k_{sf,x} \frac{\partial \langle T \rangle_f}{\partial x} \right) - \frac{\partial}{\partial y}\left(k_{sf,y} \frac{\partial \langle T \rangle_f}{\partial y} \right) - \frac{\partial}{\partial z}\left(k_{sf,z} \frac{\partial \langle T \rangle_f}{\partial z} \right) + \frac{h_{sf}}{\varepsilon_s} \frac{A_{sf}}{V_o}\left(\langle T \rangle_s - \frac{\varepsilon_s}{1-\varepsilon_s} \langle T \rangle_f \right) - \langle I_s \rangle_s = 0 . \qquad (15.1)$$

[Since $\boldsymbol{k}_{ss}$ and $\boldsymbol{k}_{sf}$ in Equation (8.3) are diagonal, three-dimensional tensors, their components in the principal directions in Equation (15.1) are identified by a single directional index for the sake of simplicity, *e.g.* x instead of xx].

Integrating the first term on the LHS of Equation (15.1) over the three-dimensional finite volume with a grid point in the centre, as shown in Figure 11.1, yields:

$$\int_t^{t+\Delta t} \int_b^t \int_s^n \int_w^e \rho_s c_{p,s} \frac{\partial \langle T \rangle_s}{\partial t} \mathrm{d}x \mathrm{d}y \mathrm{d}z \mathrm{d}t = \rho_s c_{p,s} \left(\langle T \rangle_{s,P}{}^1 - \langle T \rangle_{s,P}{}^0 \right) \Delta x \Delta y \Delta z , \qquad (15.2)$$

where superscript 0 is the quantity value at time t and superscript 1 is the quantity value at time $t+\Delta t$. Generic finite volume dimensions are shown in Figure 15.1. Indexes shown in Figure 15.1 are related according to Table 15.1.

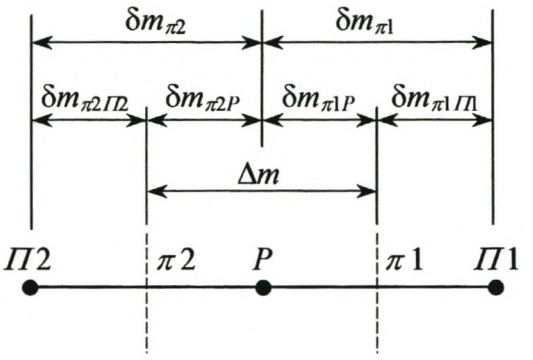

Figure 15.1 Generic finite volume dimensions.

Integrating the second, third and fourth terms on the LHS of Equation (15.1) over the finite volume shown in the Figure 11.1 yields:

$$\int_{t}^{t+\Delta t}\int_{b}^{t}\int_{s}^{n}\int_{w}^{e}\frac{\partial}{\partial m}\left(k_{ss,m}\frac{\partial\langle T\rangle_s}{\partial m}\right)\mathrm{d}x\,\mathrm{d}y\,\mathrm{d}z\,\mathrm{d}t =$$

$$\left\{f\left[\frac{k_{ss,m,\pi1}}{\delta m_{\pi1}}\left(\langle T\rangle_{s,\Pi1}{}^{1}-\langle T\rangle_{s,P}{}^{1}\right)-\frac{k_{ss,m,\pi2}}{\delta m_{\pi2}}\left(\langle T\rangle_{s,P}{}^{1}-\langle T\rangle_{s,\Pi2}{}^{1}\right)\right]+\right.$$

$$\left.(1-f)\left[\frac{k_{ss,m,\pi1}}{\delta m_{\pi1}}\left(\langle T\rangle_{s,\Pi1}{}^{0}-\langle T\rangle_{s,P}{}^{0}\right)-\frac{k_{ss,m,\pi2}}{\delta m_{\pi2}}\left(\langle T\rangle_{s,P}{}^{0}-\langle T\rangle_{s,\Pi2}{}^{0}\right)\right]\right\}\Delta m'\,\Delta m''\,\Delta t\,, \tag{15.3}$$

where $m = x$, y and z, and where f is defined as:

$$f \equiv \frac{\int_{t}^{t+\Delta t}\phi\,\mathrm{d}t+\phi^{0}\Delta t}{\left(\phi^{1}+\phi^{0}\right)\Delta t}, \tag{15.4}$$

Π	$\Pi 1$	$\Pi 2$	π	$\pi 1$	$\pi 2$	m	m'	m''	ξ
E	E	-	e	e	-	x	y	z	1
W	-	W	w	-	w	x	y	z	0
N	N	-	n	n	-	y	x	z	1
S	-	S	s	-	s	y	x	z	0
T	T	-	t	t	-	z	x	y	1
B	-	B	b	-	b	z	x	y	0

Table 15.1 Index designations.

or:

$$\int_{t}^{t+\Delta t} \phi \, \mathrm{d}t = \left[f\phi^{1} - (1-f)\phi^{0} \right] \Delta t \,. \tag{15.5}$$

The indexes $\pi 1$, $\pi 2$, $\Pi 1$ and $\Pi 2$ are correspondingly designated according to Table 15.1.

Integrating the fifth, sixth and seventh terms on the LHS of Equation (15.1) over the finite volume shown in the Figure 11.1 yields:

$$\int_{t}^{t+\Delta t}\int_{b}^{t}\int_{s}^{n}\int_{w}^{e} \frac{\partial}{\partial m}\left(k_{sf,m} \frac{\partial \langle T \rangle_{f}}{\partial m} \right) \mathrm{d}x \, \mathrm{d}y \, \mathrm{d}z \, \mathrm{d}t =$$

$$\left\{ f\left[\frac{k_{sf,m,\pi 1}}{\delta m_{\pi 1}} \left(\langle T \rangle_{f,\Pi 1}{}^{1} - \langle T \rangle_{f,P}{}^{1} \right) - \frac{k_{sf,m,\pi 2}}{\delta m_{\pi 2}} \left(\langle T \rangle_{f,P}{}^{1} - \langle T \rangle_{f,\Pi 2}{}^{1} \right) \right] + \right.$$

$$\left. (1-f)\left[\frac{k_{sf,m,\pi 1}}{\delta m_{\pi 1}} \left(\langle T \rangle_{f,\Pi 1}{}^{0} - \langle T \rangle_{f,P}{}^{0} \right) - \frac{k_{sf,m,\pi 2}}{\delta m_{\pi 2}} \left(\langle T \rangle_{f,P}{}^{0} - \langle T \rangle_{f,\Pi 2}{}^{0} \right) \right] \right\} \Delta m' \, \Delta m'' \, \Delta t \,, \tag{15.6}$$

where $m = x, y$ and z, with the indexes $\pi 1$, $\pi 2$, $\Pi 1$ and $\Pi 2$ are correspondingly designated according to Table 15.1. Integrating the eighth term on the LHS of Equation (15.1) over the finite volume shown in the Figure 11.1 yields:

$$\int_{t}^{t+\Delta t}\int_{b}^{t}\int_{s}^{n}\int_{w}^{e}\frac{h_{sf}}{\varepsilon_s}\frac{A_{sf}}{V_o}\left(\langle T\rangle_s-\frac{\varepsilon_s}{1-\varepsilon_s}\langle T\rangle_f\right)\mathrm{d}x\,\mathrm{d}y\,\mathrm{d}z\,\mathrm{d}t=$$

$$\left(\frac{h_{sf}}{\varepsilon_s}\frac{A_{sf}}{V_o}\right)_P\left[f\left(\langle T\rangle_s-\frac{\varepsilon_s}{1-\varepsilon_s}\langle T\rangle_f\right)_P^{\,1}+\right.$$

$$\left.(1-f)\left(\langle T\rangle_s-\frac{\varepsilon_s}{1-\varepsilon_s}\langle T\rangle_f\right)_P^{\,0}\right]\Delta x\,\Delta y\,\Delta z\,\Delta t. \qquad (15.7)$$

Integrating the last term on the LHS of Equation (15.1) over the finite volume, shown in Figure 11.1, yields:

$$\int_{t}^{t+\Delta t}\int_{b}^{t}\int_{s}^{n}\int_{w}^{e}\langle I\rangle_s\,\mathrm{d}x\,\mathrm{d}y\,\mathrm{d}z\,\mathrm{d}t=\left[f\langle I\rangle_s^{\,1}+(1-f)\langle I\rangle_s^{\,0}\right]\Delta x\,\Delta y\,\Delta z\,\Delta t. \qquad (15.8)$$

It is assumed that the quantity values at the grid points during the time step Δt are characterised by their values at time $t+\Delta t$. This is referred to as the fully implicit scheme (Patankar, 1980). From Definition (15.4) it then follows that $f = 1$.

Substituting Equation (15.2), Equation (15.3) and Equation (15.6) to Equation (15.8) into Equation (15.1), noting that $1-f = 0$, dropping the superscript 1, dividing by Δt and

rearranging terms, yields:

$$\left[\rho_s c_{p,s}\frac{\Delta x\Delta y\Delta z}{\Delta t}+\frac{k_{ss,x,e}\Delta y\Delta z}{\delta x_e}+\frac{k_{ss,x,w}\Delta y\Delta z}{\delta x_w}+\frac{k_{ss,y,n}\Delta x\Delta z}{\delta y_n}+\frac{k_{ss,y,s}\Delta x\Delta z}{\delta y_s}+\right.$$
$$\left.\frac{k_{ss,z,t}\Delta x\Delta y}{\delta z_t}+\frac{k_{ss,z,b}\Delta x\Delta y}{\delta z_b}+h_{sf,P}\left(\frac{A_{sf}}{V_o}\right)_P\frac{\Delta x\Delta y\Delta z}{\varepsilon_{s,P}}\right]\langle T\rangle_{s,P}=$$
$$\frac{k_{ss,x,e}\Delta y\Delta z}{\delta x_e}\langle T\rangle_{s,E}+\frac{k_{ss,x,w}\Delta y\Delta z}{\delta x_w}\langle T\rangle_{s,W}+\frac{k_{ss,y,n}\Delta x\Delta z}{\delta y_n}\langle T\rangle_{s,N}+\frac{k_{ss,y,s}\Delta x\Delta z}{\delta y_s}\langle T\rangle_{s,S}+$$
$$\frac{k_{ss,z,t}\Delta x\Delta y}{\delta z_t}\langle T\rangle_{s,T}+\frac{k_{ss,z,b}\Delta x\Delta y}{\delta z_b}\langle T\rangle_{s,B}+$$
$$\left[h_{sf,P}\left(\frac{A_{sf}}{V_o}\right)_P\frac{\Delta x\Delta y\Delta z}{1-\varepsilon_{s,P}}-\frac{k_{sf,x,e}\Delta y\Delta z}{\delta x_e}-\frac{k_{sf,x,w}\Delta y\Delta z}{\delta x_w}-\right.$$
$$\left.\frac{k_{sf,y,n}\Delta x\Delta z}{\delta y_n}-\frac{k_{sf,y,s}\Delta x\Delta z}{\delta y_s}-\frac{k_{sf,z,t}\Delta x\Delta y}{\delta z_t}-\frac{k_{sf,z,b}\Delta x\Delta y}{\delta z_b}\right]\langle T\rangle_{f,P}+$$
$$\frac{k_{sf,x,e}\Delta y\Delta z}{\delta x_e}\langle T\rangle_{f,E}+\frac{k_{sf,x,w}\Delta y\Delta z}{\delta x_w}\langle T\rangle_{f,W}+\frac{k_{sf,y,n}\Delta x\Delta z}{\delta y_n}\langle T\rangle_{f,N}+$$
$$\frac{k_{sf,y,s}\Delta x\Delta z}{\delta y_s}\langle T\rangle_{f,S}+\frac{k_{sf,z,t}\Delta x\Delta y}{\delta z_t}\langle T\rangle_{f,T}+\frac{k_{sf,z,b}\Delta x\Delta y}{\delta z_b}\langle T\rangle_{f,B}+$$
$$\langle I_s\rangle_s\,\Delta x\Delta y\Delta z+\rho_s c_{p,s}\frac{\Delta x\Delta y\Delta z}{\Delta t}\langle T\rangle_{s,P}{}^0. \qquad (15.9)$$

Although the thermal conductivities of the solid and the fluid phases are considered constant, the effective thermal conductivity k_{ss} and the coupled thermal conductivity k_{sf} are both functions of the porosity, which is a spatially variable parameter. At a finite volume boundary π, these quantities are determined from their values at the grid points by:

$$k_{ss,\pi}=\frac{\delta m_\pi}{\dfrac{\delta m_{\pi\Pi}}{k_{ss,\Pi}}+\dfrac{\delta m_{\pi P}}{k_{ss,P}}} \qquad (15.10)$$

and:

$$k_{sf,\pi} = \frac{\delta m_{\pi}}{\dfrac{\delta m_{\pi\Pi}}{k_{sf,\Pi}} + \dfrac{\delta m_{\pi P}}{k_{sf,P}}}, \tag{15.11}$$

where π = e, w, n, s, t or b. The index Π is correspondingly designated according to Table 15.1. The dimensions δm_{π}, $\delta m_{\pi\Pi}$ and $\delta m_{\pi P}$ are shown in Figure 15.1 (either as $\delta m_{\pi 1}$, $\delta m_{\pi 1\Pi 1}$ and $\delta m_{\pi 1P}$, or as $\delta m_{\pi 2}$, $\delta m_{\pi 2\Pi 2}$ and $\delta m_{\pi 2P}$).

Equation (15.9) can be written in the general form:

$$a_P\langle T\rangle_{s,P} = a_E\langle T\rangle_{s,E} + a_W\langle T\rangle_{s,W} + a_N\langle T\rangle_{s,N} + a_S\langle T\rangle_{s,S} + a_T\langle T\rangle_{s,T} + a_B\langle T\rangle_{s,B} + b, \tag{15.12}$$

with:

$$a_{\Pi} = \frac{k_{ss,m,\pi}\Delta m'\Delta m''}{\delta m_{\pi}}, \tag{15.13}$$

$$b = S_c\Delta x\Delta y\Delta z + a_P{}^0\langle T\rangle_{s,P}{}^0 + \langle I\rangle_s\,\Delta x\Delta y\Delta z, \tag{15.14}$$

$$a_P{}^0 = \rho_s\, c_{p,s}\,\frac{\Delta x\Delta y\Delta z}{\Delta t}, \tag{15.15}$$

$$a_P = a_E + a_W + a_N + a_S + a_T + a_B + a_P{}^0 + a_P' \tag{15.16}$$

and:

$$a_P' = h_{sf,P}\left(\frac{A_{sf}}{V_o}\right)_P \frac{\Delta x\Delta y\Delta z}{\varepsilon_{s,P}}. \tag{15.17}$$

The source term in Equation (15.14) can be written as:

$$S_c \Delta x \Delta y \Delta z = a_{FP}\langle T\rangle_{f,P} + a_{FE}\langle T\rangle_{f,E} + a_{FW}\langle T\rangle_{f,W} + a_{FN}\langle T\rangle_{f,N} + a_{FS}\langle T\rangle_{f,S} + a_{FT}\langle T\rangle_{f,T} + a_{FB}\langle T\rangle_{f,B}, \quad (15.18)$$

where:

$$a_{F\Pi} = \frac{k_{sf,m,\pi}\Delta m' \Delta m''}{\delta m_\pi} \quad (15.19)$$

and:

$$a_{FP} = h_{sf,P}\left(\frac{A_{sf}}{V_o}\right)_P \frac{\Delta x \Delta y \Delta z}{1-\varepsilon_{s,P}} - a_{FE} - a_{FW} - a_{FN} - a_{FS} - a_{FT} - a_{FB}. \quad (15.20)$$

In Equation (15.13) and Equation (15.19), $\Pi = E$, W, N, S, T and B, and the indexes π, m, m' and m'' are correspondingly designated according to Table 15.1.

System boundary grid points

Five kinds of system boundary conditions for the solid phase are considered. (1) A specified phasial volume-averaged temperature at a closed system boundary. (2) A specified phasial volume-averaged heat flux. (3) A closed system boundary at a specified wall temperature and a contact resistance between the wall and the solid matrix. (4) An open system boundary with fluid entering the porous domain. (5) An open system boundary with fluid leaving the porous domain.

As in the case of the discretised form of the transformed volume-averaged momentum equation at system boundary grid points, for deriving the appropriate discretised equation coefficients in each of these cases, let the closed system boundary correspond to one of the finite volume boundaries shown in Figure 11.1, denoted π, where $\pi = e$, w, n, s, t or b.

1. Closed system boundary with specified phasial volume-averaged temperature $\langle T \rangle_{s,P}$

For the grid point P of the finite volume associated with the boundary π, the coefficients of Equation (15.12), given by Equation (15.13) to Equation (15.20) reduce to:

$$a_P = 1, \tag{15.21}$$

$$b = \langle T \rangle_{s,P} \tag{15.22}$$

and:

$$a_S = a_W = a_N = a_S = a_T = a_B = 0. \tag{15.23}$$

2. Open or closed system boundary with specified phasial volume-averaged heat flux $\langle q \rangle_{s,\pi}$

Consider the conduction terms in square brackets in Equation (15.3) and Equation (15.6) describing conduction across the $\pi 1$ and $\pi 2$ boundaries, where the indexes $\pi 1$ and $\pi 2$ are designated according to Table 15.1. Using Equation (8.28), the sum of the conduction terms at either the $\pi 1$ and $\pi 2$ boundary in Equation (15.3) and Equation (15.6) can be substituted by the term:

$$-\langle q \rangle_{s,\pi}. \tag{15.24}$$

This yields the same coefficients as those given by Equation (15.13) to Equation (15.20),

except for:

$$a_{\Pi} = 0, \tag{15.25}$$

$$a_{F\Pi} = 0 \tag{15.26}$$

and:

$$b = S_c \Delta x \Delta y \Delta z + a_P{}^0 \langle T \rangle_{s,P}{}^0 + \langle I_s \rangle_s \Delta x \Delta y \Delta z + (-1)^{\xi} \langle q \rangle_{s,\pi} \Delta m' \Delta m'', \tag{15.27}$$

where $\Pi = E$, W, N, S, T or B in Equation (15.25) and Equation (15.26), which refers to the grid point excluded by the system boundary. The indexes m' and m'' in Equation (15.27) are correspondingly designated according to Table 15.1.

3. *Closed system boundary at wall temperature T_{wall}, and a contact resistance R_{ss} between the wall and the solid matrix*

Consider the conduction terms in square brackets in Equation (15.3) and Equation (15.6) describing conduction across the $\pi 1$ and $\pi 2$ boundaries, where the indexes $\pi 1$ and $\pi 2$ are designated according to Table 15.1. If the solid phase system boundary corresponds to $\pi = e$, n, or t, the sum of the conduction terms describing conduction across the $\pi 1$ boundary, can be substituted by the term:

$$\frac{1}{R_{ss,\pi}} \left(\varepsilon_{s,P} T_{wall,\pi} - \langle T \rangle_{s,P} \right), \tag{15.28}$$

where R_{ss} is defined by Definition (14.10).

Similarly, if the solid phase system boundary corresponds to $\pi = w$, s, or b, the sum of the conduction terms describing conduction across the $\pi 2$ boundary, can be substituted by the term:

$$\frac{1}{R_{ss,\pi}}\left(\langle T\rangle_{s,P} - \varepsilon_{s,P} T_{wall,\pi}\right). \tag{15.29}$$

These substitutions yield the same coefficients as those given by Equation (15.13) to Equation (15.20), except for:

$$a_{\Pi} = 0, \tag{15.30}$$

$$a_{F\Pi} = 0, \tag{15.31}$$

$$b = S_c \Delta x \Delta y \Delta z + a_P{}^0 \langle T\rangle_{s,P}{}^0 + \langle I_s\rangle_s \Delta x \Delta y \Delta z + \frac{\varepsilon_{s,P} T_{wall,\pi}}{R_{ss,\pi}} \Delta m' \Delta m'' \tag{15.32}$$

and:

$$a_P = a_E + a_W + a_N + a_S + a_T + a_B + a_P{}^0 + a_P' + \frac{\Delta m' \Delta m''}{R_{ss,\pi}}, \tag{15.33}$$

where $\Pi = E$, W, N, S, T or B in Equation (15.30) and Equation (15.31) refers to the grid point excluded by the system boundary. The indexes m' and m'' in Equation (15.32) and Equation (15.33) are correspondingly designated according to Table 15.1.

4. *Open system boundary with fluid entering the porous domain and a heat transfer coefficient $h_{sf,open,in}$ between the solid phase and the fluid phase*

Consider the conduction terms in square brackets in Equation (15.3) and Equation (15.6) describing conduction across the $\pi 1$ and $\pi 2$ boundaries, where the indexes $\pi 1$ and $\pi 2$ are designated according to Table 15.1. If the solid phase system boundary corresponds to $\pi = e$, n, or t, the sum of the conduction terms describing conduction across the $\pi 1$ boundary, can be substituted by the term:

$$h_{sf,open,in,\pi}\left(\varepsilon_{s,P} T_{f,\pi} - \langle T \rangle_{s,P}\right), \tag{15.34}$$

where $h_{sf,open,in}$ is given by Equation (14.19).

Similarly, if the solid phase system boundary corresponds to $\pi = w$, s, or b, the sum of the conduction terms describing conduction across the $\pi 2$ boundary, can be substituted by the term:

$$h_{sf,open,in,\pi}\left(\langle T \rangle_{s,P} - \varepsilon_{s,P} T_{f,\pi}\right). \tag{15.35}$$

These substitutions yield the same coefficients as those given by Equation (15.13) to Equation (15.20), except for:

$$a_{\Pi} = 0, \tag{15.36}$$

$$a_{F\Pi} = 0, \tag{15.37}$$

$$b = S_c \Delta x \Delta y \Delta z + a_P{}^0 \langle T \rangle_{s,P}{}^0 + \langle I_s \rangle_s \Delta x \Delta y \Delta z + h_{sf,open,in,\pi}\, \varepsilon_{s,P}\, T_{f,\pi} \Delta m' \Delta m'' \tag{15.38}$$

and:

$$a_P = a_E + a_W + a_N + a_S + a_T + a_B + a_P{}^0 + a_P' + h_{sf,open,in,\pi}\, \Delta m' \Delta m'', \tag{15.39}$$

where $\Pi = E$, W, N, S, T or B in Equation (15.36) and Equation (15.37) refers to the grid point excluded by the system boundary. The indexes m' and m'' in Equation (15.38) and Equation (15.39) are correspondingly designated according to Table 15.1.

5. *Open system boundary with fluid leaving the porous domain and a heat transfer coefficient $h_{sf,open,out}$ between the solid phase and the fluid phase*

Consider the conduction terms in square brackets in Equation (15.3) and Equation (15.6) describing conduction across the $\pi 1$ and $\pi 2$ boundaries, where the indexes $\pi 1$ and $\pi 2$ are designated according to Table 15.1. If the solid phase system boundary corresponds to $\pi = e$, n, or t, the sum of the conduction terms describing conduction across the $\pi 1$ boundary, can be substituted by the term:

$$h_{sf,open,out,\pi}\left(\frac{\varepsilon_{s,P}}{1-\varepsilon_{s,P}}\langle T\rangle_{f,P} - \langle T\rangle_{s,P}\right), \tag{15.40}$$

where $h_{sf,open,out}$ is given by Equation (14.26).

Similarly, if the solid phase system boundary corresponds to $\pi = w$, s, or b, the sum of the conduction terms describing conduction across the $\pi 2$ boundary, can be substituted by the term:

$$h_{sf,open,out,\pi}\left(\langle T\rangle_{s,P} - \frac{\varepsilon_{s,P}}{1-\varepsilon_{s,P}}\langle T\rangle_{f,P}\right). \tag{15.41}$$

These substitutions yield the same coefficients as those given by Equation (15.13) to

Equation (15.20), except for:

$$a_{\Pi} = 0, \tag{15.42}$$

$$a_{F\Pi} = 0, \tag{15.43}$$

$$a_P = a_E + a_W + a_N + a_S + a_T + a_B + a_P^{\,0} + a_P' + h_{sf,open,out,\pi}\,\Delta m'\,\Delta m'' \tag{15.44}$$

and:

$$a_{FP} = h_{sf,P}\left(\frac{A_{sf}}{V_o}\right)_P \frac{\Delta x\,\Delta y\,\Delta z}{1-\varepsilon_{s,P}} - a_{FE} - a_{FW} - a_{FN} - a_{FS} - a_{FT} - a_{FB} + \frac{\varepsilon_{s,P}}{1-\varepsilon_{s,P}} h_{sf,open,out,\pi}\,\Delta m'\,\Delta m'', \tag{15.45}$$

where $\Pi = E$, W, N, S, T or B in Equation (15.42) and Equation (15.43), which is the grid point excluded by the system boundary. The indexes m' and m'' in Equation (15.44) and Equation (15.45) are correspondingly designated according to Table 15.1.

15.3 Fluid phase transformed volume-averaged energy equation

In Section 8.3, the transformed volume-averaged energy equation for the fluid phase is given as:

$$\rho_f c_{p,f} \frac{\partial \langle T \rangle_f}{\partial t} = \nabla \cdot \left[\left(\boldsymbol{k}_{ff} + \boldsymbol{D}_T \right) \cdot \nabla \langle T \rangle_f \right] + \nabla \cdot \left(\boldsymbol{k}_{fs} \cdot \nabla \langle T \rangle_s \right) - \frac{h_{sf}}{\varepsilon_f} \frac{A_{sf}}{V_o} \left(\langle T \rangle_f - \frac{\varepsilon_f}{1-\varepsilon_f} \langle T \rangle_s \right) - \rho_f c_{p,f} \nabla \cdot \left(\frac{1}{\varepsilon_f} \langle \boldsymbol{v} \rangle_f \langle T \rangle_f \right) + \langle I_f \rangle_f, \tag{8.5}$$

where ρ_f is the fluid density, $c_{p,f}$ is the isobaric specific heat capacity, $\langle T \rangle_s$ and $\langle T \rangle_f$ are the phasial volume-averaged temperatures for the solid and the fluid phases respectively, t represents time, $\boldsymbol{k}_{ff}$ and $\boldsymbol{k}_{fs}$ are the effective thermal conductivity and the coupled thermal conductivities respectively of the fluid phase, $\boldsymbol{D}_T$ is the thermal dispersion tensor, h_{sf} is the interphasial heat transfer coefficient, ε_f is the porosity, [or the fluid phase volume fraction defined by Definition (II.1)], $\langle \boldsymbol{v} \rangle_f$ is the phasial volume average velocity vector for the fluid phase and $\langle I_f \rangle_f$ is the phasial volume-averaged internal heat source for the fluid phase. The fluid density and the isobaric specific heat capacity are assumed constant.

Equation (8.5) and the volume-averaged continuity equation [Equation (2.5)] can be written in a three-dimensional Cartesian coordinate system as:

$$\rho_f c_{p,f} \frac{\partial \langle T \rangle_f}{\partial t} - \frac{\partial}{\partial x}\left[\left(k_{ff,x} + D_{T,x} \right) \frac{\partial \langle T \rangle_f}{\partial x} \right] -$$

$$\frac{\partial}{\partial y}\left[\left(k_{ff,y} + D_{T,y} \right) \frac{\partial \langle T \rangle_f}{\partial y} \right] - \frac{\partial}{\partial z}\left[\left(k_{ff,z} + D_{T,z} \right) \frac{\partial \langle T \rangle_f}{\partial z} \right] -$$

$$\frac{\partial}{\partial x}\left(k_{fs,x} \frac{\partial \langle T \rangle_s}{\partial x} \right) - \frac{\partial}{\partial y}\left(k_{fs,y} \frac{\partial \langle T \rangle_s}{\partial y} \right) - \frac{\partial}{\partial z}\left(k_{fs,z} \frac{\partial \langle T \rangle_s}{\partial z} \right) + \frac{h_{sf}}{\varepsilon_f} \frac{A_{sf}}{V_o}\left(\langle T \rangle_f - \frac{\varepsilon_f}{1-\varepsilon_f} \langle T \rangle_s \right) +$$

$$\rho_f c_{p,f}\left[\frac{\partial}{\partial x}\left(\frac{1}{\varepsilon_f} \langle v_x \rangle_f \langle T \rangle_f \right) + \frac{\partial}{\partial y}\left(\frac{1}{\varepsilon_f} \langle v_y \rangle_f \langle T \rangle_f \right) + \frac{\partial}{\partial z}\left(\frac{1}{\varepsilon_f} \langle v_z \rangle_f \langle T \rangle_f \right) \right] - \langle I_f \rangle_f = 0 \tag{15.46}$$

and:

$$\frac{\partial}{\partial x} \frac{\langle v_x \rangle_f}{\varepsilon_f} + \frac{\partial}{\partial y} \frac{\langle v_y \rangle_f}{\varepsilon_f} + \frac{\partial}{\partial z} \frac{\langle v_z \rangle_f}{\varepsilon_f} + \frac{\langle v_x \rangle_f}{{\varepsilon_f}^2} \frac{\partial \varepsilon_f}{\partial x} + \frac{\langle v_y \rangle_f}{{\varepsilon_f}^2} \frac{\partial \varepsilon_f}{\partial y} + \frac{\langle v_z \rangle_f}{{\varepsilon_f}^2} \frac{\partial \varepsilon_f}{\partial z} = 0. \tag{15.47}$$

[Since $\boldsymbol{D}_T$, $\boldsymbol{k}_{ff}$ and $\boldsymbol{k}_{fs}$ in Equation (8.5) are diagonal, three-dimensional tensors, their components in the principal directions in Equation (15.46) are identified by a single directional index for the sake of simplicity, *e.g.* x instead of xx].

After multiplying by $\rho_f \langle T \rangle_f$ and noting that the density ρ_f is constant, Equation (15.47) can be written as:

$$\langle T \rangle_f \frac{\partial}{\partial x}\left(\frac{\rho_f}{\varepsilon_f}\langle v_x \rangle_f\right) + \langle T \rangle_f \frac{\partial}{\partial y}\left(\frac{\rho_f}{\varepsilon_f}\langle v_y \rangle_f\right) + \langle T \rangle_f \frac{\partial}{\partial z}\left(\frac{\rho_f}{\varepsilon_f}\langle v_z \rangle_f\right) +$$

$$\langle T \rangle_f \frac{\rho_f}{\varepsilon_f^{\,2}}\langle v_x \rangle_f \frac{\partial \varepsilon_f}{\partial x} + \langle T \rangle_f \frac{\rho_f}{\varepsilon_f^{\,2}}\langle v_y \rangle_f \frac{\partial \varepsilon_f}{\partial y} + \langle T \rangle_f \frac{\rho_f}{\varepsilon_f^{\,2}}\langle v_z \rangle_f \frac{\partial \varepsilon_f}{\partial z} = 0. \quad (15.48)$$

Substituting the identity:

$$\rho_f \frac{\partial \langle T \rangle_f}{\partial t} = \frac{\partial\left(\rho_f \langle T \rangle_f\right)}{\partial t} - \langle T \rangle_f \frac{\partial \rho_f}{\partial t} \quad (15.49)$$

into Equation (15.46), subtracting Equation (15.48), dividing by $c_{p,f}$ and substituting the definition of a total heat transfer coefficient:

$$k_{total,m} \equiv k_{ff,m} + D_{T,m}, \quad (15.50)$$

where $m = x$, y or z, yields:

$$\frac{\partial\left(\rho_f \langle T\rangle_f\right)}{\partial t} - \langle T\rangle_f \frac{\partial \rho_f}{\partial t} +$$

$$\frac{\partial}{\partial x}\left[\frac{\rho_f}{\varepsilon_f}\langle v_x\rangle_f \langle T\rangle_f - \frac{k_{total,x}}{c_{p,f}}\frac{\partial\langle T\rangle_f}{\partial x}\right] - \langle T\rangle_f \frac{\partial}{\partial x}\left(\frac{\rho_f}{\varepsilon_f}\langle v_x\rangle_f\right) +$$

$$\frac{\partial}{\partial y}\left[\frac{\rho_f}{\varepsilon_f}\langle v_y\rangle_f \langle T\rangle_f - \frac{k_{total,y}}{c_{p,f}}\frac{\partial\langle T\rangle_f}{\partial y}\right] - \langle T\rangle_f \frac{\partial}{\partial y}\left(\frac{\rho_f}{\varepsilon_f}\langle v_y\rangle_f\right) -$$

$$\frac{\partial}{\partial z}\left[\frac{\rho_f}{\varepsilon_f}\langle v_z\rangle_f \langle T\rangle_f - \frac{k_{total,z}}{c_{p,f}}\frac{\partial\langle T\rangle_f}{\partial z}\right] - \langle T\rangle_f \frac{\partial}{\partial z}\left(\frac{\rho_f}{\varepsilon_f}\langle v_z\rangle_f\right) -$$

$$\frac{\partial}{\partial x}\left(\frac{k_{fs,x}}{c_{p,f}}\frac{\partial\langle T\rangle_s}{\partial x}\right) - \frac{\partial}{\partial y}\left(\frac{k_{fs,y}}{c_{p,f}}\frac{\partial\langle T\rangle_s}{\partial y}\right) - \frac{\partial}{\partial z}\left(\frac{k_{fs,z}}{c_{p,f}}\frac{\partial\langle T\rangle_s}{\partial z}\right) +$$

$$\frac{h_{sf}}{c_{p,f}\varepsilon_f}\frac{A_{sf}}{V_o}\left(\langle T\rangle_f - \frac{\varepsilon_f}{1-\varepsilon_f}\langle T\rangle_s\right) - \frac{\langle I_f\rangle_f}{c_{p,f}} -$$

$$\langle T\rangle_f \frac{\rho_f}{\varepsilon_f^{\,2}}\langle v_x\rangle_f \frac{\partial \varepsilon_f}{\partial x} - \langle T\rangle_f \frac{\rho_f}{\varepsilon_f^{\,2}}\langle v_y\rangle_f \frac{\partial \varepsilon_f}{\partial y} -$$

$$\langle T\rangle_f \frac{\rho_f}{\varepsilon_f^{\,2}}\langle v_z\rangle_f \frac{\partial \varepsilon_f}{\partial z} = 0. \qquad (15.51)$$

Integrating Equation (15.51) over the finite volume shown in Figure 11.1, following the analytical process illustrated between Equation (15.2) and Equation (15.8), and assuming that the quantity values at the grid points during the time step Δt are characterised by their

values at time $t+\Delta t$ (fully implicit scheme), yields:

$$\left(\rho_f\langle T\rangle_{f,P}-\rho_f{}^0\langle T\rangle_{f,P}{}^0\right)\Delta x\Delta y\Delta z-\langle T\rangle_{f,P}\left(\rho_f-\rho_f{}^0\right)\Delta x\Delta y\Delta z+$$
$$\left[\left(\frac{\rho_f}{\varepsilon_f}\langle v_x\rangle_f\langle T\rangle_f-\frac{k_{total,x}}{c_{p,f}}\frac{\partial\langle T\rangle_f}{\partial x}\right)_e-\left(\frac{\rho_f}{\varepsilon_f}\langle v_x\rangle_f\langle T\rangle_f-\frac{k_{total,x}}{c_{p,f}}\frac{\partial\langle T\rangle_f}{\partial x}\right)_w\right]\Delta y\Delta z\Delta t-$$
$$\langle T\rangle_{f,P}\left[\left(\frac{\rho_f}{\varepsilon_f}\langle v_x\rangle_f\right)_e-\left(\frac{\rho_f}{\varepsilon_f}\langle v_x\rangle_f\right)_w\right]\Delta y\Delta z\Delta t+$$
$$\left[\left(\frac{\rho_f}{\varepsilon_f}\langle v_y\rangle_f\langle T\rangle_f-\frac{k_{total,y}}{c_{p,f}}\frac{\partial\langle T\rangle_f}{\partial y}\right)_n-\left(\frac{\rho_f}{\varepsilon_f}\langle v_y\rangle_f\langle T\rangle_f-\frac{k_{total,y}}{c_{p,f}}\frac{\partial\langle T\rangle_f}{\partial y}\right)_s\right]\Delta x\Delta z\Delta t-$$
$$\langle T\rangle_{f,P}\left[\left(\frac{\rho_f}{\varepsilon_f}\langle v_y\rangle_f\right)_n-\left(\frac{\rho_f}{\varepsilon_f}\langle v_y\rangle_f\right)_s\right]\Delta x\Delta z\Delta t-$$
$$\left[\left(\frac{\rho_f}{\varepsilon_f}\langle v_z\rangle_f\langle T\rangle_f-\frac{k_{total,z}}{c_{p,f}}\frac{\partial\langle T\rangle_f}{\partial z}\right)_t-\left(\frac{\rho_f}{\varepsilon_f}\langle v_z\rangle_f\langle T\rangle_f-\frac{k_{total,z}}{c_{p,f}}\frac{\partial\langle T\rangle_f}{\partial z}\right)_b\right]\Delta x\Delta y\Delta t-$$
$$\langle T\rangle_{f,P}\left[\left(\frac{\rho_f}{\varepsilon_f}\langle v_z\rangle_f\right)_t-\left(\frac{\rho_f}{\varepsilon_f}\langle v_z\rangle_f\right)_b\right]\Delta x\Delta y\Delta t-$$
$$\left[\frac{k_{fs,x,e}}{c_{p,f}\delta x_e}\left(\langle T\rangle_{s,E}-\langle T\rangle_{s,P}\right)-\frac{k_{fs,x,w}}{c_{p,f}\delta x_w}\left(\langle T\rangle_{s,P}-\langle T\rangle_{s,W}\right)\right]\Delta y\Delta z\Delta t-$$
$$\left[\frac{k_{fs,y,n}}{c_{p,f}\delta y_n}\left(\langle T\rangle_{s,N}-\langle T\rangle_{s,P}\right)-\frac{k_{fs,y,s}}{c_{p,f}\delta y_s}\left(\langle T\rangle_{s,P}-\langle T\rangle_{s,S}\right)\right]\Delta x\Delta z\Delta t+$$
$$\left[\frac{k_{fs,z,t}}{c_{p,f}\delta z_t}\left(\langle T\rangle_{s,T}-\langle T\rangle_{s,P}\right)-\frac{k_{fs,z,b}}{c_{p,f}\delta z_b}\left(\langle T\rangle_{s,P}-\langle T\rangle_{s,B}\right)\right]\Delta x\Delta y\Delta t-$$
$$\langle T\rangle_{f,P}\frac{\rho_f}{\varepsilon_{f,P}{}^2}\langle v_x\rangle_{f,P}\left(\varepsilon_{f,e}-\varepsilon_{f,w}\right)\Delta y\Delta z\Delta t-$$
$$\langle T\rangle_{f,P}\frac{\rho_f}{\varepsilon_{f,P}{}^2}\langle v_y\rangle_{f,P}\left(\varepsilon_{f,n}-\varepsilon_{f,s}\right)\Delta x\Delta z\Delta t-$$
$$\langle T\rangle_{f,P}\frac{\rho_f}{\varepsilon_{f,P}{}^2}\langle v_z\rangle_{f,P}\left(\varepsilon_{f,t}-\varepsilon_{f,b}\right)\Delta x\Delta y\Delta t+$$
$$\left[\frac{h_{sf}}{c_{p,f}\,\varepsilon_f}\frac{A_{sf}}{V_o}\left(\langle T\rangle_f-\frac{\varepsilon_f}{1-\varepsilon_f}\langle T\rangle_s\right)\right]_P\Delta x\Delta y\Delta z\Delta t-$$
$$\frac{\langle I_f\rangle_{f,P}}{c_{p,f}}\Delta x\Delta y\Delta z\Delta t=0. \qquad (15.52)$$

Although the thermal conductivities of the solid and the fluid phases are considered to be constant, the total heat transfer coefficient, defined in Definition (15.50), is a function of the porosity and the velocity distribution, and the coupled thermal conductivity k_{fs} is a function of the porosity. The porosity and the velocity are both spatially variable parameters. At a finite volume boundary π, these quantities are determined from their values at the grid points by:

$$k_{total,\pi} = \frac{\delta m_{\pi}}{\dfrac{\delta m_{\pi\Pi}}{k_{eff,\Pi}} + \dfrac{\delta m_{\pi P}}{k_{eff,P}}} \tag{15.53}$$

and:

$$k_{fs,\pi} = \frac{\delta m_{\pi}}{\dfrac{\delta m_{\pi\Pi}}{k_{fs,\Pi}} + \dfrac{\delta m_{\pi P}}{k_{fs,P}}}, \tag{15.54}$$

where $\pi = e, w, n, s, t$ or b and the index Π is correspondingly designated according to Table 15.1. The dimensions δm_{π}, $\delta m_{\pi\Pi}$ and $\delta m_{\pi P}$ are shown in Figure 15.1 (either as $\delta m_{\pi 1}$, $\delta m_{\pi 1\Pi 1}$ and $\delta m_{\pi 1P}$, or as $\delta m_{\pi 2}$, $\delta m_{\pi 2\Pi 2}$ and $\delta m_{\pi 2P}$).

From a generalised formulation by Patankar (1980), it follows that:

$$\left(\frac{\rho_f}{\varepsilon_f} \langle v_m \rangle_f \langle T \rangle_f - \frac{k_{total,m}}{c_{p,f}} \frac{\partial \langle T \rangle_f}{\partial m} - \langle T \rangle_{f,P} \frac{\rho_f}{\varepsilon_f} \langle v_m \rangle_f \right)_{\pi} =$$

$$(-1)^{\xi} \left\{ \frac{D_{ft,\pi} \rho_f}{\delta m_{\pi}} \mathrm{A}(|Pe_{\pi}|) + \max\left[(-1)^{\xi} \frac{\rho_f}{\varepsilon_{f,\pi}} \langle v_{\mathrm{m}} \rangle_{f,\pi}, 0 \right] \right\} \left(\langle T \rangle_{f,\Pi} - \langle T \rangle_{f,P} \right), \tag{15.55}$$

where D_{ft} is the thermal diffusivity defined as:

$$D_{ft,\pi} \equiv \frac{k_{total,m,\pi}}{\rho_f c_{p,f}}, \tag{15.56}$$

the Peclét number Pe is defined as:

$$Pe_{\pi} = \frac{\langle v_m \rangle_{f,\pi} \delta m_{\pi}}{\varepsilon_{f,\pi} D_{ft,\pi}} \tag{15.57}$$

and, according to Patankar's power-law scheme:

$$\mathrm{A}(|Pe_{\pi}|) = \max\left[0,\ (1 - 0.1|Pe_{\pi}|)^5\right]. \tag{15.58}$$

In Equation (15.55), Definition (15.56), Definition (15.57) and Equation (15.58), $\pi = e, w, n, s, t$ or b. The indexes Π, m and ξ are correspondingly designated according to Table 15.1.

After substituting Equation (15.55), dividing by Δt and rearranging terms, Equation (15.52) can be written in the general form:

$$a_P \langle T \rangle_{f,P} = a_E \langle T \rangle_{f,E} + a_W \langle T \rangle_{f,W} + a_N \langle T \rangle_{f,N} + a_S \langle T \rangle_{f,S} + a_T \langle T \rangle_{f,T} + a_B \langle T \rangle_{f,B} + b, \tag{15.59}$$

with:

$$a_{\Pi} = \left\{ \frac{D_{ft,\pi} \rho_f}{\delta m_{\pi}} \mathrm{A}(|Pe_{\pi}|) + \max\left[(-1)^{\xi} \frac{\rho_f}{\varepsilon_{f,\pi}} \langle v_m \rangle_{f,\pi}, 0 \right] \right\} \Delta m' \Delta m'', \tag{15.60}$$

$$a_P = a_E + a_W + a_N + a_S + a_T + a_B + a_P{}^0 + a_P', \tag{15.61}$$

$$b = S_c \Delta x \Delta y \Delta z + a_P{}^0 \langle T \rangle_{f,P}{}^0 + \frac{\langle I_f \rangle_f}{c_{p,f}} \Delta x \Delta y \Delta z, \tag{15.62}$$

$$a_P{}^0 = \rho_f{}^0 \frac{\Delta x \Delta y \Delta z}{\Delta t} \tag{15.63}$$

and:

$$a_P' = \frac{h_{sf,P}}{c_{p,f}}\left(\frac{A_{sf}}{V_o}\right)_P \frac{\Delta x \Delta y \Delta z}{\varepsilon_{f,P}} - \frac{\rho_f}{\varepsilon_{f,P}^2}\langle v_x\rangle_{f,P}\left(\varepsilon_{f,e} - \varepsilon_{f,w}\right)\Delta y \Delta z -$$

$$\frac{\rho_f}{\varepsilon_{f,P}^2}\langle v_y\rangle_{f,P}\left(\varepsilon_{f,n} - \varepsilon_{f,s}\right)\Delta x \Delta z - \frac{\rho_f}{\varepsilon_{f,P}^2}\langle v_z\rangle_{f,P}\left(\varepsilon_{f,t} - \varepsilon_{f,b}\right)\Delta x \Delta y. \quad (15.64)$$

The source term in Equation (15.62) can be written as:

$$S_c \Delta x \Delta y \Delta z = a_{SP}\langle T\rangle_{s,P} + a_{SE}\langle T\rangle_{s,E} + a_{SW}\langle T\rangle_{s,W} +$$

$$a_{SN}\langle T\rangle_{s,N} + a_{SS}\langle T\rangle_{s,S} + a_{ST}\langle T\rangle_{s,T} + a_{SB}\langle T\rangle_{s,B}, \quad (15.65)$$

where:

$$a_{S\Pi} = \frac{k_{fs,m,\pi}\Delta m' \Delta m''}{c_{p,f}\delta m_\pi} \quad (15.66)$$

and:

$$a_{SP} = \frac{h_{sf,P}}{c_{p,f}}\left(\frac{A_{sf}}{V_o}\right)_P \frac{\Delta x \Delta y \Delta z}{1-\varepsilon_{f,P}} - a_{SE} - a_{SW} - a_{SN} - a_{SS} - a_{ST} - a_{SB}. \quad (15.67)$$

In Equation (15.60) and Equation (15.66), $\Pi = E, W, N, S, T$ and B, and the indexes π, m', m'' and ξ are correspondingly designated according to Table 15.1.

System boundary grid points

Five kinds of system boundary conditions for the fluid phase are considered. (1) A specified phasial volume-averaged fluid temperature. (2) A specified phasial volume-averaged heat flux. (3) A closed system boundary at a specified wall temperature and a heat transfer coefficient between the wall and the fluid phases. (4) An open system boundary together with the fluid temperature entering the porous domain. (5) An open system boundary together with fluid leaving the porous domain.

As in the previous two cases of the discretised forms, for deriving the appropriate discretised equation coefficients in each of these cases, let the closed system boundary correspond to one of the finite volume boundaries shown in Figure 11.1, denoted π, where $\pi = e, w, n, s, t$ or b.

1. *Open or closed system boundary with specified phasial volume-averaged temperature* $\langle T \rangle_{f,P}$

For the grid point P of the finite volume associated with the boundary π, the coefficients of Equation (15.59), given by Equation (15.60) to Equation (15.67), reduce to:

$$a_P = 1, \tag{15.68}$$

$$b = \langle T \rangle_{f,P} \tag{15.69}$$

and:

$$a_S = a_W = a_N = a_S = a_T = a_B = 0. \tag{15.70}$$

2. *Open or closed system boundary with specified phasial volume-averaged heat flux* $\langle q \rangle_{f,\pi}$

Consider the conduction terms at the finite volume boundary π in Equation (15.52), given as:

$$\left(-\frac{k_{total,m}}{c_{p,f}} \frac{\partial \langle T \rangle_f}{\partial m} \right)_\pi + \frac{k_{fs,m,\pi}}{c_{p,f} \delta m_\pi} \left(\langle T \rangle_{s,P} - \langle T \rangle_{s,\Pi} \right). \tag{15.71}$$

Substituting Expression (15.71) by the term:

$$\frac{\langle q \rangle_{f,\pi}}{c_{p,f}} \tag{15.72}$$

yields the same coefficients as those given by Equation (15.60) to Equation (15.67), except for:

$$a_\Pi = 0, \tag{15.73}$$

$$a_{S\Pi} = 0 \tag{15.74}$$

and:

$$b = S_c \Delta x \Delta y \Delta z + a_P{}^0 \langle T \rangle_{s,P}{}^0 + (-1)^\xi \frac{\langle q \rangle_{f,\pi}}{c_{p,f}} \Delta m' \Delta m''. \tag{15.75}$$

In Equation (15.73) and Equation (15.74), $\Pi = E$, W, N, S, T or B, and the indexes ξ, m' and m'' are correspondingly designated according to Table 15.1.

3. *Closed system boundary at wall temperature T_{wall}, and a heat transfer coefficient h_{closed} at the closed system boundary*

The conduction terms at the finite volume boundary π in Equation (15.52), given by Expression (15.71), are substituted by the term:

$$(-1)^{\xi} \frac{h_{sf,closed,\pi}}{c_{p,f}} \left(\langle T \rangle_{f,P} - \varepsilon_{f,P} T_{wall,P} \right), \tag{15.76}$$

where $h_{sf,closed}$ is given by Equation (14.13) and where the indexes m and ξ are correspondingly designated according to Table 15.1. With no flow crossing the closed system boundary:

$$\langle v_m \rangle_f = 0 . \tag{15.77}$$

Substituting Expression (15.76) and Condition (15.77) into Equation (15.52), yields the same coefficients as those given by Equation (15.60) to Equation (15.67), except for:

$$a_{\Pi} = 0, \tag{15.78}$$

$$a_{S\Pi} = 0, \tag{15.79}$$

$$a_P = a_E + a_W + a_N + a_S + a_T + a_B + a_P^{\,0} + a_p' + \frac{h_{sf,closed,\pi}}{c_{p,f}} \Delta m' \Delta m'' \tag{15.80}$$

and:

$$b = S_c \Delta x \Delta y \Delta z + a_P^{\,0} \langle T \rangle_{s,P}^{\,0} + \frac{\langle I_f \rangle_{f,P}}{c_{p,f}} \Delta x \Delta y \Delta z + \frac{h_{sf,closed,\pi} \varepsilon_{f,P} T_{wall,\pi}}{c_{p,f}} \Delta m' \Delta m'', \tag{15.81}$$

where the designations Π in Equation (15.78) and Equation (15.79), and the indexes m' and m'' in Equation (15.80) and Equation (15.81) are correspondingly designated according to Table 15.1.

4. *Open system boundary with fluid entering the porous domain and a heat transfer coefficient $h_{sf,open,in}$ between the solid phase and the fluid phase*

Let the boundary π of a finite volume correspond to the open system boundary where fluid enters the porous domain. Using Equation (14.20) to predict the phasial volume-averaged temperature at the system boundary grid point P, the coefficients of Equation (15.59), given by Equation (15.60) to Equation (15.67), reduce to:

$$a_P = 1, \tag{15.82}$$

$$b = \left[1 - \frac{\left(1-\varepsilon_{f,P}\right)h_{sf,open,in,\pi}}{\rho_f\, c_{p,f}\, \langle v \rangle_{f,\pi}}\right] \varepsilon_{f,P}\, T_{f,\pi} + \frac{\varepsilon_{f,P}\, h_{sf,open,in,\pi}}{\rho_f\, c_{p,f}\, \langle v \rangle_{f,\pi}} \langle T \rangle_{s,P}, \tag{15.83}$$

where $h_{sf,open,in}$ is given by Equation (14.19), and:

$$a_S = a_W = a_N = a_S = a_T = a_B = 0. \tag{15.84}$$

In order to limit the effect of dispersion to the porous domain (see Section 8.7), it follows that for the inflow system boundary finite volume:

$$k_{total} = k_{ff}. \tag{15.85}$$

5. *Open system boundary with fluid leaving the porous domain and a heat transfer coefficient $h_{sf,open,out}$ between the solid phase and the fluid phase*

At an open system boundary where fluid leaves the grid domain, for the mathematical solution of the set of algebraic equations formed by Equation (15.59), it is assumed that in each finite volume along the system boundary:

$$k_{total} = 0 . \tag{15.86}$$

Condition (15.86) also limits the effect of dispersion to the porous domain (see Section 8.7).

Substituting Condition (15.86) into Definition (15.56) and Equation (15.55), Equation (15.60) becomes:

$$a_{\Pi} = \max\left[(-1)^{\xi} \frac{\rho_f}{\varepsilon_{f,\pi}} \langle v_m \rangle_{f,\pi}, 0 \right] \Delta m' \Delta m'' , \tag{15.87}$$

where Π refers to all the neighbouring grid points. For the case where one of the finite volume boundaries shown in Figure 11.1 corresponds to the open system boundary, denoted π, where $\pi = e, w, n, s, t$ or b:

$$a_{\Pi} = 0 \tag{15.88}$$

and:

$$a_{S\Pi} = 0 , \tag{15.89}$$

where Π in Equation (15.88) and Equation (15.89) is correspondingly designated according to Table 14.1.

Condition (15.86) also eliminates conduction between the grid points at the open system

boundary and the grid points immediately upstream from them. For grid points upstream of those at the open system boundary, substituting Condition (15.86) into Definition (15.56) and Equation (15.55), and noting that the velocity direction is from the upstream finite volume to the finite volume at the open system boundary, Equation (15.60) becomes:

$$a_{\Pi} = 0, \tag{15.90}$$

where Π is the outflow system boundary grid point.

15.4 Fluid phase transformed volume-averaged momentum equation

The transformed volume-averaged momentum equation, given in Section 8.2 by Equation (8.2), under steady state conditions states, after rearranging terms, that:

$$\rho_f \nabla \cdot \left(\frac{1}{\varepsilon_f} \langle \boldsymbol{v} \rangle_f \langle \boldsymbol{v} \rangle_f \right) - \nabla \cdot \left[(\mu \boldsymbol{u} + \boldsymbol{D}_P) \cdot \nabla \langle \boldsymbol{v} \rangle_f \right] + \varepsilon_f \nabla \langle p \rangle_f^f - \varepsilon_f \rho_f \langle \boldsymbol{B} \rangle_f + \mu \boldsymbol{f} \cdot \langle \boldsymbol{v} \rangle_f = 0, \tag{15.91}$$

where ρ_f is the fluid density and ε_f is the porosity [or fluid phase volume fraction, defined by Definition (II.1)]. μ is the kinematic viscosity of the fluid phase, $\boldsymbol{D}_P$ is the momentum dispersion tensor, $\boldsymbol{f}$ is the viscous shear factor and $\boldsymbol{u}$ is a unit diagonal tensor, $\langle \boldsymbol{v} \rangle_f$ is the phasial volume-averaged velocity vector, $\langle \boldsymbol{B} \rangle_f$ is a phasial volume-averaged body force and $\langle p \rangle_f^f$ is the intrinsic volume averaged pressure for the fluid phase.

Equation (15.91) can be written as a momentum balance equation in each of the three principal directions of the Cartesian coordinate system, by expanding the phasial volume-averaged velocity and the body force vectors, and the momentum dispersion tensor into

their respective components in these directions. In the x-direction, noting that the fluid density ρ_f is constant, the momentum balance equation is:

$$\frac{\partial}{\partial x}\left(\frac{\rho_f}{\varepsilon_f}\langle v_x\rangle_f\langle v_x\rangle_f\right)+\frac{\partial}{\partial y}\left(\frac{\rho_f}{\varepsilon_f}\langle v_y\rangle_f\langle v_x\rangle_f\right)+\frac{\partial}{\partial z}\left(\frac{\rho_f}{\varepsilon_f}\langle v_z\rangle_f\langle v_x\rangle_f\right)-$$
$$\frac{\partial}{\partial x}\left[(\mu+D_{P,x})\frac{\partial\langle v_x\rangle_f}{\partial x}\right]-\frac{\partial}{\partial y}\left[(\mu+D_{P,y})\frac{\partial\langle v_x\rangle_f}{\partial y}\right]-\frac{\partial}{\partial z}\left[(\mu+D_{P,z})\frac{\partial\langle v_x\rangle_f}{\partial z}\right]+$$
$$\varepsilon_f\frac{\partial\langle p\rangle_f^f}{\partial x}-\varepsilon_f\rho_f\langle B_x\rangle_f+\mu f_x\langle v_x\rangle_f=0. \qquad (15.92)$$

[Since $\boldsymbol{D}_P$ in Equation (8.2) is a diagonal, three-dimensional tensor, its components in the principal directions in Equation (15.92) are identified by a single directional index for the sake of simplicity, *e.g.* x instead of xx].

Multiplying the volume-averaged continuity equation [Equation (2.5)] by the quantity $\rho_f\langle v_x\rangle_f$ and subtracting from Equation (15.92) yields, after rearranging terms:

$$\frac{\partial}{\partial x}\left[\frac{\rho_f}{\varepsilon_f}\langle v_x\rangle_f\langle v_x\rangle_f-(\mu+D_{P,x})\frac{\partial\langle v_x\rangle_f}{\partial x}\right]-\langle v_x\rangle_f\frac{\partial}{\partial x}\frac{\rho_f\langle v_x\rangle_f}{\varepsilon_f}+$$
$$\frac{\partial}{\partial y}\left[\frac{\rho_f}{\varepsilon_f}\langle v_y\rangle_f\langle v_x\rangle_f-(\mu+D_{P,y})\frac{\partial\langle v_x\rangle_f}{\partial y}\right]-\langle v_x\rangle_f\frac{\partial}{\partial y}\frac{\rho_f\langle v_y\rangle_f}{\varepsilon_f}+$$
$$\frac{\partial}{\partial z}\left[\frac{\rho_f}{\varepsilon_f}\langle v_z\rangle_f\langle v_x\rangle_f-(\mu+D_{P,z})\frac{\partial\langle v_x\rangle_f}{\partial z}\right]-\langle v_x\rangle_f\frac{\partial}{\partial z}\frac{\rho_f\langle v_z\rangle_f}{\varepsilon_f}-$$
$$\frac{\rho_f\langle v_x\rangle_f\langle v_x\rangle_f}{\varepsilon_f^{\,2}}\frac{\partial\varepsilon_f}{\partial x}-\frac{\rho_f\langle v_x\rangle_f\langle v_y\rangle_f}{\varepsilon_f^{\,2}}\frac{\partial\varepsilon_f}{\partial y}-\frac{\rho_f\langle v_x\rangle_f\langle v_z\rangle_f}{\varepsilon_f^{\,2}}\frac{\partial\varepsilon_f}{\partial z}+$$
$$\varepsilon_f\frac{\partial\langle p\rangle_f^f}{\partial x}-\varepsilon_f\rho_f\langle B_x\rangle_f+\mu f_x\langle v_x\rangle_f=0. \qquad (15.93)$$

Integrating Equation (15.93) over the finite volume shown in Figure 11.1, following the analytical process illustrated between Equation (15.2) and Equation (15.8), and substituting the definition for an total viscous transfer coefficient μ_{total}:

$$\mu_{total,m} \equiv \mu + D_{P,m}, \tag{15.94}$$

where $m = x, y$ or z, yields:

$$\left[\left(\frac{\rho_f}{\varepsilon_f}\langle v_x\rangle_f\langle v_x\rangle_f - \mu_{total,x}\frac{\partial\langle v_x\rangle_f}{\partial x}\right)_e - \left(\frac{\rho_f}{\varepsilon_f}\langle v_x\rangle_f\langle v_x\rangle_f - \mu_{eff,x}\frac{\partial\langle v_x\rangle_f}{\partial x}\right)_w\right]\Delta y\Delta z -$$

$$\langle v_x\rangle_{f,P}\left[\left(\frac{\rho_f}{\varepsilon_f}\langle v_x\rangle_f\right)_e - \left(\frac{\rho_f}{\varepsilon_f}\langle v_x\rangle_f\right)_w\right]\Delta y\Delta z +$$

$$\left[\left(\frac{\rho_f}{\varepsilon_f}\langle v_y\rangle_f\langle v_x\rangle_f - \mu_{total,y}\frac{\partial\langle v_x\rangle_f}{\partial y}\right)_n - \left(\frac{\rho_f}{\varepsilon_f}\langle v_y\rangle_f\langle v_x\rangle_f - \mu_{eff,y}\frac{\partial\langle v_x\rangle_f}{\partial y}\right)_s\right]\Delta x\Delta z -$$

$$\langle v_x\rangle_{f,P}\left[\left(\frac{\rho_f}{\varepsilon_f}\langle v_y\rangle_f\right)_n - \left(\frac{\rho_f}{\varepsilon_f}\langle v_y\rangle_f\right)_s\right]\Delta x\Delta z -$$

$$\left[\left(\frac{\rho_f}{\varepsilon_f}\langle v_z\rangle_f\langle v_x\rangle_f - \mu_{total,z}\frac{\partial\langle v_x\rangle_f}{\partial z}\right)_t - \left(\frac{\rho_f}{\varepsilon_f}\langle v_z\rangle_f\langle v_x\rangle_f - \mu_{eff,z}\frac{\partial\langle v_x\rangle_f}{\partial z}\right)_b\right]\Delta x\Delta y -$$

$$\langle v_x\rangle_{f,P}\left[\left(\frac{\rho_f}{\varepsilon_f}\langle v_z\rangle_f\right)_t - \left(\frac{\rho_f}{\varepsilon_f}\langle v_z\rangle_f\right)_b\right]\Delta x\Delta y -$$

$$\langle v_x\rangle_{f,P}\langle v_x\rangle_{f,P}\frac{\rho_f}{\varepsilon_{f,P}^{\,2}}\left(\varepsilon_{f,e} - \varepsilon_{f,w}\right)\Delta y\Delta z -$$

$$\langle v_x\rangle_{f,P}\langle v_y\rangle_{f,P}\frac{\rho_f}{\varepsilon_{f,P}^{\,2}}\left(\varepsilon_{f,n} - \varepsilon_{f,s}\right)\Delta x\Delta z -$$

$$\langle v_x\rangle_{f,P}\langle v_z\rangle_{f,P}\frac{\rho_f}{\varepsilon_{f,P}^{\,2}}\left(\varepsilon_{f,t} - \varepsilon_{f,b}\right)\Delta x\Delta y +$$

$$\varepsilon_{f,P}\left(\langle p\rangle_{f,e}^{f} - \langle p\rangle_{f,w}^{f}\right)\Delta y\Delta z - \varepsilon_{f,P}\,\rho_f\,\langle B_x\rangle_{f,P}\Delta x\Delta y\Delta z +$$

$$\mu f_{x,P}\langle v_x\rangle_{f,P}\Delta x\Delta y\Delta z = 0. \tag{15.95}$$

[Equation (15.93) is not integrated over time since it is a steady-state equation.]

At a finite volume boundary π, the total viscous transfer coefficient μ_{total} is determined from its values at the grid points by:

$$\mu_{total,\pi} = \frac{\delta m_\pi}{\dfrac{\delta m_{\pi\Pi}}{\mu_{total,\Pi}} + \dfrac{\delta m_{\pi P}}{\mu_{total,P}}}, \tag{15.96}$$

where $\pi = e, w, n, s, t$ or b. The index Π is correspondingly designated according to Table 15.1. The dimensions δm_π, $\delta m_{\pi\Pi}$ and $\delta m_{\pi P}$ are shown in Figure 15.1 (either as $\delta m_{\pi 1}$, $\delta m_{\pi 1\Pi 1}$ and $\delta m_{\pi 1 P}$, or as $\delta m_{\pi 2}$, $\delta m_{\pi 2\Pi 2}$ and $\delta m_{\pi 2 P}$).

From a generalised formulation by Patankar (1980) it follows that:

$$\left(\frac{\rho_f}{\varepsilon_f} \langle v_m \rangle_f \langle v_x \rangle_f - \mu_{total,m} \frac{\partial \langle v_x \rangle_f}{\partial m} - \langle v_x \rangle_{f,P} \frac{\rho_f}{\varepsilon_f} \langle v_m \rangle_f \right)_\pi =$$

$$(-1)^\xi \left\{ \frac{D_{fv,\pi} \rho_f}{\delta m_\pi} \mathrm{A}(|Re_\pi|) + \max\left[(-1)^\xi \frac{\rho_f}{\varepsilon_{f,\pi}} \langle v_m \rangle_{f,\pi}, 0 \right] \right\} \left(\langle v_x \rangle_{f,\Pi} - \langle v_x \rangle_{f,P} \right), \tag{15.97}$$

where D_{fv} is the viscous diffusivity defined as:

$$D_{fv,\pi} \equiv \frac{\mu_{total,m,\pi}}{\rho_f}, \tag{15.98}$$

the Reynolds number Re is defined by:

$$Re_\pi = \frac{\langle v_m \rangle_{f,\pi} \delta m_\pi}{\varepsilon_{f,\pi} D_{fv,\pi}} \tag{15.99}$$

and, according to Patankar's power-law scheme:

$$A(|Re_\pi|) = \max\left[0,\ (1-0.1|Re_\pi|)^5\right]. \tag{15.100}$$

In Equation (15.97) to Equation (15.100), $\pi = e$, w, n, s, t or b. The indexes Π, m and ξ are correspondingly designated according to Table 15.1. The phasial volume-averaged velocity components $\langle v_m \rangle_{f,\pi}$ in Equation (15.97) and Equation (15.99) are normal to the finite volume boundaries and are determined from an interpolation between its values at the grid points. After substituting Equation (15.97), Equation (15.95) can be written, after rearranging terms, in the general form:

$$a_P \langle v_x \rangle_{f,P} = a_E \langle v_x \rangle_{f,E} + a_W \langle v_x \rangle_{f,W} + a_N \langle v_x \rangle_{f,N} + a_S \langle v_x \rangle_{f,S} + a_T \langle v_x \rangle_{f,T} + a_B \langle v_x \rangle_{f,B} + b_x + \varepsilon_{f,P}\left(\langle p \rangle^f_{f,w} - \langle p \rangle^f_{f,e}\right)\Delta y \Delta z, \tag{15.101}$$

with:

$$a_\Pi = \left\{\frac{D_{fv,\pi}\rho_f}{\delta m_\pi} A(|Re_\pi|) + \max\left[(-1)^\xi \frac{\rho_f}{\varepsilon_{f,\pi}} \langle v_m \rangle_{f,\pi}, 0\right]\right\} \Delta m' \Delta m'' \tag{15.102}$$

$$b_x = \varepsilon_{f,P}\, \rho_f \langle B_x \rangle_{f,P} \Delta x \Delta y \Delta z \tag{15.103}$$

and:

$$a_P = a_E + a_W + a_N + a_S + a_T + a_B + a_P', \tag{15.104}$$

where:

$$a_P' = \frac{\rho_f}{\varepsilon_{f,P}^2} \langle v_x \rangle_{f,P} \left(\varepsilon_{f,w} - \varepsilon_{f,e}\right)\Delta y \Delta z + \frac{\rho_f}{\varepsilon_{f,P}^2} \langle v_y \rangle_{f,P} \left(\varepsilon_{f,s} - \varepsilon_{f,n}\right)\Delta x \Delta z + \frac{\rho_f}{\varepsilon_{f,P}^2} \langle v_z \rangle_{f,P} \left(\varepsilon_{f,b} - \varepsilon_{f,t}\right)\Delta x \Delta y + \mu f_{x,P} \Delta x \Delta y \Delta z, \tag{15.105}$$

where, in Equation (15.102), $\Pi = E, W, N, S, T$ and B, and the indexes π, m', m'' and ξ are correspondingly designated according to Table 15.1.

Similar analytical processes for v_y and v_z (the respective velocity components in the y-direction and the z-direction) yield:

$$a_P\langle v_y\rangle_{f,P} = a_E\langle v_y\rangle_{f,E} + a_W\langle v_y\rangle_{f,W} + a_N\langle v_y\rangle_{f,N} + a_S\langle v_y\rangle_{f,S} + a_T\langle v_y\rangle_{f,T} + a_B\langle v_y\rangle_{f,B} + b_y + \varepsilon_{f,P}\left(\langle p\rangle^f_{f,s} - \langle p\rangle^f_{f,n}\right)\Delta x\,\Delta z \qquad (15.106)$$

and:

$$a_P\langle v_z\rangle_{f,P} = a_E\langle v_z\rangle_{f,E} + a_W\langle v_z\rangle_{f,W} + a_N\langle v_z\rangle_{f,N} + a_S\langle v_z\rangle_{f,S} + a_T\langle v_z\rangle_{f,T} + a_B\langle v_z\rangle_{f,B} + b_z + \varepsilon_{f,P}\left(\langle p\rangle^f_{f,b} - \langle p\rangle^f_{f,t}\right)\Delta x\,\Delta y\,, \qquad (15.107)$$

where a_E, a_W, a_N, a_S, a_T and a_B are given by Equation (15.102) and a_P is given by Equation (15.104). The equation for a_P' is similar to Equation (15.105), except that f_x in the last term is substituted by f_y and f_z respectively.

In Equation (15.106):

$$b_y = \varepsilon_{f,P}\,\rho_f\,\langle B_y\rangle_{f,P}\,\Delta x\,\Delta y\,\Delta z \qquad (15.108)$$

and in Equation (15.107):

$$b_z = \varepsilon_{f,P}\,\rho_f\,\langle B_z\rangle_{f,P}\,\Delta x\,\Delta y\,\Delta z\,. \qquad (15.109)$$

Pressure field and the pressure correction equation

Equation (15.101), Equation (15.106) and Equation (15.107) can be solved only when the pressure field is given or somehow estimated. Unless the correct pressure field is used, the resulting velocity field will not satisfy the volume-averaged continuity equation given in Equation (2.5). Integrating the volume-averaged continuity equation over the finite volume shown in Figure 11.1, as illustrated in Equation (15.2) to Equation (15.8), yields:

$$\left[\left(\frac{\langle v_x\rangle_f}{\varepsilon_f}\right)_e-\left(\frac{\langle v_x\rangle_f}{\varepsilon_f}\right)_w\right]\Delta y\,\Delta z+\left[\left(\frac{\langle v_y\rangle_f}{\varepsilon_f}\right)_n-\left(\frac{\langle v_y\rangle_f}{\varepsilon_f}\right)_s\right]\Delta x\,\Delta z+$$
$$\left[\left(\frac{\langle v_z\rangle_f}{\varepsilon_f}\right)_t-\left(\frac{\langle v_z\rangle_f}{\varepsilon_f}\right)_b\right]\Delta x\,\Delta y+\frac{\langle v_x\rangle_{f,P}}{\varepsilon_{f,P}^{\,2}}\left(\varepsilon_{f,e}-\varepsilon_{f,w}\right)\Delta y\,\Delta z+$$
$$\frac{\langle v_y\rangle_{f,P}}{\varepsilon_{f,P}^{\,2}}\left(\varepsilon_{f,n}-\varepsilon_{f,s}\right)\Delta x\,\Delta z+\frac{\langle v_z\rangle_{f,P}}{\varepsilon_{f,P}^{\,2}}\left(\varepsilon_{f,t}-\varepsilon_{f,b}\right)\Delta x\,\Delta y=0. \qquad (15.110)$$

The SIMPLEC solution algorithm (Van Doormaal and Raithby, 1984) improves an incorrect pressure field $\langle p\rangle_f^{f*}$, such that its resulting incorrect velocity field $\langle v_x\rangle_f{}^*$, $\langle v_y\rangle_f{}^*$ and $\langle v_z\rangle_f{}^*$, will get progressively closer to satisfying Equation (15.110). The *pressure correction* $\langle p\rangle_f^{f\prime}$ is defined as:

$$\langle p\rangle_f^{f\prime}\equiv\langle p\rangle_f^{f}-\langle p\rangle_f^{f*}, \qquad (15.111)$$

where $\langle p\rangle_f^f$ is the correct pressure field yielding a velocity field that satisfies the volume-averaged continuity equation. Similarly, the *velocity corrections* are defined as:

$$\langle v_m\rangle_f{}'\equiv\langle v_m\rangle_f-\langle v_m\rangle_f{}^*, \qquad (15.112)$$

or:

$$\langle v_m \rangle_f = \langle v_m \rangle_f' + \langle v_m \rangle_f^*, \tag{15.113}$$

where $m = x, y, z$.

The SIMPLEC algorithm proposes that the velocity correction at the boundaries of the finite volume, are functions of the pressure correction according to:

$$\langle v_m \rangle_{f,\pi}' = \frac{(-1)^{\xi} \varepsilon_{f,\pi} \left(\langle p \rangle_{f,\Pi}^f ' - \langle p \rangle_{f,P}^f ' \right) \Delta m' \Delta m''}{a_P - a_E - a_W - a_N - a_S - a_T - a_B}, \tag{15.114}$$

where $\pi = e, w, n, s, t$ and b. The indexes Π, m, m', m'' and ξ are correspondingly designated according to Table 15.1. The parameters in the denominator of Equation (15.114) are given by Equation (15.102), with one difference. Consider Equation (15.114) for $m = x$. Following the staggered grid configuration proposed by Patankar (1980), which is briefly discussed in Section 16.2, the finite volume over which Equation (15.93) is integrated, has an offset in the positive x-direction from the finite volume over which the volume-averaged continuity is integrated. This arrangement is shown in Figure 15.2. Finite Volume 1 in Figure 15.2 is that over which the pressure correction equation is integrated and Finite Volume 2 is that over which the transformed volume-averaged momentum equation is integrated. Subscript 1 refers to grid points and finite volume boundaries of Finite Volume 1 and Subscript 2 refers to grid points and finite volume boundaries of Finite Volume 2.

Similarly, consider the parameters in the denominator of Equation (15.114) for $m = y$. The finite volume, over which the transformed volume-averaged momentum equation for the y-direction is integrated to yield Equation (15.106), has an offset in the positive y-direction. This offset is again with reference to the finite volume over which the volume-averaged continuity equation is integrated. The same applies to the $m = z$, where the offset is in the positive z-direction from the finite volume over which the volume-averaged continuity is integrated.

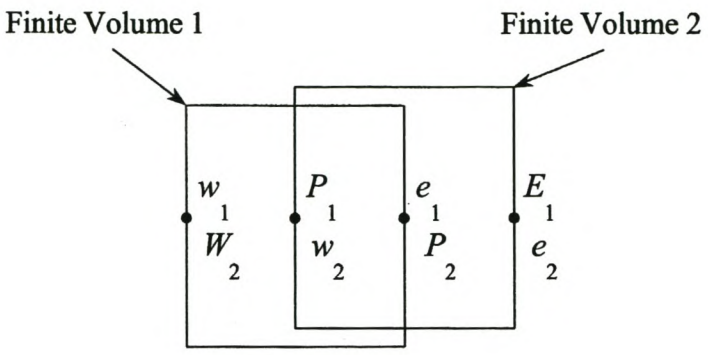

Figure 15.2 Finite volume offset arrangement.

In Equation (15.110), substituting the phasial volume-averaged velocities normal to the boundaries of the finite volume by Equation (15.113) and then substituting the velocity corrections by Equation (15.114) yields, after rearranging terms, the following discretised form of the pressure correction:

$$a_{Pp}\langle p\rangle^{f}_{f,P}{}' = a_{Ep}\langle p\rangle^{f}_{f,E}{}' + a_{Wp}\langle p\rangle^{f}_{f,W}{}' + a_{Np}\langle p\rangle^{f}_{f,N}{}' + a_{Sp}\langle p\rangle^{f}_{f,S}{}' + a_{Tp}\langle p\rangle^{f}_{f,T}{}' + a_{Bp}\langle p\rangle^{f}_{f,B}{}' + b_{p}', \tag{15.115}$$

with:

$$a_{\Pi p} = \frac{(\Delta m'\,\Delta m'')^2}{(a_P - a_E - a_W - a_N - a_S - a_T - a_B)_{\pi}}, \tag{15.116}$$

$$a_{Pp} = a_{Ep} + a_{Wp} + a_{Np} + a_{Sp} + a_{Tp} + a_{Bp} \tag{15.117}$$

and:

$$b_p = \left[\left(\frac{\langle v_x\rangle_f^*}{\varepsilon_f}\right)_w - \left(\frac{\langle v_x\rangle_f^*}{\varepsilon_f}\right)_e\right]\Delta y\Delta z + \left[\left(\frac{\langle v_y\rangle_f^*}{\varepsilon_f}\right)_s - \left(\frac{\langle v_y\rangle_f^*}{\varepsilon_f}\right)_n\right]\Delta x\Delta z +$$

$$\left[\left(\frac{\langle v_z\rangle_f^*}{\varepsilon_f}\right)_b - \left(\frac{\langle v_z\rangle_f^*}{\varepsilon_f}\right)_t\right]\Delta x\Delta y + \frac{\langle v_x\rangle_{f,P}}{\varepsilon_{f,P}^2}\left(\varepsilon_{f,w} - \varepsilon_{f,e}\right)\Delta y\Delta z +$$

$$\frac{\langle v_y\rangle_{f,P}}{\varepsilon_{f,P}^2}\left(\varepsilon_{f,s} - \varepsilon_{f,n}\right)\Delta x\Delta z + \frac{\langle v_z\rangle_{f,P}}{\varepsilon_{f,P}^2}\left(\varepsilon_{f,b} - \varepsilon_{f,t}\right)\Delta x\Delta y\,. \qquad (15.118)$$

In Equation (15.116), $\Pi = E$, W, N, S, T and B, and π, m' and m'' are correspondingly designated according to Table 15.1.

The subscripts outside the parenthesis in the denominator of Equation (15.116) refer to the locations, as shown in Figure 11.1, of the discretised transformed volume-averaged momentum equations to which the parameters in the denominators apply.

System boundary grid points

Four kinds of system boundary conditions for the fluid phase are considered. (1) A specified phasial volume-averaged velocity. (2) A closed system boundary with a specified phasial volume-averaged momentum transfer. (3) A closed system boundary with a phasial volume-averaged momentum transfer as a function of the boundary velocity. (4) An open system boundary across which the fluid phase leaves the porous domain, in which case a special condition exists upstream from grid points on that boundary.

For deriving the appropriate discretised equation coefficients in each of these cases, let the closed system boundary correspond to one of the finite volume boundaries shown in Figure 11.1, denoted π, where $\pi = e$, w, n, s, t or b.

1. Open or closed system boundary with specified phasial volume-averaged velocity in the fluid phase

For the grid point P of the finite volume associated with the boundary π, the coefficients of Equation (15.101), Equation (15.106) and Equation (15.107) reduce to:

$$a_P = 1 \tag{15.119}$$

and:

$$b = \langle v_m \rangle_{f,P,specified}, \tag{15.120}$$

where $m = x$, y or z, and:

$$a_S = a_W = a_N = a_S = a_T = a_B = 0. \tag{15.121}$$

Consider the system boundary finite volume in the staggered grid arrangement. The nearest grid point where the pressure correction equation needs to be solved, is in the negative m direction for $\pi = e$, n or t and in the positive m direction where $\pi = w$, s or b, where the index m are correspondingly designated according to Table 15.1. At this nearest grid point where the pressure correction equation needs to be solved, the coefficients of the pressure correction equation are the same as those given by Equation (15.116) to Equation (15.118), except that in Equation (15.118), the phasial volume-averaged velocity $\langle v_m \rangle_{f,P,specified}$ substitutes the corresponding incorrect phasial volume-averaged velocity $\langle v_m \rangle_f^*$. Furthermore:

$$a_{\Pi p} = 0, \tag{15.122}$$

where the index Π relates to π according to Table 15.1.

If the specified phasial volume-averaged velocity corresponds to an inflow boundary then, to limit the effect of dispersion to the porous domain (see Section 8.5), it follows that for the inflow system boundary finite volume:

$$\mu_{total} = \mu_{ff.} \tag{15.123}$$

2. *Closed system boundary with a specified phasial volume-averaged momentum transfer*

The phasial volume-averaged momentum transfer in the fluid phase at a close system boundary is defined by Equation (8.19) as:

$$\langle P_t \rangle_{f,m} = -(\mu + D_{P,m}) \frac{\partial}{\partial m} \langle v \rangle_f \,, \tag{8.19}$$

where $m = x$, y or z is the direction normal to the closed system boundary. With no flow crossing the system boundary:

$$\langle v_m \rangle_f = 0 \,. \tag{15.124}$$

The velocity components parallel to the system boundary are $\langle v_{m'} \rangle_f$ and $\langle v_{m''} \rangle_f$, where m' and m'' correspond to m, according to Table 15.1.

Substituting the momentum transfer term at the finite volume boundary π, given in Equation (15.97) for the x-direction velocity component as:

$$\left(-\mu_{total,m} \frac{\partial \langle v_x \rangle_f}{\partial m} \right)_\pi \,, \tag{15.125}$$

by the specified phasial volume-averaged momentum transfer term:

$$\langle P_t \rangle_{f,\pi}, \tag{15.126}$$

yields the same coefficients as those given by Equation (15.102) to Equation (15.105), except for:

$$a_{\Pi} = 0 \tag{15.127}$$

and:

$$b_m = \varepsilon_{f,P} \rho_f \langle B_x \rangle_{f,P} \Delta x \Delta y \Delta z + (-1)^{\xi} \langle P_t \rangle_{f,\pi} \Delta m' \Delta m''. \tag{15.128}$$

In Equation (15.127), $\Pi = E$, W, N, S, T or B, and in Equation (15.125) and Equation (15.128), the indexes ξ, m' and m'' are correspondingly designated according to Table 15.1.

At the nearest grid point where the pressure correction equations needs to be solved, the coefficients of the pressure correction equation are the same as those given by Equation (15.116) to Equation (15.118), except that in Equation (15.118):

$$\left(\langle v_m \rangle_f^* \right)_{\pi} = 0 \tag{15.129}$$

and:

$$a_{\Pi p} = 0, \tag{15.130}$$

where the indexes m and Π are correspondingly designated according to Table 15.1.

This boundary condition is also used for the case in which there is a zero velocity gradient parallel to a system boundary with no flow crossing the boundary. In this case the momentum transfer is specified as zero.

3. Closed system boundary with a phasial volume-averaged momentum transfer as a function of the boundary velocity

Substituting the momentum transfer term at the finite volume boundary π, given in Equation (15.97) by Expression (15.125) for the x-direction velocity component, by the phasial volume-averaged velocity dependent phasial volume-averaged momentum transfer given at the finite volume boundary by Definition (14.2.) as:

$$(-1)^{\xi}\,\mu c_{\pi}\langle \boldsymbol{v}\rangle_{f,P}, \tag{15.131}$$

where c is given by Equation (14.8) and where the index ξ is correspondingly designated according to Table 15.1, yields the same coefficients as those given by Equation (15.102) to Equation (15.105), except for:

$$a_{\Pi} = 0 \tag{15.132}$$

and:

$$a_P = a_E + a_W + a_N + a_S + a_T + a_B + a_P{}^{0} + a_p{}' + \mu c_{\pi}\Delta m'\Delta m'', \tag{15.133}$$

where the indexes m' and m'' in Equation (15.133) are correspondingly designated according to Table 15.1.

4. Open system boundary across which the fluid phase leaves the grid domain

For the mathematical solution of the set of algebraic equations formed by Equation (15.101), Equation (15.106) and Equation (15.107), it is assumed that in each finite volume along the system boundary:

$$\mu_{total,m,P} = 0 \tag{15.134}$$

and that the outflow phasial volume-averaged velocity is normal to the open system boundary. Condition (15.134) also limits the effect of dispersion to the porous domain (see Section 8.5).

Therefore the outflow phasial volume-averaged velocity component is equal to that at the grid point upstream of the outflow system boundary grid point. For the grid point P of this finite volume, the coefficients of the Equation (15.101), Equation (15.106) and Equation (15.107) then reduce to:

$$a_P = 1 \tag{15.135}$$

and:

$$b = a_S = a_W = a_N = a_S = a_T = a_B = 0, \tag{15.136}$$

except for the grid point upstream of the outflow system boundary grid point Π', of which the coefficient is:

$$a_{\Pi'} = 1. \tag{15.137}$$

Condition (15.134) also eliminates viscous momentum transfer between the grid points at the open system boundary and the grid points immediately upstream from them. For grid points upstream of those at the open system boundary, substituting Condition (15.134) into Equation (15.95), Definition (15.98) and then into Equation (15.97), noting that the velocity direction is from the upstream finite volume to the finite volume at the open system boundary, yields:

$$a_{\Pi} = 0, \tag{15.138}$$

where Π is the outflow system boundary grid point.

At the nearest grid point where the pressure correction equation needs to be solved, the coefficients of the pressure correction equation are the same as those given by

Equation (15.116) to Equation (15.118), except that:

$$a_{\Pi p} = 0, \tag{15.139}$$

where the index Π relates to π according to Table 15.1.

CHAPTER 16

SOLUTION ALGORITHMS

16.1 Overview

In this chapter, techniques and algorithms used in the computational solution of the discretised forms of the transformed volume-averaged momentum equation and the transformed volume-averaged energy equations for the solid and the fluid phases, are discussed. The chapter addresses the staggered grid configuration introduced in literature for the solution of pressure and velocity fields, the sequence of operations for the solution of the transformed volume-averaged momentum equation and the sequence of operations for the solution of the transformed volume-averaged energy equations for the solid and the fluid phases.

16.2 Staggered grid configuration

There is a significant benefit to be obtained by arranging the grids used for the calculation of the phasial volume-averaged velocity components in a different manner from the grid used for calculating the phasial volume-averaged temperatures of the solid and the fluid phases, and for calculating the pressure corrections (Patankar, 1980). A displaced grid (referred to as a *staggered* grid) forms the basis of the SIMPLE procedure of Patankar and Spalding (1972).

In a staggered grid, the phasial volume-averaged velocity components are calculated at locations that lie on the faces of the finite volumes used for the calculation of phasial volume-averaged temperatures and intrinsic volume-averaged pressure corrections. Thus,

the x-direction phasial volume-averaged velocity component $\langle v_x \rangle_f$ is calculated at the faces that are normal to the x-direction. Similarly, the y-direction velocity component $\langle v_y \rangle_f$ and the z-direction velocity component $\langle v_z \rangle_f$ are calculated at the faces normal to the y-direction and the z-direction respectively. It should be noted that with respect to the grid points used for the calculation of phasial volume-averaged temperatures and intrinsic volume-averaged pressure corrections, the location of grid points used for the calculations of the x, y and z phasial volume-averaged velocity components are staggered only in their corresponding directions, *i.e.* grid points used for the calculation of the x-direction phasial volume-averaged velocity component $\langle v_x \rangle_f$ is staggered only in the x-direction, *etc.* This arrangement is shown in Figure 16.1

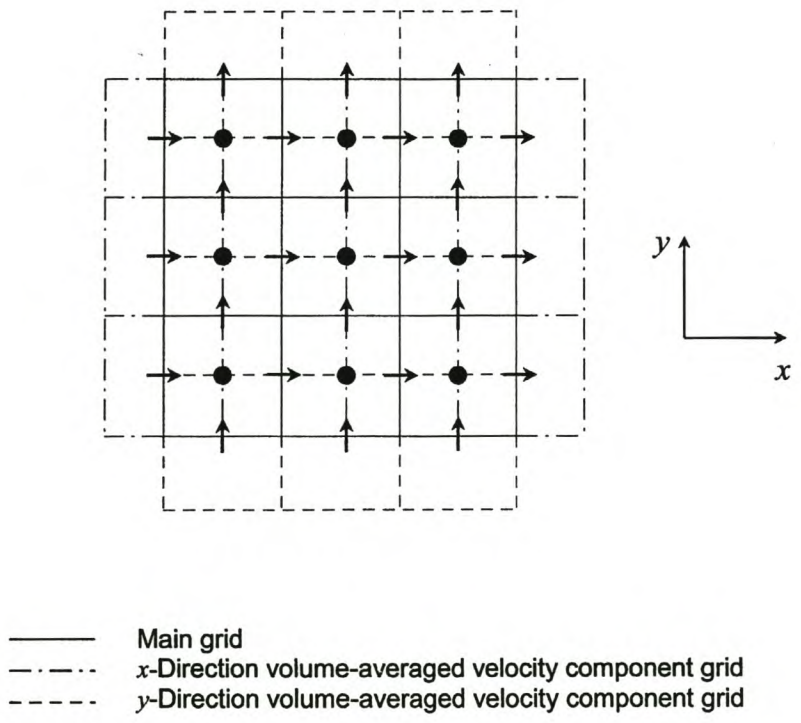

Figure 16.1 Staggered grid arrangement.

16.3 Sequence of operations for the solution of the transformed volume-averaged momentum equation

The procedure used for calculating the flow field are similar to the SIMPLE procedure of Patankar (1980). This procedure is shown in the flow chart given in Figure 16.2.

In the sequence of operations, it is often desirable to slow down the changes, from iteration to iteration, in the values of the calculated phasial volume-averaged velocity components. This process is called *underrelaxation*. Van Doormaal and Raithby (1984) introduced underrelaxation through a relaxation coefficient E, which is briefly discussed here.

The discretised form for the phasial volume-averaged velocity components given by Equation (15.101), Equation (15.106) and Equation (15.107) may be written as:

$$a_P\langle v_m\rangle_{f,P} = \sum a_\Pi \langle v_m\rangle_{f,\Pi} + b_m + \varepsilon_{f,P}\left(\langle p\rangle^f_{f,\pi 2} - \langle p\rangle^f_{f,\pi 1}\right)\Delta m'\Delta m'', \qquad (16.1)$$

where $m = x$, y or z, $\Pi = E$, W, N, S, T and B. $\pi 1$ and $\pi 2$, and the indexes m' and m'' are correspondingly designated according to Table 15.1.

Adding the quantities:

$$\frac{a_P}{E}\langle v_m\rangle_{f,P} \qquad (16.2)$$

and:

$$\frac{a_P}{E}\langle v_m\rangle_{f,P}^{\,i}, \qquad (16.3)$$

where $\langle v_m\rangle_{f,P}^{\,i}$ is the value of $\langle v_m\rangle_{f,P}$ from the previous iteration, to the LHS and the

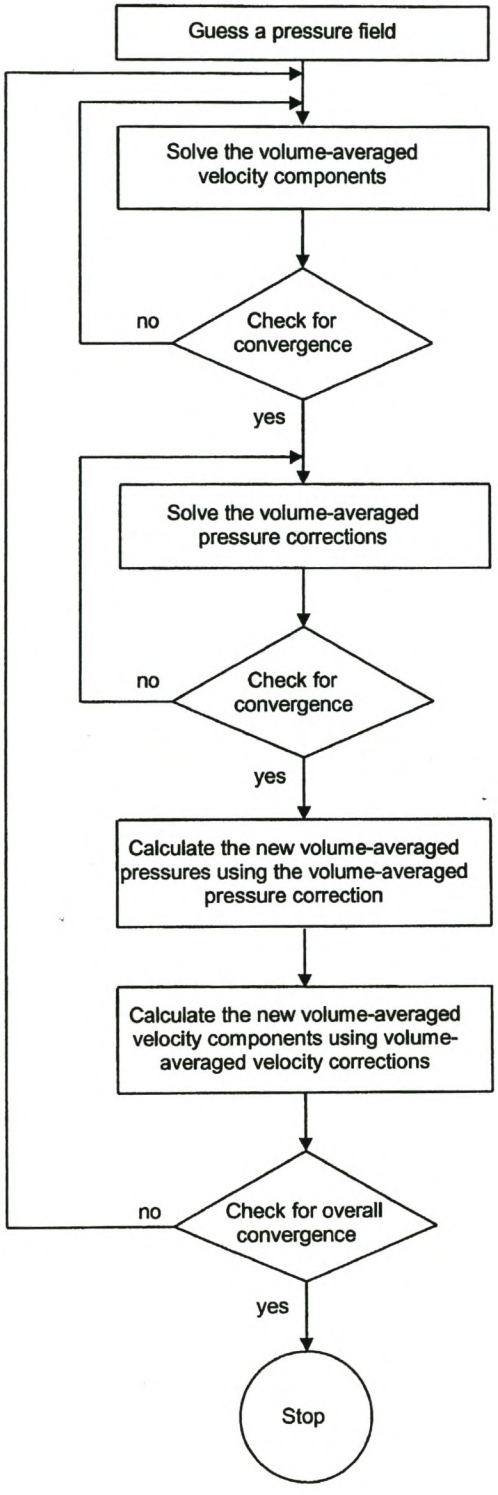

Figure 16.2 Procedure for the solution of the transformed volume-averaged momentum equation.

RHS respectively of Equation (16.1) yields:

$$a_P\left(1+\frac{1}{E}\right)\langle v_m\rangle_{f,P} = \sum a_\Pi \langle v_m\rangle_{f,\Pi} + b_x + \varepsilon_{f,P}\left(\langle p\rangle^f_{f,\pi 2} - \langle p\rangle^f_{f,\pi 1}\right)\Delta m'\,\Delta m'' + \frac{a_P}{E}\langle v_m\rangle_{f,P}{}^{i}. \tag{16.4}$$

The value of the relaxation coefficient E determines the change of $\langle v_m\rangle_{f,P}$ from iteration to iteration. When the iterations converge, that is when $\langle v_m\rangle_{f,P}$ becomes equal to $\langle v_m\rangle_{f,P}{}^{i}$, then Equation (16.4) implies that the converged values of $\langle v_m\rangle_{f,P}$ satisfy Equation (16.1).

It was also found that convergence is enhanced when it is assumed that flow leaves the porous domain normal to the outflow system boundary. Furthermore, at an outflow system boundary, a type 2 pressure boundary condition (see Section IV.2) should also not only be specified on the outflow face of the finite volume boundaries, but also at finite volume boundaries between the outflow grid points.

16.4 Sequence of operations for the solution of the transformed volume-averaged energy equations for the solid and the fluid phases

The procedure used for calculating the phasial volume-averaged temperatures of the solid and the fluid phases are given in the flow chart shown in Figure 16.3

Underrelaxation in the sequence of operations for solving the transformed volume-averaged energy equations for the solid and the fluid phases is achieved by introducing a relaxation factor α according to:

$$\langle T\rangle_{f,P} = \alpha\langle T\rangle_{f,P}{}^{i+} + (1-\alpha)\langle T\rangle_{f,P}{}^{i} \tag{16.5}$$

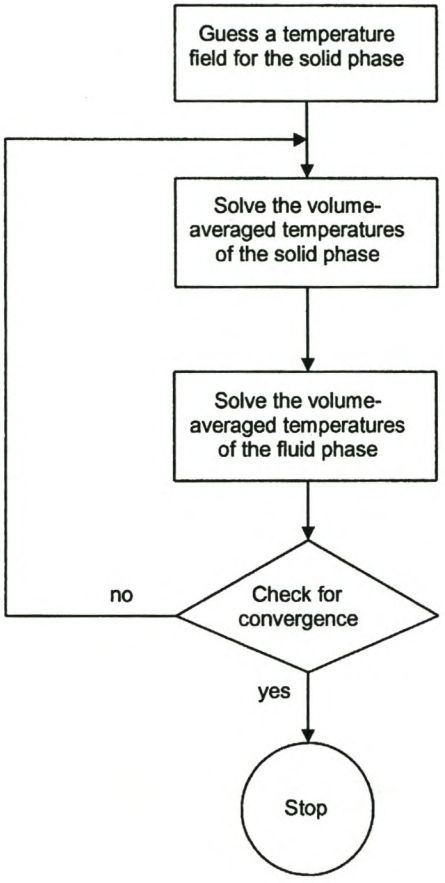

Figure 16.3 Procedure for the solution of the transformed volume-averaged energy equations for the fluid and solid phases.

and:

$$\langle T \rangle_{s,P} = \alpha \langle T \rangle_{s,P}^{\,i+} + (1-\alpha)\langle T \rangle_{s,P}^{\,i}. \tag{16.6}$$

where α is a value between zero and one, $\langle T \rangle_{f,P}^{\,i+}$ and $\langle T \rangle_{s,P}^{\,i+}$ are the newly calculated values of $\langle T \rangle_{f,P}$ and $\langle T \rangle_{s,P}$ respectively, and $\langle T \rangle_{f,P}^{\,i}$ and $\langle T \rangle_{s,P}^{\,i}$ are the values of $\langle T \rangle_{f,P}$ and $\langle T \rangle_{s,P}$ respectively from the previous iteration. The value of the relaxation factor α

determined the change of $\langle T \rangle_{f,P}$ and $\langle T \rangle_{s,P}$ from iteration to iteration. When the solution converges, that is when $\langle T \rangle_{f,P}^{i+}$ and $\langle T \rangle_{s,P}^{i+}$ become equal to $\langle T \rangle_{f,P}^{i}$ and $\langle T \rangle_{s,P}^{i}$ respectively, the LHS's equal the RHS's in Equation (16.5) and Equation (16.6) for any value of α between zero and one.

CHAPTER 17

COMPARISON BETWEEN THEORY AND EXPERIMENT

17.1 Overview

In this chapter, pressure gradient and thermal performance quantities derived from the solution of the transformed volume-averaged momentum equation [Equation (8.2)] and solutions of the transformed volume-averaged energy equations for the solid phase [Equation (8.3)] and the fluid phase [Equation (8.5)] are compared to experimentally determined pressure gradient and thermal performance results of cellular metallic foams. Experimental results were obtained from literature. The most comprehensive pressure gradient and thermal performance experimental results available were those of Bastawros *et al.* (1998). Only steady state behaviour of morphologically uniform metallic foams was considered.

17.2 Experimental design

Figure 17.1 shows the experimental configuration used by Bastawros *et al.* (1998), which consists of a heated aluminium substrate at the bottom. A 6061 aluminium foam test piece was either braised or epoxy-glued to the substrate material. The test piece is encapsulated inside a channel, which is thermally insulated. Air is passed through the test piece. The test piece length L is 40 mm and width W is 25 mm.

The solid phase thermal conductivity is 156.0 W/m·°C. Thermophysical properties of air were taken at STP conditions (25 °C, 101325 N/m^2), yielding a density ρ_f of 1.184 kg/m^3, a viscosity μ of 1.838×10^{-5} kg/s·m, a thermal conductivity k of 0.026 W/m·°C and an adiabatic specific heat capacity c_p of 1007 J/kg·°C.

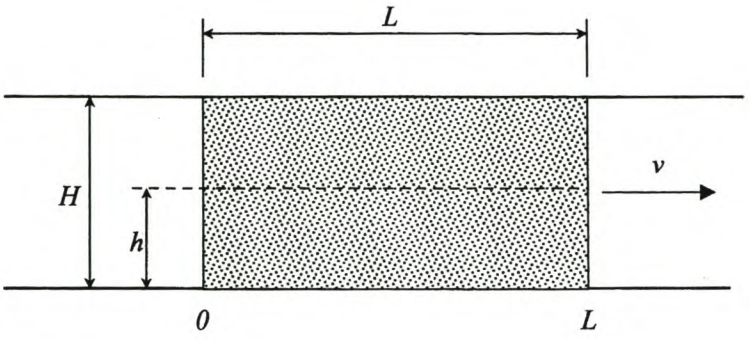

Figure 17.1 Experimental configuration.

17.3 Pressure gradient test cases

Figure 17.2 to Figure 17.4 compare experimentally determined pressure gradient data published by Bastawros *et al.* (1998) to that predicted by the transformed volume-averaged momentum equation. Pressure gradient data for three different metallic foams morphologies was published. Morphological data and characteristic RUC dimensions are given in Table 17.1.

17.4 Pressure gradient model prediction

The model predicted pressure gradients were determined analytically from a simplified form of the transformed volume-averaged momentum equation, in which a uniform phasial volume-averaged velocity was assumed throughout the porous domain (*i.e.* the viscous effect of the channel walls was neglected).

Cell size designation [pores per inch (ppi)]	10	20	30
Measured cell size a [mm]	5.2	4.5	2.7
Measured porosity ε_f	0.936	0.931	0.915
Tortuosity χ	1.308	1.321	1.359
Overall characteristic dimension d [mm]	3.068	2.661	1.606
Characteristic strand width d_s [mm]	0.4732	0.4271	0.2881
Specific surface area A_{sf}/V_o	510.0	607.5	1100.0

Table 17.1 Foam morphological data and characteristic RUC dimensions.

17.5 Pressure gradient results

Experimentally determined values are shown as data points and modelled values are shown as curves in the graphical comparisons. In this simplified form of the transformed volume-averaged momentum equation, substituting Equation (10.11) into Equation (10.1) and rearranging terms yields:

$$\nabla\langle p\rangle_f^f = -\frac{\mu}{\varepsilon_f}(3-\chi)(\chi-1)\frac{\rho_f \chi^2}{\mu \varepsilon_f{}^2 d}\left(\frac{3C_{D,v}}{2}+\frac{C_{D,f}}{4}\right)\langle \boldsymbol{v}\rangle_f\langle v\rangle_f . \qquad (17.1)$$

Figure 17.2 to Figure 17.4 show the absolute value of pressure gradient.

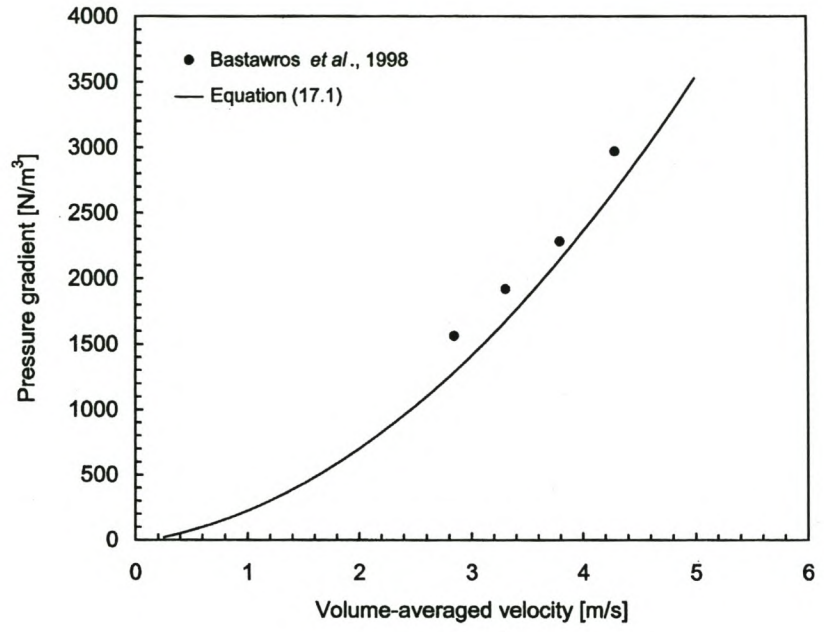

Figure 17.2 Comparison between model predicted and experimentally determined pressure gradient in 10 ppi metallic foam.

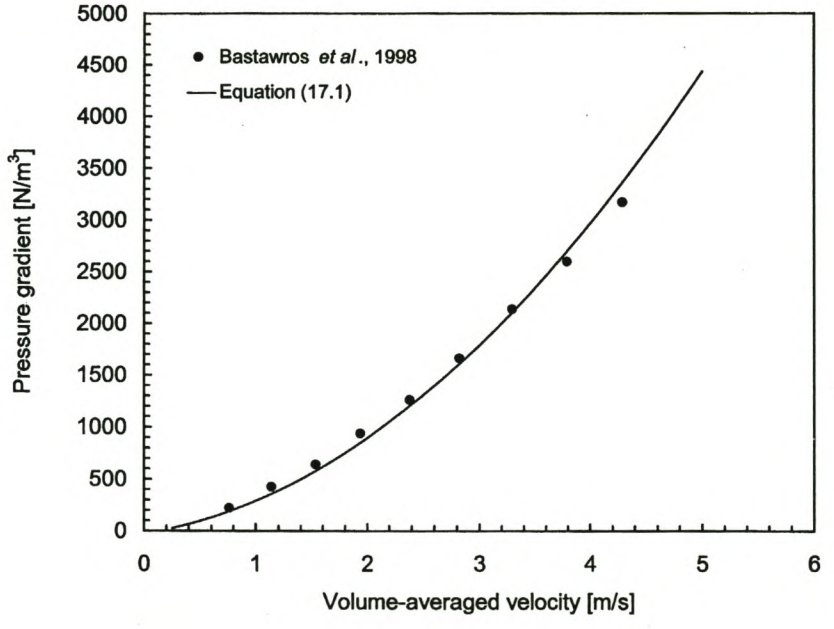

Figure 17.3 Comparison between model predicted and experimentally determined pressure gradient in 20 ppi metallic foam.

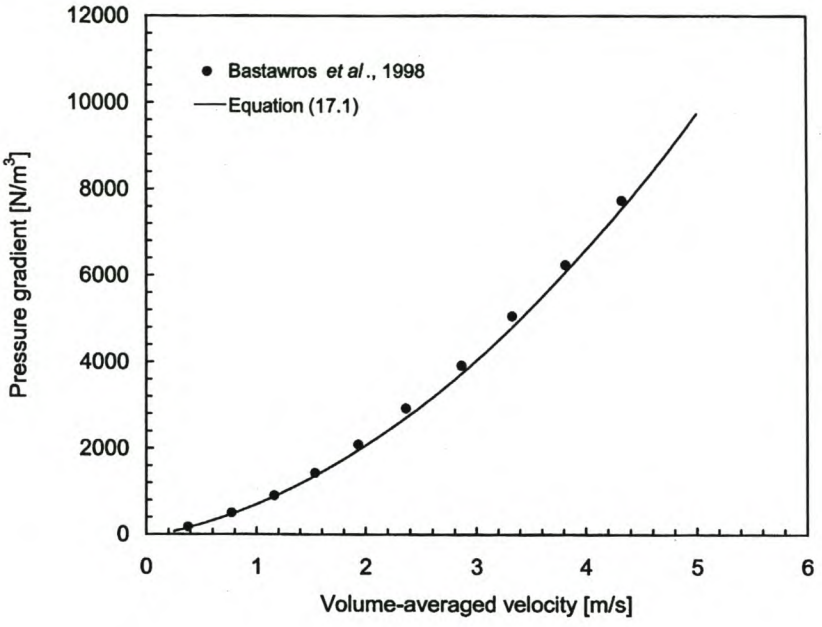

Figure 17.4 Comparison between model predicted and experimentally determined pressure gradient in 30 ppi metallic foam.

17.6 Heat transfer test cases

Only one foam sample, namely the 30 ppi designation in Table 17.1, was used in the heat transfer experiments.

Seven different heat transfer case studies (designated Case Study 1 to Case Study 7) were considered, all representing steady-state thermal conditions. Table 17.2 summarises the case study configuration parameters.

The graphical comparisons of solid temperature distributions show only every fourth data point from the complete temperature data presented by Bastawros *et al.* (1998). In the experimental data the wall temperature in the experiments was reported to be in the order of 100 °C. In three cases, namely Figure 7a, Figure 7b and Figure 7c in Bastawros *et al.* (1998), the wall temperature was specifically reported as 93 °C, 93 °C and 90 °C

Case Study	1	2	3	4	5	6	7
Substrate temperature, T_s [°C]	93	93	93	93	93	90	93
Flow velocity, v [m/s]	0-8	0-6	0-3	0-6	1.0	1.0	2.0
Fluid inlet temperature, T_f [°C]	20.0	20.0	20.0	20.0	20.0	20.0	20.0
Test piece height, H [mm]	7.2	10.25	15.7	10.15	10.0	16.0	16.0
Substrate bonding*	Br	Br	Br	Ep	Br	Br	Br
Overall contact resistance**, R_{ss} [m·°C/W]	0	0	0	1.4×10^{-4}	0	0	0

*Br - braised, Ep - epoxy
** See comments regarding overall thermal contact resistance

Table 17.2 Experimental configurations.

respectively. In the solutions of the transformed volume-averaged energy equations, a wall temperature of 93 °C was assumed everywhere, except for the one case where a wall temperature of 90 °C was reported (Figure 7c, Bastawros *et al.*, 1998).

17.7 Heat transfer model predictions

The thermal performance of the seven case studies was also predicted from the computational solution of the transformed volume-averaged momentum equation and the transformed volume-averaged energy equations of the solid and the fluid phases. The MacFlow and MacSolidFluid computer codes, discussed in Appendix IV, were used for this purpose. A uniform inlet velocity was assumed at the inflow boundary for the solution of the transformed volume-averaged momentum equation. The viscous effect of the two vertical channel walls (25 mm apart) was assumed negligible. With the top surface and the two sidewalls offering complete thermal insulation, the modelling of flow and thermal behaviour in the test piece is essentially reduced to a two-dimensional steady-state solution of the transformed volume-averaged equations.

The discretised forms of the transformed volume-averaged equations were solved using the direct method of King (1976), at the grid points of a two-dimensional 32 × 27 grid in the domain enclosed by the test piece. Grid points were spaced closer together in regions of higher temperature gradients, *i.e.* near the solid wall and near the inflow system boundary. Table 17.3 gives finite volume sizes as percentages of the overall dimension. Finite volumes are indexed in a standard Cartesian coordinate system, starting at the origin.

Within the current framework, no attempt was made to identify the hydraulic entrance length within the metallic foam needed to reach fully developed flow. Other studies for flow in porous media (granular media with low porosity) have demonstrated that this entrance length is very small, in the order of halve the cell diameter for $Re < 10^4$. (Sangani and Behl, 1989; Kaviany, 1995, p. 70)

Finite volume	Size [%]
x-direction:	
1	0.00025
2-21	2.5
22-31	5.0
32	0.00025
y-direction:	
1	0.00025
2-11	1.25
12-16	2.5
17-21	5.0
22-26	10.0
27	0.00025

Table 17.3 Grid configuration.

17.8 Heat transfer results

Experimentally determined values are shown as data points and modelled values are shown as curves in the graphical comparisons shown in Figure 17.5 to Figure 17.14. For Case Studies 1 to 4, Figure 17.5 to Figure 17.8 compare the mean heat flux with reference to the substrate area, as a function of the open channel flow velocity, which is equivalent to the uniform inlet phasial volume-averaged velocity $\langle v \rangle_f$ in the porous domain.

The overall heat exchange in Figure 17.5 to Figure 17.8 was determined from the enthalpy gained by the fluid phase over the length L, which is given by:

$$Q = \dot{m} c_{p,f} \left[T_f(L) - T_f(0) \right], \tag{17.2}$$

where $\dot{m}$ is the mass flow rate per unit channel width given as:

$$\dot{m} = \rho_f H v, \tag{17.3}$$

where T_f is the mean fluid temperature and v the mean flow velocity across a plane normal to the flow direction. The mean fluid temperature T_f was determined either experimentally (Bastawros *et al.*, 1998), or from the solution of Equation (8.3) and Equation (8.5).

Figure 17.5 also shows the mean heat flux through the substrate in an open channel not containing a test piece. In the model prediction for the open channel solution, the transformed volume-averaged momentum equation was not solved. Instead, a velocity profile associated with two-dimensional fully developed laminar flow between parallel walls (Couette-Poiseuille flow) was assumed between the top and bottom channel walls. To simulate an open channel, a porosity of one was specified in the solution of the transformed volume-averaged energy equation for the fluid phase.

In Case Study 4, the metallic foam sample is attached to the substrate material using a high thermal conductivity epoxy glue. In general, with relatively thick epoxy layers the overall thermal resistance between the substrate material and the metallic foam is primarily determined by the thermal conductivity of the epoxy layer. However, with thin epoxy layers bonding aluminium (<500 μm), the thermal contact resistance between the epoxy and aluminium becomes relevant in the overall thermal resistance (Brenner, 1999).

Due to its high viscosity, an epoxy is often unable to fill pits and pores in the oxide layer, which forms on an exposed aluminium surface. The resulting thermal contact resistance of a bonded surface has been found to be a function of the epoxy cure temperature (which affects its viscosity), the pressure applied during the curing process and the anodising technique used. Special methods of anodising have been developed to reduce thermal contact resistance. Quantifying the thermal contact resistance is therefore rather subjective.

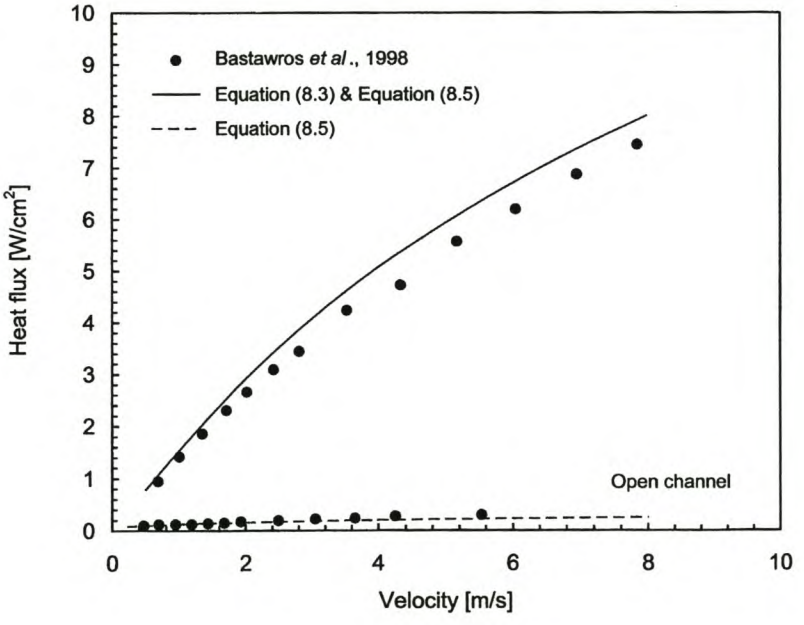

Figure 17.5 Mean heat flux for Case Study 1.

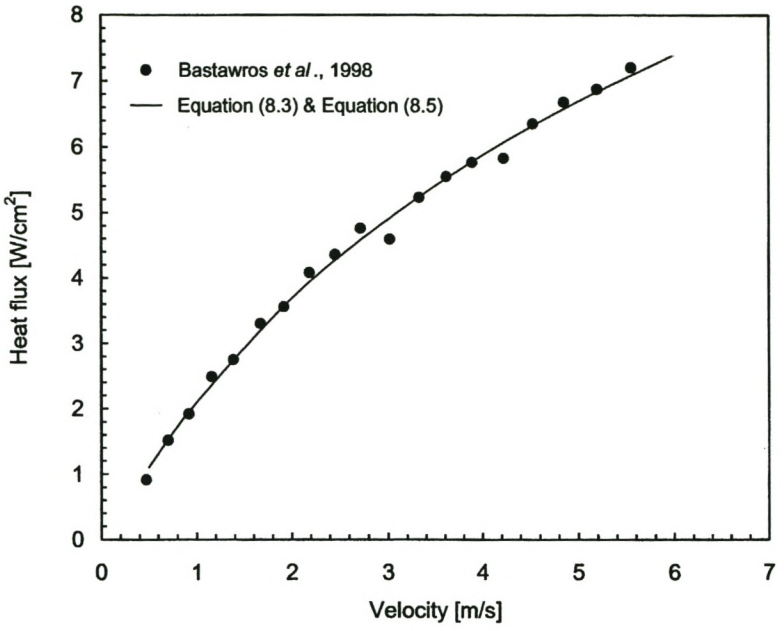

Figure 17.6 Mean heat flux for Case Study 2.

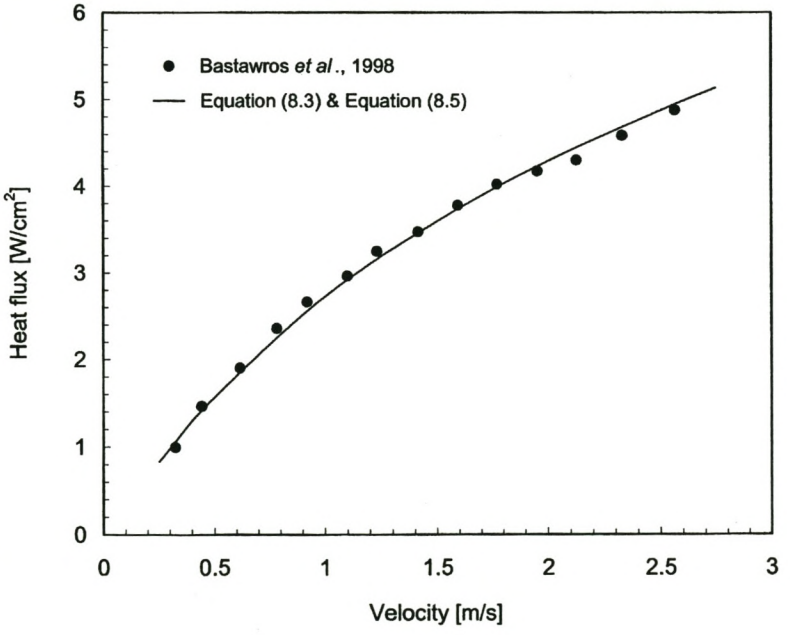

Figure 17.7 Mean heat flux for Case Study 3.

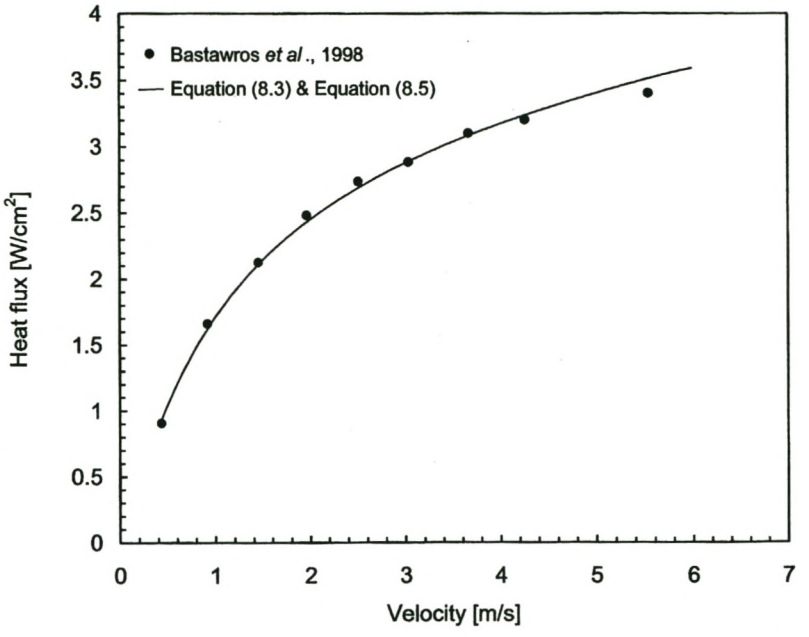

Figure 17.8 Mean heat flux for Case Study 4.

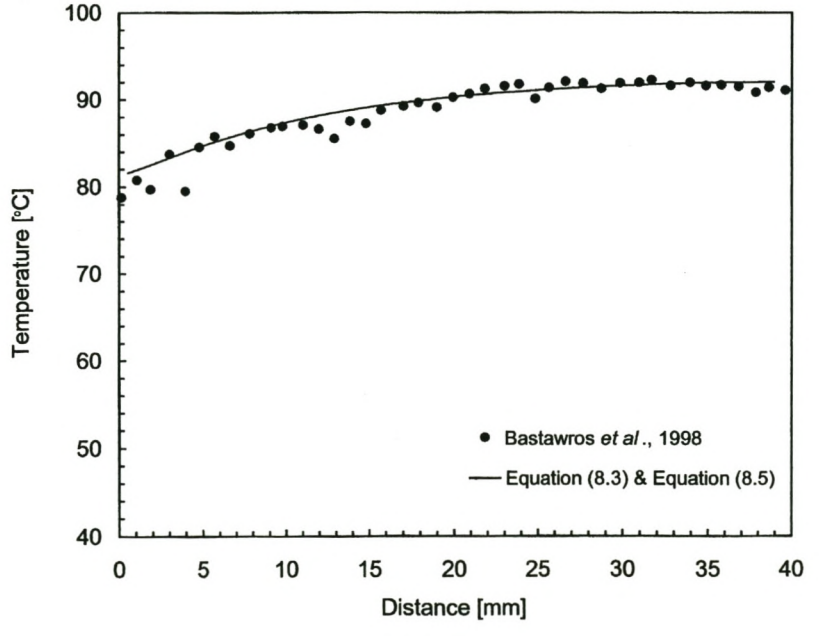

Figure 17.9 Solid phase temperature distribution for Case Study 5 at h = 1.1 mm.

Figure 17.8 shows results from Equation 8.3 and Equation 8.5, based on an overall thermal resistance of 1.4×10^{-4} m^2·°C/W. The specified thermal conductivity of Master Bond™ grade EP21ANHT epoxy (used in the Case Study) is 3.3 W/m·°C. With an epoxy bond thickness of ≈200 μm, the thermal resistance of the epoxy layer alone is 6.1×10^{-5} m^2·°C/W. The remaining 7.9×10^{-5} m^2·°C/W comes from the two thermal contact resistances on either side of the epoxy glue.

Figure 17.9 to Figure 17.11 compare the temperature distribution in the solid phase along the length of the test piece, for Case Study 5. The temperature distributions are at distances 1.1 mm, 5.1 mm and 9.8 mm respectively from the substrate material.

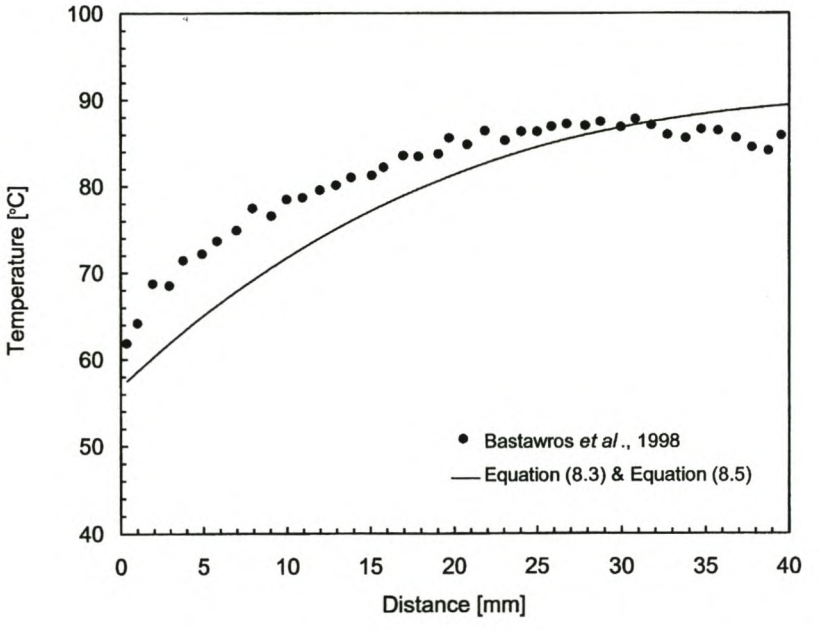

Figure 17.10 Solid phase temperature distribution for Case Study 5 at h = 5.1 mm.

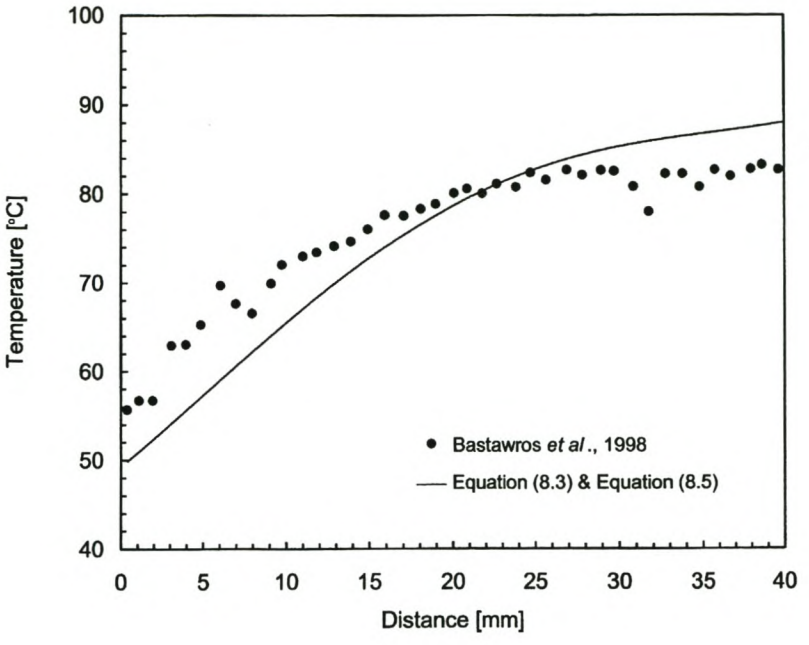

Figure 17.11 Solid phase temperature distribution for Case Study 5 at $h = 9.8$ mm.

Figure 17.12 to Figure 17.14 show the temperature distribution in the solid phase along the length of the test piece, for Case Study 6, at distances 0.8 mm, 8.4 mm and 15.4 mm respectively from the substrate material.

Figure 17.15 shows the solid phase temperature distribution map for Case Study 7. The corresponding temperature distribution determined from the solution of the transformed volume-averaged equations is shown in Figure 17.16.

Figure 17.17 shows the fluid phase temperature distribution map for Case Study 7. The corresponding temperature distribution determined from the solution of the transformed volume-averaged equations is shown in Figure 17.18.

The spatial distributions of temperatures in the solid and the fluid phases, shown in Figure 17.9 to Figure 17.15 and Figure 17.17, were monitored through a high-resolution infrared camera with a 256 × 256 array and 30 μm pixel size. A 50 mm IR lens was used to provide a magnification of 0.175 mm/pixel.

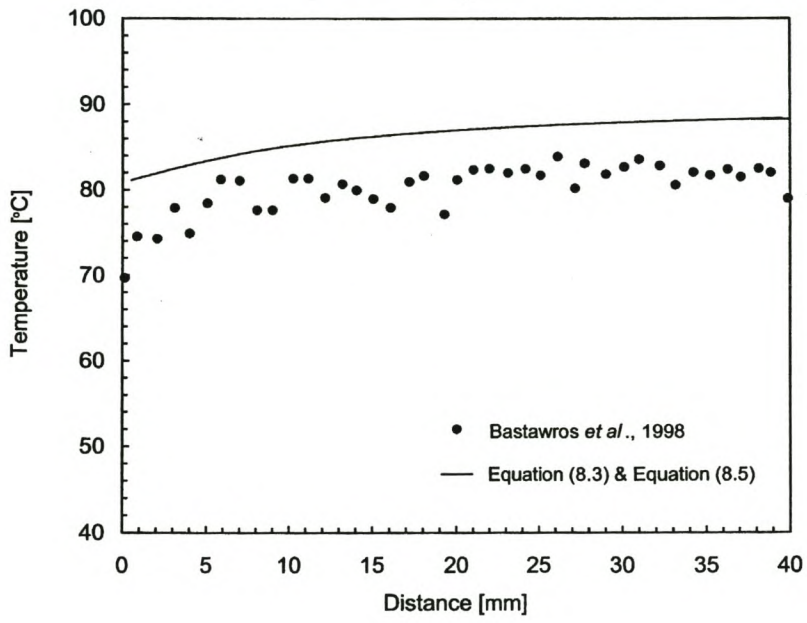

Figure 17.12 Solid phase temperature distribution for Case Study 6 at h = 0.8 mm.

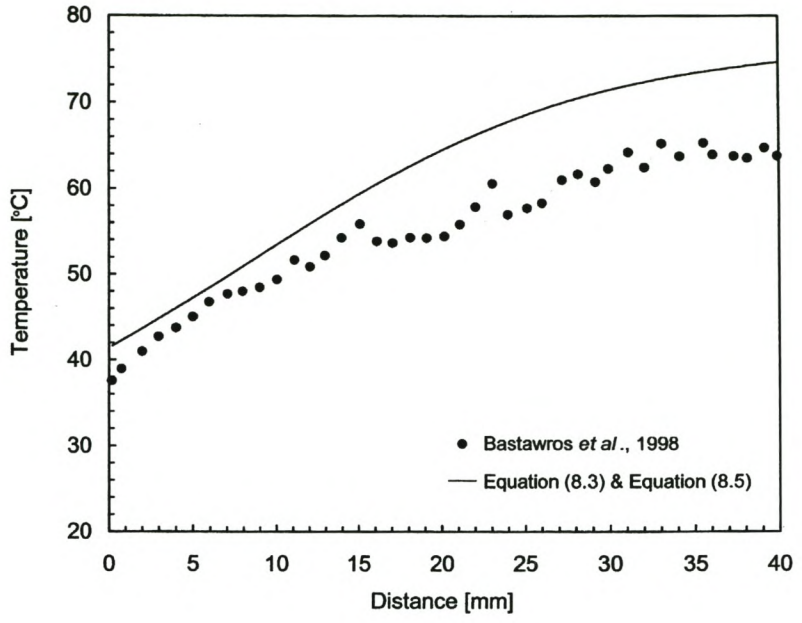

Figure 17.13 Solid phase temperature distribution for Case Study 6 at h = 8.4 mm.

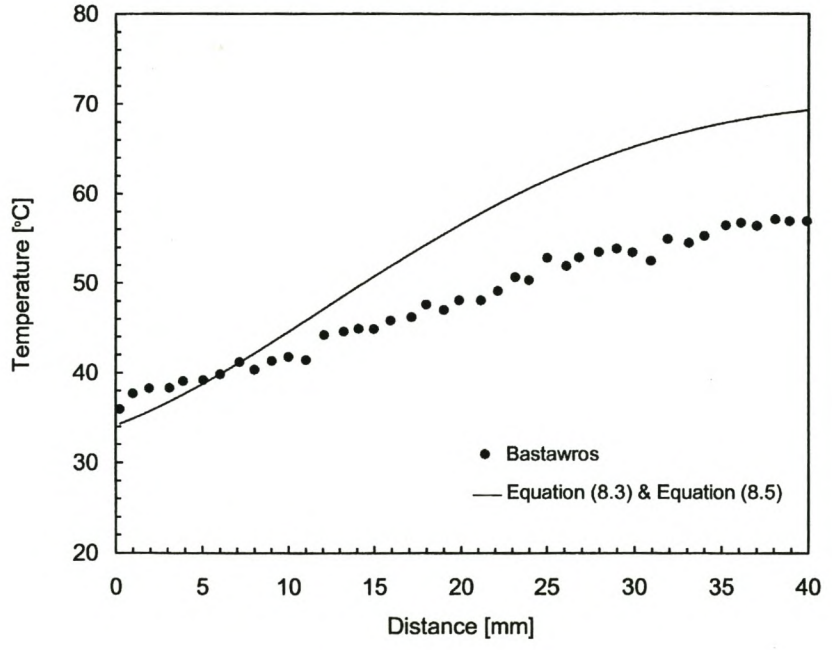

Figure 17.14 Solid phase temperature distribution for Case Study 6 at h = 15.4 mm.

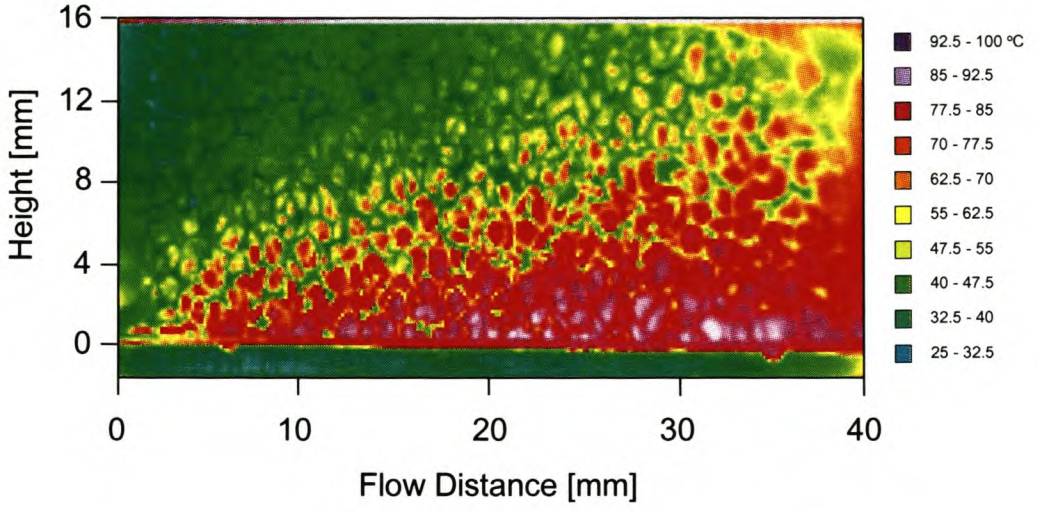

Figure 17.15 IR measured temperature distribution map in the solid phase for Case Study 7.

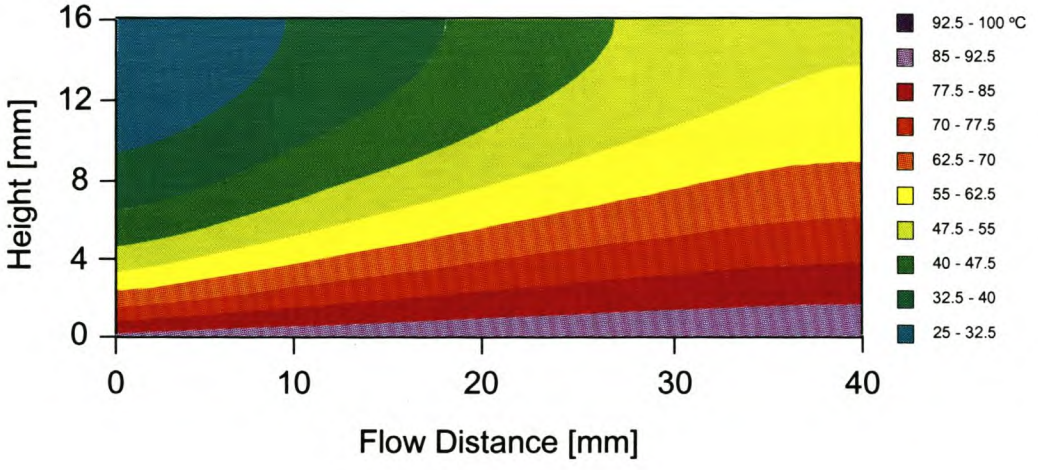

Figure 17.16 Model predicted temperature distribution map in the solid phase for Case Study 7

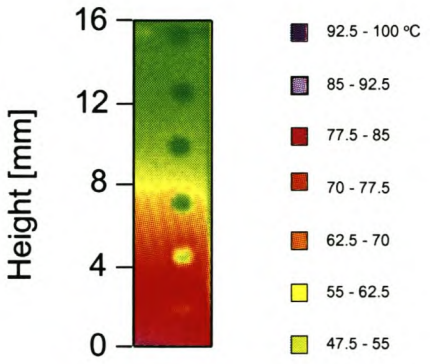

Figure 17.17 IR measured temperature distribution map in the fluid phase when leaving the foam sample, for Case Study 7

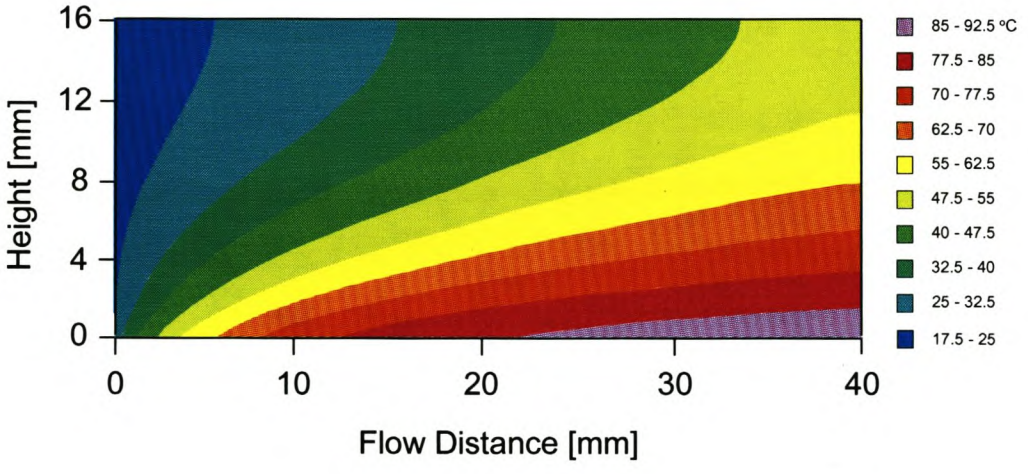

Figure 17.18 Model predicted temperature distribution map in the fluid phase for Case Study 7

CHAPTER 18

CONCLUSION

A set of elliptic partial differential governing equations and a computational solution algorithm were developed to describe fluid flow and heat transfer in stationary cellular metallic foams saturated with a fluid in motion. Fluid flow is described by a momentum balance differential equation of the spatial distribution of locally mean velocities. By including a momentum balance equation in the set of partial differential equations, the relevance of the model is extended to porous domains of variable locally mean fluid velocity distributions. Heat transfer is described by two separate energy balance differential equations of the spatial and temporal distribution of locally mean temperature. One equation is for the fluid and the other is for the solid matrix. With separate energy balance equations for the fluid and the solid matrix, the model applies to a thermal equilibrium and a thermal non-equilibrium state between the fluid and the solid matrix. A thermal non-equilibrium state is created either by thermal contact between the solid matrix and a solid wall of temperature different to that of the fluid, or by an energy source present in the fluid or the solid matrix.

Differential momentum and energy balance equations of locally mean velocities and temperatures were derived by applying the analytical process of volume averaging to the microscopic momentum equation (Navier-Stokes equation) and the microscopic energy equation. This process attempts to capture the most important behavioural trends of momentum and energy transport due to convection, diffusion and dispersion in the metallic foam, in terms of the locally mean velocity of the fluid, and the locally mean temperatures of the fluid and the solid matrix.

A useful form of the set of governing equations requires a momentum and energy balance description at locally mean (or macroscopic) level to be presented in terms of locally mean velocity and temperature only. However, applying the analytical process of volume

averaging to the microscopic momentum equation yields certain momentum dispersion processes, which are described as integrals of microscopic processes presented in terms of microscopic intensive quantities. The same predicament occurs in the application of volume averaging to the microscopic energy equation. In that case, thermal conduction, interphasial heat transfer and thermal dispersion processes are described as integrals of microscopic processes presented in terms of microscopic intensive quantities.

A solution is presented which involves the transformation of integrals of microscopic processes presented in terms of microscopic intensive quantities into a description in terms of locally mean intensive quantities. Integrals describing dispersion (momentum and thermal) and interphasial heat transfer in terms of microscopic intensive quantities were transformed to be presented in terms of locally mean intensive quantities by substituting established theoretical models obtained from literature. These substitutions introduced certain transport parameters into the model. The transformation of the integral describing conduction in terms of microscopic intensive quantities was accomplished by a novel approach in the analytical volume-averaging process of the microscopic energy equation. This process introduced two additional transport parameters in the form of effective thermal conductivities, which were defined directly from the formulation of the analytical process.

Analytical, numerical and experimental methods were used to derive, evaluate and qualify mathematical relationships for the transport parameters. These mathematical relationships are presented as functions of the local foam morphology parameter as well as the thermophysical properties of the fluid and the solid matrix. The local foam morphology is completely defined by the local porosity and cell size. The mathematical relationships for the transport parameters are based on a rigorous geometric model of the metallic foam morphology. None of the transport parameters include any calibration coefficients that require *a priori* judgement of the flow and thermal behaviour of a particular metallic foam configuration.

A discretisation process based on a finite-volume algebraic approximation applied at a number of discrete grid points allowed for the partial differential equations to be replaced by three sets of linear algebraic equations. This process was carried out on the differential

momentum balance equation for the fluid phase and the differential energy balance equations for the solid and the fluid phases. In thermal systems employing metallic foams to enhance heat transfer, the flow is hardly ever regulated, even under dynamic thermal loading, and for practical reasons never undergoes rapid changes. Therefore, only the steady-state version of the differential momentum equation was considered.

Two computer programs, MacFlow and MacSolidFluid, were developed to solve the sets of linear algebraic equations for the steady-state two-dimensional phasial volume-averaged velocity components of the fluid phase and the steady-state two-dimensional phasial volume-averaged temperatures of the solid and the fluid phases.

The computational solution of the set of partial differential equations in the porous domain of a cellular metallic foam heat exchanger allows for the prediction of its thermal performance and the flow power requirements. Results obtained from the computational solution show excellent agreement with experimentally determined pressure drop and thermal performance parameters of a metallic foam heat exchanger. The model can therefore be used with confidence to assist in the selection of a porosity and cell size configuration that will to maximise heat transfer per flow power requirement, and will eliminate the potential occurrence of hot spots in the porous domain and substrate material. The differential form of the set of equations allows for its application to cellular metallic foam heat exchangers of arbitrary shapes exposed to spatially and temporally variable heat loads in a variety of forms.

The mathematical description of fluid flow and heat transfer in the fluid, and the computational solution algorithms facilitate a conjugate solution of flow and heat transfer in the gaseous and liquid parts in a porous domain that is partially liquid filled. In the current version of the MacFlow and MacSolidFluid computer programs, the geometry of the free boundary between the gaseous and liquid phase and the variation of thermophysical properties across the free boundary must be specified manually.

The mathematical description of heat transfer in the solid matrix and the computational solution algorithm facilitate a conjugate solution of heat transfer in a porous domain and a solid substrate material adjacent to the porous domain. In that case, the solid material is

merely described as a metallic foam with a porosity of zero. The treatment of system boundaries and the MacSolidFluid computer program are currently not sufficient for a conjugate computational heat transfer solution.

Future work therefore includes the treatment of system boundaries for a conjugate solution of heat transfer in a porous domain and an adjacent solid substrate material, and the extension of the MacFlow and MacSolidFluid computer programs to handle partially liquid filled porous domains.

Other future work includes the extension of the geometric model to represent the non-isentropic nature of compressed metallic foams, which is increasingly being used to enhance heat transfer under certain conditions (Antohe *et al.*, 1996). Advancements in the modelling of transport parameters include the development of a sufficient conceptual representation of longitudinal dispersion. Further advancements in the quantification of transport parameters include a large-scale experimental verification of the interphasial heat transfer coefficient.

In the experimental evaluation of Equation (13.2) for the prediction of transverse dispersivity, Figure 13.28 shows an exponential relationship between dispersivity and flow velocity for each of the metallic foam samples tested. The energy required for high Peclét number transverse dispersion is obtained from the same flow momentum transfer phenomena that manifests itself in the form of the flow pressure gradient. The exponential relationship between transverse dispersivity and flow velocity may therefore be correlated with the exponential relationship between flow pressure gradient and flow velocity, shown in Figure 17.2 to Figure 17.4. Many of the innovative experimental imaging and data processing techniques introduced in Chapter 13 may be further developed for dispersion experiments.

Although most of the work in this study is dedicated to the modelling of heat transfer in cellular metallic foams, most of the analytical fundamentals, and numerical and experimental techniques apply to the modelling of heat transfer in consolidated porous media in general. The approach used in this study lays the foundation for the mathematical modelling of fluid flow and heat transfer in consolidated porous structures

media other than cellular metallic foams. The conduction model can also be extended to include unconsolidated porous media and to accommodate fluids of variable thermophysical properties.

APPENDIX I

GENERAL CONTINUITY EQUATION, MASS CONSERVATION EQUATION FOR AN INDIVIDUAL SPECIE IN A MIXTURE, MOMENTUM EQUATION AND ENERGY EQUATION

I.1 Overview

The general continuity equation, the continuity equation for an individual specie in a mixture, the momentum equation and the energy equation have been presented in literature in many different forms (compare Bird *et al.*, 1960, p. 315 and Rohsenow and Choi, 1961, p.170). This appendix is devoted to deriving a general form of these equations as they are used in the thesis.

There are generally two main approaches toward the derivation of the differential form of the general continuity equation, the continuity equation for an individual specie in a mixture, the momentum equation and the energy equation, namely the differential volume approach and the integral approach. Both approaches relate the transient behaviour of some extensive quantity in an inertial control volume of fixed shape to the net transfer of that quantity across the boundaries of the control volume. In the differential volume approach though, this relation is with reference to a differential volume within a particular coordinate system. The resulting balance equation is then usually generalised to apply to any coordinate system. The integral approach on the other hand, is universal to any coordinate system throughout the derivation process, and is used in this appendix.

I.2 Reynolds Transport Theorem

In the integral approach, a general balance law is written in terms of the substantial derivative of an extensive quantity Φ, or:

$$\frac{\mathrm{D}\Phi}{\mathrm{D}t} = \frac{\partial \Phi}{\partial t} + \boldsymbol{v} \cdot \nabla \Phi . \tag{I.1}$$

The substantial derivative is then substituted by an expression for the transient behaviour of the extensive quantity in an inertial control volume of fixed shape and volume V, and an expression for the net transfer of the extensive quantity across the boundaries A of the control volume. This is done using the Reynolds Transport Theorem (Zucrow and Hoffman, 1976, p. 83) which states that:

$$\frac{\mathrm{D}\Phi}{\mathrm{D}t} = \int_V \frac{\partial(\rho\phi)}{\partial t} \mathrm{d}V + \int_A \rho\phi \boldsymbol{v} \cdot \boldsymbol{n} \, \mathrm{d}A , \tag{I.2}$$

where Φ is an extensive quantity, ϕ is a corresponding intensive quantity, ρ is the fluid density, t represents time, $\boldsymbol{n}$ is a unit surface vector on the boundary of the control volume and $\boldsymbol{v}$ is a velocity vector. The extensive quantity Φ and the intensive quantity ϕ are related by:

$$\mathrm{d}\Phi = \rho\phi \, \mathrm{d}V \tag{I.3}$$

or:

$$\Phi = \int_V \rho\phi \, \mathrm{d}V . \tag{I.4}$$

I.3 Continuity equation

In order to derive the general continuity equation, consider the law of Conservation of Total Mass (Zucrow and Hoffman, 1976, p. 84) in a control volume, which states that:

$$\frac{\mathrm{D}M}{\mathrm{D}t} = 0, \tag{I.5}$$

where M represents total mass. Since mass in the control volume is defined as:

$$M = \int_V \rho \, \mathrm{d}V, \tag{I.6}$$

it follows from Equation (I.6) and Equation (I.4) that $\phi = 1$, which reduces the Reynolds Transport Theorem to:

$$\int_V \frac{\partial \rho}{\partial t} \mathrm{d}V + \int_A \rho \boldsymbol{v} \cdot \boldsymbol{n} \, \mathrm{d}A = 0. \tag{I.7}$$

Applying the Divergence Theorem (Kreyszig, 1993, p. 545) to the second term on the LHS of Equation (I.7) yields:

$$\int_V \frac{\partial \rho}{\partial t} \mathrm{d}V + \int_V \nabla \cdot (\rho \boldsymbol{v}) \mathrm{d}V = 0. \tag{I.8}$$

Reducing the control volume V in Equation (I.8) to a differential size $\mathrm{d}V$, the limiting value of integrals become the integrands, thus:

$$\frac{\partial \rho}{\partial t} + \nabla \cdot (\rho \boldsymbol{v}) = 0. \tag{I.9}$$

Expanding the second term on the LHS of Equation (I.9) and rearranging terms, yields the

general form of the continuity equation:

$$\frac{\partial \rho}{\partial t} + \boldsymbol{v} \cdot \boldsymbol{\nabla} \rho = -\rho \boldsymbol{\nabla} \cdot \boldsymbol{v}, \tag{I.10}$$

or:

$$\frac{\mathrm{D}\rho}{\mathrm{D}t} = -\rho \boldsymbol{\nabla} \cdot \boldsymbol{v}. \tag{I.11}$$

I.4 Continuity equation for an individual specie in a mixture

The law of Conservation of Mass in a control volume of an individual specie in a mixture states that:

$$\frac{\mathrm{D}M_A}{\mathrm{D}t} = J_A, \tag{I.12}$$

where M_A represents mass of specie A and J_A is the mass transferred across the external boundaries into the control volume by molecular diffusion. The mass of the individual specie A in the control volume is defined as:

$$M_A = \int_V \rho c_A \, \mathrm{d}V, \tag{I.13}$$

where c_A is the mass fraction of specie A in the mixture. From Equation (I.13) and Equation (I.4) it follows that $\phi = c_A$. Mass transferred across the external boundaries of the control volume by molecular diffusion is represented by the term:

$$J_A = -\int_A \boldsymbol{j}_A \cdot \boldsymbol{n} \, \mathrm{d}A, \tag{I.14}$$

where $\boldsymbol{j}_A$ is the mass flux per unit area of specie A. Substituting the Reynolds Transport Theorem [Theorem (I.2)] with $\phi = c_A$ into the LHS of Equation (I.12) and Equation (I.14) into the RHS of Equation (I.12) yields:

$$\int_V \frac{\partial(\rho c_A)}{\partial t} \mathrm{d}V + \int_A \rho c_A \boldsymbol{v} \cdot \boldsymbol{n} \, \mathrm{d}A = -\int_A \boldsymbol{j}_A \cdot \boldsymbol{n} \, \mathrm{d}A . \tag{I.15}$$

Applying the Divergence Theorem (Kreyszig, 1993, p. 545) to the surface integrals in Equation (I.15) converts them to volume integrals, giving:

$$\int_V \frac{\partial(\rho c_A)}{\partial t} \mathrm{d}V + \int_V \nabla \cdot (\rho c_A \boldsymbol{v}) \mathrm{d}V = -\int_V \nabla \cdot \boldsymbol{j}_A \, \mathrm{d}V . \tag{I.16}$$

Reducing the control volume V in Equation (I.16) to a differential size $\mathrm{d}V$ yields:

$$\frac{\partial(\rho c_A)}{\partial t} + \nabla \cdot (\rho c_A \boldsymbol{v}) = -\nabla \cdot \boldsymbol{j}_A . \tag{I.17}$$

Expanding the term on the LHS of Equation (I.17) yields:

$$\rho \left(\frac{\partial c_A}{\partial t} + \boldsymbol{v} \cdot \nabla c_A \right) + c_A \left[\frac{\partial \rho}{\partial t} + \nabla \cdot (\rho \boldsymbol{v}) \right] = -\nabla \cdot \boldsymbol{j}_A . \tag{I.18}$$

Rewriting the terms in the parenthesis in Equation (I.18) in terms of a substantial derivative and substituting the continuity Equation (I.9) into the last term on the RHS of Equation (I.18), yields the equation for the mass conservation of an individual specie in a mixture:

$$\rho \frac{\mathrm{D}c_A}{\mathrm{D}t} = -\nabla \cdot \boldsymbol{j}_A . \tag{I.19}$$

I.5 Momentum equation

Newton's second law for the control volume states that:

$$\frac{\mathrm{D}\boldsymbol{P}}{\mathrm{D}t} = \boldsymbol{F}_{ext}, \tag{I.20}$$

where $\boldsymbol{P}$ is the momentum vector associated with the fluid in the control volume given by:

$$\boldsymbol{P} = \int_V \rho \boldsymbol{v}\, \mathrm{d}V. \tag{I.21}$$

$\boldsymbol{F}_{ext}$ is the external force acting on the control volume. This force can be divided into body forces and surface forces. Body forces are determined by the integral term:

$$\int_V \rho \boldsymbol{B}\, \mathrm{d}V, \tag{I.22}$$

where $\boldsymbol{B}$ denotes the body force vector per unit mass. The surface forces are those forces acting on the boundaries of the control volume, by virtue of its contact with the surroundings. The surface forces consist of pressure forces given by the integral expression:

$$-\int_A p\, \boldsymbol{n}\, \mathrm{d}A \tag{I.23}$$

and viscous forces given by:

$$-\int_A \boldsymbol{\tau} \cdot \boldsymbol{n}\, \mathrm{d}A, \tag{I.24}$$

where p is the pressure and $\boldsymbol{\tau}$ denotes the stress tensor. The three normal components and six tangential components of the stress tensor are discussed in Schlichting (1979, p.52). From Equation (I.21) and Equation (I.4) it follows that $\phi = \boldsymbol{v}$. Substitution into the Reynolds Transport Theorem [Theorem (I.2)] and subsequently into the LHS of Equation (I.20) and substituting Equation (I.22) to Equation (I.24) into the RHS of Equation (I.20), yields:

$$\int_V \frac{\partial(\rho \boldsymbol{v})}{\partial t} \mathrm{d}V + \int_A \rho \boldsymbol{n} \cdot \boldsymbol{v}\boldsymbol{v} \mathrm{d}A = \int_V \rho \boldsymbol{B} \mathrm{d}V - \int_A p \boldsymbol{n} \mathrm{d}A - \int_A \boldsymbol{\tau} \cdot \boldsymbol{n} \mathrm{d}A . \tag{I.25}$$

Applying the Divergence Theorem (Kreyszig, 1993 p. 545) on the surface integrals in Equation (I.25) converts them to volume integrals:

$$\int_V \frac{\partial(\rho \boldsymbol{v})}{\partial t} \mathrm{d}V + \int_V \nabla \cdot (\rho \boldsymbol{v}\boldsymbol{v}) \mathrm{d}V = \int_V \rho \boldsymbol{B} \, \mathrm{d}V - \int_V \nabla p \, \mathrm{d}V - \int_V \nabla \cdot \boldsymbol{\tau} \, \mathrm{d}V . \tag{I.26}$$

Reducing the control volume V in Equation (I.26) to a differential size $\mathrm{d}V$ yields:

$$\frac{\partial(\rho \boldsymbol{v})}{\partial t} + \nabla \cdot (\rho \boldsymbol{v}\boldsymbol{v}) = \rho \boldsymbol{B} - \nabla p - \nabla \cdot \boldsymbol{\tau} . \tag{I.27}$$

Expanding the two terms on the LHS of Equation (I.27) yields:

$$\rho \frac{\partial \boldsymbol{v}}{\partial t} + \boldsymbol{v} \frac{\partial \rho}{\partial t} + \boldsymbol{v}[\nabla \cdot (\rho \boldsymbol{v})] + \rho \boldsymbol{v} \cdot (\nabla \boldsymbol{v}) = \rho \boldsymbol{B} - \nabla p - \nabla \cdot \boldsymbol{\tau} , \tag{I.28}$$

or, after rearranging terms:

$$\rho \frac{\partial \boldsymbol{v}}{\partial t} + \boldsymbol{v} \left[\frac{\partial \rho}{\partial t} + \nabla \cdot (\rho \boldsymbol{v}) \right] + \rho \boldsymbol{v} \cdot (\nabla \boldsymbol{v}) = \rho \boldsymbol{B} - \nabla p - \nabla \cdot \boldsymbol{\tau} . \tag{I.29}$$

Substituting the continuity Equation (I.9) into Equation (I.29) yields the general conservation of momentum equation:

$$\rho\frac{\partial \boldsymbol{v}}{\partial t}+\rho\boldsymbol{v}\cdot(\nabla\boldsymbol{v})=\rho\boldsymbol{B}-\nabla p-\nabla\cdot\boldsymbol{\tau}, \tag{I.30}$$

or, using the identity of the substantial derivative:

$$\rho\frac{\mathrm{D}\boldsymbol{v}}{\mathrm{D}t}=\rho\boldsymbol{B}-\nabla p-\nabla\cdot\boldsymbol{\tau}. \tag{I.31}$$

I.6 Energy equation

The first law of thermodynamics for flow through an inertial control volume of fixed shape states that:

$$\frac{\mathrm{D}E}{\mathrm{D}t}=P, \tag{I.32}$$

where E is the stored energy and P represents power in the form of energy transferred across the external boundaries of the control volume as well as energy internally generated or consumed. For a pure substance, the stored energy consists of the internal energy and kinetic energy:

$$E=\int_V \rho\left(u_i+\frac{1}{2}v^2\right)\mathrm{d}V, \tag{I.33}$$

where u_i is the internal energy per unit mass and v is the magnitude of the velocity vector $\boldsymbol{v}$. Potential energy is generally also considered to form part of the stored energy of a pure substance. In an inertial control volume, the potential energy is constant with

reference to any datum elevation. From Equation (I.33) and Equation (I.4) it follows that $\phi = u_i + \frac{1}{2}v^2$. Energy transferred across the external boundaries of the control volume consists of heat transferred by thermal conduction:

$$-\int_A \boldsymbol{q}\cdot\boldsymbol{n}\,\mathrm{d}A, \tag{I.34}$$

work done by viscous forces:

$$-\int_A (\boldsymbol{\tau}\cdot\boldsymbol{v})\cdot\boldsymbol{n}\,\mathrm{d}A \tag{I.35}$$

and work done by pressure forces:

$$-\int_A p\boldsymbol{v}\cdot\boldsymbol{n}\,\mathrm{d}A. \tag{I.36}$$

In Expression (I.34) to Expression (I.36), $\boldsymbol{q}$ is the heat flux per unit area, $\boldsymbol{\tau}$ denotes the stress tensor (Schlichting, 1979, p. 52) and p is pressure.

The energy quantities internally generated and consumed are due to body forces:

$$\int_V \rho\boldsymbol{v}\cdot\boldsymbol{B}\,\mathrm{d}V, \tag{I.37}$$

where $\boldsymbol{B}$ denotes the body force vector per unit mass, and an internal heat source or heat sink (*i.e.* negative heat source):

$$\int_V I\,\mathrm{d}V. \tag{I.38}$$

Substituting the Reynolds Transport Theorem [Theorem (I.2)], where $\phi = u_i + \frac{1}{2}v^2$, into the LHS of Equation (I.32) and substituting Expression (I.34) to Expression (I.38) into the RHS of Equation (I.32), yields:

$$\int_V \frac{\partial}{\partial t}\rho\left(u_i + \frac{1}{2}v^2\right)\mathrm{d}V + \int_A \rho \boldsymbol{v}\left(u_i + \frac{1}{2}v^2\right)\cdot \boldsymbol{n}\,\mathrm{d}A =$$

$$-\int_A \boldsymbol{q}\cdot\boldsymbol{n}\,\mathrm{d}A + \int_V \rho \boldsymbol{v}\cdot\boldsymbol{B}\,\mathrm{d}V - \int_A p\boldsymbol{v}\cdot\boldsymbol{n}\,\mathrm{d}A - \int_A (\boldsymbol{\tau}\cdot\boldsymbol{v})\cdot\boldsymbol{n}\,\mathrm{d}A + \int_V I\,\mathrm{d}V\,. \quad \text{(I.39)}$$

Converting surface integrals in Equation (I.39) to volume integrals by applying the Divergence Theorem (Kreiszig, 1993, p. 545) yields:

$$\int_V \frac{\partial}{\partial t}\rho\left(u_i + \frac{1}{2}v^2\right)\mathrm{d}V + \int_V \nabla\cdot\rho\boldsymbol{v}\left(u_i + \frac{1}{2}v^2\right)\mathrm{d}V =$$

$$-\int_V \nabla\cdot\boldsymbol{q}\,\mathrm{d}V + \int_V \rho\boldsymbol{v}\cdot\boldsymbol{B}\,\mathrm{d}V - \int_V \nabla\cdot(p\boldsymbol{v})\mathrm{d}V - \int_V \nabla\cdot(\boldsymbol{\tau}\cdot\boldsymbol{v})\mathrm{d}V + \int_V I\,\mathrm{d}V\,. \quad \text{(I.40)}$$

Reducing the control volume V in Equation (I.40) to a differential size $\mathrm{d}V$ yields:

$$\frac{\partial}{\partial t}\rho\left(u_i + \frac{1}{2}v^2\right) + \nabla\cdot\rho\boldsymbol{v}\left(u_i + \frac{1}{2}v^2\right) = -\nabla\cdot\boldsymbol{q} + \rho\boldsymbol{v}\cdot\boldsymbol{B} - \nabla\cdot(p\boldsymbol{v}) - \nabla\cdot(\boldsymbol{\tau}\cdot\boldsymbol{v}) + I\,. \quad \text{(I.41)}$$

Expanding the two terms on the LHS of Equation (I.41) and rearranging terms yields:

$$\rho\left[\frac{\partial}{\partial t}\left(u_i + \frac{1}{2}v^2\right)v^2 + \boldsymbol{v}\cdot\nabla\left(u_i + \frac{1}{2}v^2\right)\right] + \left(u_i + \frac{1}{2}v^2\right)\left(\frac{\partial\rho}{\partial t} + \nabla\cdot(\rho\boldsymbol{v})\right) =$$

$$-\nabla\cdot\boldsymbol{q} + \rho\boldsymbol{v}\cdot\boldsymbol{B} - \nabla\cdot(p\boldsymbol{v}) - \nabla\cdot(\boldsymbol{\tau}\cdot\boldsymbol{v}) + I\,. \quad \text{(I.42)}$$

Rewriting the terms in the square brackets in Equation (I.42) in terms of a substantial derivative and substituting the continuity equation [Equation (I.9)] into the last term on the LHS of Equation (I.42) yields:

$$\rho\frac{\mathrm{D}}{\mathrm{D}t}\left(u_i+\frac{1}{2}v^2\right)=-\nabla\cdot\boldsymbol{q}+\rho\boldsymbol{v}\cdot\boldsymbol{B}-\nabla\cdot(p\boldsymbol{v})-\nabla\cdot(\boldsymbol{\tau}\cdot\boldsymbol{v})+I, \tag{I.43}$$

or, after expanding the term on the LHS of Equation (I.43):

$$\rho\frac{\mathrm{D}u_i}{\mathrm{D}t}+\rho\frac{\mathrm{D}}{\mathrm{D}t}\left(\frac{1}{2}v^2\right)=-\nabla\cdot\boldsymbol{q}+\rho\boldsymbol{v}\cdot\boldsymbol{B}-\nabla\cdot(p\boldsymbol{v})-\nabla\cdot(\boldsymbol{\tau}\cdot\boldsymbol{v})+I. \tag{I.44}$$

Equation (I.44) can be simplified by considering the vector product between the velocity vector $\boldsymbol{v}$ and the general momentum equation [Equation (I.31)]:

$$\rho\boldsymbol{v}\cdot\frac{\mathrm{D}\boldsymbol{v}}{\mathrm{D}t}=\rho\boldsymbol{v}\cdot\boldsymbol{B}-\boldsymbol{v}\cdot\nabla p-\boldsymbol{v}\cdot(\nabla\cdot\boldsymbol{\tau}). \tag{I.45}$$

Using the identities:

$$\boldsymbol{b}\cdot\mathrm{d}\boldsymbol{b}=\mathrm{d}\left(\tfrac{1}{2}\boldsymbol{b}\cdot\boldsymbol{b}\right)=\mathrm{d}\left(\tfrac{1}{2}b^2\right), \tag{I.46}$$

$$\nabla\cdot(a\boldsymbol{b})=(\nabla a)\cdot\boldsymbol{b}+a(\nabla\cdot\boldsymbol{b}) \tag{I.47}$$

and:

$$\boldsymbol{c}:(\nabla\boldsymbol{b})+\boldsymbol{b}\cdot(\nabla\cdot\boldsymbol{c})=\nabla\cdot(\boldsymbol{c}\cdot\boldsymbol{b}), \tag{I.48}$$

where a is a scalar quantity, $\boldsymbol{b}$ is a vector quantity and $\boldsymbol{c}$ is a tensor quantity, the term on the LHS of Equation (I.45) and the second and third terms on the RHS of Equation (I.45) can be rewritten as:

$$\rho\frac{\mathrm{D}}{\mathrm{D}t}\left(\frac{1}{2}v^2\right)=p(\nabla\cdot\boldsymbol{v})-\nabla\cdot(p\boldsymbol{v})+\rho\boldsymbol{v}\cdot\boldsymbol{B}-\nabla\cdot(\boldsymbol{\tau}\cdot\boldsymbol{v})+\boldsymbol{\tau}:\nabla\boldsymbol{v}. \tag{I.49}$$

Subtracting Equation (I.49) from Equation (I.44) yields:

$$\rho\frac{\mathrm{D}u_i}{\mathrm{D}t} = -\boldsymbol{\nabla}\cdot\boldsymbol{q} - p(\boldsymbol{\nabla}\cdot\boldsymbol{v}) - \boldsymbol{\tau}:\boldsymbol{\nabla}\boldsymbol{v} + I\,. \tag{I.50}$$

The substantial derivative of the internal energy on the LHS of Equation (I.50) can be written in terms of a substantial derivative of temperature. This is accomplished by deriving three general equations for a fluid consisting of a pure substance, which undergoes a differential change from one equilibrium state to another. The differential change takes place in a closed system without kinetic or potential energy.

Under these conditions, the first law of thermodynamics states:

$$\mathrm{d}u_i = \delta Q_R - p\,\mathrm{d}v, \tag{I.51}$$

where Q_R is the reversible energy exchange across the boundaries of the closed system and v is the specific volume. The second law of thermodynamics states that the differential entropy change associated with this reversible energy change is:

$$\mathrm{d}s = \frac{\delta Q_R}{T}\,. \tag{I.52}$$

Substituting Equation (I.52) into Equation (I.51) yields:

$$\mathrm{d}u_i = T\,\mathrm{d}s - p\,\mathrm{d}v. \tag{I.53}$$

The enthalpy of the fluid is defined as:

$$h \equiv u_i + pv \tag{I.54}$$

and the differential enthalpy change from one equilibrium state to another is:

$$\mathrm{d}h = \mathrm{d}u_i + p\,\mathrm{d}v + v\,\mathrm{d}p. \tag{I.55}$$

Substituting Equation (I.53) into Equation (I.55) yields:

$$\mathrm{d}h = T\,\mathrm{d}s + v\,\mathrm{d}p. \tag{I.56}$$

The Gibbs function G (Faires and Simmang, 1978, p. 131) for a fluid consisting of a pure substance in a closed system having no kinetic or potential energy states that:

$$G = h - Ts \tag{I.57}$$

and the differential change from one equilibrium state to another states is:

$$\mathrm{d}G = \mathrm{d}h - T\,\mathrm{d}s - s\,\mathrm{d}T. \tag{I.58}$$

Substituting Equation (I.56) into Equation (I.58) yields:

$$\mathrm{d}G = v\,\mathrm{d}p - s\,\mathrm{d}T. \tag{I.59}$$

Equation (I.53), together with Equation (I.56) and Equation (I.59), will now be used to rewrite the substantial derivative on the LHS of Equation (I.50).

The Maxwell relation I (Faires and Simmang, 1978, p. 278) for Equation (I.53) states that:

$$T = \left(\frac{\partial h}{\partial s}\right)_p, \tag{I.60}$$

or, when multiplied by $\left(\frac{\partial s}{\partial T}\right)_p$ and rearranging terms:

$$\left(\frac{\partial s}{\partial T}\right)_p = \frac{1}{T}\left(\frac{\partial h}{\partial T}\right)_p. \tag{I.61}$$

The Maxwell relation IV (Faires and Simmang, 1978, p. 278) for Equation (I.59) states

that:

$$\left(\frac{\partial s}{\partial p}\right)_T = -\left(\frac{\partial v}{\partial T}\right)_p . \tag{I.62}$$

Let the entropy s in Equation (I.53) be a function of the temperature T and the pressure p. A differential entropy change can then be written as:

$$\mathrm{d}s = \left(\frac{\partial s}{\partial T}\right)_p \mathrm{d}T + \left(\frac{\partial s}{\partial p}\right)_T \mathrm{d}p . \tag{I.63}$$

Substituting Equation (I.61) and Equation (I.62) into Equation (I.63) yields:

$$\mathrm{d}s = \frac{1}{T}\left(\frac{\partial h}{\partial T}\right)_p \mathrm{d}T - \left(\frac{\partial v}{\partial T}\right)_p \mathrm{d}p . \tag{I.64}$$

Substituting Equation (I.64) into Equation (I.53) yields:

$$\mathrm{d}u_i = \left(\frac{\partial h}{\partial T}\right)_p \mathrm{d}T - T\left(\frac{\partial v}{\partial T}\right)_p \mathrm{d}p - p\,\mathrm{d}v . \tag{I.65}$$

Substituting the definition for the isobaric specific heat capacity:

$$c_p \equiv \left(\frac{\partial h}{\partial T}\right)_p \tag{I.66}$$

into Equation (I.65) and noting that $\rho = \frac{1}{v}$ yields:

$$\mathrm{d}u_i = c_p \mathrm{d}T + \frac{T}{\rho^2}\left(\frac{\partial \rho}{\partial T}\right)_p \mathrm{d}p + \frac{p}{\rho^2}\mathrm{d}\rho . \tag{I.67}$$

The substantial derivative of the internal energy u_i is therefore:

$$\mathrm{D}u_i = c_p \mathrm{D}T + \frac{T}{\rho^2}\left(\frac{\partial \rho}{\partial T}\right)_p \mathrm{D}p + \frac{p}{\rho^2}\mathrm{D}\rho \,. \tag{I.68}$$

Multiplying Equation (I.68) by $\frac{\rho}{\mathrm{D}t}$ yields:

$$\rho \frac{\mathrm{D}u_i}{\mathrm{D}t} = \rho c_p \frac{\mathrm{D}T}{\mathrm{D}t} + \frac{T}{\rho}\left(\frac{\partial \rho}{\partial T}\right)_p \frac{\mathrm{D}p}{\mathrm{D}t} + \frac{p}{\rho}\frac{\mathrm{D}\rho}{\mathrm{D}t} \,. \tag{I.69}$$

Substituting the continuity equation [Equation (I.11)] into Equation (I.69) and then into Equation (I.50) yields, after rearranging terms, a general form of the conservation of energy equation:

$$\rho c_p \frac{\mathrm{D}T}{\mathrm{D}t} = -\nabla \cdot \boldsymbol{q} - \frac{1}{\rho}\left(\frac{\partial \rho}{\partial T}\right)_p T \frac{\mathrm{D}p}{\mathrm{D}t} - \boldsymbol{\tau} : \nabla \boldsymbol{v} + I \,. \tag{I.70}$$

APPENDIX II

VOLUME AVERAGING

II.1 Overview

The principles, definitions, rules and theorems of the volume-averaging method are described in this appendix. Volume averaging relates phenomena at microscopic level to those at macroscopic level by associating the phenomena in the vicinity of any point in a spatial domain, with that point. Volume averaging of phenomena in a spatial domain is accomplished by the integration of those phenomena over a representative finite averaging volume, one of which is associated with every point in the spatial domain. In general, a representative finite averaging volume is a sub-domain such that an average of phenomena in the sub-domain well represents a meaningful statistical average of the phenomena at that point. Details are presented regarding the representative finite averaging volume as well as principles, definitions, rules and theorems involved in the analytical process of volume averaging.

II.2 Representative elementary volume

Details regarding the selection and conditions of such a representative finite averaging volume, which is referred to in literature as a *representative elementary volume* (REV), are outlined in Bear and Bachmat (1986) and Whitaker (1967). The REV should be much smaller than the entire domain but much larger than a single pore. Figure II.1 schematically shows such a REV in a two-phase system, which consists of a solid phase s and a fluid phase f, with normal surface unit vectors $\boldsymbol{n}_{sf}$, $\boldsymbol{n}_{fs}$, $\boldsymbol{n}_{ss}$, and $\boldsymbol{n}_{ff}$. It is generally

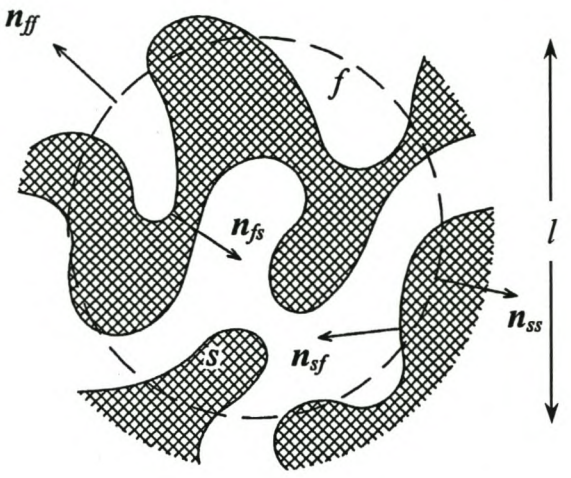

Figure II.1 Representative Elementary Volume (REV).

assumed that $d << l << L$, where d is the characteristic length of the void space, l is the characteristic length of the REV as shown in Figure II.1 and L is the characteristic length of the entire porous domain.

II.3 Volume averaging principles, definitions, rules and theorems

The solid phase s and fluid phase f volume fractions are defined by:

$$\varepsilon_\gamma \equiv \frac{V_\gamma}{V_o}, \tag{II.1}$$

where $\gamma = s$ or f and V_o is the overall volume of the solid and fluid phases in the REV. The fluid phase volume fraction ε_f is also referred to as the porosity of the porous

medium. For an intensive quantity ϕ, the overall volume average is defined by:

$$\langle \phi \rangle \equiv \frac{1}{V_o} \int_{V_o} \phi \, \mathrm{d}V \,, \tag{II.2}$$

the phasial volume average is defined by:

$$\langle \phi \rangle_\gamma \equiv \frac{1}{V_o} \int_{V_\gamma} \phi \, \mathrm{d}V \tag{II.3}$$

and the intrinsic volume average is defined by:

$$\langle \phi \rangle_\gamma^\gamma \equiv \frac{1}{V_\gamma} \int_{V_\gamma} \phi \, \mathrm{d}V \,. \tag{II.4}$$

At any position within a phase in the REV, the deviation of an intensive quantity from its intrinsic phasial volume average value is defined by:

$$\overset{\circ}{\phi} \equiv \phi - \langle \phi \rangle_\gamma^\gamma, \tag{II.5}$$

which is referred to as Gray's decomposition (Gray, 1975). The intrinsic phasial volume average $\langle \phi \rangle_\gamma^\gamma$ in Definition (II.4) is with reference to an REV that has its origin at the position at which the deviation is considered.

From Definition (II.1), Definition (II.2) and Definition (II.3) it follows that:

$$\langle \phi \rangle_\gamma = \varepsilon_\gamma \langle \phi \rangle_\gamma^\gamma. \tag{II.6}$$

If both phases are consolidated with reference to a certain direction m (see Section 4.2), then Slattery's averaging theorem (Slattery, 1967) states that:

$$\frac{\partial}{\partial m}\int_{V_\gamma} \phi \boldsymbol{m}\, \mathrm{d}V = \int_{A_{\gamma\gamma}} \phi \boldsymbol{n}_{m,\gamma\gamma}\, \mathrm{d}A\,, \tag{II.7}$$

where $\boldsymbol{m}$ is the unit vector in the m-direction and $\boldsymbol{n}_{m,\gamma\gamma}$ is the component in the m-direction of the unit normal surface vector $\boldsymbol{n}_{\gamma\gamma}$ to the differential surface $\mathrm{d}A$. If both phases are consolidated in all directions, Theorem (II.7) can be written as:

$$\nabla \int_{V_\gamma} \phi\, \mathrm{d}V = \int_{A_{\gamma\gamma}} \phi \boldsymbol{n}_{\gamma\gamma}\, \mathrm{d}A\,. \tag{II.8}$$

Applying the Divergence Theorem (Kreyszig, 1993, p. 545) to each of the two phases within the REV and substituting Theorem (II.8) yields:

$$\int_{V_\gamma} \nabla\phi\, \mathrm{d}V = \nabla \int_{V_\gamma} \phi\, \mathrm{d}V + \int_{A_{sf}} \phi \boldsymbol{n}_{\gamma\varphi}\, \mathrm{d}A\,, \tag{II.9}$$

where $\gamma = s$ and $\varphi = f$, or *vice versa.* Dividing Equation (II.9) by V_o and substituting Definition (II.3) yields:

$$\langle \nabla\phi \rangle_\gamma = \nabla \langle \phi \rangle_\gamma + \frac{1}{V_o}\int_{A_{sf}} \phi\, \boldsymbol{n}_{\gamma\varphi}\, \mathrm{d}A\,. \tag{II.10}$$

Whitaker's transport theorem (Whitaker, 1973) states that:

$$\left\langle \frac{\partial\phi}{\partial t} \right\rangle_\gamma = \frac{\partial \langle \phi \rangle_\gamma}{\partial t} - \frac{1}{V_o}\int_{A_{sf}} \phi\, \boldsymbol{v}_\gamma \cdot \boldsymbol{n}_{\gamma\varphi}\, \mathrm{d}A\,. \tag{II.11}$$

Under the condition of one phase consisting of a rigid, stationary, solid structure, it then follows that at A_{sf}:

$$\boldsymbol{v}_s \cdot \boldsymbol{n}_{sf} = -\boldsymbol{v}_f \cdot \boldsymbol{n}_{fs} = 0. \tag{II.12}$$

Substituting Condition (II.12) into Theorem (II.11) yields:

$$\left\langle \frac{\partial \phi}{\partial t} \right\rangle_\gamma = \frac{\partial \langle \phi \rangle_\gamma}{\partial t}. \tag{II.13}$$

A useful relation is obtained when Equation (II.9) is applied to the intensive quantity $\phi = 1$. Noting that $\nabla 1 = 0$, it follows after rearranging terms that:

$$\nabla \int_{V_\gamma} \mathrm{d}V = -\int_{A_{sf}} \boldsymbol{n}_{\gamma\varphi}\, \mathrm{d}A. \tag{II.14}$$

Dividing Equation (II.14) by a constant REV volume V_o, and substituting Definition (II. 1) yields:

$$\nabla \varepsilon_\gamma = -\frac{1}{V_o} \int_{A_{sf}} \boldsymbol{n}_{\gamma\varphi}\, \mathrm{d}A. \tag{II.15}$$

APPENDIX III

QUALIFICATION OF THE INTERPHASIAL HEAT TRANSFER MODEL AND THE CONDUCTION MODEL

III.1 Overview

This appendix is devoted to a quantitative evaluation and qualification of the interphasial heat transfer model for conductive heat transfer and the conduction model developed in Chapter 5 and Chapter 6 respectively.

The conduction model concerns conductive heat transfer only and convection is not considered in the evaluation of the interphasial heat transfer model. Therefore, since conduction is the only means of heat transfer and the physical processes of conduction are the same in both the solid and the fluid phases, these phases will not be identified as solid and fluid, but instead as the *α-phase* and the *β-phase*.

The evaluation proceeded as follows: (1) A two-phase geometry is selected in which thermal conduction in a particular phase is affected by that of the other phase (*i.e.* in a direction of interest, conduction in one phase will take a "shortcut" route through the other phase). (2) Steady-state microscopic temperature distributions under the same thermal non-equilibrium conditions are then obtained by the computational solution of the steady-state energy equation. (3) Microscopic temperature distributions are transformed into macroscopic temperature distributions by averaging them over defined regions in each of the two phases. (4) Parameters of the conduction model and the interphasial heat transfer model are determined for the selected two-phase geometry. (5) Steady-state macroscopic temperature distributions for each phase are obtained by numerically solving the transformed volume-averaged energy equation for the solid phase (Equation 8.3), which also apply to the fluid phase in the absence of convection. Solutions are obtained under thermal non-equilibrium conditions discussed in Section III.2. (6) Macroscopic

temperature distributions obtained in steps (2) and (3) are compared to those obtained in steps (4) and (5).

III.2 Thermal non-equilibrium conditions in phases and thermal non-equilibrium states in porous media

A thermal non-equilibrium state in a two-phase system can occur under different conditions. Heat locally transferred between two phases in thermal non-equilibrium can *e.g.* be locally generated in one phase while it is conducted away in the other phase, or heat can be conducted in one phase from a high temperature source some distance away and locally dissipated in the other phase, which is at a uniformly constant temperature. The identification of all possible conditions for the evaluation of the conduction model requires a closer look at heat flow within two phases that are not in thermal equilibrium.

At a certain location, where the phases are not in thermal equilibrium, heat is transferred from one phase to the other. If a steady-state condition prevails in the phase from which heat is transferred, heat either originates at that location from a source within that phase, is transferred through that phase from a heat source nearby, or is the result of a combination of both. If heat is transferred through the phase from a heat source nearby, then that heat source is referred to as the *transfer origin*. On the other hand, if a steady-state condition prevails in the phase to which the heat is transferred, the heat is either dissipated at that location by a heat sink (negative heat source) within that phase, transferred through that phase to a heat sink nearby, or a combination of both. If heat is transferred through the phase to a heat sink nearby, that heat sink is referred to as the *transfer destination*. In order for a phase to transfer heat from a transfer origin or to a transfer destination, the phase has to be consolidated (see Section 4.2) between that position and the transfer origin or destination. This transfer of heat could either be by conduction within a stationary phase or a combination of conduction and convection within a moving fluid phase.

At the location in a two-phase system where the phases are not in thermal equilibrium, the *thermal non-equilibrium condition* in a particular phase identifies whether all the heat transferred across the interface between the two phases, is transferred from a transfer origin or to a transfer destination, or whether some or all of that heat is locally generated or dissipated at that location. If all the heat transferred across the interface between two phases is transferred either from a transfer origin or to a transfer destination within a single phase, then a *transfer thermal non-equilibrium condition* is said to exist within that phase. The distance between the location where the phases are not in thermal equilibrium and the transfer origin or transfer destination is referred to as the *transfer distance*. On the other hand, if some or all of the heat transferred across the interface between two phases is generated or dissipated at the location in a phase where the phases are not in thermal equilibrium, then a *source thermal non-equilibrium condition* is said to exist within that phase.

A source thermal non-equilibrium condition can be classified into two categories according to the nature of the heat source or heat sink within a phase. In the first category, the heat generated or dissipated per unit volume is fixed and the microscopic temperature varies within the phase. This is referred to as a *variable temperature (VT) source* and the phase is said to be in a *VT source thermal non-equilibrium condition*. In the second category, the microscopic temperature is fixed and the heat generated or dissipated per unit volume varies within the phase. This is referred to as a *fixed temperature (FT) source* and the phase is said to be in an *FT source thermal non-equilibrium condition.*

Since the consolidation of a phase in a two-phase system is directional (*i.e.*, a phase is consolidated or non-consolidated with reference to a particular direction), a thermal non-equilibrium condition in a phase is also directional.

Refer back to Figure 4.1 and suppose that the four boundaries normal to the x- and the z-axis were thermally insulated and different temperatures were specified in the two phases at the two boundaries normal to the y-axis (the direction in which the solid phase is consolidated). A transfer thermal non-equilibrium condition can now prevail in both phases (at least near the top and bottom boundaries) if different boundary temperatures in

the two phases are established at the top and bottom. However, if the two boundaries normal to the y-axis were thermally insulated, then the solid phase could not be in a transfer thermal non-equilibrium condition. Only a source thermal non-equilibrium condition could then exist in the solid phase.

Consider now a phase that is non-consolidated in all directions, *e.g.* the solid elements in a fluidised bed. A transfer thermal non-equilibrium condition is not possible in such a phase and only a source thermal non-equilibrium condition can exist.

Whereas the thermal non-equilibrium condition describes the nature of heat transfer within a phase, the *thermal non-equilibrium state* refers to the thermal non-equilibrium conditions within each of the two phases. The thermal non-equilibrium state in two consolidated phases can be classified under six different combinations of the thermal non-equilibrium conditions in the phases, namely: (1) *transfer - transfer*, (2) *FT source - transfer*, (3) *VT source - transfer*, (4) *FT source - VT source*, (5) *VT source - VT source* and (6) *FT source - FT source*. The conduction model and the interphasial heat transfer model are evaluated under the first five thermal non-equilibrium states. Although the conduction model applies to an FT source - FT source thermal non-equilibrium state, a solution is not required since the temperature is specified in both phases.

Where a two-phase system is in a transfer - transfer or an FT source - transfer thermal non-equilibrium state with reference to two consolidated phases, the non-equilibrium state will exist from the transfer origin or transfer destination, up to some distance away from that transfer origin or transfer destination where thermal equilibrium between the phases is established. This distance is referred to as the *thermal non-equilibrium penetration depth*. The phasial volume-averaged temperatures will approach each other asymptotically between the transfer origin or transfer destination and the position where thermal equilibrium (or some defined level of equilibrium) between the phases is established.

III.3 Case Studies

Five case studies were used in the evaluation, one for each of the first five different thermal non-equilibrium states discussed. The case studies were designated Case Study 1 to Case Study 5 in the order in which the thermal non-equilibrium states are listed in Section III.2. A two-phase geometry that was used for all five case studies was arbitrarily selected. Transfer properties, boundary conditions and internal heat sources were selected to establish the five different thermal non-equilibrium states.

III.4 Two-phase system geometry and temperature distribution

The two-dimensional, two-phase geometry is shown in Figure III.1. Each phase is made up of an array of geometrically similar units of similar size and of ordered spatial distribution. The system consists of fifty single unit rows and three single unit columns. A single geometric unit and a set of lattice vectors can mathematically represent the two-phase system. This single geometric unit has generally been referred to in literature as a *unit cell* (UC). The UC is considered the most elementary geometric configuration that defines the complete geometry.

Both phases are consolidated with reference to the y-direction in Figure III.1. The two phases are composed both in series and in parallel with reference to the y-direction. The dashed lines represent the boundaries between the UC's. The two phases are geometrically periodic in every alternate horizontal row and vertical column of UC's.

There is a thin layer of material with a variable thermal conductivity between the two phases. Changing the thermal conductivity of this layer (*i.e.* the thermal contact resistance between the two phases) controls heat transfer between the phases. In a transfer-transfer or an FT source-transfer thermal non-equilibrium state, increasing the thermal contact resistance between the two phases increases the non-equilibrium thermal

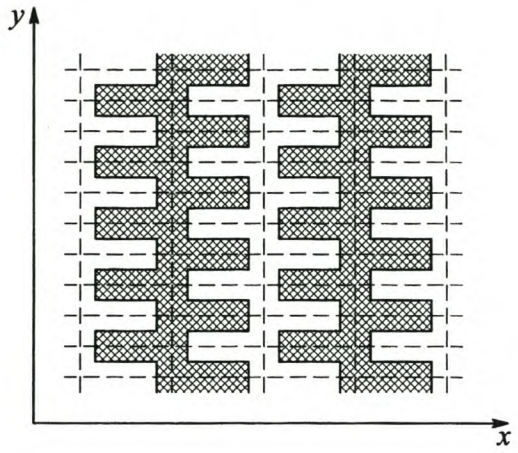

Figure III.1 Two-phase system geometry.

penetration depth. However, a high thermal contact resistance reduces the overall effect that conduction in one phase will have on conduction in the other phase.

Since the intent of this exercise was to illustrate the ability of the conduction model to treat the thermal effect of one phase upon another with the thermal non-equilibrium penetration depth extending over a number of UC's, a ratio of the characteristic UC dimension in the direction of net heat transfer to that in the transverse direction was selected as twelve to one. Figure III.2 shows the UC dimensions in millimetres.

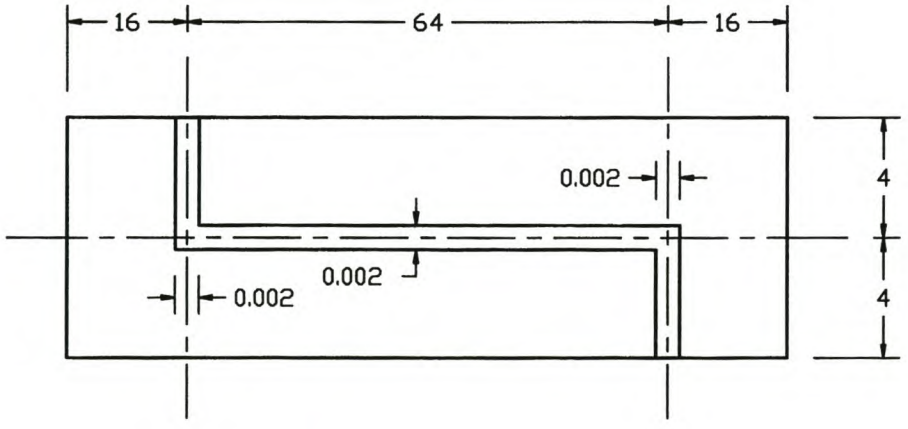

Figure III.2 Unit cell dimensions (in millimetres).

III.5 Transfer properties

The thermal conductivities of the α-phase and the β-phase are 40.0 W/m·°C and 200.0 W/m·°C respectively. The thermal conductivity of the thermal resistance material depends on the thermal resistance required between the phases. The thermal conductivity is related to the thermal resistance by:

$$k_r = \frac{0.000002}{R_{sf}}, \tag{III.1}$$

where the unit of k_r is W/m·°C and that of R_{sf} is m^2·°C/W.

III.6 Case study specifications

For each case study, Table III.1 gives the thermal non-equilibrium condition within each of the two phases as well as the phasial volume-averaged temperature boundary conditions. Where applicable, thermal resistance between the phases, heat sources and heat sinks in each phase, mean fixed microscopic temperature and microscopic temperature gradient in each phase are also given in the table.

III.7 Unit cell configurations

The five case studies employ four different UC configurations. Table III.2 gives the four configurations, the thermal contact resistances between the phases, whether or not an FT source is present in one phase and the case studies in which the UC configurations were used.

Case study	1	2	3	4	5
Thermal non-equilibrium condition, α-phase	transfer	transfer	transfer	VT source	VT source
Thermal non-equilibrium condition, β-phase	transfer	FT source	VT source	FT source	VT source
Northern boundary intrinsic α-phase volume-averaged temperature [°C]	112.9494	74.5743	10.0588	20.2117	9.0157
Southern boundary intrinsic α-phase volume-averaged temperature [°C]	56.9323	38.2702	10.0588	20.2117	9.0157
Northern boundary intrinsic β-phase volume-averaged temperature [°C]	41.1132	20.0	8.5797	20.0	5.9960
Southern boundary intrinsic β-phase volume-averaged temperature [°C]	20.9454	20.0	8.5797	20.0	5.9960
Thermal contact resistance [m^2·°C /W]	0.1333	0.2667	n/a	n/a	n/a
Heat source, α-phase [W/ m^3]	0.0	0.0	40000.0	20000.0	80000.0
Heat source, β-phase [W/ m^3]	0.0	0.0	0.0	0.0	-20000.0
Fixed microscopic temperature [°C]	n/a	20.0	n/a	20.0	n/a
Fixed microscopic temperature gradient [°C/m]	n/a	0.0	n/a	0.0	n/a

Table III.1 Case study specifications.

III.8 Numerical solution of the microscopic temperature distribution

A microscopic temperature distribution in the two-phase system was obtained from the numerical solution of the energy equation for a rigid, solid substance [Equation (2.36)]. When conduction under steady-state conditions is the predominant means of heat transfer, Equation (2.36) reduces to:

$$\nabla \cdot (k \nabla T) + I = 0. \tag{III.2}$$

Equation (III.2) was numerically solved for the 3 × 50 UC matrix. The top and bottom sections of this matrix are shown in Figure III.3.

UC Configuration	Thermal resistance between the phases [°Cm²/W]	FT source present in one phase	Case studies to which the UC applies.
1	0.1333	no	1
2	0.2667	yes	2
3	n/a	no	3, 5
4	n/a	yes	4

Table III.2 Unit cell configurations.

Grid layout

Figure III.4 shows a single UC made up of sections, each with a particular grid arrangement. The finite volumes of the grid arrangements are dimensionally equal in each section. Table III.3 gives the number of rows and columns in each section, as well as the finite volume dimensions.

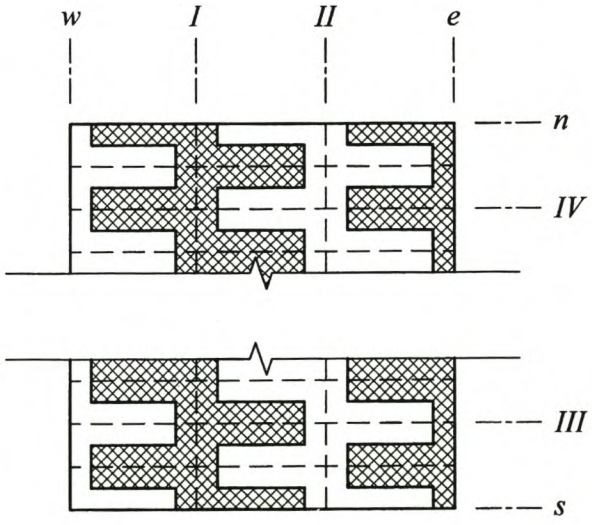

Figure III.3 Top and bottom section of a 3 × 50 unit cell matrix.

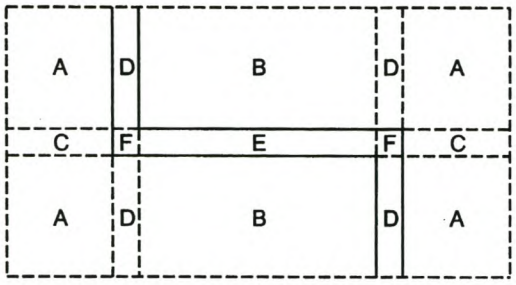

Figure III.4 Unit cell sections.

Grid points are located at the centre of the finite volumes. For the purpose of assigning specified boundary temperatures on all four sides of the UC matrix, an additional column and an additional row of finite volumes were added at the eastern and western sides, and at the northern and southern sides respectively of the matrix. This arrangement yields a 158 × 302 grid with a total of 47716 grid points in the 3 × 50 UC matrix. Equation (III.2) was discretised at the grid points using Patankar's (1980) finite volume method for conductive heat transfer.

section	# rows	# columns	Δx [mm]	Δy [mm]
A	8	2	1.999875	1.9995
B	32	2	1.999375	1.9995
C	8	2	1.999875	0.0010
D	2	2	0.001000	1.9950
E	32	2	1.999375	0.0010
F	2	2	0.001000	0.0010

Table III.3 Grid dimensions.

Boundary conditions

Boundary temperatures of the UC matrix were specified in such a way that the two-dimensional microscopic temperature distribution obtained yields a net heat transfer, which corresponds only to the y-direction in Figure III.1. The net heat flux in the x-direction is zero. The microscopic temperature has a periodic distribution in every alternate vertical column of UC's. These boundary conditions were established by making use of the geometric similarity between alternating vertical columns and between alternating horizontal rows of UC's, as shown in Figure III.3, where interfaces *I* and *II*, and *III* and *IV* are geometrically similar to the eastern and western, and southern and northern sides respectively in the UC matrix. Within every row of UC's, at every grid at the eastern side:

$$T_e = T_I \tag{III.3}$$

and at every grid at the western side:

$$T_w = T_{II} . \tag{III.4}$$

In every column of UC's, the temperature distributions at the northern and southern sides of the UC matrix are related to the temperature distributions at interfaces *III* and *IV* respectively, according to certain mathematical relations. These relations depend on the thermal non-equilibrium state in the two-phase system and are given in Table III.4. The description of the thermal non-equilibrium state in Table III.4 gives the thermal non-equilibrium condition of the α-phase followed by that of the β-phase. $T_{n,l}$, $T_{n,r}$, $T_{s,l}$ and $T_{s,r}$ refer to the temperatures at the left hand and right hand corners of the northern and southern sides respectively of each column of UC's, as shown in Figure III.3. $T_{n,FT}$ and $T_{s,FT}$ refer to the temperatures at the northern and southern corners respectively of each column of UC's, in the phases in which an FT source thermal non-equilibrium condition exists. Values for $T_{n,l}$, $T_{n,r}$, $T_{s,l}$ and $T_{s,r}$ were arbitrarily selected.

Thermal non-equilibrium state	Mathematical relation
transfer - transfer	$\frac{T_n - T_{n,l}}{T_{n,r} - T_{n,l}} = \frac{T_{III} - T_{III,l}}{T_{III,r} - T_{III,l}}$ $\frac{T_s - T_{s,l}}{T_{s,r} - T_{s,l}} = \frac{T_{IV} - T_{IV,l}}{T_{IV,r} - T_{IV,l}}$
FT source - transfer	$\frac{T_n - T_{n,FT}}{T_{n,tr} - T_{n,FT}} = \frac{T_{III} - T_{III,FT}}{T_{III,tr} - T_{III,FT}}$ $\frac{T_s - T_{s,FT}}{T_{s,tr} - T_{s,FT}} = \frac{T_{IV} - T_{IV,FT}}{T_{IV,tr} - T_{IV,FT}}$
VT source - transfer	$T_n - T_{n,l} = T_{III} - T_{III,l}$ $T_s - T_{s,l} = T_{IV} - T_{IV,l}$
FT source - VT source	$T_n - T_{n,FT} = T_{III} - T_{III,FT}$ $T_s - T_{s,FT} = T_{IV} - T_{IV,FT}$
VT source - VT source	$T_n - T_{n,l} = T_{III} - T_{III,l}$ $T_s - T_{s,l} = T_{IV} - T_{IV,l}$

Table III.4 Boundary condition mathematical relations.

Solution of linear equations

With boundary temperatures established around the UC matrix, a direct solution algorithm, presented by King (1976), was used to solve the set of simultaneous linear algebraic equations, yielding temperatures at each grid point.

Volume averaging

In the capacity of the UC as a single cell representation of an REV (representative elementary volume, discussed in Section II.2), each UC acts as a defined geometry for

averaging the computed microscopic temperature distribution. Intrinsic volume-averaged temperature values obtained in this way were assigned to a location corresponding to the centre of the UC. In this manner, the microscopic temperature distribution is transformed into a one-dimensional macroscopic temperature distribution.

Great care should however be taken in this averaging process. Consider any row from the UC matrix that is partly shown in Figure III.3. Within the western UC of that particular row of three, the location of the α-phase is either at the bottom or at the top of the UC and vice versa within the centre UC. The averaging process in the western UC yields α-phase and β-phase intrinsic volume-averaged temperatures that are different than those in the centre UC. In order to obtain a one-dimensional distribution of the intrinsic volume-averaged temperature, the averaging process was carried out in both UC's simultaneously, yielding a single value α-phase and β-phase intrinsic volume-averaged temperature for that row. This is the same as defining an alternative UC consisting of two of the original UC's, one with the α-phase located at the bottom and the β-phase at the top, and another with the reverse.

III.9 Transport parameters

Equilibrium and non-equilibrium temperature distributions in a UC

The interphasial heat transfer coefficient $h_{\alpha\beta}$ is defined in Section 5.2 as the ratio of the net heat transfer per interface area between two phases in an REV, to the difference between the intrinsic volume-averaged temperatures of each phase. This definition applies to a non-directional, non-equilibrium temperature distribution T_{nn} in the REV. This ratio is fixed for a two-phase system of fixed geometry and thermal conductivities. Equation (5.2), together with Definition (II.3) suggests that once a T_{nn} temperature distribution is established within an REV, the value for the interphasial heat transfer coefficient $h_{\alpha\beta}$ can be determined from an analysis of the microscopic temperature gradient at the interface and the microscopic temperature within the phases.

Also, according to Definition (6.8) and Definition (6.9), in a direction m, in which both phases are consolidated, the coefficients of the components of the equilibrium thermal conductivities, $k_{e,\alpha,m}$ and $k_{e,\beta,m}$, and the non-equilibrium thermal conductivities, $k_{nd,\alpha,m}$ and $k_{nd,\beta,m}$, are defined as follows: The thermal conductivity of the phase multiplied by the ratio of the phasial volume-averaged temperature gradient $\left\langle \frac{\partial T}{\partial m} \right\rangle_\gamma$ in the REV, to the gradient in the phasial volume-averaged temperature $\frac{\partial \langle T \rangle_\gamma}{\partial m}$ in the REV, where $\gamma = \alpha$ or β. These ratios are fixed for a two-phase system of fixed geometry and thermal conductivities. These definitions respectively apply with an equilibrium temperature distribution T_e and a directional, non-equilibrium temperature distribution T_{nd} within the REV. Definition (6.8) and Definition (6.9), together with Definition (II.3) suggest that with a T_e and T_{nd} temperature distribution established respectively within an REV, the equilibrium thermal conductivities and the non-equilibrium thermal conductivities can be determined from an analysis of the microscopic temperature distributions in the phases within that REV.

With a T_{nn} temperature distribution within the REV, the phases are in a thermal non-equilibrium state with a zero gradient in the volume-averaged temperature of each phase. Conversely, with T_e and T_{nd} temperature distributions within the REV, the phases are in a thermal equilibrium state, with a non-zero gradient in the volume-averaged temperature of each phase.

In its capacity as a single cell representation of an REV, a UC was used in which T_{nn}, T_e and T_{nd} temperature distributions were established to determine the interphasial heat transfer coefficient $h_{\alpha\beta}$, the equilibrium thermal conductivity $k_{e,\gamma,m}$ and the non-equilibrium thermal conductivity $k_{nd,\gamma,m}$ respectively. A UC employed for this purpose is referred to as a *principal UC*.

The T_{nn} temperature distribution must resemble the transfer, FT source and VT source thermal non-equilibrium conditions of the two-phase system that it represents. On the other hand, the T_e and T_{nd} temperature distributions must resemble only the transfer and

the FT source thermal non-equilibrium conditions of the two-phase system that it represents. A transfer thermal non-equilibrium condition was established within a phase by specifying appropriate thermal boundary conditions for that phase. An FT source thermal non-equilibrium condition was established by specifying the microscopic temperature and a VT source thermal non-equilibrium condition was established by specifying a heat source or heat sink within that phase. Arbitrary values were selected for these parameters. In a VT source - VT source thermal non-equilibrium state, for T_{nn}, T_e and T_{nd} temperature distributions, the ratio of the heat source values in the two phases must be the same as that of the two-phase system that it represents.

In some cases, depending on the geometry of the two-phase system and the thermal contact resistance between the two phases, at a certain ratio of the thermal conductivities of the two phases, the term in the denominator of Definition (6.96) approaches zero when the boundary conditions were specified in a way that Condition (4.9) and Condition (4.13) are satisfied. The non-equilibrium thermal conductivity will show a discontinuity in a plot against the thermal conductivity ratio. Whenever the thermal conductivity ratio of the phases of a two-phase system happens to be near the discontinuity, then Definition (6.9) will yield excessively high positive or negative values for the non-equilibrium thermal conductivity. However, inspection of Definition (6.18) and Definition (6.19) revealed that wherever a thermal non-equilibrium thermal conductivity was used in the calculation of the effective thermal conductivity tensor and the coupled thermal conductivity tensor, it is multiplied by a term of the order $O(1/k_{nd,\gamma})$, cancelling out with the excessively high positive or negative thermal non-equilibrium thermal conductivity.

For certain simple geometries it is possible to find exact or approximate analytical expressions for the interphasial heat transfer coefficient and the equilibrium and non-equilibrium thermal conductivities. For more complex two-phase geometries, one must rely on experimental or computational means to find a microscopic temperature distribution or a microscopic temperature gradient distribution within a principal UC.

Boundary conditions, heat sources and heat sinks

In these case studies, T_{nn}, T_e and T_{nd} temperature distributions were established in a principal UC by specifying appropriate boundary conditions, heat sources and heat sinks for the numerical solution of Equation (III.2). The boundary conditions, heat sources and heat sinks were specified in such a way that the thermal non-equilibrium state in the principal UC resembles that of the two-phase system while satisfying the conditions of the respective temperature distributions.

Instead of establishing these temperature distributions by solving Equation (III.2) in a single principal UC, the principal UC was surrounded by eight other UC's to form a 3 × 3 UC matrix as shown in Figure III.5.

The geometry of a 3 × 3 UC matrix, as in the case of the 3 × 50 UC matrix, shows alternating vertical columns of UC's to be geometrically similar. This feature was used to establish boundary conditions at the eastern and western sides of the matrix. In Figure III.5, interfaces *I* and *II* are geometrically similar to the eastern and the western sides respectively of the UC matrix. The T_{nn} and the T_e temperature distributions respectively have the same distribution in each vertical column of UC's. Therefore Equation (III.3) and Equation (III.4) apply to every horizontal row of grid points in the 3 × 3 UC matrix.

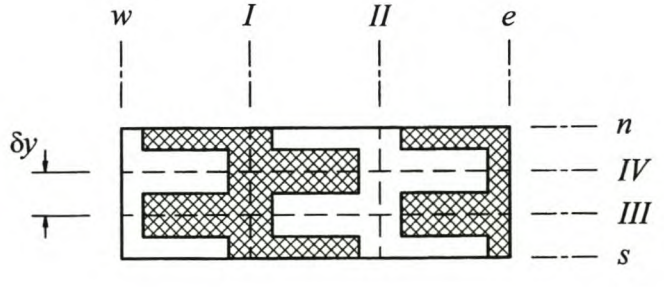

Figure III.5 3 × 3 Unit cell matrix.

The geometry of the 3 × 3 UC matrix also indicates alternating horizontal rows of UC's to be geometrically similar. Figure III.5 shows interfaces *III* and *IV* to be geometrically similar to northern and southern sides respectively of the UC matrix. In every vertical column of UC's in the 3 × 3 matrix, the grid point temperatures at the northern and southern sides of the matrix are mathematically related to corresponding grid point temperatures at the interfaces *III* and *IV*. For creating the T_{nn} temperature distribution, these temperatures are related by the same mathematical relations used in the numerical solution of Equation (III.2) in the complete two-phase system (3 × 50 matrix), as given in Table III.4. In the case of the T_e temperature distribution, in every vertical column of UC's in the 3 × 3 matrix, the temperatures at the northern boundary are related by:

$$T_{e,n} - T_{e,n,l} = T_{e,III} - T_{e,III,l} \tag{III.5}$$

and the temperatures at the southern side are related by:

$$T_{e,s} - T_{e,s,l} = T_{e,IV} - T_{e,IV,l} \ , \tag{III.6}$$

where the subscripts *n* and *s* refer to the *northern* and *southern* sides respectively of the UC matrix and subscript *l* refers to the left hand side of every vertical column of UCs.

Finite volumes were selected in each UC according to the arrangement shown in Figure III.4, with Table III.3 giving the number of rows and columns of finite volumes as well as the finite volume dimensions in each section. Grid points are located at the centre of each finite volume. For the purpose of assigning specified boundary temperatures on all four sides of the UC matrix, an additional column and an additional row of finite volumes were added at the eastern and western sides respectively, and at the northern and southern sides of the matrix. This arrangement yields a 158 × 20 grid in the 3 × 3 UC matrix, with a total of 3160 grid points. Equation (III.2) was discretised at the grid points according to Patankar's (1980) finite volume method for conduction heat transfer.

The nature of the T_{nd} temperature distribution, which is graphically illustrated by Figure 4.5, is such that when a 3 × 3 UC matrix is used to obtain a temperature distribution in a

principal UC, heat is exchanged between the phases in the northern row of UC's as well as between the phases in the southern row of UC's. Unless a sufficiently high thermal contact resistance exists at the interface between the phases, the resulting temperature distributions in the northern and southern row of UC's will fail to establish an adequately large gradient in the volume-averaged temperature in the principal UC. Therefore, instead of using a 3 × 3 UC matrix, the principal UC is contained in a 3 × 1 UC matrix shown in Figure III.6.

A set of boundary temperatures for the northern and southern sides of the 3 × 1 UC matrix was determined from an additional two 3 × 3 matrices. Both matrices correspond to that shown in Figure III.5, with a finite volume layout corresponding to Figure III.4 and Table III.3. The set of boundary temperatures of the 3 × 1 matrix was determined by solving Equation (III.2) in each of the 3 × 3 matrices, under the same conditions as those of the T_{nn} temperature distribution. For the northern side boundary, temperatures were determined from:

$$T_{nd,n} = \frac{T_{ind,III} + T_{ind,n}}{2} \tag{III.7}$$

and for the southern side they were determined from:

$$T_{nd,s} = \frac{T_{ind,IV} + T_{ind,s}}{2}, \tag{III.8}$$

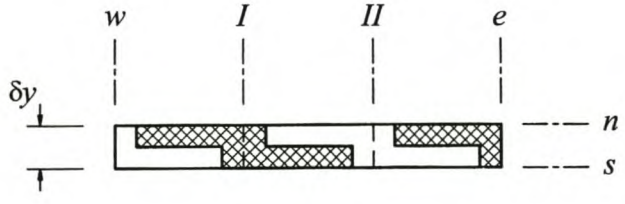

Figure III.6 3 × 1 Unit cell matrix.

where subscript *ind* refers to the two independent 3 × 3 matrices with interfaces *III*, *V*, *n* and *s* corresponding to those shown in Figure III.5.

With this arrangement, Equation (III.3) and Equation (III.4) also apply to every horizontal row of grid points in the 3 × 1 UC matrix, yielding a set of boundary temperatures for the eastern and western sides of that matrix.

The finite volume layout of the 3 × 1 matrix corresponds to Figure III.4 and Table III.3. This arrangement yields a 158 × 8 grid with a total of 1264 grid points. Equation (III.2) is discretised at the grid points according to Patankar's (1980) finite volume method for conduction heat transfer.

The direct solution algorithm presented by King (1976) was used to solve the temperature at each grid point in all the matrices.

Equilibrium and non-equilibrium temperature conditions

When establishing the T_{nn} temperature distribution in the 3 × 3 matrix, Condition (4.11) is satisfied in the principal UC when:

$$\left[\langle T_{nn}\rangle_{\gamma}\right]_{n} = \left[\langle T_{nn}\rangle_{\gamma}\right]_{s}, \tag{III.9}$$

where $\gamma = \alpha$ or β and subscript n and s refer to the UC's on the northern and southern sides respectively of the principal UC in the 3 × 3 matrix. The computed T_{nn} values at the grid points in the matrix satisfy Condition (4.11) when:

$$\left[\frac{\sum_{V_{\gamma}} T_{nn}\,\Delta x\Delta y}{\sum_{V_{\gamma}} \Delta x\Delta y}\right]_{n} = \left[\frac{\sum_{V_{\gamma}} T_{nn}\,\Delta x\Delta y}{\sum_{V_{\gamma}} \Delta x\Delta y}\right]_{s}. \tag{III.10}$$

Condition (4.3) is satisfied when:

$$\sum_{A_{\alpha\beta}} \frac{k_r \Delta y}{\delta x}\left(T_{e,1} - T_{e,2}\right) + \sum_{A_{\alpha\beta}} \frac{k_r \Delta x}{\delta y}\left(T_{e,1} - T_{e,2}\right) = 0 \qquad \text{(III.11)}$$

in all the UC's in the 3 × 3 matrix. Grid points 1 and 2 are located adjacent to each other on either side of the interface between the two phases. Both grid points are contained within the thermal resistance control layer with a thermal conductivity k_r. Condition (4.4) is satisfied when:

$$\frac{\sum_{V_\alpha} T_e \Delta x \Delta y}{\sum_{V_\alpha} \Delta x \Delta y} = \frac{\sum_{V_\beta} T_e \Delta x \Delta y}{\sum_{V_\beta} \Delta x \Delta y} \qquad \text{(III.12)}$$

in all the UC's in the 3 × 3 matrix.

In the 3 × 1 matrix, Condition (4.13) is satisfied when:

$$\sum_{V_\alpha}\left(\frac{k_n}{2}\frac{T_{nd,N} - T_{nd,P}}{\delta y_n} + \frac{k_s}{2}\frac{T_{nd,P} - T_{nd,S}}{\delta y_s}\right)\Delta x \Delta y = -\sum_{V_\beta}\left(\frac{k_n}{2}\frac{T_{nd,N} - T_{nd,P}}{\delta y_n} + \frac{k_s}{2}\frac{T_{nd,P} - T_{nd,S}}{\delta y_s}\right)\Delta x \Delta y \qquad \text{(III.13)}$$

in the principal UC. N and S refer to the nearest grid points on the northern and southern sides respectively of the grid point P as shown in Figure 11.2. The thermal conductivities k_n and k_s at the finite volume boundaries are given by:

$$k_n = \frac{\delta y_n}{\frac{\delta y_{nP}}{k_P} + \frac{\delta y_{nN}}{k_N}} \qquad \text{(III.14)}$$

and:

$$k_s = \frac{\delta y_s}{\frac{\delta y_{sP}}{k_P} + \frac{\delta y_{sS}}{k_S}}, \tag{III.15}$$

where the dimensions are shown in Figure 11.2.

In the principal UC, Condition (4.8) is satisfied when:

$$\sum_{A_{\alpha\beta}} \frac{k_r \Delta y}{\delta x}\left(T_{nd,1} - T_{nd,2}\right) + \sum_{A_{\alpha\beta}} \frac{k_r \Delta x}{\delta y}\left(T_{nd,1} - T_{nd,2}\right) = 0 \tag{III.16}$$

and Condition (4.9) is satisfied when:

$$\frac{\sum_{V_\alpha} T_{nd}\,\Delta x \Delta y}{\sum_{V_\alpha} \Delta x \Delta y} = \frac{\sum_{V_\beta} T_{nd}\,\Delta x \Delta y}{\sum_{V_\beta} \Delta x \Delta y}. \tag{III.17}$$

Interphasial heat transfer coefficient

The interphasial heat transfer coefficient $h_{\alpha\beta}$ was calculated from:

$$h_{\alpha\beta} = \frac{\sum_{A_{\alpha\beta}} \frac{k_r \Delta y}{\delta x}\left(T_{nn,1} - T_{nn,2}\right) + \sum_{A_{\alpha\beta}} \frac{k_r \Delta x}{\delta y}\left(T_{nn,1} - T_{nn,2}\right)}{\left(\sum_{A_{\alpha\beta}} \Delta y + \sum_{A_{\alpha\beta}} \Delta x\right)\left(\frac{\sum_{V_\beta} T_{nn}\Delta x \Delta y}{\sum_{V_\beta} \Delta x \Delta y} - \frac{\sum_{V_\alpha} T_{nn}\,\Delta x \Delta y}{\sum_{V_\alpha} \Delta x \Delta y}\right)}, \tag{III.18}$$

where V_α, V_β and $A_{\alpha\beta}$ apply only to the principal UC in the 3 × 3 matrix. Grid points 1 and 2 are located adjacent to each other on either side of the interface between the two phases. Both grid points are contained within the thermal resistance control layer with thermal conductivity k_r. The interphasial heat transfer coefficients for the four different UC configurations detailed in Table III.2, are given in Table III.5.

Effective and coupled thermal conductivities

The effective and coupled thermal conductivities were determined from the equilibrium and non-equilibrium thermal conductivities according to Definition (6.18) and Definition (6.19). The equilibrium and non-equilibrium thermal conductivities were calculated from:

$$k_{\gamma,e,y} = k_{\gamma,nd,y} = \frac{\sum_{V_\gamma}\left(\frac{k_n}{2}\frac{T_N - T_P}{\delta y_n} + \frac{k_s}{2}\frac{T_P - T_S}{\delta y_s}\right)\Delta x \Delta y}{\left(\sum_{V_\alpha}\Delta x\Delta y + \sum_{V_\beta}\Delta x\Delta y\right)\frac{\Delta\langle T\rangle_{\gamma,y}}{\delta y}}, \qquad \text{(III.19)}$$

where $T = T_e, T_{nd}$. V_γ, V_α and V_β applies only to the principal UC. N and S refer to the nearest grid points on the northern and southern sides respectively of the grid point P as shown in Figure 11.2. The thermal conductivities, k_n and k_s, at the boundaries of the finite volumes are given by Equation (III.14) and Equation (III.15).

For the equilibrium thermal conductivity, the gradient in the phasial volume-averaged temperature in Equation (III.19) was determined in the 3 × 3 matrix from:

$$\frac{\Delta\langle T_e\rangle_{\gamma,y}}{\delta y} = \frac{\varepsilon_\gamma}{2\delta y\sum_{V_\gamma}\Delta x\Delta y}\left(\left[\sum_{V_\gamma}T_e\Delta x\Delta y\right]_n - \left[\sum_{V_\gamma}T_e\Delta x\Delta y\right]_s\right). \qquad \text{(III.20)}$$

UC		1	2	3		4
Thermal non- equilibrium state*		a	b	c	e	d
$h_{\alpha\beta}$	[W/ m^2·°C]	7.285	7.320	959.0	1057.0	5039.0
$k_{\alpha,e,y}$	[W/m·°C]	13.79	13.61	57.52		40.0
$k_{\beta,e,y}$	[W/m·°C]	68.78	200.0	112.4		200.0
$k_{\alpha,nd,y}$	[W/m·°C]	14.63	14.54	49.80		43.17
$k_{\beta,nd,y}$	[W/m·°C]	73.11	200.0	3295.0		200.0
$k_{\alpha\alpha,y}$	[W/m·°C]	14.48	14.48	49.91		42.61
$k_{\alpha\beta,y}$	[W/m·°C]	-0.7000	-0.8719	7.610		2.609
$k_{\beta\beta,y}$	[W/m·°C]	69.50	n/a	159.8		n/a
$k_{\beta\alpha,y}$	[W/m·°C]	0.7218	n/a	-47.39		n/a

*a	transfer vs. transfer
b	FT source vs. transfer
c	VT source vs. transfer
d	FT source vs. VT source
e	VT source vs. VT source, source ratio (S_α/S_β) = 4/-1

Table III.5 Conduction model transport parameters.

Subscripts n and s refer to the UC's neighbouring the principal UC on the northern and the southern sides respectively, and δy is as shown in Figure III.5. Similarly, the gradient in the phasial volume-averaged non-equilibrium temperature in Equation (III.19), was determined in the 3 × 1 matrix from:

$$\frac{\Delta\langle T_{nd}\rangle_{\gamma,y}}{\delta y} = \frac{\varepsilon_\gamma}{\delta y \sum_{V_\gamma} \Delta x \Delta y}\left(\left[\sum_{V_\gamma} T_{nd}\Delta x\Delta y\right]_{ind,row1,n} - \left[\sum_{V_\gamma} T_{nd}\Delta x\Delta y\right]_{ind,row1,s}\right). \tag{III.21}$$

Subscripts *ind,row*1,*n* and *ind,row*2,*s* refer to the first rows (either top or bottom) of the two independent 3 × 3 matrices used to determine boundary temperatures on the northern and the southern sides respectively of the 3 × 1 UC matrix. The vertical dimension δy is as shown in Figure III.6.

The equilibrium and non-equilibrium thermal conductivities for the four different UC configurations as detailed in Table III.2, are given in Table III.5. The effective and coupled thermal conductivities are also given.

III.10 Numerical solution of the transformed volume-averaged energy equation

With boundary temperatures specified in the manner described in the previous section, a steady-state, one-dimensional version of the transformed volume-averaged energy equation for the solid phase [Equation (8.3)] will sufficiently describe the conservation of heat in each phase at a macroscopic level. In a steady-state, one-dimensional form, Equation (8.3) gives for the α-phase:

$$\frac{\partial}{\partial y}\left(k_{\alpha\alpha,y}\frac{\partial}{\partial y}\langle T\rangle_\alpha\right)+\frac{\partial}{\partial y}\left(k_{\alpha\beta,y}\frac{\partial}{\partial y}\langle T\rangle_\beta\right)-h_{\alpha\beta}\frac{A_{\alpha\beta}}{\varepsilon_\alpha V_o}\left(\langle T\rangle_\alpha-\frac{\varepsilon_\alpha}{1-\varepsilon_\alpha}\langle T\rangle_\beta\right)+\langle I_\alpha\rangle_\alpha=0 \tag{III.22}$$

and for the β-phase:

$$\frac{\partial}{\partial y}\left(k_{\beta\beta,y}\frac{\partial}{\partial y}\langle T\rangle_\beta\right)+\frac{\partial}{\partial y}\left(k_{\beta\alpha,y}\frac{\partial}{\partial y}\langle T\rangle_\alpha\right)-h_{\alpha\beta}\frac{A_{\alpha\beta}}{\varepsilon_\beta V_o}\left(\langle T\rangle_\beta-\frac{\varepsilon_\beta}{1-\varepsilon_\beta}\langle T\rangle_\alpha\right)+\langle I_\beta\rangle_\beta=0\,. \tag{III.23}$$

Grid layout

The dimensions for the finite volumes in the grid arrangement were selected to correspond to the dimensions of the UC's. This yields a 1 × 50 grid arrangement. Grid points are located at the centres of the finite volumes.

Boundary conditions

For each of the five case studies, Table III.1 gives the boundary conditions for the two phases. The boundary conditions originate from the volume averaging of the microscopic temperature distribution in the bottom and top UC's of the 3 × 50 matrix, as discussed in Section III.8.

Solution of governing equations

Equation (III.22) and Equation (III.23) were solved using the MacSolidFluid computer code (see Appendix IV) developed for the simultaneous computational solution of the two-dimensional, steady-state form of Equation (8.3) and Equation (8.5). Pure conduction heat transfer was achieved in the fluid phase by specifying a zero flow velocity at all locations. A one-dimensional solution was obtained by specifying a zero macroscopic heat flux condition for both the solid and the fluid phases, at the boundaries parallel to that dimension.

III.11 Results

For Case Study 1 to Case Study 5, Tables III.6 to Table III.10 compares the numerical solutions of the energy equation to the numerical solution of the transformed volume-averaged energy equations of the α-phase and the β-phase respectively, incorporating the conduction model and the interphasial heat transfer model. Each table shows the solution of four equations: (1) the energy equation in the α-phase [Equation (III.2)] and (2) the energy equation in the β-phase [Equation (III.2)], both intrinsically volume-averaged over each UC, (3) the transformed volume-averaged energy equation for the α-phase [Equation (III.22)] and (4) the transformed volume-averaged energy equation for the β-phase

[Equation (III.23)]. The phasial volume-averaged temperatures obtained from the solution of the transformed volume-averaged energy equations were converted to intrinsic volume-averaged temperatures [using Equation (II.6)], for comparison in the tables.

Figure III.7 to Figure III.11 graphically compare the numerical values presented in Table III.6 to Table III.10. Each figure shows the solution results for the four equations discussed in the previous paragraph. In all five figures, the upper distribution represents the intrinsic volume-averaged temperature of the α-phase and the bottom distribution that of the β-phase. Smoothed curves are shown through the solution of the energy equation and dots represent values of the numerical solution of the transformed volume-averaged energy equations of the α-phase and the β-phase.

UC	$\langle T \rangle^{\alpha}_{\alpha,\text{Eq.III.2}}$ [°C]	$\langle T \rangle^{\alpha}_{\alpha,\text{Eq.III.22}}$ [°C]	$\langle T \rangle^{\beta}_{\beta,\text{Eq.III.2}}$ [°C]	$\langle T \rangle^{\beta}_{\beta,\text{Eq.III.23}}$ [°C]
1	56.932300	56.932301	20.945394	20.945400
2	55.188804	55.189606	21.934541	21.934088
3	53.644516	53.645779	22.883798	22.883011
4	52.284179	52.285912	23.796287	23.795147
5	51.094299	51.096405	24.674644	24.673214
6	50.062446	50.064907	25.521373	25.519684
7	49.177516	49.180187	26.338754	26.336803
8	48.429184	48.432068	27.128789	27.126608
9	47.808300	47.811352	27.893306	27.890934
10	47.306556	47.309753	28.634000	28.631439
11	46.916534	46.919849	29.352338	29.349607
12	46.631568	46.635010	30.049633	30.046764
13	46.445884	46.449364	30.727117	30.724085
14	46.354217	46.357754	31.385772	31.382601
15	46.352104	46.355690	32.026496	32.023205
16	46.435691	46.439331	32.650093	32.646675
17	46.601768	46.605450	33.257186	33.253651
18	46.847683	46.851410	33.848281	33.844658
19	47.171379	47.175148	34.423835	34.420113
20	47.571334	47.575161	34.984123	34.980316
21	48.046608	48.050488	35.529357	35.525459
22	48.596771	48.600712	36.059581	36.055626
23	49.221946	49.225952	36.574813	36.570789
24	49.922699	49.926868	37.074836	37.070820
25	50.700504	50.704662	37.559627	37.555477
26	51.556854	51.561089	38.028602	38.024410
27	52.494125	52.498463	38.481391	38.477158
28	53.515213	53.519680	38.917415	38.913139
29	54.623649	54.628246	39.335952	39.331657
30	55.823600	55.828285	39.736206	39.731884
31	57.119770	57.124577	40.117195	40.112862
32	58.517696	58.522591	40.477825	40.473495
33	60.023403	60.028538	40.816780	40.812546
34	61.644378	61.649395	41.132972	41.128620
35	63.387596	63.392963	41.424339	41.420155
36	65.262725	65.267914	41.689685	41.685413
37	67.278396	67.283897	41.926513	41.922470
38	69.446243	69.451538	42.133316	42.129204
39	71.776992	71.782555	42.307106	42.303261
40	74.284576	74.289856	42.445941	42.442070
41	76.982116	76.987595	42.546348	42.542793
42	79.886322	79.891304	42.605838	42.602325
43	83.012901	83.017998	42.620399	42.617268
44	86.381805	86.386276	42.586921	42.583900
45	90.011657	90.016487	42.500801	42.498154
46	93.926315	93.930855	42.358146	42.355587
47	98.149948	98.153633	42.153190	42.151344
48	102.70903	102.71129	41.881366	41.880135
49	107.63170	107.63271	41.537048	41.536182
50	112.94944	112.94940	41.113231	41.113201

Table III.6 Intrinsic volume-averaged temperature distributions of Case Study 1.

UC	$\langle T \rangle^{\alpha}_{\alpha,\text{Eq.III.2}}$ [°C]	$\langle T \rangle^{\alpha}_{\alpha,\text{Eq.III.22}}$ [°C]	$\langle T \rangle^{\beta}_{\beta,\text{Eq.III.2}}$ [°C]	$\langle T \rangle^{\beta}_{\beta,\text{Eq.III.23}}$ [°C]
1	38.270248	38.270199	20.000000	20.000000
2	37.077953	37.087494	19.999996	20.000000
3	35.990737	36.008457	19.999996	20.000000
4	35.001319	35.026554	20.000007	20.000000
5	34.103912	34.135822	20.000001	20.000000
6	33.292907	33.330856	19.999990	20.000000
7	32.563427	32.606773	20.000001	20.000000
8	31.910938	31.959177	20.000003	20.000000
9	31.331451	31.384144	20.000009	20.000000
10	30.821428	30.878181	20.000009	20.000000
11	30.377735	30.438219	20.000009	20.000000
12	29.997627	30.061588	19.999988	20.000000
13	29.678855	29.746004	20.000009	20.000000
14	29.419380	29.489552	20.000009	20.000000
15	29.217647	29.290674	20.000009	20.000000
16	29.072414	29.148163	20.000009	20.000000
17	28.982780	29.061157	20.000003	20.000000
18	28.948219	29.029131	20.000003	20.000000
19	28.968507	29.051886	20.000003	20.000000
20	29.043767	29.129560	20.000003	20.000000
21	29.174461	29.262629	20.000003	20.000000
22	29.361389	29.451897	20.000003	20.000000
23	29.605705	29.698511	20.000003	20.000000
24	29.908836	30.003971	19.999969	20.000000
25	30.272815	30.370129	20.000003	20.000000
26	30.699714	30.799204	20.000003	20.000000
27	31.192199	31.293802	20.000003	20.000000
28	31.753288	31.856924	20.000003	20.000000
29	32.386413	32.491982	20.000003	20.000000
30	33.095462	33.202839	20.000003	20.000000
31	33.884780	33.993801	20.000003	20.000000
32	34.759220	34.869667	19.999998	20.000000
33	35.724048	35.835754	19.999961	20.000000
34	36.785461	36.897919	20.000042	20.000000
35	37.949493	38.062607	19.999961	20.000000
36	39.223827	39.336895	20.000042	20.000000
37	40.615699	40.728500	19.999961	20.000000
38	42.134246	42.245869	20.000042	20.000000
39	43.788143	43.898216	19.999961	20.000000
40	45.588180	45.695557	20.000042	20.000000
41	47.544731	47.648804	19.999961	20.000000
42	49.670463	49.769806	20.000042	20.000000
43	51.977691	52.071430	19.999961	20.000000
44	54.481330	54.567642	20.000042	20.000000
45	57.195896	57.273590	19.999961	20.000000
46	60.138931	60.205688	20.000042	20.000000
47	63.327438	63.381729	19.999961	20.000000
48	66.781982	66.820992	19.999961	20.000000
49	70.523117	70.544319	20.000038	20.000000
50	74.574325	74.574303	19.999961	20.000000

Table III.7 Intrinsic volume-averaged temperature distributions of Case Study 2.

UC	$\langle T \rangle^{\alpha}_{\alpha,\text{Eq.III.2}}$ [°C]	$\langle T \rangle^{\alpha}_{\alpha,\text{Eq.III.22}}$ [°C]	$\langle T \rangle^{\beta}_{\beta,\text{Eq.III.2}}$ [°C]	$\langle T \rangle^{\beta}_{\beta,\text{Eq.III.23}}$ [°C]
1	10.058773	10.058800	8.5796820	8.5797000
2	13.674816	13.671906	12.195776	12.195759
3	17.140209	17.135504	15.661130	15.661160
4	20.454917	20.449116	18.975868	18.975870
5	23.618967	23.612463	22.139900	22.139910
6	26.632326	26.625423	25.153274	25.153294
7	29.495046	29.487852	28.015987	28.016003
8	32.207092	32.199726	30.728031	30.728033
9	34.768463	34.760979	33.289405	33.289398
10	37.179161	37.171604	35.700107	35.700077
11	39.439201	39.431576	37.960136	37.960087
12	41.548522	41.540890	40.069465	40.069427
13	43.507263	43.499550	42.028198	42.028107
14	45.315284	45.307541	43.836223	43.836109
15	46.972648	46.964878	45.493591	45.493450
16	48.479332	48.471546	47.000274	47.000118
17	49.835350	49.827549	48.356296	48.356117
18	51.040714	51.032883	49.561645	49.561451
19	52.095390	52.087547	50.616325	50.616116
20	52.999401	52.991547	51.520340	51.520119
21	53.752754	53.744884	52.273689	52.273457
22	54.355423	54.347549	52.876358	52.876122
23	54.807441	54.799549	53.328373	53.328121
24	55.108673	55.100883	53.629612	53.629452
25	55.259445	55.251549	53.780372	53.780117
26	55.259441	55.251545	53.780380	53.780113
27	55.108779	55.100876	53.629715	53.629448
28	54.807449	54.799541	53.328376	53.328114
29	54.355423	54.347542	52.876373	52.876118
30	53.752761	53.744877	52.273689	52.273453
31	52.999412	52.991543	51.520351	51.520119
32	52.095397	52.087540	50.616340	50.616116
33	51.040618	51.032867	49.561569	49.561443
34	49.835456	49.827530	48.356391	48.356106
35	48.479255	48.471523	47.000198	47.000099
36	46.972747	46.964851	45.493675	45.493423
37	45.315212	45.307514	43.836158	43.836079
38	43.507354	43.499516	42.028289	42.028065
39	41.548500	41.540852	40.069442	40.069386
40	39.439285	39.431549	37.960220	37.960052
41	37.179115	37.171570	35.700058	35.700043
42	34.768539	34.760956	33.289474	33.289368
43	32.207042	32.199703	30.727985	30.728006
44	29.495121	29.487835	28.016056	28.015982
45	26.632301	26.625408	25.153255	25.153271
46	23.619018	23.612461	22.139946	22.139902
47	20.454887	20.449106	18.975845	18.975861
48	17.140180	17.135492	15.661113	15.661149
49	13.674845	13.671898	12.195802	12.195754
50	10.058755	10.058800	8.5796710	8.5797000

Table III.8 Intrinsic volume-averaged temperature distributions of Case Study 3.

UC	$\langle T \rangle^{\alpha}_{\alpha,\text{Eq.III.2}}$ [°C]	$\langle T \rangle^{\alpha}_{\alpha,\text{Eq.III.22}}$ [°C]	$\langle T \rangle^{\beta}_{\beta,\text{Eq.III.2}}$ [°C]	$\langle T \rangle^{\beta}_{\beta,\text{Eq.III.23}}$ [°C]
1	20.211700	20.211700	20.000000	20.000000
2	20.211700	20.211700	19.999996	20.000000
3	20.211696	20.211700	19.999996	20.000000
4	20.211706	20.211700	20.000007	20.000000
5	20.211700	20.211700	20.000001	20.000000
6	20.211692	20.211700	19.999990	20.000000
7	20.211700	20.211700	20.000001	20.000000
8	20.211702	20.211700	20.000003	20.000000
9	20.211708	20.211700	20.000009	20.000000
10	20.211708	20.211700	20.000009	20.000000
11	20.211708	20.211700	20.000009	20.000000
12	20.211689	20.211700	19.999988	20.000000
13	20.211708	20.211700	20.000009	20.000000
14	20.211708	20.211700	20.000009	20.000000
15	20.211708	20.211700	20.000009	20.000000
16	20.211708	20.211700	20.000009	20.000000
17	20.211708	20.211700	20.000003	20.000000
18	20.211708	20.211700	20.000003	20.000000
19	20.211708	20.211700	20.000003	20.000000
20	20.211708	20.211700	20.000003	20.000000
21	20.211708	20.211700	20.000003	20.000000
22	20.211708	20.211700	20.000003	20.000000
23	20.211708	20.211700	20.000003	20.000000
24	20.211669	20.211700	19.999969	20.000000
25	20.211708	20.211700	20.000003	20.000000
26	20.211708	20.211700	20.000003	20.000000
27	20.211708	20.211700	20.000003	20.000000
28	20.211708	20.211700	20.000003	20.000000
29	20.211708	20.211700	20.000003	20.000000
30	20.211708	20.211700	20.000003	20.000000
31	20.211708	20.211700	20.000003	20.000000
32	20.211702	20.211700	19.999998	20.000000
33	20.211666	20.211700	19.999961	20.000000
34	20.211740	20.211700	20.000042	20.000000
35	20.211666	20.211700	19.999961	20.000000
36	20.211740	20.211700	20.000042	20.000000
37	20.211666	20.211700	19.999961	20.000000
38	20.211740	20.211700	20.000042	20.000000
39	20.211666	20.211700	19.999961	20.000000
40	20.211740	20.211700	20.000042	20.000000
41	20.211666	20.211700	19.999961	20.000000
42	20.211740	20.211700	20.000042	20.000000
43	20.211666	20.211700	19.999961	20.000000
44	20.211740	20.211700	20.000042	20.000000
45	20.211666	20.211700	19.999961	20.000000
46	20.211740	20.211700	20.000042	20.000000
47	20.211666	20.211700	19.999961	20.000000
48	20.211666	20.211700	19.999961	20.000000
49	20.211738	20.211700	20.000038	20.000000
50	20.211666	20.211700	19.999961	20.000000

Table III.9 Intrinsic volume-averaged temperature distributions of Case Study 4.

UC	$\langle T \rangle^{\alpha}_{\alpha,\text{Eq.III.2}}$ [°C]	$\langle T \rangle^{\alpha}_{\alpha,\text{Eq.III.22}}$ [°C]	$\langle T \rangle^{\beta}_{\beta,\text{Eq.III.2}}$ [°C]	$\langle T \rangle^{\beta}_{\beta,\text{Eq.III.23}}$ [°C]
1	9.015744	9.015700	5.995985	5.995999
2	14.439807	14.436039	11.420126	11.419456
3	19.637889	19.631618	16.618156	16.616918
4	24.609964	24.601954	21.590267	21.588394
5	29.356041	29.346759	26.336311	26.333888
6	33.876091	33.865857	30.856380	30.853403
7	38.170173	38.159142	35.150451	35.146940
8	42.238227	42.226550	39.218517	39.214499
9	46.080287	46.068041	43.060569	43.056083
10	49.696338	49.683593	46.676624	46.671690
11	53.086391	53.073191	50.066673	50.061322
12	56.250381	56.236827	53.230674	53.224978
13	59.188480	59.174495	56.168769	56.162659
14	61.900520	61.886193	58.880806	58.874364
15	64.386558	64.371918	61.366851	61.360094
16	66.646606	66.631670	63.626884	63.619848
17	68.680625	68.665447	65.660919	65.653627
18	70.488662	70.473249	67.468940	67.461430
19	72.070678	72.055077	69.050964	69.043258
20	73.426704	73.410929	70.406997	70.399110
21	74.556716	74.540806	71.537002	71.528988
22	75.460739	75.444707	72.441024	72.432889
23	76.138748	76.122633	73.119033	73.110815
24	76.590621	76.574584	73.570907	73.562766
25	76.816757	76.800559	73.797042	73.788742
26	76.816764	76.800559	73.797042	73.788742
27	76.590744	76.574584	73.571044	73.562766
28	76.138748	76.122633	73.119041	73.110815
29	75.460746	75.444707	72.441032	72.432889
30	74.556724	74.540806	71.537017	71.528988
31	73.426712	73.410929	70.406997	70.399110
32	72.070694	72.055077	69.050979	69.043258
33	70.488540	70.473249	67.468849	67.461430
34	68.680763	68.665447	65.661056	65.653627
35	66.646484	66.631670	63.626777	63.619848
36	64.386703	64.371918	61.366981	61.360094
37	61.900421	61.886193	58.880725	58.874364
38	59.188602	59.174495	56.168891	56.162659
39	56.250343	56.236827	53.230655	53.224978
40	53.086494	53.073191	50.066783	50.061322
41	49.696262	49.683593	46.676567	46.671690
42	46.080387	46.068041	43.060661	43.056083
43	42.238166	42.226550	39.218460	39.214499
44	38.170249	38.159142	35.150528	35.146940
45	33.876045	33.865857	30.856353	30.853403
46	29.356098	29.346759	26.336372	26.333888
47	24.609924	24.601954	21.590238	21.588394
48	19.637865	19.631618	16.618141	16.616918
49	14.439832	14.436039	11.420148	11.419456
50	9.015725	9.015700	5.995978	5.995999

Table III.10 Intrinsic volume-averaged temperature distributions of Case Study 5.

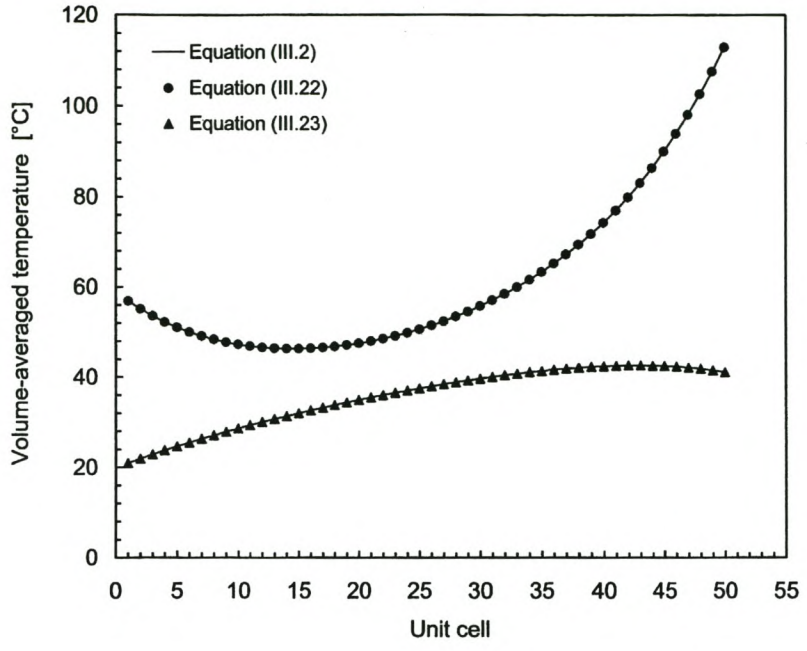

Figure III.7 Intrinsic volume-averaged temperature distributions of Case Study 1.

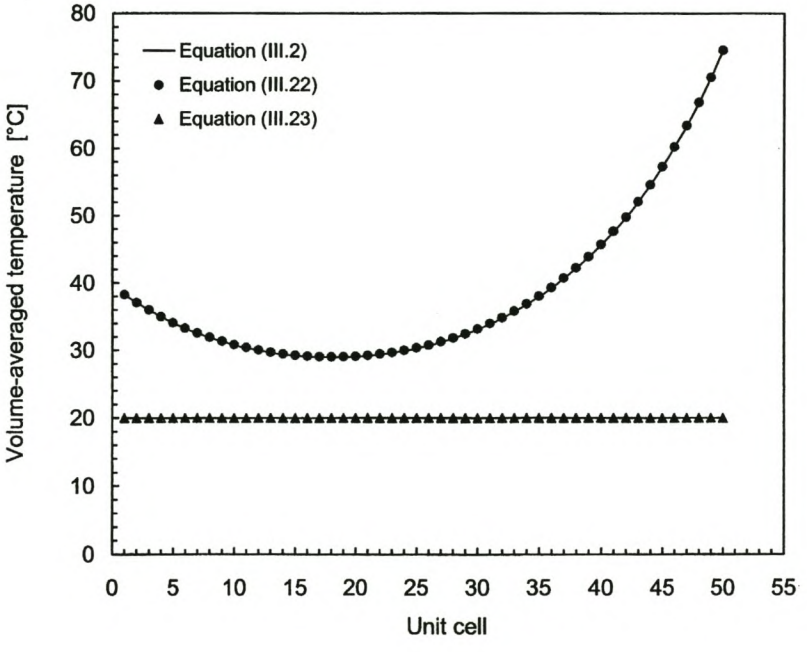

Figure III.8 Intrinsic volume-averaged temperature distributions of Case Study 2.

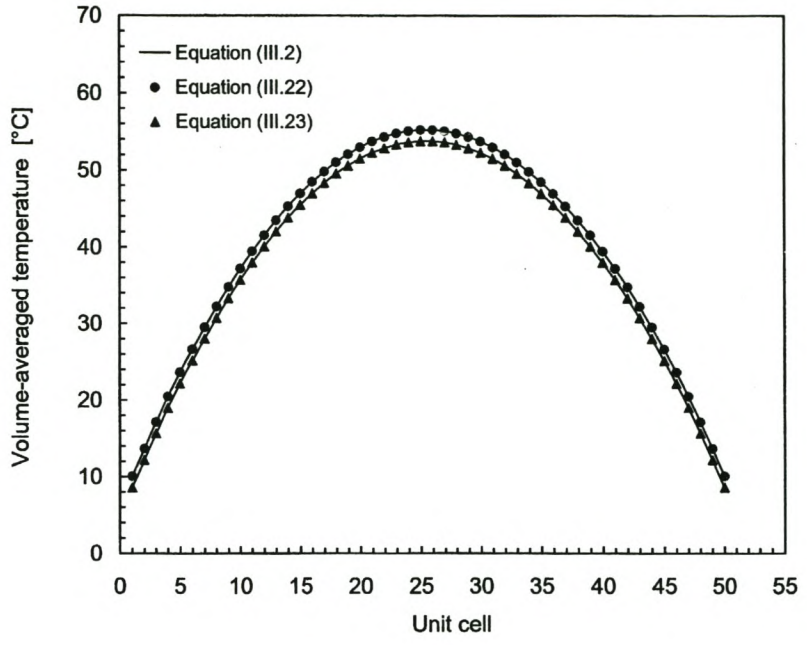

Figure III.9 Intrinsic volume-averaged temperature distributions of Case Study 3.

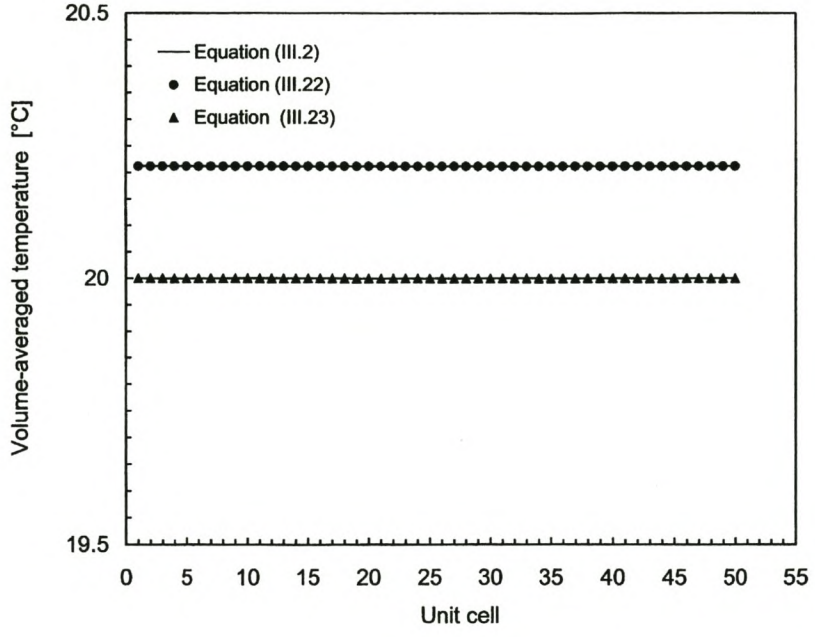

Figure III.10 Intrinsic volume-averaged temperature distributions of Case Study 4.

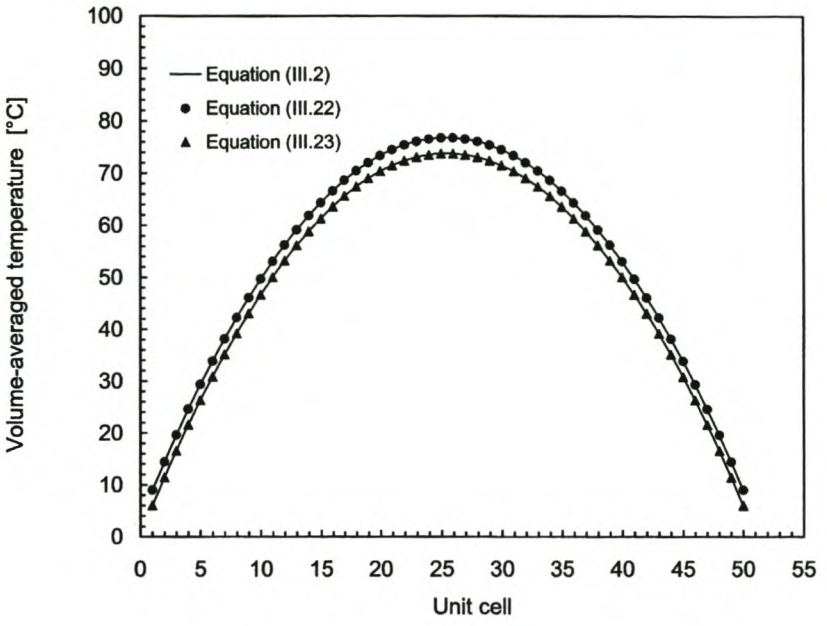

Figure III.11 Intrinsic volume-averaged temperature distributions of Case Study 5.

III.12 Conclusion

Results from these comparisons show excellent agreement between the microscopic and macroscopic approaches. They prove that the conduction model and the interphasial heat transfer model can be employed to accurately describe the conservation of heat in each phase of a two-phase system at macroscopic level, even when the phases are not in thermal equilibrium.

The procedure demonstrates a technique to determine the transport parameters of the transformed volume-averaged energy equation from established typical temperature distributions in a single UC. It further demonstrates how the accuracy of these parameters is improved by employing a matrix of UC's when the two-phase system consists of cells of periodic spatial distribution.

APPENDIX IV

COMPUTER PROGRAM USER'S GUIDE

IV.1 Overview

Two computer codes, MacFlow and MacSolidFluid, were developed to solve the sets of linear algebraic equations for the steady-state two-dimensional phasial volume-averaged velocity components of the fluid phase and the steady-state two-dimensional phasial volume-averaged temperatures of the solid and the fluid phases. The forms of the linear algebraic equations are derived in Chapter 15 by discretising the transformed volume-averaged momentum equation and the transformed volume-averaged energy equations for the solid and the fluid phases. These equations are derived and discussed in Chapter 8. Solution algorithms discussed in Chapter 16 were used in the computer codes.

Input files, output files, data files, and the functionalities of the main program and subroutines are discussed for each of the two computer codes. In the input files, input data is grouped together under different *namelists*. Input data is discussed with reference to the namelist and input file to which the data belongs. Information in braces { } given with the input data refers to the options available or the recommended range of values. Information in square brackets [ ] indicates the measuring units of the input data. A colon in an array index indicates a range of index values, *e.g.* CVBX(1:IN+1) refers to: CVBX(1), CVBX(2), ... CVBX(IN+1).

IV.2 Program file: MacFlow.for

Input files

File name: MacFlow.inp

Namelist CONVERGENCE_CONTROL:

FLOWFIELD_INPUT: Determines whether flow field calculations are initialised with x-direction and y-direction phasial volume-averaged velocity component values and intrinsic volume-averaged pressure values read from the FlowField.dat data file. {y/n} (If FLOWFIELD_INPUT = 'n', x-direction and y-direction phasial volume-averaged velocity component values and intrinsic volume-averaged pressure values are initialised as zero, requiring more solution iterations before convergence in achieved.)

RANGE_E: Determines whether a range of relaxation coefficients is used as apposed to a single relaxation coefficient. {y/n}

E: Relaxation coefficient value. {0.5 – 20} (To be specified when RANGE_E = 'n')

E_INIT: Initial relaxation coefficient value. (To be specified when RANGE_E = 'y'.)

E_FINAL: Final relaxation coefficient value. (To be specified when RANGE_E = 'y')

E_INCR: Increment in the range of relaxation coefficient values. (To be specified when RANGE_E = 'y'.)

ITERMAXMAIN: Maximum number of the main iterations allowed. {100 – 200} (For an illustration of the main iteration loop, consider the flow chart shown in Figure 16.2. Convergence may be achieved before the final iteration is reached.)

ITERMAXUV: Maximum number of phasial volume-averaged velocity component solution sub-iterations allowed. {>10, typically 20} (For an illustration of the phasial volume-averaged velocity component sub-iteration loop, consider the flow chart shown in Figure 16.2. All iterations are executed.)

ITERMAXP: Maximum number of intrinsic volume-averaged pressure correction solution sub-iterations allowed. {>50, typically 100} (For an illustration of the intrinsic volume-averaged pressure correction sub-iteration loop, consider the flow chart shown in Figure 16.2. Convergence may be achieved before the final iteration is reached.)

OUTFLOW_NODE: Determines whether a finite volume(s) exists at which flow leaves the porous domain. {y/n}

CONCRT: Determines the level of convergence required. {1–6} (Higher numbers refer to higher levels of convergence.)

DIVERGENCE_CHECK: Determines whether calculations should proceed to the next relaxation coefficient value, when a range of relaxation coefficients are tried, before a "floating point overflow" error occurring during the execution for a particular relaxation coefficient value stops the program. {y/n} (Specifying DIVERGENCE_CHECK= 'y' does not guarantee that a "floating point overflow" error will not occur during the execution for any particular relaxation coefficient value.)

Namelist FILEOUTPUT_CONTROL:

FLOWFIELD_OUTPUT: Determines whether calculated x-direction and y-direction phasial volume-averaged velocity component values and intrinsic volume-averaged pressure values are written to the FlowField.dat data file at the end of the program. {y/n}

PRINTINC: Main iteration increments at which intermediate data output is required. (For an illustration of the main iteration loop, consider the flow chart shown in Figure 16.2. Data to be included in the intermediate output is specified by the next five intermediate output parameters. If no intermediate file output is required, select PRINTINC > ITERMAINMAX.)

VEL_ITER: Determines whether the phasial volume-averaged velocity component values are included in the intermediate data output. {y/n} (To be specified when PRINTINC < ITERMAINMAX.)

VELCFF_ITER: Determines whether the discretised phasial volume-averaged velocity component equation coefficient values are included in the intermediate data output. {y/n} (To be specified when PRINTINC < ITERMAINMAX.)

PRESS_ITER: Determines whether the intrinsic volume-averaged pressure values are included in the intermediate data output. {y/n} (To be specified when PRINTINC < ITERMAINMAX.)

PRESSCRR_ITER: Determines whether the intrinsic volume-averaged pressure correction values are included in the intermediate data output. {y/n} (To be specified when PRINTINC < ITERMAINMAX.)

PRESSCRRCFF_ITER: Determines whether the intrinsic volume-averaged pressure correction equation coefficient values are included in the intermediate data output. {y/n} (To be specified when PRINTINC < ITERMAINMAX.)

VEL_FINAL: Determines whether the phasial volume-averaged velocity component values are included in the final data output. {y/n}

MOM_FINAL: Determines whether the diffusive, convective and total momentum transfer values across the finite volume boundaries are included in the final data output. {y/n}

VELCFF_FINAL: Determines whether the discretised phasial volume-averaged velocity component equation coefficient values are included in the final data output. {y/n}

PRESS_FINAL: Determines whether the intrinsic volume-averaged pressure values are included in the final data output. {y/n}

PRESSCRR_FINAL: Determines whether the intrinsic volume-averaged pressure correction values are included in the final data output. {y/n}

PRESSCRRCFF_FINAL: Determines whether the intrinsic volume-averaged pressure correction equation coefficient values are included in the final data output. {y/n}

Namelist CONSOLEOUTPUT_CONTROL:

ITERMAINWRITE: Determines whether the main iteration value is written to the console during execution. {y/n}

ITERUVWRITE: Determines whether the velocity solution sub-iteration value is written to the console during execution. {y/n}

ITERPWRITE: Determines whether the intrinsic volume-averaged pressure solution sub-iteration value is written to the console during execution. {y/n}

Namelist GRID_DIMENSION:

IN: Number of finite volumes of the main grid in the x-direction.

JN: Number of finite volumes of the main grid in the y-direction.

CVBX(1:IN+1): Main grid finite volume boundary positions in the x-direction. [m]

CVBY(1:JN+1): Main grid finite volume boundary positions in the y-direction. [m]

(The width of finite volumes along the system boundaries, *i.e.* the dimension perpendicular to the system boundary, is recommended to be very small, typically 10^{-6}m.)

Namelist GEO:

UNIPOROSITY: Determines whether the porosity is uniform (single-valued) in the porous domain. {y/n}

UNICELLSIZE: Determines whether the cell size is uniform (single-valued) in the porous domain. {y/n}

UNIEPSF: Single-valued uniform porosity. (To be specified if UNIPOROSITY = 'y'.)

UNIA: Single-valued uniform cell size. [m] (To be specified if UNICELLSIZE = 'y'.)

EPSF(1:IN, 1:JN): Variable porosity values at main grid points. (To be specified if UNICELLSIZE = 'n'.)

A(1:IN, 1:JN): Variable cell size values at main grid points. [m] (To be specified if UNICELLSIZE = 'n'.)

Namelist BOUNDARY_TYPE_VX:

TPBDEVX(IN, 1:JN): System boundary type for the phasial volume-averaged velocity component in the x-direction along the eastern system boundary. {1/2/3/4/44} (See the list below.)

TPBDWVX(0, 1:JN): System boundary type for the phasial volume-averaged velocity component in the x-direction along the western system boundary. {1/2/3/4/44} (See the list below.)

TPBDNVX(0:IN, JN): System boundary type for the phasial volume-averaged velocity component in the x-direction along the northern system boundary. {1/2/3/4/44} (See the list below.)

TPBDSVX(0:IN, 1): System boundary type for the phasial volume-averaged velocity component in the x-direction along the southern system boundary. {1/2/3/4/44} (See the list below.)

0: No system boundary (internal grid point).
1: Specified phasial volume-averaged velocity component.
2: Specified momentum transfer.
3: Momentum transfer as a function of boundary velocity.
4: Outflow without phasial volume-averaged velocity specification.
44: Boundary of a finite volume bordering, on the upstream side, a finite volume that has a type-4 boundary condition. (A type-44 boundary condition applies only to the boundary adjacent to the finite volume that has a type-4 boundary condition. This arrangement is shown in Figure IV.1)

Note: Type-0 phasial volume-averaged velocity component boundary conditions are automatically assigned to all finite volume boundaries. Only non-type-0 boundary conditions need to be specified. Momentum transfer (type-2 and type-3 phasial volume-averaged velocity component boundary conditions) can only be specified parallel to the particular velocity component, *i.e.* only on the northern and southern boundaries of the x-direction phasial volume-averaged velocity component.

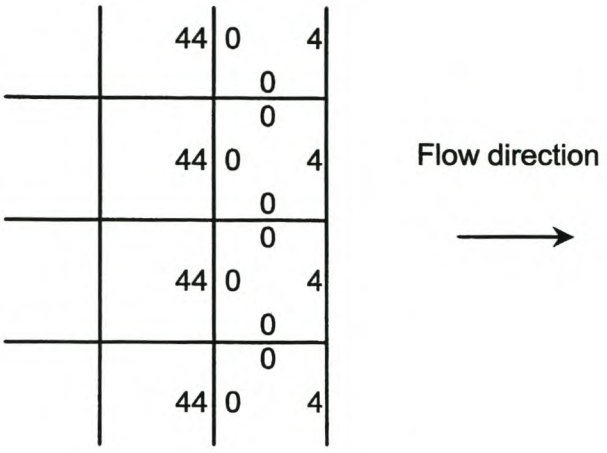

Figure IV.1 Velocity boundary type arrangement at an outflow open system boundary.

Namelist BOUNDARY_VEL_VX:

VXEI(0:IN,1:JN): Specified values for the phasial volume-averaged velocity component in the x-direction. [m/s] (To be specified at grid points of finite volumes with one or more type-1 phasial volume-averaged velocity component boundary conditions.)

Namelist BOUNDARY_TYPE_VY:

TPBDEVY(IN, 0:JN): System boundary type for the phasial volume-averaged velocity component in the y-direction along the eastern system boundary. {1/2/3/4/44} (See the list below.)

TPBDWVY(1, 0:JN): System boundary type for the phasial volume-averaged velocity component in the y-direction along the western system boundary. {1/2/3/4/44} (See the list below.)

TPBDNVY(1:IN, JN): System boundary type for the phasial volume-averaged velocity component in the y-direction along the northern system boundary. {1/2/3/4/44} (See the list below.)

TPBDSVY(1:IN, 0): System boundary type for the phasial volume-averaged velocity component in the y-direction along the southern system boundary. {1/2/3/4/44} (See the list below.)

0: No system boundary (internal grid point).
1: Specified phasial volume-averaged velocity component.
2: Specified momentum transfer.
3: Momentum transfer as a function of boundary velocity.
4: Outflow without phasial volume-averaged velocity specification.
44: Boundary of a finite volume bordering, on the upstream side, a finite volume that has a type-4 boundary condition. (A type-44 boundary condition applies only to the boundary adjacent to the finite volume that has a type-4 boundary condition. The arrangement is shown in Figure IV.1)

Note: Type-0 phasial volume-averaged velocity component boundary conditions are automatically assigned to all finite volume boundaries. Only non-type-0 boundary conditions need to be specified. Momentum transfer (type-2 and type-3 phasial volume-averaged velocity component boundary conditions) can only be specified parallel to the particular velocity component, *i.e.* only on the eastern and western boundaries of the y-direction phasial volume-averaged velocity component.

Namelist: BOUNDARY_VEL_VY:

VYNI(1:IN, 0:JN): Specified value for the phasial volume-averaged velocity component in the y-direction. [m/s] (To be specified at grid points of finite volumes with one or more type-1 phasial volume-averaged velocity component boundary conditions.)

Namelist: BOUNDARY_TYPE_P:

TPBDEP(IN, 1:JN): System boundary type for the intrinsic volume-averaged pressure correction along the eastern system boundary. {1/2} (See the list below.)

TPBDWP(1, 1:JN): System boundary type for the intrinsic volume-averaged pressure correction along the western system boundary. {1/2} (See the list below.)

TPBDNP(1:IN, JN): System boundary type for the intrinsic volume-averaged pressure correction along the northern system boundary. {1/2} (See the list below.)

TPBDSP(1:IN, 1): System boundary type for the intrinsic volume-averaged pressure correction along the southern system boundary. {1/2} (See the list below.)

0: No system boundary (internal grid point).
1: Specified intrinsic volume-averaged pressure correction value.
2: Specified phasial volume-averaged velocity or an outflow without a phasial volume-averaged velocity specification.

Note: Type-0 intrinsic volume-averaged pressure correction boundary conditions are automatically assigned to all finite volume boundaries. Only non-type-0 boundary conditions need to be specified. For a flow field with fluid leaving the porous domain (OUTFLOW_NODE = 'y'), one of the corner finite volumes along the line of outflow finite volumes must have type-1 intrinsic volume-averaged pressure correction boundary conditions at the two corner faces of the finite volume, as well as the face adjacent to the neighbouring outflow finite volume. Furthermore, along the line of outflow finite volumes, type-2 intrinsic volume-averaged pressure correction boundary conditions are specified between neighbouring outflow finite volumes. This arrangement is shown in Figure IV.2. For a flow field with no outflow (OUTFLOW_NODE = 'n'), a pressure correction value is not specified anywhere.

Namelist: BOUNDARY_VALUE_P:

PACSI(1:IN, 1:JN): Specified value for the intrinsic volume-averaged pressure correction. [N/m^2] (To be specified at grid points of finite volumes with one or more type-1 intrinsic volume-averaged pressure correction boundary conditions. For a flow field with fluid leaving the porous domain *i.e.* OUTFLOW_NODE = 'y', the corner finite volumes along the line of outflow finite volumes where type-1 intrinsic volume-averaged pressure correction boundary conditions are assigned, a specified intrinsic volume-averaged pressure correction value of zero is recommended.)

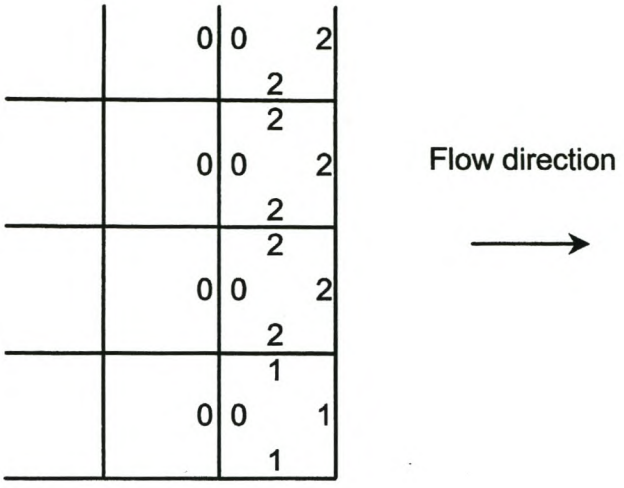

Figure IV.2 Pressure correction boundary type arrangement at an outflow open system boundary.

Namelist: BOUNDARY_MOM_VX:

TAUN(0:IN, JN): Specified momentum transfer at the northern boundary. [N/m^2] (To be specified only at type-2 phasial volume-averaged velocity component boundary condition.)

TAUS(0:IN, 1): Specified momentum transfer at the southern boundary. [N/m^2] (To be specified only at type-2 phasial volume-averaged velocity component boundary condition.)

Namelist: BOUNDARY_MOM_VY:

TAUE(IN, 0:JN): Specified momentum transfer at the eastern boundary. [N/m^2] (To be specified only at type-2 phasial volume-averaged velocity component boundary condition.)

TAUW(1, 0:IN): Specified momentum transfer at the western boundary. [N/m^2] (To be specified only at type-2 phasial volume-averaged velocity component boundary condition.)

Namelist: ABS_PRESSURE:

PRS(1:IN, 1:JN): Specified intrinsic volume-averaged pressure value. [N/m^2] (To be specified only at grid points with a SPECP = 1 designation.)

SPECP(1:IN, 1:JN): Type of intrinsic volume-averaged pressure grid point. {0/1} (See the list below.)

0: Intrinsic volume-averaged pressure value to be calculated.
1: Specified intrinsic volume-averaged pressure value.

Note: A specified intrinsic volume-averaged pressure corresponds to a type-1 intrinsic volume-averaged pressure correction boundary condition with a specified intrinsic volume-averaged pressure correction of zero.

Namelist: PROPERTIES:

MU: Fluid viscosity [kg/m·s]

RHOF: Fluid density [kg/m^3]

Output files

File name: MacFlow.out
Contains output information according to the output data specifiers in Namelist FILEOUTPUT_CONTROL.

Data files

File name: FlowField.dat

Namelist FLOWFIELD:

VXE: X-direction phasial volume-averaged velocity component values [m/s].

VYN: Y-direction phasial volume-averaged velocity component values [m/s].

PRS: Intrinsic volume-averaged pressure values [N/m^2].

(The data file FlowField.dat is required when FLOWFIELD_INPUT = 'y' in namelist CONVERGENCE_CONTROL, of the input file MacFlow.inp. The data file FlowField.dat is created when FLOWFIELD_OUTPUT = 'y' in namelist FILEOUTPUT_CONTROL, of the input file MacFlow.inp.)

Functionalities

Main program:

Opens the input file MacFlow.inp for reading and the output file MacFlow.out for writing. Reads namelists CONVERGENCE_CONTROL, FILEOUTPUT_CONTROL, CONSOLEOUTPUT_CONTROL and GRAPHICS_FILE from the input file MacFlow.inp. The solution procedure shown in Figure 16.2 is initialised by calling subroutines: GRIDDIM, BOUNDMAIN, GEOMETRY, BOUND, BOUNDSPEC, PRESSURE, PROPS, INITPRESS, ITERINITP, ITERINITVXVY and ITERMAININITVXVY. Subroutine FLOWFIELDIN is called when FLOWFIELD_INPUT = 'y' in namelist CONVERGENCE_CONTROL in the input file MacFlow.inp. The phasial volume-averaged velocity component iteration loop is executed by calling subroutines: PRESSDIFF, SHEARFACTOR, WALLCOEFFIC, DISPERSION, INTERFC, COEFFICVXVY, TDMASOLVEVXVY and ITERUPDATEVXVY. Subroutine DIV_CHK is called when DIVERGENCE_CHECK = 'y' in namelist FLOWFILED_INPUT in the input file MacFlow.inp. The intrinsic volume-averaged pressure correction iteration loop is executed by calling subroutines: COEFFICP, TDMASOLVEP, RESIDUALS, ITERUPDATEP, CORRECTP, CORRECTVXVY, ITERMAINUPDATEVXVY and

CONV_CHK. Subroutine NORMALISEP is called when OUTFLOW_NODE = 'n' in namelist CONVERGENCE_CONTROL in the input file MacFlow.inp. Intermediate and final output data is written to the output file according to specifications in namelist FILEOUTPUT_CONTROL in the input file MacFlow.inp. Subroutine FLOWFIELDOUT is called when FLOWFIELD_OUTPUT = 'y' in namelist FILEOUTPUT_CONTROL in the input file MacFlow.inp.

Subroutine BOUND:

Initialises the system boundary type indicator of all the finite volumes to zero, indicating a "no system boundary" condition. Reads namelists BOUNDARY_TYPE_VX, BOUNDARY_VEL_VX, BOUNDARY_TYPE_VY, BOUNDARY_VEL_VY, BOUNDARY_TYPE_P and BOUNDARY_VALUE_P from the input file MacFlow.inp.

Note: Each boundary of every finite volume has a boundary condition type designation. Finite volume boundaries not aligned with a system boundary are assigned (with one exception) with a type-0 phasial volume-averaged velocity component boundary condition. Finite volume boundaries aligned with a system boundary are assigned with non-type-0 type boundary conditions.

Subroutine BOUNDMAIN:

Initialises the main grid system boundary type indicator of all finite volumes to zero, indicating a "no system boundary" condition. Assigns a main grid system boundary type indicator value of one (1) to the faces of system boundary finite volumes aligned with system boundaries.

Subroutine BOUNDSPEC:

Reads namelists BOUNDARY_MOM_VX and BOUNDARY_MOM_VY from the input file MacFlow.inp.

Subroutine COEFFICP:

Calculates porosity values at the main grid finite volume boundaries by linear interpolation between porosity values at the grid points of the main grid. Calculates coefficient values for the discretised intrinsic volume-averaged pressure correction equation.

Subroutine COEFFICVXVY:

Calculates porosity values at the main grid finite volume boundaries by linear interpolation between porosity values at the grid points of the main grid. Calculates coefficient values for the discretised phasial volume-averaged velocity component equations.

Subroutine CONV_CHK:

Tests whether convergence has been achieved according to the convergence criteria specified by the convergence parameter CONCRT in namelist CONVERGENCE_CONTROL in the input file MacFlow.inp.

Subroutine CORRECTP:

Calculates corrected intrinsic volume-averaged pressure values from the "previous iteration" intrinsic volume-averaged pressure values and the intrinsic volume-averaged pressure correction values.

Subroutine CORRECTVXVY:

Calculates corrected phasial volume-averaged velocity component values from the "previous iteration" phasial volume-averaged velocity component values.

Subroutine DISPERSION:

Calculates the transverse momentum dispersion coefficient and the total viscous transfer coefficient.

Subroutine DIV_CHK:

Tests whether divergence of calculated phasial volume-averaged velocity component values is occurring from iterations to iteration. This subroutine is called when DIVERGENCE_CHECK = 'y' in namelist CONVERGENCE_CONTROL in the input file MacFlow.inp.

Subroutine FLOWFIELDIN:

Opens the data file FlowField.dat for reading. Reads namelist FLOWFIELD from the data file. Initialises intrinsic volume-averaged pressure and velocity component values from

the input data. Closes the data file. This subroutine is called when FLOWFIELD_INPUT = 'y' in namelist CONVERGENCE_CONTROL in the input file MacFlow.inp.

Subroutine FLOWFIELDOUT:

Opens the data file FlowField.dat for writing. Writes namelist FLOWFIELD to the data file. Closes the data file. This subroutine is called when FLOWFIELD_OUTPUT = 'y' in namelist FILEOUTPUT_CONTROL in the input file MacFlow.inp.

Subroutine GEOMETRY:

Reads namelist GEO from the input file MacFlow.inp. Assigns uniform porosity and cell size values at the grid points if UNIPOROSITY = 'y' and UNICELLSIZE = 'y'. Calculates the strand side length, tortuosity, RUC characteristic length and the fluid phase mean linear distance.

Subroutine GRIDDIM:

Reads namelist GRID_DIMENSION from the input file MacFlow.inp. Calculates the positions of the grid points and the finite volume sizes of the main grid. Calculates the finite volume boundary positions of the phasial volume-averaged velocity component grids. Calculates the grid point positions and finite volume sizes of the phasial volume-averaged velocity component grids.

Subroutine INITPRESS:

Initialises intrinsic volume-averaged pressure values at grid points where the intrinsic volume-averaged pressure value is not specified, to zero if FLOWFIELD_INPUT = 'n' in namelist CONVERGENCE_CONTROL in the input file MacFlow.inp, or else, to data read from the data file FlowField.dat.

Subroutine INTERFC:

Calculates the total viscous transfer coefficients, porosities, and phasial volume-averaged velocity component values at the finite volume boundaries of the main grid and at the finite volume boundaries of the phasial volume-averaged velocity component grids, by linear interpolation. Calculates the viscous diffusivity, Reynolds number and the

Reynolds number function (A), at the finite volume boundaries of the phasial volume-averaged velocity component grids.

Subroutine ITERINITP:
Initialises intrinsic volume-averaged pressure correction values to zero.

Subroutine ITERINITVXVY:
Initialises phasial volume-averaged velocity component values at grid points where the intrinsic volume-averaged pressure values are not specified. Phasial volume-averaged velocity component values are initialised to zero if FLOWFIELD_INPUT = 'n' in namelist CONVERGENCE_CONTROL in the input file MacFlow.inp. Otherwise it is initialised to data read from the data file FlowField.dat.

Subroutine ITERMAININITVXVY:
Initialises "previous-iteration" values of phasial volume-averaged velocity components.

Subroutine ITERMAINUPDATEVXVY:
Updates "previous-iteration" values before calculating new phasial volume-averaged velocity component values in every main iteration. (For an illustration of the main iteration loop, consider the flow chart shown in Figure 16.2.)

Subroutine ITERUPDATEP:
Updates "previous-iteration" values before calculating new intrinsic volume-averaged pressure correction values in every intrinsic volume-averaged pressure correction sub-iteration. (For an illustration of the intrinsic volume-averaged pressure correction sub-iteration loop, consider the flow chart shown in Figure 16.2.)

Subroutine ITERUPDATEVXVY:
Updates "previous-iteration" values before calculating new phasial volume-averaged velocity component values in every phasial volume-averaged velocity component sub-iteration. (For an illustration of the phasial volume-averaged velocity component sub-iteration loop, consider the flow chart shown in Figure 16.2.)

Subroutine MOMENTFLUX:

Calculates diffusive, convective and total momentum transfer at the boundaries of every finite volume in each phasial volume-averaged velocity grid.

Subroutine NORMALISEP:

Normalises the intrinsic volume-averaged pressure values if there are no specified intrinsic volume-averaged pressure values in the flow field. This subroutine is called when OUTFLOW_NODE = 'n' in namelist CONVERGENCE_CONTROL in the input file MacFlow.inp.

Subroutine OUTPUT2:

Writes phasial volume-averaged velocity component values to the output file MacFlow.out. This subroutine is called when VEL_ITER = 'y' or VEL_FINAL = 'y' in namelist FILEOUTPUT_CONTROL in the input file MacFlow.inp.

Subroutine OUTPUT4:

Writes diffusive, convective and total momentum transfer values to the output file MacFlow.out. This subroutine is called when MOM_FINAL = 'y' in namelist FILEOUTPUT_CONTROL in the input file MacFlow.inp.

Subroutine OUTPUT5:

Writes coefficient values of the discretised phasial volume-averaged velocity component equations to the output file MacFlow.out. This subroutine is called when VELCFF_ITER = 'y' or VELCFF_FINAL = 'y' in namelist FILEOUTPUT_CONTROL in the input file MacFlow.inp.

Subroutine OUTPUT6:

Writes the intrinsic volume-averaged pressure values to the output file MacFlow.out. This subroutine is called when PRESS_ITER = 'y' or PRESS_FINAL = 'y' in namelist FILEOUTPUT_CONTROL in the input file MacFlow.inp.

Subroutine OUTPUT7:

Writes the intrinsic volume-averaged pressure correction values to the output file MacFlow.out. This subroutine is called when PRESSCRR_ITER = 'y' or PRESSCRR_FINAL = 'y' in namelist FILEOUTPUT_CONTROL in the input file MacFlow.inp.

Subroutine OUTPUT8:

Writes coefficients values of the discretised intrinsic volume-averaged pressure correction equation to the output file MacFlow.out. This subroutine is called when PRESSCRRCFF_ITER = 'y' or PRESSCRRCFF_FINAL = 'y' in namelist FILEOUTPUT_CONTROL in the input file MacFlow.inp.

Subroutine PRESSDIFF:

Calculates the intrinsic volume-averaged pressure difference between grid points of the main grid.

Subroutine PRESSURE:

Initialises the parameter SPECP at all the grid points to zero. Reads namelist ABS_PRESSURE from the input file MacFlow.inp.

Subroutine RESIDUALS:

Calculates residuals of the intrinsic volume-averaged pressure correction values.

Subroutine SHEARFACTOR:

Calculates the solid phase characteristic length and the viscous shear factor at the grid points of the main grid. Calculates the viscous shear factor at the grid points of the phasial volume-averaged velocity component grids by linear interpolation.

Subroutine TDMA:

Executes a single sweep of the TDMA procedures (Patankar, 1980) on a specified set of equations.

Subroutine TDMASOLVEP:

Calls subroutine TDMA to execute the TDMA procedure (Patankar, 1980) on the intrinsic volume-averaged pressure correction values.

Subroutine TDMASOLVEVXVY:

Calls subroutine TDMA to execute the TDMA procedures (Patankar, 1980) on the phasial volume-averaged velocity component values.

Subroutine WALLCOEFFIC:

Calculates the porosity and the mean linear distance at the grid points of the phasial volume-averaged velocity component grids by linear interpolation between porosity and mean linear distance values at the grid points of the main grid. Calculates momentum transfer coefficients at the finite volume boundaries of the phasial volume-averaged velocity component grids where a type-3 phasial volume-averaged velocity component boundary condition is specified.

IV.3 Program file: MacSolidFluid.for

Input files

File name: FlowField.dat

Namelist: FLOWFIELD:

VXE: x-Direction phasial volume-averaged velocity component values.

VYN: y-Direction phasial volume-averaged velocity component values.

PRS: Intrinsic volume-averaged pressure values.

File name: MacSolidFluid.inp

Namelist ITERATIONS:

ITERMAX: Maximum number of iterations allowed. {100 – 200} (Convergence may be achieved before the final iteration is reached.)

ALPHA: Relaxation factor α. {0.01 – 0.99}

Namelist FILEOUTPUT_CONTROL:

VELOCITY: Determines whether the phasial volume-averaged velocity component values are included in the output. {y/n}

TEMPSOLID: Determines whether the phasial volume-averaged temperature values of the solid phase are included in the data output. {y/n}

HEATFLUXSOLID: Determines whether solid phase conduction heat transfer values across the finite volume boundaries are included in the data output. {y/n}

TEMPCOEFFSOLID: Determines whether the solid phase discretised phasial volume-averaged temperature equation coefficient values are included in the data output. {y/n}

SECFLUXSOLID: Determines whether values of the solid phase secondary conduction heat transfer across the finite volume boundaries are included in the data output. {y/n}

TEMPFLUID: Determines whether the phasial volume-averaged temperature values of the fluid phase are included in the data output. {y/n}

HEATFLUXFLUID: Determines whether the fluid phase conduction, convection and total heat transfer values across the finite volume boundaries are included in the data output. {y/n}

TEMPCOEFFFLUID: Determines whether the fluid phase discretised phasial volume-averaged temperature equation coefficient values are included in the data output. {y/n}

INTERPHASIALFLUX: Determines whether heat transfer values across the interface between the fluid phase and the solid phase are included in the data output. {y/n}

SECFLUXFLUID: Determines whether values of the fluid phase secondary conduction heat transfer across the finite volume boundaries, are included in the data output. {y/n}

Namelist GRID_DIMENSION:

IN: Number of finite volumes in the x-direction.

JN: Number of finite volumes in the y-direction.

CVBX(1:IN+1): Finite volume boundary positions in the x-direction. [m]

CVBY(1:JN+1): Finite volume boundary positions in the y-direction. [m]

(The width of finite volumes along the system boundaries, *i.e.* the dimension perpendicular to the system boundary, is recommended to be very small, typically 10^{-6}m.)

Namelist GEO:

UNIPOROSITY: Determines whether the porosity is uniform (single-valued) in the porous domain. {y/n}

UNICELLSIZE: Determines whether the cell size is uniform (single-valued) in the porous domain. {y/n}

UNIEPSF: Single-valued uniform porosity. (To be specified if UNIPOROSITY = 'y'.)

UNIA: Single-valued uniform cell size. [m] (To be specified if UNICELLSIZE = 'y'.)

EPSF(1:IN, 1:JN): Variable porosity values at grid points. (To be specified if UNICELLSIZE = 'n'.)

A(1:IN, 1:JN): Variable cell size values at grid points. [m] (To be specified if UNICELLSIZE = 'n'.)

Namelist FLOWFIELDINPUT:

UNIFLOW: Determines whether the flow field is uniform (single-valued) in the porous domain. {y/n}

UNIVX: Single-valued uniform phasial volume-averaged velocity component in the x-direction. [m/s] (To be specified only if UNIFLOW = 'y'.)

UNIVY: Single-valued uniform phasial volume-averaged velocity component in the y-direction. [m/s] (To be specified only if UNIFLOW = 'y'.)

Namelist PROPERTIESSOLID:

KS: Solid phase thermal conductivity. [W/m·°C]

KF: Fluid phase thermal conductivity. [W/m·°C]

UNISOURCES: Determines whether a uniform (single-valued) solid phase heat source exists in the porous domain. {y/n}.

UNIINTSOURCES: Single-valued uniform heat source. [W/m^3] (To be specified only if UNISOURCES = 'y'.)

Namelist PROPERTIESFLUID:

KF: Fluid phase thermal conductivity. [W/m·°C]

KS: Solid phase thermal conductivity. [W/m·°C]

CPF: Fluid phase specific heat capacity. [J/kg·°C]

MU: Fluid phase viscosity. [kg/m·s]

RHOF: Fluid phase density. [kg/m^3]

UNISOURCEF: Determines whether a uniform (single-valued) fluid phase heat source exists in the porous domain. {y/n}

UNIINTSOURCEF: Single-valued uniform heat source. [W/m^3] (To be specified if UNISOURCEF = 'y'.)

Namelist BOUNDSOLID:

TPBDET(IN, 1:JN): System boundary type for the solid phase phasial volume-averaged temperature along the eastern system boundary. {1/2/3/4/5} (See the list below.)

TPBDNT(1:IN, JN): System boundary type for the solid phase phasial volume-averaged temperature along the northern system boundary. {1/2/3/4/5} (See the list below.)

TPBDWT(1, 1:JN): System boundary type for the solid phase phasial volume-averaged temperature along the western system boundary. {1/2/3/4/5} (See the list below.)

TPBDST(1:IN, 1): System boundary type for the solid phase phasial volume-averaged temperature along the southern system boundary. {1/2/3/4/5} (See the list below.)

0: No system boundary (internal grid point).
1: Specified phasial volume-averaged temperature.
2: Specified heat transfer.
3: Specified wall temperature value and thermal contact resistance.
4: Inflow at an open system boundary.
5: Outflow at an open system boundary.

Note: Type-0 boundary conditions are automatically assigned to all finite volume boundaries. Only non-type-0 boundary conditions need to be specified.

Namelist BOUNDSPECSOLID:

TEMPBSE(IN, 1:JN): Specified solid phase phasial volume-averaged temperature value at the eastern boundary. [°C] (To be specified at grid points of finite volumes with one or more type-1 boundary conditions.)

TEMPBSW(1, 1:JN): Specified solid phase phasial volume-averaged temperature value at the western boundary. [°C] (To be specified at grid points of finite volumes with one or more type-1 boundary conditions.)

TEMPBSN(1:IN, JN): Specified solid phase phasial volume-averaged temperature value at the northern boundary. [°C] (To be specified at grid points of finite volumes with one or more type-1 boundary conditions.)

TEMPBSS(1:IN, 1): Specified solid phase phasial volume-averaged temperature value at the southern boundary. [°C] (To be specified at grid points of finite volumes with one or more type-1 boundary conditions.)

HFSPECE(IN, 1:JN): Specified solid phase heat transfer at the eastern boundary. [W/m^2] (To be specified at type-2 boundary conditions.)

HFSPECW(1, 1:JN): Specified solid phase heat transfer at the western boundary. [W/m^2] (To be specified at type-2 boundary conditions.)

HFSPECN(1:IN, JN): Specified solid phase heat transfer at the northern boundary. [W/m^2] (To be specified at type-2 boundary conditions.)

HFSPECS(1:IN, 1): Specified solid phase heat transfer at the southern boundary. [W/m^2] (To be specified at type-2 boundary conditions.)

RSSE(IN, 1:JN): Specified thermal contact resistance at the eastern boundary. [$m^2 \cdot °C/W$] (To be specified at type-3 boundary conditions.)

RSSW(1, 1:JN): Specified thermal contact resistance at the western boundary. [$m^2 \cdot °C/W$] (To be specified at type-3 boundary conditions.)

RSSN(1:IN, JN): Specified thermal contact resistance at the northern boundary. [$m^2 \cdot °C/W$] (To be specified at type-3 boundary conditions.)

RSSS(1:IN, 1): Specified thermal contact resistance at the southern boundary. [$m^2 \cdot °C/W$] (To be specified at type-3 boundary conditions.)

TWALLE(IN, 1:JN): Specified wall temperature value at the eastern boundary. [°C] (To be specified at type-3 boundary conditions.)

TWALLW(1, 1:JN): Specified wall temperature value at the western boundary. [°C] (To be specified at type-3 boundary conditions.)

TWALLN(1:IN, JN): Specified wall temperature value at the northern boundary. [°C] (To be specified at type-3 boundary conditions.)

TWALLS(1:IN, 1): Specified wall temperature value at the southern boundary. [°C] (To be specified at type-3 boundary conditions.)

TFLUIDE(IN, 1:JN): Specified fluid temperature value at the eastern boundary. [°C] (To be specified at type-4 boundary conditions.)

TFLUIDW(1, 1:JN): Specified fluid temperature value at the western boundary. [°C] (To be specified at type-4 boundary conditions.)

TFLUIDN(1:IN, JN): Specified fluid temperature value at the northern boundary. [°C] (To be specified at type-4 boundary conditions.)

TFLUIDS(1:IN, 1): Specified fluid temperature value at the southern boundary. [°C] (To be specified at type-4 boundary conditions.)

Namelist BOUNDFLUID:

TPBDET(IN, 1:JN): System boundary type for the fluid phase phasial volume-averaged temperature along the eastern system boundary. {1/2/3/4/5/55} (See the list below.)

TPBDWT(1, 1:JN): System boundary type for the fluid phase phasial volume-averaged temperature along the western system boundary. {1/2/3/4/5/55} (See the list below.)

TPBDNT(1:IN, JN): System boundary type for the fluid phase phasial volume-averaged temperature along the northern system boundary. {1/2/3/4/5/55} (See the list below.)

TPBDST(1:IN, 1): System boundary type for the fluid phase phasial volume-averaged temperature along the southern system boundary. {1/2/3/4/5/55} (See the list below.)

0: No system boundary (internal grid point).

1: Specified phasial volume-averaged temperature.

2: Specified heat transfer.

3: Specified wall temperature.

4: Inflow at an open system boundary.

5: Outflow at an open system boundary.

55: Boundary of a finite volume bordering, on the upstream side, a finite volume that has a type-5 boundary condition. (The type-55 boundary condition applies only to the boundary adjacent to the finite volume that has a type-5 boundary condition. This arrangement is shown in Figure IV.3.)

Note: Type-0 boundary conditions are automatically assigned to all finite volume boundaries. Only non-type-0 boundary conditions need to be specified.

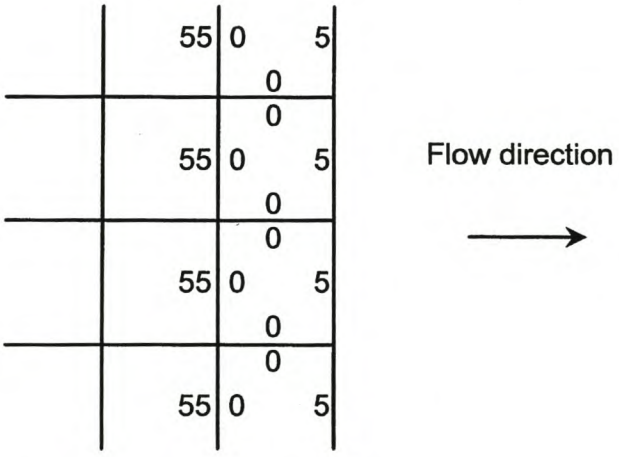

Figure IV.3 Temperature boundary type arrangement at an outflow open system boundary.

Namelist BOUNDSPECFLUID

TEMPBFE(IN, 1:JN): Specified fluid phase phasial volume-averaged temperature value at the eastern boundary. [°C] (To be specified at grid points of finite volumes with one or more type-1 boundary conditions.)

TEMPBFW(1, 1:JN): Specified fluid phase phasial volume-averaged temperature value at the western boundary. [°C] (To be specified at grid points of finite volumes with one or more type-1 boundary conditions.)

TEMPBFN(1:IN, JN): Specified fluid phase phasial volume-averaged temperature value at the northern boundary. [°C] (To be specified at grid points of finite volumes with one or more type-1 boundary conditions.)

TEMPBFS(1:IN, 1): Specified fluid phase phasial volume-averaged temperature value at the southern boundary. [°C] (To be specified at grid points of finite volumes with one or more type-1 boundary conditions.)

HFSPECE(IN, 1:JN): Specified fluid phase heat transfer at the eastern boundary. [W/m^2] (To be specified at type-2 boundary conditions.)

HFSPECW(1, 1:JN): Specified fluid phase heat transfer at the western boundary. [W/m^2] (To be specified at type-2 boundary conditions.)

HFSPECN(1:IN, JN): Specified fluid phase heat transfer at the northern boundary. [W/m^2] (To be specified at type-2 boundary conditions.)

HFSPECS(1:IN, 1): Specified fluid phase heat transfer at the southern boundary. [W/m^2] (To be specified at type-2 boundary conditions.)

TWALLE(IN, 1:JN): Specified wall temperature value at the eastern boundary. [°C] (To be specified at type-3 boundary conditions.)

TWALLW(1, 1:JN): Specified wall temperature value at the western boundary. [°C] (To be specified at type-3 boundary conditions.)

TWALLN(1:IN, JN): Specified wall temperature value at the northern boundary. [°C] (To be specified at type-3 boundary conditions.)

TWALLS(1:IN, 1): Specified wall temperature value at the southern boundary. [°C] (To be specified at type-3 boundary conditions.)

TFLUIDE(IN, 1:JN): Specified fluid temperature value at the eastern boundary. [°C] (To be specified at type-4 boundary conditions.)

TFLUIDW(1, 1:JN): Specified fluid temperature value at the western boundary. [°C] (To be specified at type-4 boundary conditions.)

TFLUIDN(1:IN, JN): Specified fluid temperature value at the northern boundary. [°C] (To be specified at type-4 boundary conditions.)

TFLUIDS(1:IN, 1): Specified fluid temperature value at the southern boundary. [°C] (To be specified at type-4 boundary conditions.)

Output files

File name: MacSolidFluid.out
Contains output information according to the output data specifiers in Namelist FILEOUTPUT_CONTROL.

Data files

File name: MacFluid.dat
Contains input information read in Subroutine INITF. Contains output information written by Subroutine OUTPUTF1
(The data file MacFluid.dat is always required when running the program.)

File name: MacSolid.dat

Contains input information read in Subroutine INITS. Contains output information written by Subroutine OUTPUTS1.

(The data file MacSolid.dat is always required when running the program.)

File name: FlowField.dat

Namelist FLOWFIELD:

VXE: X-direction phasial volume-averaged velocity component values. [m/s].

VYN: Y-direction phasial volume-averaged velocity component values. [m/s].

PRS: Intrinsic volume-averaged pressure values. [N/m^2].

(The data file FlowField.dat is required when FLOWFIELD_INPUT = 'y' in namelist CONVERGENCE_CONTROL of the input file MacFlow.inp.)

Functionalities

Main program:

Opens the input files MacSolidFluid.inp and the data files, MacSolid.dat and MacFluid.dat for reading. Opens output file MacSolidFluid.out for writing. Reads namelists ITERATIONS and FILEOUTPUT_CONTROL from the input file MacSolidFluid.inp. The solution procedure shown in Figure 16.3 is initialised by calling subroutines: GRIDDIM, BOUND, INITS, INITF, GEOMETRY, FLOW, PROPSS, PROPSF, BOUNDS, BOUNDSPECS, BOUNDF and BOUNDSPECF. The iteration loop shown in Figure 16.3 is executed by calling subroutines INIT, INTERFACEHT, COEFFICS, PSOLVEPREPS, RELAXS, HEATFLUXS, OUTPUTSCREENS, COEFFICF, PSOLVEPREPF, RELAXF, HEATFLUXF and OUTPUTSCREENF. The data file TempField.dat is written by Subroutine TEMPFIELDOUT. Opens the data files MacSolid.dat and MacFluid.dat for writing. Writes data to the data files.

Subroutine BOUND:

Initialises the main grid system boundary type indicator of all finite volumes to zero, indicating a "no system boundary" condition. Assigns a main grid system boundary type indicator value of one (1) to the faces of system boundary finite volumes aligned with system boundaries.

Subroutine BOUNDF:

Initialises the system boundary type indicator of all the finite volumes to zero, indicating a "no system boundary" condition. Reads namelist BOUNDFLUID from the input file MacSolidFluid.inp.

Note: Each boundary of every finite volume of the fluid phase has a boundary condition type designation. Finite volume boundaries not aligned with a system boundary are assigned (with one exception) with a type-0 boundary condition. Finite volume boundaries aligned with a system boundary are assigned with a non-type-0 boundary condition.

Subroutine BOUNDS:

Initialises the system boundary type indicator of all the finite volumes to zero, indicating a "no system boundary" condition. Reads namelist BOUNDSOLID from the input file MacSolidFluid.inp.

Note: Each boundary of every finite volume of the solid phase has a boundary condition type designation. Finite volume boundaries not aligned with a system boundary are assigned (with one exception) with a type-0 boundary condition. Finite volume boundaries aligned with a system boundary are assigned with a non-type-0 boundary condition.

Subroutine BOUNDSPECF:

Reads namelist BOUNDSPECFLUID from the input file MacSolidFluid.inp. Calculates and assigns fluid phase system boundary heat transfer parameters.

Subroutine BOUNDSPECS:

Reads namelist BOUNDSPECSOLID from the input file MacSolidFluid.inp. Calculates and assigns solid phase system boundary heat transfer parameters.

Subroutine COEFFICF:

Calculates porosity values at the finite volume boundaries of the main grid by linear interpolation between porosity values at the grid points of the main grid. Calculates the fluid phase total heat transfer coefficient coupled thermal conductivity thermal diffusivity, Peclét number and the Peclét number function (A), at the finite volume boundaries of the main grid. Calculates coefficient values for the discretised fluid phase phasial volume-averaged temperature equation.

Subroutine COEFFICS:

Calculates the solid phase effective thermal conductivity and coupled thermal conductivity at the finite volume boundaries of the main grid. Calculates coefficient values for the discretised solid phase phasial volume-averaged temperature equation.

Subroutine FLOW:

Reads namelist FLOWFIELDINPUT. Assigns uniform phasial volume-averaged velocity component values UNIVX and UNIVY to all the finite volume boundaries if UNIFLOW = 'y'. If UNIFLOW = 'n', the data file FlowField.dat is opened and namelist FLOWFIELD is read.

Subroutine GEOMETRY:

Reads namelist GEO from the input file MacFlow.inp. Assigns uniform porosity and cell size values at the grid points if UNIPOROSITY = 'y' and UNICELLSIZE = 'y'. Calculates the strand side length, tortuosity, RUC characteristic length, specific interface area, solid phase mean linear distance and the fluid phase mean linear distance.

Subroutine GRIDDIM:

Reads namelist GRID_DIMENSION from the input file MacFlow.inp. Calculates the positions of the grid points and the finite volume sizes of the main grid.

Subroutine HEATFLUXF:

Calculates the fluid phase conduction, convection and total heat transfer at the boundaries of every finite volume.

Subroutine HEATFLUXS:

Calculates the solid phase conduction at the boundaries of every finite volume.

Subroutine INIT:

Initialises "previous-iteration" values of the phasial volume-averaged temperature of the solid and the fluid phases.

Subroutine INITF:

Initialises fluid phase heat transfer values. Reads initial fluid phase phasial volume-averaged temperature values from the data file MacFluid.dat.

Subroutine INITS:

Initialises solid phase heat transfer values. Reads initial solid phase phasial volume-averaged temperature values from the data file MacSolid.dat.

Subroutine INTERFACEHT:

Calculates heat transfer across the interface between the solid and the fluid phases.

Subroutine OUTPUT2:

Writes the fluid phase phasial volume-averaged velocity component values to the output file MacSolidFluid.out. This subroutine is called when VELOCITY = 'y' in namelist FILEOUTPUT_CONTROL in the input file MacSolidFluid.inp.

Subroutine OUTPUTSCREENF:

Writes to the console the fluid phase phasial volume-averaged temperature value of a particular grid point from the present iteration, and the difference between the present iteration and the previous iteration values for that particular grid point.

Subroutine OUTPUTF1:

Writes the fluid phase phasial volume-averaged temperature values to the data file MacFluid.dat.

Subroutine OUTPUTF2:

Writes the fluid phase phasial volume-averaged temperature values to the output file MacSolidFluid.out. This subroutine is called when TEMPFLUID = 'y' in namelist FILEOUTPUT_CONTROL in the input file MacSolidFluid.inp.

Subroutine OUTPUTF4:

Writes values for the conduction, convection and total heat transfer across the finite volume boundaries to the output file MacSolidFluid.out. This subroutine is called when HEATFLUXFLUID = 'y' in namelist FILEOUTPUT_CONTROL in the input file MacSolidFluid.inp.

Subroutine OUTPUTF5:

Writes the coefficient values of the discretised fluid phase phasial volume-averaged temperature equations to the output file MacSolidFluid.out. This subroutine is called when TEMPCOEFFFLUID = 'y' in namelist FILEOUTPUT_CONTROL in the input file MacSolidFluid.inp.

Subroutine OUTPUTF6:

Writes the values for heat transfer across the interface between the solid and the fluid phases to the output file MacSolidFluid.out. This subroutine is called when INTERPHASIALFLUX = 'y' in namelist FILEOUTPUT_CONTROL in the input file MacSolidFluid.inp.

Subroutine OUTPUTF7:

Calculates the fluid phase secondary conduction heat transfer across the finite volume boundaries. Writes the calculated values to the output file MacSolidFluid.out. This subroutine is called when SECFLUXFLUID = 'y' in namelist FILEOUTPUT_CONTROL in the input file MacSolidFluid.inp.

Subroutine OUTPUTSCREENS:

Writes to the console the solid phase phasial volume-averaged temperature value of a particular grid point from the present iteration, and the difference between the present iteration and the previous iteration values for that particular grid point.

Subroutine OUTPUTS1:

Writes the solid phase phasial volume-averaged temperature values to the data file MacSolid.dat.

Subroutine OUTPUTS2:

Writes the solid phase phasial volume-averaged temperature values to the output file MacSolidFluid.out. This subroutine is called when TEMPSOLID = 'y' in namelist FILEOUTPUT_CONTROL in the input file MacSolidFluid.inp.

Subroutine OUTPUTS4:

Writes values for the conduction across the finite volume boundaries to the output file MacSolidFluid.out. This subroutine is called when HEATFLUXSOLID = 'y' in namelist FILEOUTPUT_CONTROL in the input file MacSolidFluid.inp.

Subroutine OUTPUTS5:

Writes the coefficient values of the discretised solid phase phasial volume-averaged temperature equations to the output file MacSolidFluid.out. This subroutine is called when TEMPCOEFFSOLID = 'y' in namelist FILEOUTPUT_CONTROL in the input file MacSolidFluid.inp.

Subroutine OUTPUTS7:

Calculates the solid phase secondary conduction heat transfer across the finite volume boundaries. Writes the calculated values to the output file MacSolidFluid.out. This subroutine is called when SECFLUXSOLID = 'y' in namelist FILEOUTPUT_CONTROL in the input file MacSolidFluid.inp.

Subroutine PROPSF:

Reads namelist PROPERTIESFLUID. Calculates the fluid phase effective thermal conductivity and coupled thermal conductivity. Assigns the uniform fluid phase heat

source value UNIINTSOURCEF to all the finite volume boundaries if UNISOURCEF = 'y'. Calculates the transverse thermal dispersion coefficient and the total energy transfer coefficient.

Subroutine PROPSS:

Reads namelist PROPERTIESSOLID. Calculates the solid phase effective thermal conductivity and coupled thermal conductivity. If UNISOURCES = 'y', the uniform fluid phase heat source value UNIINTSOURCES is assigned to all the finite volume boundaries.

Subroutine PSOLVE:

Executes a direct solution procedure on a specified set of equations.

Subroutine PSOLVEPREPF:

Calls subroutine PSOLVE to execute a direct solution procedure on the set of fluid phase phasial volume-averaged temperature linear algebraic equations.

Subroutine PSOLVEPREPS:

Calls subroutine PSOLVE to execute a direct solution procedure on the set of solid phase phasial volume-averaged temperature linear algebraic equations.

Subroutine RELAXF:

Relaxes the newly calculated fluid phase phasial volume-averaged temperature values after every iteration.

Subroutine RELAXS:

Relaxes the newly calculated solid phase phasial volume-averaged temperature values after every iteration.

Subroutine TEMPFIELDOUT:

Opens the data file TempField.dat and writes namelist TEMPFIELD to the data file.

Codes for the computer programs are included on Compact Disc

REFERENCES

Adler, P. M., 1992. *Porous Media: Geometry and Transports*. Butterworth-Heinemann, Toronto

Allen, M. B., G. A. Behie and J. A. Trangenstein, 1988. Multiphase flow in porous media: mechanics, mathematics and numerics. In: *Lecture Notes in Eng.*, **34**, Berlin, Springer

Anderson, T. B. and R. Jackson, 1967. A fluid mechanical description of fluidised beds. *Ind. Eng. Chem. Fundam.*, **6**, pp. 527-539

Angirasa, D. and G. P. Peterson, 1996. Forced convection heat transfer augmentation in a channel with a localized heat source using fibrous materials. *ASME Heat Transfer Div. Publ. HTD*, **330**, pp. 141-149

Antohe, B. V., J. L. Lage, D. C. Price and R. M. Weber, 1996. Numerical characterization of micro heat exchangers using experimentally tested porous aluminium layers. *Int. J. Heat Fluid Flow*, **17**, pp. 594-603

Auriault J. L. and P. Royer, 1993. Double conductivity media: a comparison between phenomenological and homogenisation approaches. *Int. J. Heat Mass Transfer*, **36**, pp. 2613-2621

Baron, T., 1952. Generalized graphic method for the design of fixed bed catalytic reactors. *Chem. Eng. Prog.*, **48**, pp. 118-124

Bastawros, A. F., A. G. Evans and H. A. Stone, 1998. *Evaluation of Cellular Metal Heat Transfer Media*. Report MECH 325. Division of Engineering and Applied Sciences, Harvard University, Cambridge, MA

Bauer, T. H., 1993. A general analytical approach toward the thermal conductivity of porous media. *Int. J. Heat Mass Transfer*, **36**, pp. 4181-4191

Bear, J., 1972. *Dynamics of Fluids in Porous Media*. American Elsevier, New York

Bear, J., 1988. *Dynamics of Fluids in Porous Media*. Dover

Bear, J. and Y. Bachmat, 1967. A generalized theory on hydrodynamics in porous media. *International Association of Scientific Hydrology Symposium*, Haifa, Publ. **72**, pp. 7-16

Bear, J. and Y. Bachmat, 1984. Transport phenomena in porous media - Basic equations. *Proc. 1982 NATO - Advanced Study Institute on the Fundamentals of Transport Phenomena in Porous Media*, Martinus Nijhoff, Dordrecht, pp. 3-61

Bear, J. and Y. Bachmat, 1986. Macroscopic modelling of transport phenomena in porous media: 2. Applications to mass, momentum and energy transport. *Transp. Porous Media*, **1,** pp. 241-269

Bear, J. and Y. Bachmat, 1991. Theory and applications of transport in porous media. In: *Introduction to Modelling of Transport Phenomena in Porous Media.* **4**. Ed.: J. Bear. Kluver Academic Publishers, Dordrecht

Bennethum, L. S. and T. Giorgi, 1997. Generalized Forchheimer equation for two-phase flow based on hybrid mixture theory. *Transp. Porous Media*, **26,** pp. 261-275

Bensoussan, A., J. L. Lions and G. Papanicolaou, 1987. *Asymptotic Analysis for Periodic Structures*. North-Holland

Bird, R. B., W. E. Steward and E. N. Lightfoot, 1960. *Transport Phenomena.* John Wiley and Sons, Inc., New York

Brenner, Dr. Walter, 1999. Maser Bond, Inc., Hackensack, NJ. Private communication

Brodkey, R. S. and H. C. Hershey, 1988. *Transport Phenomena*. McGraw-Hill Book Co.

Calmidi, V. V. and R. L. Mahajan, 1999. The effective thermal conductivity of high porosity fibrous metal foams. *ASME J. Heat Transfer*, **121**, pp. 466-470

Carberry, J. J., 1976. *Chemical and Catalytic Reaction Engineering*. McGraw-Hill, New York

Carbonell, R. G. and S. Whitaker, 1983. Dispersion in pulsed systems II. *Chem. Eng. Sci.*, **38**, pp. 1795-1802

Carbonell, R. G. and S. Whitaker, 1984. Heat and mass transfer in porous media. In: *Fundamentals of Transport Phenomena in Porous Media*. Eds.: J. Bear and M. A. Corapcioglu. Martinus Nijhof, pp. 121-198

Carlson, F. P., 1977. *Introduction to Applied Optics for Engineers*. Academic Press

Churchill, S. W. and R. Usagi, 1972. A general expression for the correlation of rates of transfer and other phenomena. *AIChE J.*, **18**, pp. 1121-1128

Combarnous, M. A. and S. A. Bories, 1975. Hydrothermal convection in saturated porous media. *Adv. Hydrosci.*, **10**, pp. 231-307

Darcy, H., 1856. *Les Fontains Publiques de la ville de Dijon*. Dalmont, Paris

De Josselin de Jong, G., 1958. Longitudinal and transverse diffusion in granular deposits. *Trans. Amer. Geophys. Union*, **39**, pp. 67-74

Didierjean, S., H. P. A. Souto, R. Delannay and C. Moyne, 1997. Dispersion in periodic porous media. *Chem. Eng. Sci.*, **52**, pp. 1861-1874

Dobran, F., 1991. *Theory of Structured Multiphase Mixtures*. Springer-Verlag, Berlin

Dullien, F. A. L, 1979. *Porous Media: Fluid Transport and Pore Structure*. Academic Press, New York

Du Plessis, J. P., 1989. Unified porous media modelling. *Proceedings of the 31st Heat Transfer and Fluid Mechanics Institute*. Eds.: F. H. Reardon and N. D. Thinh. California State University, California, USA, June 1-2, pp. 309-320

Du Plessis, J. P., 1991a. Pore-scale modelling of flow through different types of porous environments. In: *Heat and Mass Transfer in Porous Media*. Eds.: M. Quintard and M. Todorovic. Elsevier, Amsterdam, pp. 249-262

Du Plessis, J. P., 1991b. Saturated crossflow through a two-dimensional porous medium. *Adv. Water Resour.*, **14**, pp. 131-137

Du Plessis, J. P. and J. H. Masliyah, 1988. Mathematical modelling of flow through consolidated isotropic porous media. *Transp. Porous Media*, **3**, pp. 145-161

Du Plessis, J. P. and J. Van der Westhuizen, 1993. Laminar crossflow through prismatic porous domains. *R&D J. SAIME*, **9**, pp. 18-24

Du Plessis, J. P., A. Montillet, J. Comiti and J. Legrand, 1994. Pressure drop prediction for flow through high porosity metallic foams. *Chem. Eng. Sci.*, **49**, pp. 3545-3553

Du Plessis, J. P. and J. P. Diedericks, 1997. Pore-scale modelling of interstitial transport phenomena. In: *Fluid Transport in Porous Media*. Ed. J. P. du Plessis. Computational Mechanics Publications, pp. 61-104

Dybbs, A. and R. V. Edwards, 1984. A new look at porous media fluid mechanics – Darcy to turbulent. In: *Fundamentals of Transport in Porous Media*. Eds.: J. Bear and M. Y. Corapcioglu. Martinus Nijhoff Publishers, pp. 199-254

Eckert E. R. and E. Soengen, 1952. Distribution of heat transfer coefficients around circular cylinders in crossflow at Reynolds numbers from 20 to 500. *Trans. ASME*, **70**, pp. 343-347

Ene, H. I. and D. Polisevski, 1987. *Thermal Flow in Porous Media*, Reidel, Dordrecht

Faires, V. M and C. M. Simmang, 1978. *Thermodynamics*, 6th ed. Macmillan, New York

Fara, H. and A. E. Scheidegger, 1961. Statistical geometry of porous media. *J. Geophys. Res.*, **66**, pp. 3279-3294

Flamant, G., N. Fatah, G. Olalde and D. Hernandez, 1992. Temperature distribution near a heat exchanger wall immersed in high-temperature packed and fluidised beds. *ASME J. Heat Transfer*, **114**, pp. 50-55

Fortes, M. A., 1986. The average number of grain boundaries per grain in a polycrystal. *Acta Metall.*, **34**, pp. 33-36

Forchheimer, P. H., 1901. Wasserbewegung durch boden. *Z. Ver. Dtsch. Ing.*, **45**, pp. 1782-1788

Fortini A. J. and R. H. Tuffias, 1998. *Foam Heat Exchangers*, Report LEW-16579, NASA Lewis Research Center, Cleveland, Ohio, USA

Fried, J. J., 1975. *Groundwater Pollution*. Elsevier Scientific Publishing Company, Amsterdam

Froment, G. F. and K. B. Bischoff, 1979. *Chemical Reactor Analysis and Design*. Wiley, New York

Gibson, L. J. and M. F. Ashby, 1988. *Cellular Solids*. Cambridge University Press, New York

Glatzmaier, G. C. and W. F. Ramirez, 1988. Use of volume averaging for the modelling of thermal properties of porous materials. *Chem. Eng. Sci.*, **30**, pp. 3157-3169

Gnielinski, V., A. Zukauskas and A. Skrinsk, 1987. Banks of plain and finned tubes. In: *Heat Exchanger Design Handbook*. Eds.: B. A. Bodling and M. Prescott. Hemisphere Publishing Co.

Gray, W. G., 1975. A derivation of the equations for multiphase transport. *Chem. Eng. Sci.*, **30**, pp. 229-233

Guilleminot, J. J. and J. M. Gurgel, 1990. Heat transfer intensification in adsorbent beds of adsorption thermal devices. Proceedings of *Solar Engineering 1990 – The 12th Annual International Solar Engineering Conference*, Miami, FL, USA. ASME Publication, pp. 69-74

Guilleminot, J. J., A. Choisier, J. B. Chalfen, S. Nikolas and J. L. Reymoney, 1993. Heat transfer intensification in fixed bed adsorbers. *Heat Recovery Syst. CHP*, **13**, pp. 297-300

Harlow, F. H. and J. E. Welsh, 1965. Numerical calculation of time-dependent viscous incompressible flow of fluid with free surface. *Phys. Fluids*, **8**, pp. 2182-2189

Hassanizadeh, M. and W. G. Gray, 1979a. General conservation equations for multi-phase systems: 1. Averaging procedure. *Adv. Water Resour.*, **2**, pp. 131-190

Hassanizadeh, M. and W. G. Gray, 1979b. General conservation equations for multi-phase systems: 2. Mass, momentum, energy and entropy equations. *Adv. Water Resour.*, **2**, pp. 191-240

Holman, J. P., 1976. *Heat Transfer*. McGraw-Hill Inc., New York

Hsu, C. T., 1994. Modified Zehner-Schlunder models for stagnant thermal conductivity of porous media. *Int. J. Heat Mass Transfer*, **37**, pp. 2751-2759

Hunt, M. L. and C. L. Tien, 1988. Effects of thermal dispersion on forced convection in fibrous media. *Int. J. Heat Mass Transfer*, **31**, pp. 301-309

Imai, I., 1957. Second approximation to the laminar boundary layer flow over a flat plate. *J. Aeronaut Sci.*, **24**, pp. 155-156

Isaacson, E. and H. B. Keller, 1966. *Analysis of Numerical Methods.* John Wiley and Sons, Inc.

Jacob, M., 1949. *Heat Transfer*, **1**, John Wiley and Sons, Inc.

Karniadakis, G. E., B. B. Mikic and A. T. Patera, 1988. Minimum dissipation transport enhancement by flow destabilization: Reynolds analogy revised. *J. Fluid Mech.*, **192**, pp. 365-391

Katinas V., J. Ziugzda and A. Zukauskas, 1971. Heat transfer from curved bodies in transverse flow of viscous fluids. *Heat Transfer Sov. Res.*, **3** (6), pp. 10-33

Kaviany, M., 1985. Laminar flow through a porous channel bounded by isothermal parallel plates. *Int. J. Heat Mass Transfer*, **28**, pp. 851-858

Kaviany, M., 1995. *Principles of Heat Transfer in Porous Media.* Springer-Verlag, NewYork

King, H. H., 1976. A Poisson equation solver for rectangular and annular regions. *Int. J. Num. Methods Eng.*, **10**, pp. 799-807

Koch D. L. and J. F. Brady, 1985. Dispersion in fixed beds. *J. Fluid Mech.*, **154**, pp. 399-427

Koch D. L. and J. F. Brady, 1986. The effective diffusivity of fibrous media. *AIChE J.*, **32**, pp. 575-591

Koch D. L., R. G. Cox, H. Brenner and J. F. Brady, 1989. The effect of order on dispersion in porous media. *J. Fluid Mech.*, **200**, pp. 173-188

Kreyszig, E., 1993. *Advanced Engineering Mathematics.* John Wiley & Sons, Inc.

Kuzai, T. M., J. T. Collins, A. M. Khounsary and G. Morales, 1991. Enhanced heat transfer with metal wool filled tubes. *Proceedings of the ASME/JSME Thermal Engineering Conference*, pp. 145-151

Lakatos, I., 1976. In: *Proofs and Refutations, the Logic of Mathematical Discovery*. Eds. J. Worrall and E. Zahar. Cambridge University Press, Cambridge

Levec, J. and R. G. Carbonell, 1985a. Longitudinal and lateral dispersion in packed beds – I: Theory. *AIChE J.*, **31**, pp. 581-590

Levec, J. and R. G. Carbonell, 1985b. Longitudinal and lateral dispersion in packed beds – II: Comparison between theory and experiments. *AIChE J.*, **31**, pp. 591-602

Lindemuth, J. E., D. M. Johnson and J. H. Rosenfeld, 1994. Evaluation of porous metal heat exchangers for high heat flux applications. In: *Heat Transfer in High Heat Flux Systems*. Eds. A. M. Khonsary, T. W. Simon, R. D. Boyd and A. J. Ghajar. ASME – HTD, **301**, pp. 93-98

Lu T. J., A. G. Evans and J. W. Hudchinson, 1998a. The effects of material properties on heat dissipation in high power electronics. *ASME J. Electr. Packaging*, **120**, pp. 280-289

Lu T. J., H. A. Stone and M. F. Ashby, 1998b. Heat transfer in open-cells metal foams. *Acta Mater.*, **46**, pp. 3619-3635

Marle, C. M., 1967. Ecoulements monophasiques en milieu porex. *Rev. Inst. Fr. Pet.*, **22**, pp. 1471-1509

Mazza, G. D. and G. F. Baretto, 1988. The gas contribution to heat transfer between fluidised beds and of large particles and immersed surfaces. *Int. J. Heat Mass Transfer*, **31**, pp. 603-614

Megerlin, F. E., R. W. Murphy and A. E. Bergles, 1974. Augmentation of heat transfer in tubes by use of mesh and brush inserts. *ASME J. Heat Transfer*, **96**, pp. 145-151

Mei, C. C., 1992. Method of homogenisation applied to dispersion in porous media. *Transp. Porous Media*, **9**, pp. 261-274

Moyne, C., 1997. Two-equation model for a diffusion process in porous media using the volume averaging method with an unsteady-state closure. *Adv. Water Resour.*, **20**, pp. 63-76

Nield, D. A. and A. Bejan, 1992. *Convection in Porous Media*. Springer-Verlag, New York

Nitsche, L. C. and H. Brenner, 1989. Eulerian kinematics of flow through spatially periodic models of porous media. *Arch. Rational Mech. Anal.*, **107**, pp. 225-292

Nozad, I., R. G. Carbonel and S. Whitaker, 1985. Heat conduction in multiphase systems: I. Theory and experiment for two-phase systems. *Chem. Eng. Sci.*, **40,** pp. 843-855

Patankar, S. V., 1980. *Numerical Heat Transfer and Fluid Flow*. Hemisphere Publ. Co., New York

Patankar, S.V. and D. B. Spalding, 1972. A calculation procedure for heat, mass and momentum transfer in three-dimensional parabolic flows. *Int. J. Heat Mass Transfer*, **15**, pp. 1787-1805

Pepper, D. W. and A. J. Baker, 1988. Finite differences versus finite elements. In: *Handbook of Numerical Heat Transfer*. Eds.: W. J. Minkowycz, E. M. Sparrow, G. E. Schneider and R. H. Pletcher. John Wiley & Sons, Inc.

Peng, X. F., B. X. Wang, G. P. Peterson and H. B. Ma, 1995. Experimental investigation of heat transfer in flat plates with rectangular microchannels. *Int. J. Heat Mass Transfer*, **38**, pp. 127-137

Pereira Duarte, S. I., O. A. Ferretti and N. O. Lemcoff, 1984. A heterogeneous one-dimensional model for non-adiabatic fixed bed catalytic reactors. *Chem. Eng. Sci.*, **30**, pp. 1025-1031

Polhausen, E., 1921. Der Wärmeaustausch zwischen festern Körpen und Flüssigkeiten mit kleiner Reibang und kleiner Wärmeleitung. *Z. Angew. Math. Mech.*, **1**, pp. 115-121

Quintard, M., M. Kaviany and S. Whitaker, 1997. Two-medium treatment of heat transfer in porous media: Numerical results for effective properties. *Adv. Water Resour.*, **20**, pp. 77-94

Quintard, M and S. Whitaker, 1993. One- and two-equation models for transient diffusion processes in two-phase systems. *Adv. Heat Transfer*, **23**, pp. 369-464

Quintard, M. and S. Whitaker, 1994a. Transport in ordered and disordered porous media, I: The cellular average and the use of weighting functions. *Transp. Porous Media*, **14**, pp. 163-177

Quintard, M. and S. Whitaker, 1994b. Transport in ordered and disordered porous media, II: Generalized volume averaging, the cellular average and the use of weighting functions. *Transp. Porous Media*, **14**, pp. 179-206

Reis, J. F. G., E. N. Lightfoot, P. T. Noble and A. S. Chiang, 1979. Chromatography in beds of spheres. *Separation Sci. Tech.*, **14**, p. 367-394

Rohsenow, W. M. and H. Y. Choi, 1961. *Heat, Mass and Momentum Transfer*. Prentice-Hall

Rubenstein, J. and R. Mauri, 1986. Dispersion and convection in porous media. *SIAM J. Appl. Math.*, **46**, pp. 1018-1023

Saffman, P. G., 1959a. Dispersion in flow through a network of capillaries. *Chem. Eng. Sci.*, **11**, pp. 125-129

Sahraoui, M. and M. Kaviany, 1994. Slip and no-slip temperature boundary conditions at interface of porous, plain media: convection. *Int. J. Heat Mass Transfer*, **37**, pp. 1029-1044

Sanchez-Palencia, E., 1980. Non-homogeneous media and vibration theory. *Lecture Notes in Phys.*, **127**

Sangani, A. S. and S. Behl, 1989. The planar singular solution of Stokes and Laplace equations and their application to transport processes near porous surfaces. *Phys. Fluids*, **A**, pp. 21-37

Scheidegger, A. E., 1974. *The physics of flow through porous media*, 3rd ed. University of Toronto Press

Schlichting, H., 1979. *Boundary Layer Theory*. McGraw-Hill, New York

Schlünder, E. U., 1975. Equivalence of one- and two-phase models for heat transfer processes in backed beds: one-dimensional theory. *Chem. Eng. Sci.*, **30**, pp. 449-452

Shah, R.K., and A. L. London, 1987. Laminar flow forced convection in ducts. *Adv. Heat Transfer*, Suppl. 1. Eds. F. I. Thomas and J. P. Hartnett. Academic Press, London

Slattery, J. C., 1967. Flow of viscoelastic fluids through porous media. *AIChE J.*, **13**, pp. 1066-1071

Smit, G. J. F and J. P. Du Plessis, 1999. Modelling of non-Newtonian purely viscous flow through isotropic high porosity synthetic foams. *Chem. Eng. Sci.*, **54**, pp. 645-654

Spielman, L. and S. L. Goren, 1968. Model for predicting pressure drop and filtration efficiency in fibrous media. *Envir. Sci. Tech.*, **2**, pp. 279-287

Taylor, G. I., 1953. Dispersion of soluble matter in solvent flowing slowly through a tube. *Proc. Roy. Soc. London*, **A219**, pp. 186-203

Taylor, G. I., 1954. Conditions under which dispersion of solute in a stream of solvent can be used to measure molecular diffusion. *Proc. Roy. Soc. London*, **A225**, pp. 473-477

Tien, K. and K. Vafai, 1990. Convective and radiative heat transfer in porous media. *Adv. Appl. Mech.*, **27**, pp. 225-281

Vafai, K. and M. Sözen, 1990. Analysis of energy and momentum transport for fluid flow through a porous bed. *ASME J. Heat Transfer*, **112**, pp. 690-699

Van Doormaal, J. P. and G. D. Raithby, 1984. Enhancements of the SIMPLE method for predicting incompressible fluid flows. *Numer. Heat Transfer*, **7**, pp. 147-163

Vortmeyer, D. and R. J. Schaefer, 1974. Equivalence of one- and two-phase models for heat transfer processes in backed beds, one-dimensional theory. *Chem. Eng. Sci.*, **29**, pp. 485-491

Vortmeyer, D., 1975. Axial heat dispersion in backed beds. *Chem. Eng. Sci.*, **30**, pp. 999-1001

Weaire, D. and N. Rivier, 1984. Soap, cells and statistics – random patterns in two dimensions. *Contemp. Phys*, **25**, pp. 59-99

Whitaker, S., 1967. Diffusion and dispersion in porous media. *AIChE J.*, **13,** pp. 420-427

Whitaker, S., 1973. Transport equations for multiphase systems. *Chem. Eng. Sci.*, **28**, pp. 139-147

Whitaker, S., 1977. Simultaneous heat, mass and momentum transfer in porous media: A theory of drying. *Adv. Heat Transfer*, **13,** pp. 119-203

Whitaker, S., 1980. Heat and mass transfer in granular porous media. *Adv. Drying*, **1**, pp. 23-61

Whitaker, S., 1983. Diffusion and reaction in a micropore-macropore model of a porous medium. *Lat. Am. J. Chem. Eng. Appl. Chem.*, **13**, pp. 143-183

Whitaker, S., 1989. Heat transfer catalytic packed bed reactors. In: *Handbook of Heat and Mass Transfer*. Vol. 3, Catalysis, Kinetics & Reactor Engineering. Ed.: N.P. Cheremisinoff, Ch. 10. Gulf Publishers, New Jersey.

Whitaker, S., 1991. Improved constraints for the principle of lacal thermal equilibrium. *Ind. Eng. Chem. Res. Dev.*, **30**, pp. 983-997

White, F. M., 1991. *Viscous Fluid Flow*, 2nd ed. McGraw-Hill Inc.

Zanotti, F. and R. G. Carbonell, 1984a. Development of transport equations for multiphase systems. I. General development for two-phase systems. *Chem. Eng. Sci.*, **39**, pp. 263-278

Zanotti, F. and R. G. Carbonell, 1984b. Development of transport equations for multiphase systems. II. Application to one-dimensional axi-symmetric flows of two phases. *Chem. Eng. Sci.*, **39**, pp. 279-297

Zanotti, F. and R. G. Carbonell, 1984c. Development of transport equations for multiphase systems. III. Application to heat transfer in packed bed. *Chem. Eng. Sci.*, **39**, pp. 299-311

Zuber, N., 1964. On the dispersed flow in the laminar flow regime. *Chem. Eng. Sci.*, **19**, pp. 897-917

Zucrow, M. J. and J. D. Hoffman, 1976. *Gas Dynamics*. **1**. John Wiley & Sons, Inc.

Zukauskas, A., 1987. Heat transfer from tubes in crossflow. *Adv. Heat Transfer*, **18**, pp. 87-159

Zukauskas, A. and J. Ziugzda, 1985. *Heat Transfer of a Cylinder in Crossflow*. Hemisphere Publ.Co.

Zukauskas, A. and R. Ulinskas, 1983. Banks of plain and finned tubes. In: *Heat Exchanger Design Handbook*. Eds. B. A. Bodling and M. Prescott. Hemisphere Publishing Co.